

REPORT DOCUMENTATION PAGE		READ INSTRUCTIONS BEFORE COMPLETING FORM
1. REPORT NUMBER AFWAL-TR-80-4140	2. GOVT ACCESSION NO.	3. RECIPIENT'S CATALOG NUMBER
4. TITLE (and Subtitle) VISCOPLASTIC AND CREEP CRACK GROWTH ANALYSIS BY THE FINITE ELEMENT METHOD		5. TYPE OF REPORT & PERIOD COVERED July 1977 - June 1980 PhD Dissertation
7. AUTHOR(s) Terry D. Hinnerichs, Captain, USAF		6. PERFORMING ORG. REPORT NUMBER
9. PERFORMING ORGANIZATION NAME AND ADDRESS Materials Laboratory Air Force Wright Aeronautical Laboratories Air Force Systems Command Wright-Patterson Air Force Base, Ohio 45433		8. CONTRACT OR GRANT NUMBER(s)
11. CONTROLLING OFFICE NAME AND ADDRESS Materials Laboratory Air Force Wright Aeronautical Laboratories Wright-Patterson Air Force Base, Ohio 45433		10. PROGRAM ELEMENT PROJECT, TASK AREA & WORK UNIT NUMBERS P.E. 61102F 2307-P1-02
14. MONITORING AGENCY NAME & ADDRESS (if different from Controlling Office)		12. REPORT DATE July 1981
		13. NUMBER OF PAGES 177
		15. SECURITY CLASS. (of this report)  UNCLASSIFIED
		15a. DECLASSIFICATION DOWNGRADING SCHEDULE
16. DISTRIBUTION STATEMENT (of this Report)  Approved for public release; distribution unlimited.		
17. DISTRIBUTION STATEMENT (of the abstract entered in Block 20, if different from Report)		
18. SUPPLEMENTARY NOTES		
19. KEY WORDS (Continue on reverse side if necessary and identify by block number)  Creep Crack Growth Finite Element Method Viscoplasticity		
20. ABSTRACT (Continue on reverse side if necessary and identify by block number)  Creep crack growth in a nickel base alloy at elevated temperatures was analyzed through a hybrid experimental-numerical (HEN) procedure. This HEN procedure consisted of simultaneous use of creep crack growth test displacement data from center cracked plate specimens of IN-100 at 1350°F and a theoretical finite element model of the test specimen.  A two-dimensional (constant strain triangular) finite element program was developed which accounts for both nonlinear viscoplastic material behavior and changing boundary conditions due to crack growth. Three viscoplastic material		

models -- (1) Malvern Flow Law, (2) Norton's Creep Law, and (3) Bodner-Partom Flow Law -- were incorporated into the program. These time dependent material models were numerically integrated through time by a linear Euler extrapolation technique. A variable time step algorithm was included that maximized time step size during the analysis while maintaining good accuracy. This program was used as the plane stress theoretical model for the HEN procedure to analyze sustained load creep crack growth.

A method for getting creep crack growth behavior solely from high resolution displacement measurements, in conjunction with a cracked specimen model which utilizes realistic constitutive relationships, has been developed. The constitutive law, in the form of the Bodner-Partom material model, was especially tailored to the nickel-base alloy studied which displays time dependent nonlinear inelastic behavior at elevated temperatures. It has been demonstrated that the technique can be applied where crack extension is very small and could not otherwise be resolved by conventional experimental crack measuring techniques. This method provides realistic monotonically increasing crack growth values. The predictions agreed to within 10% of post-test measurements.

Crack growth rate and crack growth criteria were studied. Crack tip strain and crack opening displacement were studied in the HEN results for a unique parameter controlling crack growth. Because the parameters were not independent of time due to apparent environmental degradation, it became necessary to establish an empirical criterion for crack growth based on the best fit of HEN results. A damage accumulation criterion based on creep rupture formulations was also developed and applied with promising results.

Several crack growth rate criteria were investigated, one of which is the stress intensity factor. The K criterion matched fairly well with an extrapolation of published results. But two other criteria, based on the  $C^*$  integral and load point displacement rate which are closely related theoretically, were found to be ineffective as crack growth rate criteria.

AFWAL-TR-80-4140

## PREFACE

This report was prepared by the Metals Behavior Branch, Metals and Ceramics Division, Materials Laboratory, Air Force Wright Aeronautical Laboratories, Wright-Patterson Air Force Base, Ohio 45433. The research reported herein was conducted under Project No. 2307, "Solid Mechanics," Task 2307P102, "Failure Prediction in Metals." The work was performed during the period July 1977 to June 1980 by Terry D. Hinnerichs as project engineer.

The author would like to express his gratitude to Professor A. N. Palazotto for his patience, technical guidance, and encouragement during the course of this study. Thanks goes to Dr. T. Nicholas of the Air Force Wright Aeronautical Laboratories for his helpful suggestions, as well as sponsoring the study and supplying the computer resources. Thanks also goes to Professors D. W. Breuer and D. D. Hardin for their valuable suggestions and interest in the topic. Appreciation is also extended to Dr. A. Grandt for suggesting the topic for this study.

*Contrails*

## TABLE OF CONTENTS

SECTION		PAGE
I	INTRODUCTION	1
	1. Background	1
	2. Approach	3
II	LITERATURE REVIEW	6
	1. Analytical Creep Crack Growth Studies	8
	2. Finite Element Analysis Related to Quasi-Static Time Dependent Crack Growth	11
	a. Elastic-Plastic (Time Independent) Analysis	11
	b. Visco-Plastic and Creep (Time Dependent) Analysis	14
III	FINITE ELEMENT COMPUTER PROGRAM DEVELOPMENT	16
	1. Visco-Plastic Material Models	16
	a. Malvern (Overstress) Flow Law	18
	b. Norton's Law for Secondary Creep	21
	c. Bodner Viscoplastic Flow Law	22
	2. Solution Procedure for Elastic-Viscoplastic Structures	27
	3. Variable Time Step Integration of Viscoplastic Flow Laws	32
	a. Malvern Model	36
	b. Bodner Model	36
	4. Validation Examples	38
	a. Infinite Sheet with Pressurized Hole	40
	b. Thick Cylinder with Internal Pressure	41
	c. V-Notched Plate in Tension	41
	d. Cracked Three Point Bend Specimen	47
	e. Center Cracked Plate with Bodner Model	53

## TABLE OF CONTENTS (CONTINUED)

SECTION		PAGE
III	5. Summary of Findings	60
IV	HYBRID EXPERIMENTAL-NUMERICAL PROCEDURE TO ANALYZE CREEP CRACK GROWTH	62
	1. Crack Length Versus Time	62
	2. Matching Experimental Displacement Data	66
	3. Crack Tip Node Release Methods	66
V	APPLICATION OF THE HYBRID EXPERIMENTAL-NUMERICAL PROCEDURE TO CREEP CRACK GROWTH	69
	1. Crack Growth Predictions	79
	a. Comparison of Results from Using Different Node Unloading Methods	96
	b. Dependence on Deformation History	97
	c. Crack Growth Results	102
	2. Crack Growth Criterion	108
	a. Critical Strain Criterion	108
	b. Critical Crack Opening Displacement Criterion	115
	c. Critical Damage Accumulation Criterion	115
	3. Crack Growth Rate Criteria	120
	a. Stress Intensity Factor Criterion	128
	b. Net Section Stress Criterion	130
	c. $C^*$ Integral Criterion	130
	d. Load Point Displacement Rate Criterion	132
VI	SUMMARY AND CONCLUSIONS	133
	REFERENCES	138
	APPENDIX A FINITE ELEMENT FORMULATION	145
	1. Displacement Model	145

## TABLE OF CONTENTS (CONCLUDED)

SECTION	PAGE
a. Displacement Function	146
b. Element Strain	148
2. Elastic Analysis	148
a. Method of Solution	149
3. Elastic-Plastic Analysis	150
a. Yield Criterion	150
b. Flow Theory	151
4. Elastic-Plastic Solution Techniques	153
a. Initial Stress Method	154
b. Initial Strain Method	155
APPENDIX B    ITERATIVE SOLUTION TECHNIQUE FOR NODE POINT DISPLACEMENTS	160
APPENDIX C    THE J AND C* INTEGRALS	164
1. J Integral	164
2. C* Integral	166
APPENDIX D    DETERMINATION OF BODNER MATERIAL MODEL CONSTANTS	168
1. Short Time Response Constants	169
2. Creep Constants	171

LIST OF ILLUSTRATIONS

FIGURE		PAGE
1	Three Stages of Creep Behavior	7
2	Line Integral Paths for J and C*	7
3	Variation of Malvern Model Behavior with $\gamma_p$ Under Constant Strain Rate Loading Conditions	19
4	Stress-Strain Behavior of Bodner Model (IN-100 Constants)	28
5	Creep Behavior of Bodner Model at 127.3 ksi (IN-100 Constants)	29
6	Creep Behavior of Bodner Model at 72.0 ksi (IN-100 Constants)	30
7	V-Notched Plate Model	35
8	Radial & Tangential Stresses for the Infinite Plate with Pressurized Hole	42
9a	Thick Cylinder with Internal Pressure, Tangential Stress Profile	43
9b	Thick Cylinder with Internal Pressure, Finite Element Mesh	43
10	Stress Profile for V-Notched Plate in Tension	45
11	Plastic Zone in V-Notched Plate	46
12	Three-Point Bend Specimen with Crack	48
13	Three-Point Bend Finite Element Model	49
14	Crack Opening Displacement Profile @ $U_A = .050$ In. for Three-Point Bend Model	50
15	Crack Mouth Opening Displacement vs. Load for Three-Point Model	51
16	Load Point Displacement vs. Load for Three-Point Bend Model	52
17	Center Cracked Plate Finite Element Model, $a/W = 0.1367$	55
18	Stress vs. Strain at the Crack Tip for Bodner, Malvern-Norton, and Norton Material Models	56



## LIST OF ILLUSTRATIONS (Continued)

FIGURE		PAGE
19	Effective Stress & Strain vs. Time at the Crack Tip for Bodner, Malvern-Norton, and Norton Material Models	57
20	Crack Mouth Displacements in Center Cracked Plate for Bodner, Malvern-Norton, and Norton Material Models	58
21	Center Cracked Plate Test Specimen	63
22	Displacement Under Constant Load	63
23	Experimental Load vs. Time	65
24	Experimental Compliance Changes with Time	65
25	Elastic Compliance vs. Crack Length	65
26a	Crack Tip Node Unload Methods, Finite Element Crack Tip	68
26b	Crack Tip Node Unload Methods, 5 Sec. Node Unload Method	68
26c	Crack Tip Node Unload Methods, Continuous Node Unload Method	68
27	Experimental Creep Crack Growth Specimen	70
28	Center Cracked Plate Finite Element Model, $a/W = 0.1367$	71
29	Center Cracked Plate Finite Element Model, $a/W = 0.2367$	72
30	Center Cracked Plate Finite Element Model, $a/W = 0.3117$	73
31	Uniform Mesh Ahead of Crack Tip	75
32	Comparison of Compliance from VISCO with Eftis & Liebowitz for the Center Cracked Plate	77
33	Elastic Crack Opening Displacement Profiles from VISCO	78
34	Fracture Surface of Specimen No. 2	83
35	Post-Test Crack Growth Measurements	84

## LIST OF ILLUSTRATIONS (Continued)

FIGURE		PAGE
36a	J Integral Paths Used by VISCO	86
36b	Stress Intensity Factors from VISCO J Integrals & Equation 57	86
37a	Test 5 HEN VISCO Results, Displacements Matched to Test Data	90
37b	Test 5 HEN VISCO Results, Crack Growth	90
38a	Test 6 HEN VISCO Results, Displacements Matched to Test Data	91
38b	Test 6 HEN VISCO Results, Crack Growth	91
39a	Test 8a HEN VISCO Results, Displacements Matched to Test Data	92
39b	Test 8a HEN VISCO Results, Crack Growth	92
40a	Test 9 HEN VISCO Results, Displacements Matched to Test Data	93
40b	Test 9 HEN VISCO Results, Crack Growth	93
41a	Test 12a HEN VISCO Results, Displacements Matched to Test Data	94
41b	Test 12b HEN VISCO Results, Crack Growth	94
42a	Test 12b HEN VISCO Results, Displacements Matched to Test Data	95
42b	Test 12b HEN VISCO Results, Crack Growth	95
43	Crack Tip Effective Stress at the Time the Crack Tip Node Is Begun to be Released	98
44	Crack Tip Plastic Strain at the Time the Crack Tip Node Is Begun to be Released	99
45	Load History Dependence of Displacements	101
46	Comparison of Crack Growth from Experimental Compliance with HEN VISCO Results	104
47	Schematic of Displacements Used to Calculate Crack Growth by Equation 59	106

## LIST OF ILLUSTRATIONS (Continued)

FIGURE		PAGE
48	Crack Opening Displacement Profiles During Creep Crack Growth	109
49a	VISCO Critical Strain Crack Growth Criterion, Resulting Displacements Due to Crack Growth	112
49b	VISCO Critical Strain Crack Growth Criterion, Resulting Crack Growth	112
50	Time Dependent Critical Strain Crack Growth Criterion	113
51	VISCO Critical C.O.D. Criterion, Resulting Displacements	116
52	Schematic Representation of Creep Crack Propagation	118
53a	Test 5 - VISCO Critical Damage Accumulation Criterion Displacement Results	122
53b	Test - VISCO Critical Damage Accumulation Criterion Crack Growth Results	122
54a	Test 6 - VISCO Critical Damage Accumulation Criterion Displacement Results	123
54b	Test 6 - VISCO Critical Damage Accumulation Criterion Crack Growth Results	123
55a	Test 8a - VISCO Critical Damage Accumulation Criterion Displacement Results	124
55b	Test 8a - VISCO Critical Damage Accumulation Criterion Crack Growth Results	124
56a	Test 9 - VISCO Critical Damage Accumulation Criterion Displacement Results	125
56b	Test 9 - VISCO Critical Damage Accumulation Criterion Crack Growth Results	125
57a	Test 12a - VISCO Critical Damage Accumulation Criterion Displacement Results	126
57b	Test 12a - VISCO Critical Damage Accumulation Criterion Crack Growth Results	126
58a	Test 12b - VISCO Critical Damage Accumulation Criterion Displacement Results	127

## LIST OF ILLUSTRATIONS (Concluded)

FIGURE		PAGE
58b	Test 12b - VISCO Critical Damage Accumulation Criterion Crack Growth Results	127
59	Crack Growth Rate vs. Stress Intensity Factor	129
60	Crack Growth Rate vs. Net Section Stress	131
A-1	Constant Strain Triangular Element	147
A-2	Uniaxial "Initial" Stress Iteration Schematic	156
A-3	Initial Stress Algorithm	157
A-4	Uniaxial Initial Strain Iteration Schematic	159
C-1	J Integral Paths within a Constant Strain Triangular Finite Element Model	165

## LIST OF TABLES

TABLE		PAGE
1	Plastic Strain Energy Variations in the V-Notched Plate Using the Malvern Model	37
2	Plastic Strain Energy Variations in the V-Notched Plate Using the Bodner Model	39
3	Summary of Sharpe Test Data	80
4	Summary of Measured Vs. Calculated Initial Crack Lengths and Applied Finite Element Model, $K_{FE}$ vs. Effective Experimental, $K_{eff}$	81
5	Summary of Hybrid Experimental-Numerical VISCO Runs	88
6	Summary of VISCO Runs with No Crack Growth	89
7	Summary of Measured and Calculated Crack Growth	103
8	Summary of VISCO Runs with Critical Strain Criteria	111
9	Summary of VISCO Runs with Critical C.O.D. Criteria	111
10	Summary of VISCO Runs with Damage Accumulation Criterion	121

LIST OF SYMBOLS

$\dot{(\ )}$	Time rate of change of ( )
$a$	Half crack length in center cracked plate/full length of crack in three point bend specimen
$a_o$	Crack length used in finite element model
$a_c$	Crack length determined by compliance
$A$	Empirical constant/Bodner material constant
$b$	Empirical constant
$B$	Empirical constant
$B_o$	Ramberg-Osgood equation constant
$[B]$	Matrix relating total strain to nodal displacements
$C$	Empirical constant
$C_E$	Experimental compliance
$C_{FE}$	Finite element model compliance
$C^*$	The $C^*$ integral
$dt^i$	The $i^{th}$ time step
$dt_M$	Maximum stable time step size for Malvern model
$dt_N$	Maximum stable time step size for Norton model
$d\epsilon_{ij}$	Incremental component of total strain
$d\epsilon_{ij}^P$	Incremental component of plastic strain
$D$	Empirical constant
$D_o$	Bodner material constant
$D_2^P$	Second invariant of the plastic strain rate
$[D]$	Elastic material matrix relating stress to total elastic strain

LIST OF SYMBOLS (Continued)

$E$	Elastic modulus
$f_y$	Crack tip node restraint force
$\{f\}$	Nodal force vector
$H'$	Slope of stress vs plastic strain curve
$i,j$	Indices
$J$	The J integral
$J_2$	Second invariant of the deviatoric stress
$K$	Stress intensity factor
$K_{eff}$	Stress intensity factor based on test conditions
$K_{FE}$	Stress intensity factor based on finite element model
$[K]$	Global elastic stiffness matrix
$m$	Bodner material constant/Ramberg-Osgood equation constant
$M$	Empirical constant
$n$	Bodner material constant/Ramberg-Osgood equation constant
$P$	Maximum value of $P_\sigma$ or $P_\epsilon$ at any given time/ applied pressure/applied load
$P_\epsilon$	Strain tolerance parameter
$P_\sigma$	Stress tolerance parameter
$\{P\}$	Applied load vector
$\{Q\}$	Plastic load vector
$r$	Bodner material constant/Polar coordinate
$R$	Ramberg-Osgood equation constant
$s$	Distance along integration path

LIST OF SYMBOLS (Continued)

$S_{ij}$	Deviatoric stress
$t$	Elapsed total time
$t_A$	Crack tip arrival time
$t_r$	Crack rupture time
$T$	Temperature/Crack tip exposure time
$T_i$	Traction component
$T_0$	Empirical constant
$u_i$	Components of displacement
$\{U\}$	Generalized nodal displacement vector
$v$	Displacement in y-direction
$W$	Width of specimen
$W(\epsilon_{ij})$	Elastic strain energy density
$W^*(\dot{\epsilon}_{ij})$	Strain energy rate density
$W_p$	Plastic strain energy density
$x, y$	Cartesian coordinates
$\dot{y}$	Load-point displacement rate
$Z$	Bodner model internal state variable
$Z_0, Z_1, Z_i$	Bodner material constant
$\alpha, \beta, \eta, \zeta$	Empirical constants
$\gamma_c$	Fluidity constant in Norton Creep Law
$\gamma_p$	Fluidity constant in Malvern Flow Law
$\Gamma$	Integration path for $C^*$ and $J$ integrals



LIST OF SYMBOLS (Continued)

$\delta$	Process zone size ahead of crack tip
$\delta_{\text{test}}$	Experimental displacement
$\delta_v$	No crack growth displacement in VISCO model
$\Delta a$	Incremental change in crack length
$\Delta a_m$	Measured creep crack growth increment
$\Delta a_1$	Crack growth increment determined by HEN VISCO results
$\Delta a_2$	Crack growth increment determined by Equation 59
$\Delta_3$	Crack growth increment determined by compliance method
$\Delta c$	Incremental change in compliance
$\epsilon$	Total uniaxial strain
$\epsilon_{ij}$	Components of total strain
$\epsilon_{ij}^E$	Elastic components of total strain
$\epsilon_{ij}^P$	Plastic components of total strain
$\epsilon_e^P$	Total effective plastic strain
$\epsilon_{\text{crit}}$	Critical strain at crack tip for crack growth to occur
$\epsilon_0$	Initial strain/empirical constant
$\epsilon_{\text{tol}}$	Strain tolerance
$\epsilon_{\text{total}}$	Scalar representation of multiaxial total strain
$\lambda$	Positive scalar constant

## LIST OF SYMBOLS (Concluded)

$\nu$	Poisson's ratio
$\sigma$	Uniaxial stress
$\sigma_n$	Net section stress
$\sigma_{ij}$	Components of stress
$\sigma_e$	Effective stress
$\bar{\sigma}$	Strain hardening yield stress
$\bar{\sigma}_0$	Initial yield stress
$\sigma_{tol}$	Stress tolerance

## SECTION I

### INTRODUCTION

#### 1. BACKGROUND

The United States Air Force currently places strict fracture mechanics requirements on airframe construction and maintenance (References 1,2). These requirements involve detection of flaws by periodic nondestructive inspection and then predicting the remaining useful life of the part through specified fracture mechanics techniques. Consequently, if an airframe part is examined and found to have no flaws that can grow to critical size prior to the next periodic examination, it can be returned to service.

In contrast to the airframe, low-cycle-fatigue limited jet engine parts may be retired from service when no flaws have yet been found in them. This situation occurs because the retirement of engine disks is based on a "crack initiation" criterion. Under this criterion all components of a given population are considered to have failed as soon as a crack of some finite size (e.g., .031 inches) has statistically formed in the member of the population which has minimum strength properties (Reference 3). No attempt is made to utilize the additional life associated with the remaining population members which have statistically higher properties and are expected to be uncracked.

From a safety standpoint, this approach has been generally very successful. But for real materials and real design situations, lifetimes based on time crack initiation of the minimum member tends to be extremely conservative for a component population.

It has been estimated that replacement costs for low-cycle-fatigue limited jet engine disk components could reach the \$100,000,000 level by the 1980 to 1985 time period (Reference 4). A significant reduction of this cost could be realized if a procedure was developed to provide

accurate assessment of useful residual life in retired engine disks. This procedure would require both improved inspection and fracture mechanics life prediction techniques.

The present research is aimed at developing more accurate fracture mechanics life prediction capabilities. Various controlling aspects of fatigue crack growth are strain, stress, stress intensity, temperature, load application frequency, and environment. Speidel (Reference 5) provides an excellent discussion of the relative effects of each of the above aspects on fatigue crack growth rates at high temperatures. It was shown that at each elevated temperature there is a critical frequency below which the crack growth rate is creep dependent (i.e. dependent on exposure time to load) and this creep dependency increases with decreasing frequency. Also the effects of an aggressive environment is another time-dependent phenomenon that results in a frequency dependence of the crack growth rate which is very similar to that brought about by creep.

Various engine missions may include long dwell times at high stress levels. Crack growth controlling aspects may then be reduced to stress and strain levels, stress intensity, temperature and environment since load cycling is not occurring during these dwell periods.

Due to the high stress concentration in the vicinity of the crack tip, (i.e., infinite stress concentration using linear elastic fracture mechanics) and the high temperature environment for an engine disk, the stress-strain relations for the material are nonlinear and time-dependent. The high stress concentration causes the material to yield and envelop the crack tip with a plastic zone. Simultaneously, the high temperature allows the material under load to flow with time, the phenomena known as creep, (i.e., increase strain with no increase in stress). Also the environment, both temperature and atmosphere, may be changing the ductility of the material thereby lowering its ability to strain before fracture.

AFWAL-TR-80-4140

Creep crack growth studies of metals in a vacuum indicate that removal of air from the crack can reduce the crack growth rates by two orders of magnitude (Reference 5). This result demonstrates the importance of recognizing environmental effects in addition to what may be called mechanical effects on crack growth. Environmental effects may be thought to dictate the critical level of strain at fracture whereas mechanical effects determine the rate at which the material moves to the critical strain levels.

The present work mainly deals with the mechanical aspects of crack growth under fixed load in materials that deform with time (creep crack growth). But since the experimental data used here, came from elevated temperature tests in laboratory air, some environmental effects were also considered.

A theoretical model for creep crack growth under varying and fixed loads must be able to account for the changing boundary conditions associated with crack growth. In the event of total unloading and reloading between two different fixed loads the possibility of crack closure and separation needs to be taken into account. These changing boundary conditions coupled with nonlinear time dependent material behavior are well suited for the finite element method.

## 2. APPROACH

The modeling effort considered here involved developing a two-dimensional (plane stress/plane strain) nonlinear, time dependent, finite element program to investigate creep crack growth under constant load. The finite element analysis incorporated the constant-strain triangular element. The nonlinear time-dependent material constitutive model took the form of the Bodner-Partom viscoplastic flow law (References 6,7,8,9). This flow law was integrated through time by an Euler extrapolation scheme (Reference 10) and incorporated into the overall finite element program by means of the residual force method (Reference 11). Material

constants for the Bodner material model were determined by Stouffer (Reference 12) to best match the behavior of IN-100 (Reference 13), a current jet engine turbine disk alloy.

Time step sizes of the Euler scheme were maximized subject to specified amounts of change in stress and strain over a given time step. This time step maximization scheme provided the ability to transition from small fraction of a second time step for the load up phase to large time steps of the order of minutes or even hours for the constant load creep phase. This variable time step capability was a necessity to make a numerical study of creep crack growth computationally feasible.

Crack growth and possible crack closure during unloading was accounted for by simple modifications to the structural stiffness matrix. These simple modifications were made possible by choosing an iterative Gauss-Seidel linear equation solver (Reference 14) which requires no explicit factorization of the stiffness matrix. Hence between time steps, pertinent terms of the stiffness matrix could be easily changed to account for crack growth and the general procedure continued without costly matrix factorization time required.

The finite element program which includes the capability of accounting for material creep behavior and crack growth was used to study the creep crack growth in a center cracked plate test specimen. Several finite element models were incorporated to study different initial crack lengths in the plate geometry. These models were subjected to various loads that were chosen to coincide with a parallel experimental program conducted by W. Sharpe (Reference 15).

The primary objectives in the present research were to determine the actual rate of creep crack growth in test specimens from experimental displacement and compliance measurements and to determine the most reliable criterion for predicting creep crack growth in a typical jet engine turbine disk alloy. Specifically the interest was in IN-100 at

AFWAL-TR-80-4140

1350°F. These objectives were to be accomplished by the so-called hybrid experimental-numerical procedure (Reference 16). In this procedure, crack growth rates would be estimated, imposed on the finite element simulation, and then the finite element model displacement results would be compared with experimental data for the same geometry and loading conditions. A similar method is to allow the crack to grow sufficiently so that predicted crack opening displacement rates from the finite element model match experimental data for the same geometry and loading conditions. After good correlation of displacements between model and experiment was achieved, fracture criteria were sought out from the calculated parameters in the finite element model such as stress, strain, and displacement. Criteria were sought which could match the now determined experimental crack growth rates, displacement, or displacement rates over a range of crack length and load levels.

Once a reliable creep crack growth criterion is determined and found to be independent of specimen geometry it can then be applied to an actual turbine disk specimen. With the determination of flaw sizes in the disk through nondestructive examination techniques, the crack growth criterion could then be used to predict the remaining time for these flaws to grow to critical dimensions under constant load applications.



SECTION II  
LITERATURE REVIEW

Creep crack growth in general may be thought of as subcritical crack growth in a material that deforms with time under constant external load. This time dependent deformation or creep may be reversible (i.e., anelastic creep) or it may be permanent (i.e., plastic creep). At elevated temperature, metals generally exhibit nonlinear time dependent deformation. Under uniaxial tensile loading, the strain in a smooth bar increases with time until failure ultimately occurs. Based on similar response of many materials, researchers have subdivided the creep curve into three regions as shown in Figure 1. After the initial instantaneous strain  $\epsilon_0$ , materials often undergo a period of transient response where the strain rate,  $\dot{\epsilon}$ , decreases with time to a minimum steady-state value that persists for a substantial portion of the materials life. These two regions are referred to as transient or primary stage and steady-state or secondary stage respectively. Final failure with rupture life  $t_R$  occurs soon after the creep rate begins to increase during the third or tertiary stage of creep. A common empirical relationship between creep strain rate and stress in the secondary stage of creep is given as:

$$\dot{\epsilon} = \gamma_c (\sigma)^\beta \quad (1)$$

where  $\sigma$  is the uniaxial stress,  $\dot{\epsilon}$  is the creep strain rate, and  $\gamma_c$  and  $\beta$  are empirical constants chosen to match creep test results.

Creep crack growth has been studied using viscoelastic (References 17-20), viscoelastic-plastic (Reference 21), and plastic creep material models for metals as indicated in a literature review by Fu (Reference 22). The viscoelastic modeling, a form of anelastic behavior, pertains mainly to nonmetals such as elastomers, polymers, and solid rocket propellants. The material of interest in this investigation is a current jet engine turbine disk alloy known as IN-100 (Reference 13).



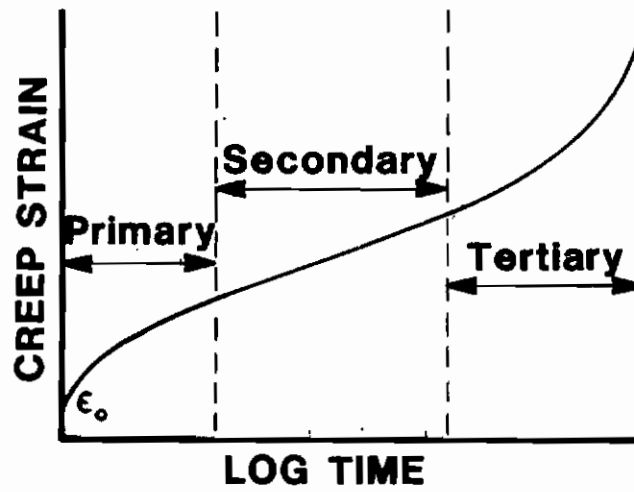


Figure 1. Three Stages of Creep Behavior

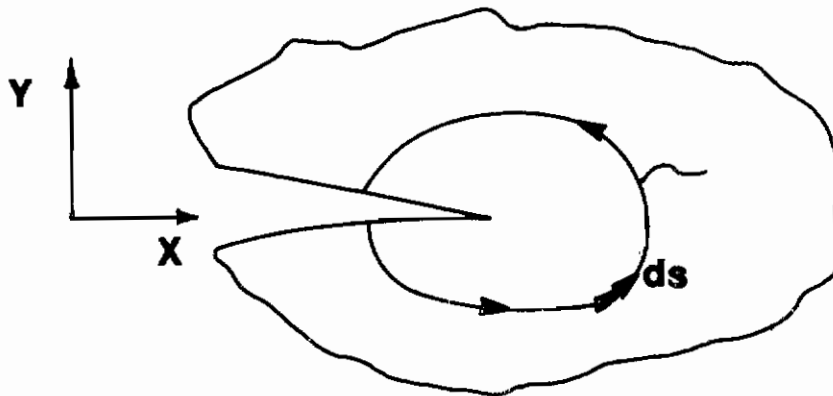


Figure 2. Line Integral Paths for J and  $C^*$

In the present study all time dependent deformation of IN-100 is treated as permanent and consequently any anelastic behavior is considered negligible. However, a brief review of some anelastic (i.e. viscoelastic) creep crack growth studies will be addressed later.

The next two review sections will consider recent creep crack growth studies of an analytical or closed form nature as well as applications of the finite element method to creep crack growth.

## 1. ANALYTICAL CREEP CRACK GROWTH STUDIES

Knauss (Reference 17) analytically modeled steady crack growth in a viscoelastic sheet. In his study the plastic zone, which was assumed small, was accounted for by prescribed fixed and finite stress distributions in the crack tip region. No interaction between crack tip and the far field stresses were allowed. This means the stress profile ahead of the moving crack tip remained constant and independent of the far field stresses. Magnitudes and gradients of the stress in this crack tip region were studied along with two crack growth criteria. The two criteria were maximum strain and a maximum strain energy criterion.

Schapery (References 18,19,20) performed a viscoelastic crack growth analysis similar to Knauss but placed no significant restrictions on the nature of the failing material at the crack tip. It could be highly nonlinear and rate sensitive. An energy criterion for failure was also used here.

Wnuk (Reference 21) included plasticity with viscoelasticity for his quasistatic extension of a tensile crack analysis. A "final stretch" crack growth criterion was proposed. This criterion postulates that the amount of deformation which occurs within the crack tip region or process zone during the time interval just prior to decohesion of this zone is a material constant. In contrast to the maximum strain criterion, the "final stretch" criterion is path-dependent.

Fu's review (Reference 22) of quasi-static crack growth in metals at elevated temperature presents four different creep crack growth rate equations:

$$\dot{a} = A (K)^{\alpha} \quad (2)$$

$$\dot{a} = B (\sigma_n)^{\beta} \quad (3)$$

$$\dot{a} = C (\dot{y})^{\eta} \quad (4)$$

$$\dot{a} = D (C^*)^{\ell} \quad (5)$$

where  $\dot{a}$  is the crack growth rate,  $K$  is the linear elastic stress intensity factor,  $\sigma_n$  is the net section stress, (e.g., load divided by remaining uncracked ligament in a center cracked plate geometry),  $\dot{y}$  in general is the load-point displacement rate, and  $C^*$  is a line integral related to the rate of change of potential energy release per unit of crack growth (References 22-25). The  $C^*$  integral also discussed in Appendix C, is obtained directly from Rice's  $J$  integral by introducing strain rate and displacement rate instead of strain and displacement such that:

$$J = \oint_{\Gamma} [W(\epsilon_{ij}) dy - T_i \frac{\partial u_i}{\partial x} ds] \quad (6)$$

becomes

$$C^* = \oint_{\Gamma} [W^*(\dot{\epsilon}_{ij}) dy - T_i \frac{\partial \dot{u}_i}{\partial x} ds] \quad (7)$$

where

$$W(\epsilon_{ij}) = \int_0^{\epsilon_{mn}} \sigma_{ij} d\epsilon_{ij} \quad (8)$$

$$W^*(\dot{\epsilon}_{ij}) = \int_0^{\dot{\epsilon}_{mn}} \sigma_{ij} d\dot{\epsilon}_{ij} \quad (9)$$

$T_i$  = traction vector

$u_i, \dot{u}_i$  = displacement and displacement rate respectively

$\epsilon_{ij}, \dot{\epsilon}_{ij}$  = strain and strain rate respectively

$\Gamma, x, ds$  - see Figure 2

AFWAL-TR-80-4140

There are available experimental data supporting any of the rate, see Equations 2 through 5 as listed by Fu.

The following conclusions have been extracted from the literature:

1. The stress exponent  $\beta$  in Equation 1 plays an important role in determining the characterization of the crack tip behavior. For  $\beta \leq 5$  the stress intensity factor approach, Equation 2 may be used, and for  $\beta \geq 7$  the net section stress approach may be used (References 26,27).
2. Critical test conditions for evaluating a creep crack growth criterion should consist of at least two geometries which have different stress-intensity-factor divided-by-stress ratios (Reference 23). Some crack growth criteria have been found to be dependent on geometry and therefore have no general application. Use of two or more test geometries helps determine how dependent a crack growth criterion is on geometry.
3. Creep crack growth results from two competing processes. These processes are: (1) growth and coalescence of defects which contribute to crack advancement and (2) the creep deformation process that causes retardation and even arrest of crack growth (Reference 25).
4. Creep crack growth rates are very sensitive to environmental effects. Removal of air from the crack can reduce the crack growth rates by two orders of magnitude (Reference 5).
5. Crack opening displacement crack growth theories indicate that failure times due to creep crack growth are controlled by the stress intensity factor at large stresses and by net section stresses at very low stresses (Reference 28). However, a counter viewpoint is stated in Reference 29 where it is concluded that creep crack growth does not correlate well with the stress intensity factor at relatively high stress levels.

AFWAL-TR-80-4140

6. Creep crack growth rates correlate with the energy rate integral  $C^*$ . This method holds great promise for design calculations because  $C^*$  can be calculated using finite element analysis as well as measured empirically in constant displacement rate tests (Reference 24).

7. An approximation to  $C^*$  in the form of the product of net section stress and load line displacement rate, referred to as  $\dot{J}$ , gives good correlation of creep crack growth rates in specimens of different geometries (Reference 29).

8. Crack growth theories generally fall into one of two categories. Either they are of an energy nature (e.g.,  $J$  or  $C^*$  integrals), or they deal with some localized crack tip parameter such as strain or crack opening displacement.

## 2. FINITE ELEMENT ANALYSIS RELATED TO QUASI-STATIC TIME DEPENDENT CRACK GROWTH

The general technique of approximating a continuum with simple discrete elements such as uniaxial bar elements dates back to the 1940's (Reference 30). The history of the finite element method in structural analysis, as it is known today, is well described by Zienkiewicz (Reference 31). The application of the method to the problem of nonlinear material behavior has also been developed (Reference 31). The purpose of this section is to briefly review the use of the finite element method for the stress analysis of cracked plates where nonlinear time independent and time dependent materials models were employed.

### a. Elastic-Plastic (Time Independent) Analysis

The finite element method has been widely used to determine the stress and strain fields around cracks in nonlinear materials where time independent elastic-plastic materials models were incorporated (References 32-45). Several of these use the "initial stress" or "initial strain" approach to elastic-plastic modeling as described in

AFWAL-TR-80-4140

Appendix A. During the last few years many reports have been published on this subject. This review will not cover all these publications, but, it will concentrate on two areas: (1) crack tip element selection and (2) crack growth modeling by the finite element method.

There are several choices to consider when selecting finite elements to model the vicinity of a crack tip. These choices might best be classified into two categories. The first category is to use the same element type incorporated in the model remote from the crack tip (e.g., constant strain triangles). The second category is to use a special crack tip element that has functions to include the specific stress or strain singularity desired at the crack tip.

There are of course benefits and disadvantages to each choice. Using the same element such as a constant strain triangle both at the crack tip and remote definitely has the benefit of simplicity. However, the cost of this simplicity is the requirement to use large numbers of such elements around the crack tip to obtain acceptable results. Also in a fully plastic material, some elements do not accurately model incompressible strain behavior (Reference 46). The bilinear displacement quadrilateral is most susceptible to this inaccuracy, furthermore the constant strain triangle is one of the least susceptible.

The selection of a special crack tip element requires knowledge of the stress or strain singularity around the crack tip. Several authors have developed the inverse square root " $r$ " singularity for linear elastic crack tip behavior. Accordingly many special elements have been addressed to this singularity. In a paper entitled "Crack Tip Finite Elements Are Unnecessary" (Reference 47), the authors describe the modification of the eight noded isoparametric element such that it incorporated the  $1/\sqrt{r}$  stress singularity. Therefore, any existing finite element program that had the eight noded isoparametric element in it also effectively has one form of a special crack tip element capability for elastic analysis.

AFWAL-TR-80-4140

Further considerations of the local crack tip stress and strain distributions in an elastic-plastic material have led to the expressions (Reference 48)

$$\begin{aligned}\sigma_{ij} &= K_{\sigma} r^{-\frac{1}{n+1}} f_{ij}(\theta) \\ \epsilon_{ij} &= K_{\epsilon} r^{-\frac{n}{n+1}} g_{ij}(\theta)\end{aligned}\tag{10}$$

where  $K_{\sigma}$ ,  $K_{\epsilon}$  are plastic-intensity factors and  $n$  is a strain hardening exponent. This type of singularity was embedded in a crack tip element and used to evaluate the plastic intensity factors as a function of applied loading (Reference 49). The advantage of this method was that the large strain gradients in the crack tip region are accounted for by Equation 10. For elastic-plastic and creep type materials the singularity changes between initiation and growth of the crack and in general is not known. The development of a special crack tip element in the case where the singularity is not known to begin with would be an extensive undertaking by itself (Reference 37) without bringing in the additional complexity of a moving crack tip.

Finite element researchers have considered the crack growth problem. Kobayashi, Chiu, and Beeukes (Reference 43) analyzed an extending crack under monotonically increasing load. Crack extension was achieved by applying a relief force equal in magnitude but opposite in direction to the restraining force at the crack tip node. This relief force was applied in 100 equal increments or in one single increment. The crack opening displacements at the node adjacent to the crack tip computed by the single increment method were less than 5 percent smaller than the corresponding displacements computed with the 100 increment method. Lee and Liebowitz (Reference 35) using a similar technique demonstrated that plastic strain energy increased linearly with crack length as the crack grew in their analysis. Anderson (Reference 36) also made use of relaxing the crack tip node force incrementally to simulate crack growth in the finite element model.



AFWAL-TR-80-4140

Shih, DeLorenzi, and Andrews (Reference 42) analyzed crack initiation and stable crack growth in elastic-plastic material by special use of eight-node isoparametric elements. Initial crack tip blunting was modeled followed by crack extension. Crack extension was modeled by a combination of crack tip node shifting and then releasing it to move on to the next element's nodes. Moving these nodes within elements at the crack tip required approximations to be made about Gauss point location and relocation. These approximations are not necessary when only a node release method and elements such as constant strain triangles are employed to model crack growth. The  $1/r$  strain singularity provided by the special use of these eight noded isoparametric elements may better model the crack tip singularity for a fixed crack length and a theoretical continuum. However, when the crack initiates and grows in a creep type material the strain singularity is unknown, especially when considering a grain structure around the crack tip rather than a continuum and the fact that a creep crack follows an intergranular path.

#### b. Visco-Plastic and Creep (Time Dependent) Analysis

Several references have been found on viscous or time dependent material models being incorporated into finite element programs (References 50-60). In general these material models may be similar to Equation 1 for pure creep with the addition of time independent elastic-plastic relationships, or they may have short-term response viscoplastic relationships that only model the load up phase. Zienkiewicz (Reference 10) proposed placing a short-term response viscoplastic equation in series with a long-term response creep law, similar to Equation 1. This would be a unified time dependent material model where no direct coupling is assumed between short-term plastic strains and long-term creep strains.

Only a few papers have been found to date that use a time dependent material model and the finite element technique to model crack growth. Ohtani and Nakamura (Reference 61) analyzed creep crack propagation with an elastic-secondary creep material model. The secondary creep law was



AFWAL-TR-80-4140

identical to Equation 1 in its uniaxial form. A critical strain criterion (i.e. average effective plastic strain at the crack tip) was used for determining the time to grow the crack in the finite element model of a center cracked plate. Crack tip nodes were released to simulate crack growth. Goodall and Chubb did a similar analysis on the compact tension specimen (Reference 62). A critical strain crack growth criterion was again used. Finally Zaphir and Bodner (Reference 63) incorporated the time dependent Bodner-Partom viscoplastic flow law into the NONSAP finite element code to analyze a double-centilever-beam cracked geometry. In this case, high loading rates were studied over short time periods relative to creep analyses. Consequently the "recovery term", as described in a later section and used to best model creep, was not included. No crack growth was allowed here.

In each of the finite element solutions referred to previously, a unified time-dependent material model that not only accurately models the short-term load up stage of material response, but also transition smoothly into the pure creep stage was never considered. In addition, the hybrid experimental-numerical technique was not used with high resolution experimental crack opening displacement data. It was anticipated, in the present research, that the combination of a more realistic time dependent material model and high resolution test data would result in a much better understanding of what controls creep crack growth than provided by these prior analyses.

### SECTION III

#### FINITE ELEMENT COMPUTER PROGRAM DEVELOPMENT

This section describes the development and validation of a finite element computer program called "VISCO". VISCO is a two-dimensional plane stress/plane strain program that incorporates three different nonlinear time dependent viscoplastic material models. It uses constant strain triangular elements with the option to release fixed nodes and thus has the capability to simulate crack growth. Results from VISCO are compared with other published solutions to check its validity.

The approach selected for elastic-viscoplastic analysis with the finite element technique employs the "residual force method" (Reference 11) (see Appendix A for a complete discussion on this particular approach). In the residual force method the elastic stiffness is used during the entire analysis and any nonlinear elastic-viscoplastic deformation that occurs must be accounted for by developing so-called plastic-load vectors that add to the force side of the governing equilibrium equation. In general, the matrix equation which governs the response of a discretized structure can be written as

$$[K] \{U\}^i = \{P\}^i + \{Q\}^{i-1} \quad (11)$$

where  $[K]$  is the elastic stiffness matrix  $\{U\}^i$  is the generalized nodal displacement vector for the  $i$ th time step,  $\{P\}^i$  is the load vector after the  $i$ th time step due to external forces, and  $\{Q\}^{i-1}$  is the plastic-load vector computed from plastic strains accumulated prior to the  $i$ th time step. For each element, these plastic-load vectors are self-equilibrating. The viscoplastic strain rate expressions which develop plastic strains with time under load are described.

#### 1. VISCOPLASTIC MATERIALS MODELS

In solid mechanics it is customary to separate the two important groups of phenomena described respectively by "creep" and "plasticity".

AFWAL-TR-80-4140

The first includes all time dependent effects and results in creep strains accumulating at a finite rate. The second group develops permanent (plastic) strains instantaneously since time does not enter directly into consideration as in the elastic-plastic approaches given in Appendix A. From a physical point of view, creep and plasticity cannot be treated separately as only the combined effect is measurable. Also the concept of time independent or instantaneous plasticity is only a convenient mathematical approximation and not experimentally based.

Viscoplasticity, in a complete sense, is the combination of these two strain groups into a unified plastic strain rate model. A model with this capability is the Bodner-Partom viscoplastic flow law (References 6-9) from hereon referred to as the Bodner model. The superposition of Malvern's overstress law (References 66,67) with Norton's law for secondary creep has also been proposed as a unified viscoplastic flow law (Reference 10).

Each of these flow laws has been incorporated into VISCO by assuming small strains and decomposing the total strain rate into elastic (reversible) and plastic (nonreversible) components.

$$\dot{\epsilon}_{ij} = \dot{\epsilon}_{ij}^E + \dot{\epsilon}_{ij}^P \quad (12)$$

which in general are both nonzero for all loading/unloading conditions. Anelastic stresses and strains corresponding to time dependent reversible deformations with energy losses are not considered in this formulation and are assumed to be relatively unimportant. This assumption seems quite justified based on the good correlation between predicted and test results to be shown later.

AFWAL-TR-80-4140

The elastic strain rate  $\dot{\epsilon}_{ij}^E$  is related to the stress rate by the time derivative of Hooke's law. The plastic strain  $\dot{\epsilon}_{ij}^P$ , assuming incompressibility and isotropy, is taken to follow the Prandtl-Reuss flow law of classical plasticity

$$\dot{\epsilon}_{ij}^P = \lambda S_{ij} \quad (13)$$

where  $S_{ij}$  are the components of the deviatoric stress tensor and  $\lambda$  is a scalar that reflects the viscosity of the material. The specific form of  $\lambda$  is presented below for each of the viscoplastic flow laws.

#### a. Malvern (Overstress) Flow Law

A portion of a total viscoplastic model that accounts for the so-called instantaneous plasticity during loading might take the form as given by Malvern (References 66,67), otherwise known as the "overstress" model:

$$\dot{\epsilon}_{ij}^P = \begin{cases} \gamma_p \left[ \frac{\sigma_e}{\bar{\sigma}(\epsilon_e^P)} - 1 \right] \frac{3}{2} \frac{S_{ij}}{\sigma_e} & \text{if } \sigma_e > \bar{\sigma}(\epsilon_e^P) \\ 0 & \text{if } \sigma_e \leq \bar{\sigma}(\epsilon_e^P) \end{cases} \quad (14)$$

where  $\gamma_p$  is a fluidity constant whose magnitude will determine the strain rate sensitivity of the model, see Figure 3,  $\sigma_e$  is the effective stress defined as  $\sqrt{3 J_2}$  where  $J_2$  is the second invariant of the deviatoric stress defined as  $J_2 = 1/2 S_{ij} S_{ij}$ , and  $\bar{\sigma}(\epsilon_e^P)$  is the strain hardening yield stress shown to be a function of the effective plastic strain,  $\epsilon_e^P$ , defined incrementally as  $d\epsilon_e^P = \sqrt{\frac{2}{3}} d\epsilon_{ij}^P d\epsilon_{ij}^P$ . The strain hardening stress function, within VISCO, takes one of two forms, either a linear relationship such as

$$\bar{\sigma}(\epsilon_e^P) = \bar{\sigma}_0 + H' * \epsilon_e^P \quad (15)$$

or a Ramberg-Osgood type

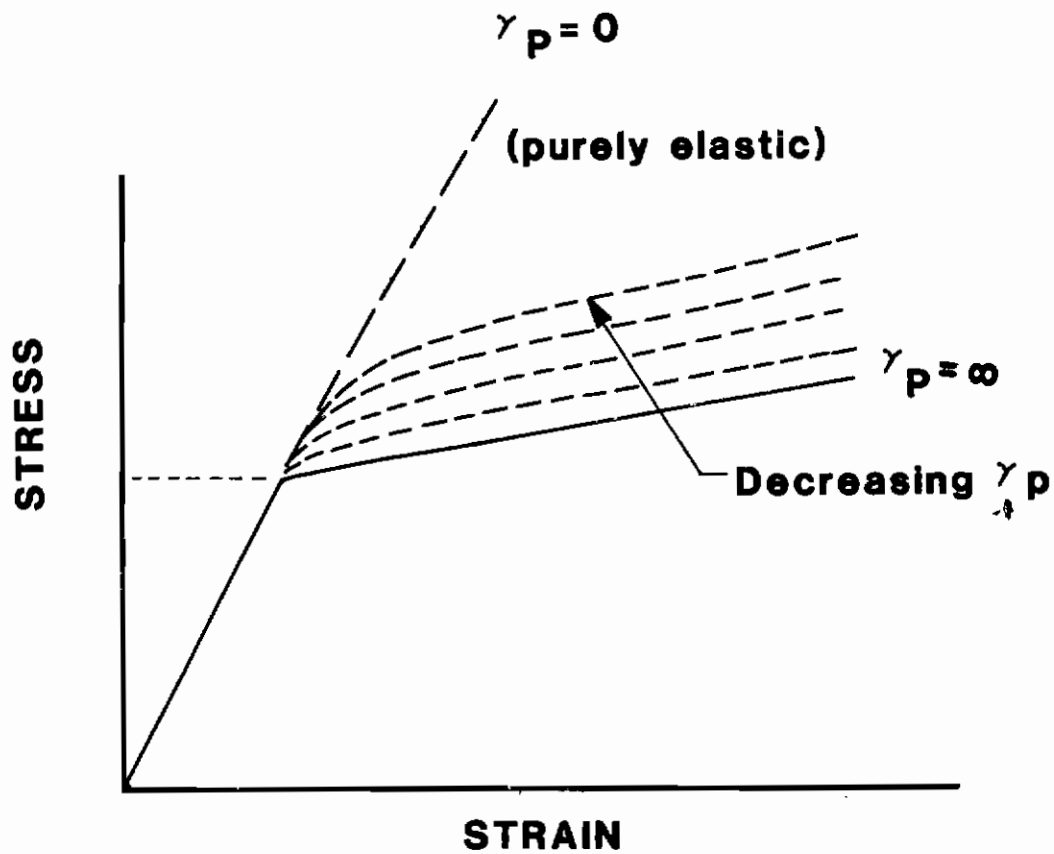


Figure 3. Variation of Malvern Model Behavior with  $\gamma_p$  Under Constant Strain Rate Loading Conditions

$$\bar{\sigma}(\epsilon_e^P) = \begin{cases} R(\epsilon_e^P)^{\frac{1}{m}} & \text{if } R(\epsilon_e^P)^{\frac{1}{m}} \geq \bar{\sigma}_0 \\ \bar{\sigma}_0 & \text{if } R(\epsilon_e^P)^{\frac{1}{m}} < \bar{\sigma}_0 \end{cases} \quad (16)$$

where  $\bar{\sigma}_0$  is the initial yield stress, the constant  $H'$  represents the slope of the stress versus plastic strain curve, and  $R$  and  $m$  are constants of a Ramberg-Osgood type stress-strain curve. In Equation 16, note that if the effective plastic strain  $\epsilon_e^P$  is at or near zero such that the function  $R(\epsilon_e^P)^{\frac{1}{m}}$  is less than the initial yield stress,  $\bar{\sigma}_0$ , then  $\bar{\sigma}(\epsilon_e^P)$  is set equal to  $\bar{\sigma}_0$ .

Implementation of the Malvern model then requires selection of Equation 15 or Equation 16. This selection would depend on the best fit of the material's uniaxial stress-strain curve developed under strain rates at or near the lowest strain rate expected to be modeled with the Malvern Law. If Equation 15 were chosen, the initial yield stress,  $\bar{\sigma}_0$ , and slope,  $H'$  would be determined from this experimental curve. A similar determination would be done if Equation 16 were selected. The fluidity constant,  $\gamma_p$ , would be chosen to best reflect the strain rate sensitivity of the material (see Figure 3) displayed by experimental stress-strain data developed at high strain rates.

The Malvern model may also be used to perform time independent elastic-plastic solutions. In this case time becomes a fictitious parameter and thus the fluidity constant,  $\gamma_p$ , may take on any nonzero positive value. The elastic-plastic solution is the steady state value of the stresses, strains, and displacements after the load has been applied. This has been found to occur in approximately 30 time-steps after maximum load application unless total section yielding develops.

An Euler linear extrapolation scheme is employed within VISCO for the time integration of the viscoplastic strain rate expressions. The Malvern model is integrated in VISCO as follows

$$\{\dot{\epsilon}_{ij}^P\}^i = \begin{cases} 0 & \text{if } \sigma_e^{i-1} < \bar{\sigma}(\epsilon_e^P)^{i-1} \\ \gamma_P \left[ \frac{\sigma_e^{i-1}}{\bar{\sigma}(\epsilon_e^P)^{i-1}} - 1 \right] \frac{3}{2} \frac{\{S_{ij}\}^{i-1}}{\sigma_e^{i-1}} & \text{if } \sigma_e^{i-1} > \bar{\sigma}(\epsilon_e^P)^{i-1} \end{cases} \quad (17)$$

$$\{d\epsilon_{ij}^P\}^i = \{\dot{\epsilon}_{ij}^P\}^i dt^i \quad (18)$$

$$(\epsilon_e^P)^i = (\epsilon_e^P)^{i-1} + \sqrt{\frac{2}{3} \{d\epsilon_{ij}^P\}^i \{d\epsilon_{ij}^P\}^i} \quad (19)$$

$$\bar{\sigma}(\epsilon_e^P)^i = \begin{cases} \bar{\sigma}_0 + H' * (\epsilon_e^P)^i \\ \text{or} \\ R [(\epsilon_e^P)^i]^{\frac{1}{m}} \end{cases} \quad (20)$$

where the superscript  $i$  refers to the time-step and a subscript  $i$  refers to specific components of stress or strain.

#### b. Norton's Law for Secondary Creep

Another portion of a total viscoplastic flow law that complements the Malvern model and accounts for long-term creep is given by Norton's creep law (Reference 68) written in multiaxial form as

$$\dot{\epsilon}_{ij}^P = \gamma_C (\sigma_e)^\beta \frac{3}{2} \frac{S_{ij}}{\sigma_e} \quad (21)$$

where  $\gamma_C$  and  $\beta$  are constants determined from uniaxial creep test results. Creep test data at two different stress levels are required. A straight line is fitted to each test's secondary stage of creep strain plotted versus time (Figure 1). The slope of this line or strain rate and stress level from each test is substituted into Equation 21 which provides two



AFWAL-TR-80-4140

equations to solve for the two unknown constants. After taking the natural logarithm of Equation 21, the simultaneous solution of the two equations is straightforward.

The Euler extrapolation scheme for integrating Equation 21 in VISCO is similar to the one given for the Malvern model and will not be repeated here.

It appears that the combination of the Malvern and Norton laws would provide a complete viscoplastic flow law. But, metals at elevated temperature have been observed to display a phenomenon called "recovery" (Reference 69). Recovery is the softening of cold-worked metal or it may be characterized as a fading memory of prior strain hardening.

In creep crack growth at elevated temperature and under constant load, consider material well ahead of, but in the path of the crack. During load up this material will plastically deform and strain harden depending on its proximity to the initial crack tip. Later, during the sustained load phase, the phenomena of recovery will allow this material to soften prior to the arrival of the crack tip at which time additional loading will occur. The amount of recovery prior to the arrival of the crack tip should then have some effect on the values of stress and strain developed around the crack tip when it reaches the material being considered. Therefore, this investigation will focus on the following viscoplastic flow law which does include the phenomenon of recovery.

### c. Bodner Viscoplastic Flow Law

In this formulation by Bodner and Partom (References 6-9) the  $\lambda$  parameter from Equation 13 is expressed in terms of second invariants by making use of the square of Equation 3

$$\frac{1}{2} \dot{\epsilon}_{ij}^P \dot{\epsilon}_{ij}^P = D_2^P = \frac{1}{2} \lambda^2 S_{ij} S_{ij} = \lambda^2 J_2 \quad (22)$$

where  $D_2^P$  is the second invariant of the plastic strain rate and  $J_2$  is the second invariant of the deviatoric stress.



Rather than specifying a specific yield criterion as in classical plasticity, this formulation by Bodner and Partom is based on the assumption that a continuous functional relationship exists between the plastic deformation rate and the stress invariants, i.e.

$$\dot{D}_2^P = D_2^P(J_2, Z_k, T) \quad (23)$$

where  $Z_k$  are one or more internal (viscoplastic) state variables and  $T$  is the temperature. Introducing Equation 23 into Equation 22 and solving for  $\lambda$  gives

$$\lambda = [D_2^P(J_2, Z_k, T) / J_2]^{1/2} \quad (24)$$

The general form for the evolution equation, i.e. history dependence, of the viscoplastic state variables  $Z_k$  is

$$\dot{Z}_k = F_k(J_2, Z_k, T) \quad (25)$$

For conditions of uniaxial stress of constant sign, the hardened state with respect to plastic flow is assumed to be represented by a single state variable  $Z$  which depends on plastic work. This single state variable  $Z$  also corresponds to isotropic hardening. Additional state variables are necessary for such characteristics as kinematic hardening which will not be employed here.

The particular form chosen for  $D_2^P(J_2, Z, T)$  was motivated by the equations of dislocation dynamics and given by Bodner and Partom as

$$\dot{D}_2^P = D_0^2 \exp\left[-\left(\frac{Z^2}{3J_2}\right)^n \frac{n+1}{n}\right] \quad (26)$$

The factor  $(n + 1)/n$  was introduced at an early stage in the development of the equations for numerical purposes and only affects the numerical values of some of the material constants. The constant  $D_0$  is described as the limiting value of the plastic strain rate in shear. Its value can be arbitrarily chosen and is usually taken to be the same large number

for all materials. A value  $D_0 = 10^4 \text{ sec}^{-1}$  is generally adequate except for conditions of very high rates of straining.

The parameter  $n$  controls strain rate sensitivity and also influences the overall inelastic level of the stress-strain curves. A decrease of  $n$  leads to increasing strain rate sensitivity and lowering of the level of the stress-strain curves.

As stated previously,  $Z$  is assumed to be a function of plastic work,  $W_p$ , and the following relationship is introduced

$$Z = Z(W_p) = Z_1 - (Z_1 - Z_0) \exp[-m W_p] \quad (27)$$

The quantity  $Z_1$  is the maximum value of  $Z$  which is necessary if the deformations do not revert to elastic behavior at large values of  $W_p$ .  $Z_0$  is the value of  $Z$  for which  $W_p = 0$  and can therefore be the initial state point from which plastic work is measured. It is noted that the general function (Equation 27) would be a basic material property and that  $W_p$  is the relative amount of plastic work done from some initial state, (i.e.,  $W_p$  is not an absolute parameter).

$$W_p = \int S_{ij} \dot{\epsilon}_{ij}^P dt \quad (28)$$

The quantity  $m$  in Equation 27 is a material constant that relates to the rate of work hardening.

At high temperatures, it is generally necessary to consider the thermal recovery of hardening generated by plastic deformation. In this case the plastic work,  $W_p$ , is redefined as follows:

$$W_p = \int S_{ij} \dot{\epsilon}_{ij}^P dt + \int \frac{\dot{Z}_{rec}}{m(Z_1 - Z)} dt \quad (29)$$

where

$$\dot{Z}_{\text{rec}} = -A \left( \frac{Z-Z_1}{Z_1} \right)^r Z_1 \quad (30)$$

where  $Z_1$  is the stable, (i.e., non-work hardened) value of  $Z$  at a given temperature, and  $A$  and  $r$  are additional material constants chosen to match the models behavior to creep test data as was done for the Norton model. Note that the second term on the right of Equation 29 (i.e., the recovery term) makes a negative contribution to  $\dot{W}_p$  due to the negative sign on  $A$ , since  $Z$  is always greater than or equal to  $Z_1$ .

The recovery term in Equation 29 is essential if the material model is to be able to represent secondary creep. Secondary creep is the balanced condition when the rate of work hardening equals the rate of thermal recovery or, setting the time derivative of Equation 29 to zero,

$$\dot{W}_p = S_{ij} \dot{\epsilon}_{ij}^p + \frac{\dot{Z}_{\text{rec}}}{m(Z_1-Z)} = 0 \quad (31)$$

At relatively high strain rates, the thermal recovery in Equation 29 is relatively unimportant and the steady state condition is realized when  $Z$  reaches its saturation value  $Z_1$ .

Again, VISCO employs the Euler extrapolation scheme for the numerical time integration of the Bodner equations. During each time step Equation 13 and Equations 24 through 30 are integrated as follows for each element

$$Z^i = Z_1 - (Z_1 - Z_0) \exp[-m W_p^{i-1}] \quad (32)$$

$$(D_2^p)^i = D_0^2 \exp\left[-\left(\frac{(Z^i)^2}{3 J_2^{i-1}}\right)^n \frac{n+1}{n}\right] \quad (33)$$

$$\{\dot{\epsilon}_{ij}^p\}^i = [(D_2^p)^i / J_2^{i-1}]^{1/2} \{S_{ij}\}^{i-1} \quad (34)$$

$$\{d\epsilon_{ij}^p\}^i = \{\dot{\epsilon}_{ij}^p\}^i dt^i \quad (35)$$

$$\dot{Z}_{rec}^i = -A \left( \frac{Z^i - Z_1}{Z_1} \right)^r Z_1 \quad (36)$$

$$W_p^i = W_p^{i-1} + \{S_{ij}\}^{i-1} \{de_{ij}^p\}^i + \dot{Z}_{rec}^i dt^i / [m(Z_1 - Z^i)] \quad (37)$$

where the superscript  $i$  refers to the time-step and a subscript  $i$  refers to a specific material constant,  $Z_i$ , or to specific components of stress and strain.

The specific material constants required for the Bodner model in this investigation were determined to best fit the behavior of IN-100 at the temperature of 1350°F. This material was characterized by performing uniaxial tensile stress-strain tests and creep tests at different stress levels at 1350°F. The following constants for the Bodner model were developed by Stouffer (Reference 12) and the details of this procedure are summarized in Appendix D. The  $A$  and  $r$  constants defined by Stouffer are different than the constants used in the present formulation:

$$D_0 = 10^4 \text{ sec}^{-1}$$

$$n = 3.50$$

$$Z_0 = 224.4 \text{ ksi}$$

$$Z_1 = 251.5 \text{ ksi}$$

$$m = 3.750 \text{ ksi}^{-1}$$

This first group of constants is based on stress-strain curve data.

$$A = 1.142 \times 10^{-2} \text{ sec}^{-1}$$

$$r = 3.52$$

$$Z_i = 100 \text{ ksi}$$

This second group of constants is based on creep test data. The elastic modulus at 1350°F was determined to be

$$E = 26.3 \times 10^6 \text{ psi}$$

and Poisson's ratio was arbitrarily chosen as

$$\nu = .3$$

Figure 4 shows a comparison of the stress-strain behavior of the Bodner model (using the given IN-100 material constants) and experimental stress-strain data. Each of the curves displays the response of the Bodner model under the loading condition of a given constant strain rate. The experimental data were generated at a strain rate of  $.83 \times 10^{-3} \text{ sec}^{-1}$  and compare quite well with the Bodner curve for the same strain rate. Some variation occurs in the region of initial inelastic behavior but this difference is small.

Figures 5 and 6 compare creep behavior of the Bodner model with experimental data at the stress levels of 127.3 ksi and 72 ksi, respectively. Note the initial experimental curve's slope or strain rate is duplicated by the Bodner model in both figures. However, the strain magnitudes differ somewhat due to the initial time required for the Bodner model to reach steady state creep at these stress levels. Also as the experimental strain rate increases with time the Bodner model cannot closely follow since its formulation restricts it to only secondary type creep in this situation (i.e., constant strain rate for constant stress).

## 2. SOLUTION PROCEDURE FOR ELASTIC-VISCOPLASTIC STRUCTURES

In elastic-plastic analysis, it is necessary to apply loads incrementally to satisfy the appropriate yield condition (e.g., von Mises) and flow rule (e.g., Prandtl-Reuss) associated with incremental plasticity (Reference 64). Similarly, with elastic-viscoplastic behavior an incremental procedure is required, but here time is incremented directly while load, strain, stress, etc. are incremented indirectly through the time integration procedure. The algorithm used for a typical time-step in the elastic-viscoplastic residual force method (Reference 10) is summarized as follows:

1. Add time increment  $dt^i$  to the preceding time  $t^{i-1}$  to obtain the current time  $t^i$ .

AFWAL-TR-80-4140

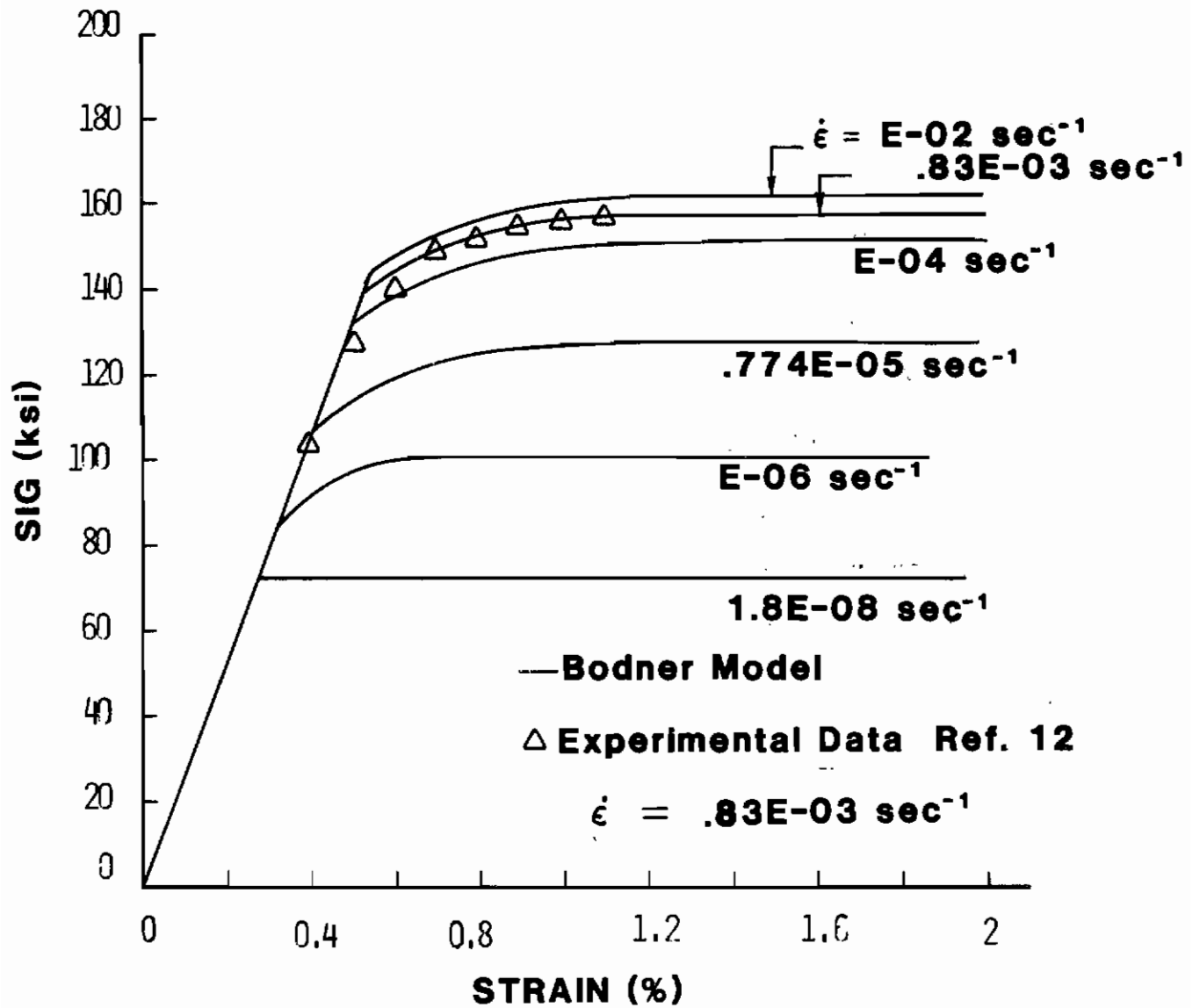


Figure 4. Stress-Strain Behavior of Bodner Model (IN-100 Constants)

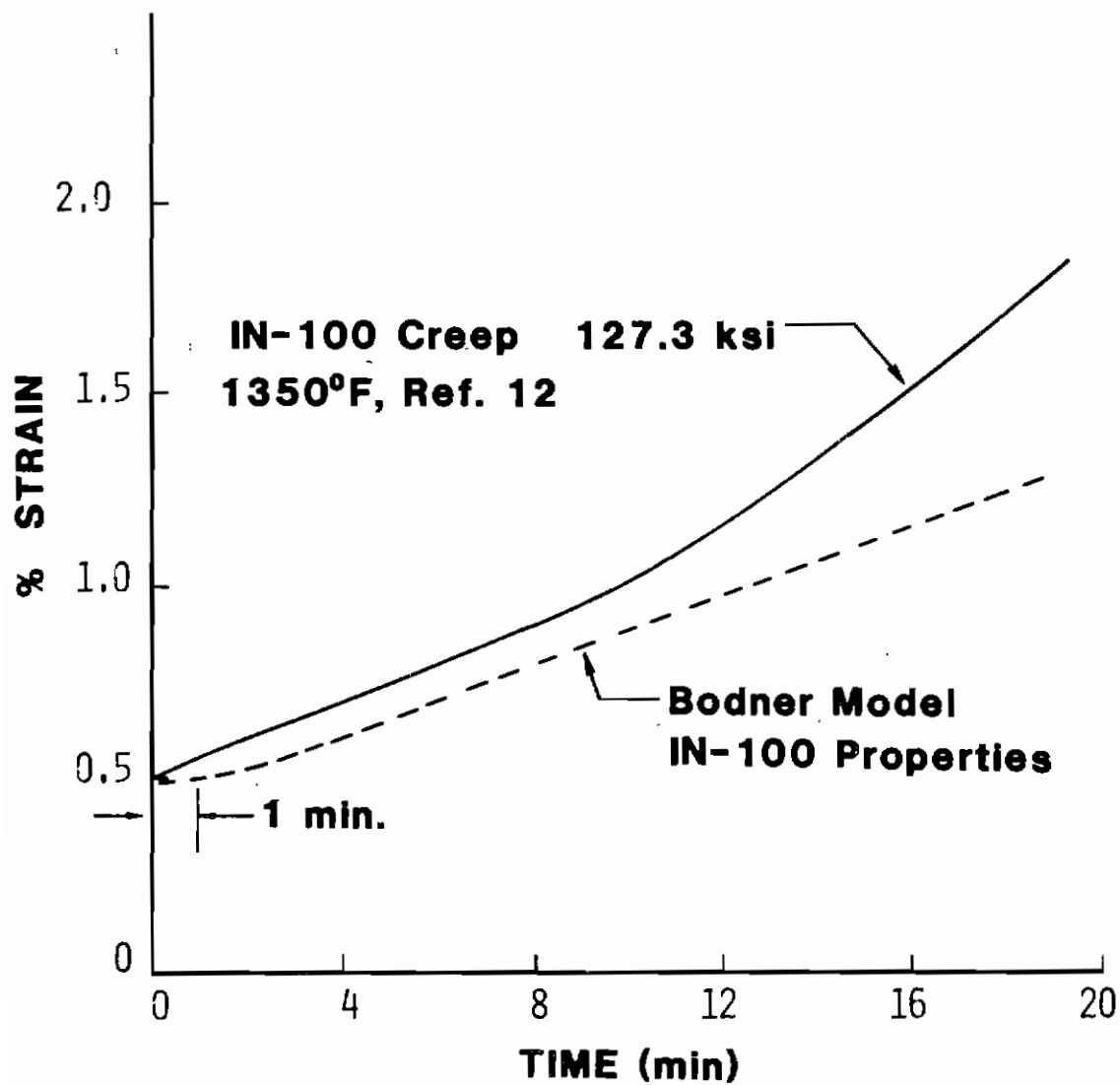


Figure 5. Creep Behavior of Bodner Model at 127.3 ksi (IN-100 Constants)



AFWAL-TR-80-4140

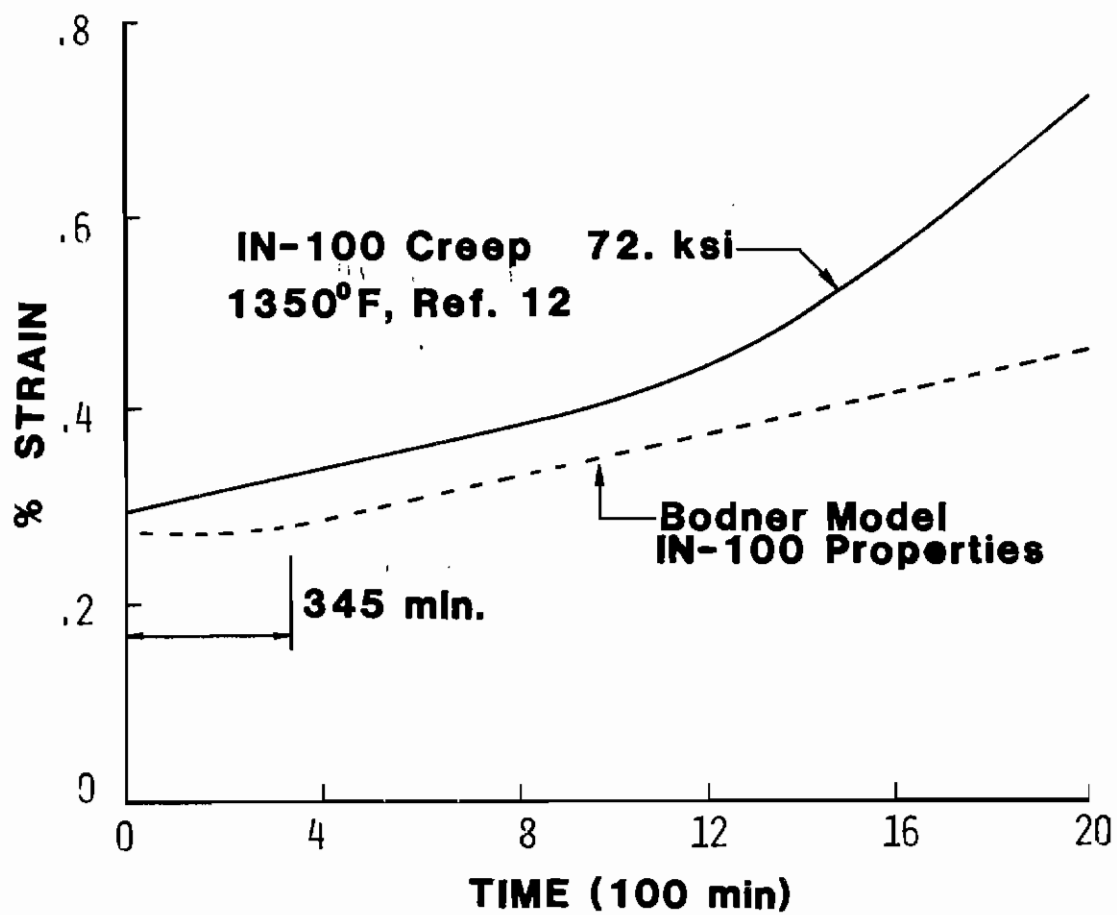


Figure 6. Creep Behavior of Bodner Model at 72.0 ksi (IN-100 Constants)

2. Compute increments of plastic strain,  $\{\dot{\epsilon}_{ij}^P\}^i = \{\dot{\epsilon}_{ij}^P\}^i dt^i$  and add to preceding plastic strain,  $\{\epsilon_{ij}^P\}^i = \{\epsilon_{ij}^P\}^{i-1} + \{\dot{\epsilon}_{ij}^P\}^i$ . In general the plastic strain rate,  $\{\dot{\epsilon}_{ij}^P\}$ , is a function of the material's viscosity and the given stress level (see the Viscoplastic Material Models section).
3. Compute the plastic load vector  $\{Q\}^{i-1} = \int_{vol} [B] [D] \{\epsilon_{ij}^P\}^i dvol$ .
4. Compute the current external load vector  $\{P\}^i = \{\dot{P}\}^i dt^i + \{P\}^{i-1}$ .
5. Compute the nodal displacements  $\{U\}^i$  from Equation 11,  

$$\{U\}^i = [K]^{-1} \{ \{P\}^i + \{Q\}^{i-1} \}.$$
6. Compute the current total strain  $\{\epsilon_{ij}\}^i$  from the strain displacement relationship,  $\{\epsilon_{ij}\}^i = [B]\{U\}^i$ .
7. Compute the current stress  $\{\sigma\}^i$  as follows,  $\{\sigma_{ij}\}^i = [D]\{ \{\epsilon_{ij}\}^i - \{\epsilon_{ij}^P\}^i \}$ .
8. Check the time-step size in terms of prescribed stress and strain change tolerances per time-step (see the following section on Variable Time Step Integration of Viscoplastic Flow Laws). If these tolerances are not exceeded the time-step size may be increased for the next time-step or left the same value. But if the tolerances are exceeded, the time-step size is reduced and steps 1 through 8 are repeated for this same time-step in an effort to satisfy the stress and strain change tolerances.
9. Repeat steps 1 through 8 until the desired simulation time is reached.

### 3. VARIABLE TIME-STEP INTEGRATION OF VISCOPLASTIC FLOW LAWS

One of the final objectives in the development of VISCO was to be able to accurately model nonlinear material behavior both in the high strain rate load up stage and during the low strain rate constant load creep stage. For stable accurate results, the time-step size must be orders of magnitude less during the load up stage compared to the creep stage. Therefore to be computationally feasible in a large problem (many degrees of freedom) some method is necessary to determine the maximum time-step during each stage of the analysis while maintaining reasonable accuracy. Corneau (Reference 65) investigated the numerical stability of simple time marching schemes used in elastic-viscoplastic analysis. The Malvern and Norton models were studied among others. For the Malvern model the following maximum time-step size was determined

$$dt_M \leq \frac{4}{3} \frac{(1+\nu) \bar{\sigma}}{\gamma_p E} \quad (38)$$

where  $\nu$  is Poisson's ratio and all other parameters are as defined earlier. For the Norton model the maximum time-step was

$$dt_N \leq \frac{4}{3} \frac{(1+\nu)}{\gamma_c E B \sigma_e^{B-1}} \quad (39)$$

In general  $dt_N$  is several orders of magnitude larger than  $dt_M$ . If the Malvern model or the Norton model are used separately Corneau has shown Equations 38 and 39 to work well. However, if the Norton and Malvern models are coupled together for a more complete flow law a method is necessary to provide the maximum time-step during transition from load up (Malvern dominated phase) to creep (Norton dominated phase). In addition, this time-step maximizing scheme is all the more required when numerically integrating the Bodner equations since Corneau's analysis does not directly apply to the Bodner viscoplastic flow law. Consequently, the following logic which is also similar to the MARC program (Reference 57), was incorporated into VISCO.

This time-step maximizing logic continually tries to increase the time-step size subject to a stress and strain constraint. These constraints are the allowable amounts of change in stress,  $\sigma_{tol}$ , and strain,  $\epsilon_{tol}$ , during a given time-step and their values will be discussed later in this section. The computer algorithm is based around parameters  $P_\sigma$  and  $P_\epsilon$  defined as follows

$$P_\sigma = \frac{\sigma_e^i - \sigma_e^{i-1}}{\sigma_e^{i-1} \sigma_{tol}} \quad (40)$$

$$P_\epsilon = \frac{(d\epsilon_e^P)^i}{\epsilon_{total}^i \epsilon_{tol}} \quad (41)$$

where  $\epsilon_{total} = \sqrt{\epsilon_x^2 + \epsilon_z^2 + .50 \gamma_{xy}^2}$  and the superscript  $i$  refers to the time-step. Note that if the change in effective stress between time-steps  $i$  and  $i-1$  just satisfies the stress constraint or stress tolerance,  $\sigma_{tol}$ , then Equation 40 will give a value of unity for  $P_\sigma$ . Similarly, if the effective plastic strain increment for time-step  $i$ ,  $(d\epsilon_e^P)^i$ , just satisfies the strain constraint or strain tolerance,  $\epsilon_{tol}$ , then  $P_\epsilon$  will equal unity from Equation 41.

The parameters  $P_\sigma$  and  $P_\epsilon$  are calculated for every element and  $P$  is set equal to the largest one. One method of changing the time-step size based on  $P$  is

$$dt^i = dt^{i-1} / P \quad (42)$$

Note that if  $P$  is unity no change in the time-step size,  $dt$ , occurs. However, if  $P$  is less than one,  $dt^i$  is greater than  $dt^{i-1}$  and if  $P$  is greater than one  $dt^i$  is less than  $dt^{i-1}$ . In the case of  $P$  being greater than one, the amount of change in stress or strain has exceeded its respective tolerance and recalculations for that time-step are necessary using the reduced time-step size from Equation 42.

AFWAL-TR-80-4140

To avoid several successive recalculation steps that develop when  $P$  is greater than one and Equation 42 is used, the following substitute for Equation 42 was employed.

$$\begin{aligned} dt^i &= .8 dt^{i-1}/P && \text{If } P > 1 \\ dt^i &= dt^{i-1} && \text{If } .8 \leq P \leq 1 \\ dt^i &= 1.25 dt^{i-1} && \text{If } .65 \leq P < .8 \\ dt^i &= 1.5 dt^{i-1} && \text{If } P < .65 \end{aligned} \tag{43}$$

Note that Equation 43 reduces the time-step size more than Equation 42 if  $P$  is greater than one but if  $P$  is less than one Equation 43 increases the time-step size slower than does Equation 42. Both of these differences between Equations 43 and 42 tend to reduce the number of calculation steps required.

Determination of the values for the stress and strain tolerances,  $\sigma_{tol}$  and  $\epsilon_{tol}$  respectively, was accomplished by employing VISCO to analyze a plate with a V-notch. This particular geometry was chosen since it has a high stress concentration around the notch and is therefore somewhat similar to a plate with a crack which is the geometry of ultimate interest in this research effort. But the V-Notch geometry can be modeled with far less elements than a cracked plate requires and still compare with other V-notch solutions in the literature (Reference 40). Figure 7 shows the finite element mesh employed for the V-notch plate. Only one quarter of the plate is modeled due to symmetry. Element sizes were made smallest near the V-notch in order to capture the stress concentration there. A total of 182 constant strain triangular elements were employed which is somewhat less than Yamada et. al. (Reference 40) used. However, good agreement with Yamada was achieved and this will be demonstrated later in the Validation Examples section.

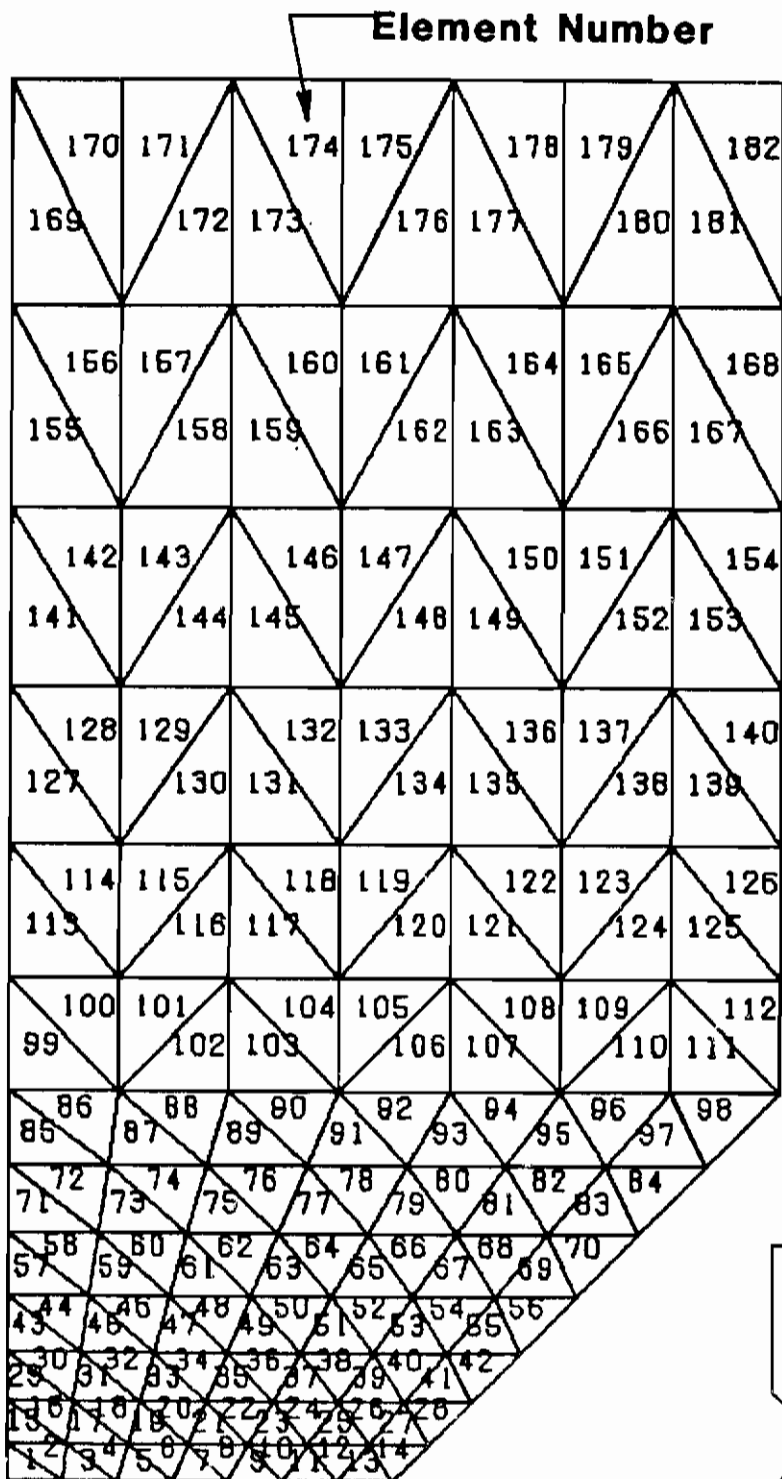


Figure 7. V-Notched Plate Model

AFWAL-TR-80-4140

a. Malvern Model

An elastic-perfectly VISCO plastic (i.e.  $\bar{\sigma}(\epsilon_e^P) = \text{constant}$ ) plane stress analysis was carried out using the Malvern model. The ratio of elastic modulus  $E$  to the yield stress was 288 and the ratio of applied remote stress to yield stress was 0.593. Poisson's ratio was 0.2. The load was applied in nondimensional time of  $\gamma_p t = 10^{-4}$  where  $\gamma_p$  is the fluidity constant in the Malvern model (Equation 14). Results were taken after all stress and strain rates were zero. This may be defined as the steady state condition which was observed to occur after  $\gamma_p t = 0.4$ .

Several analyses of the V-notch were performed using different values for the stress and strain tolerances. Examination of the results found that between displacements near the notch, plastic strain near the notch, and total plastic strain energy in the model, the last one was most sensitive to stress/strain tolerance variations. Table 1 displays the percent variation in plastic strain energy as stress/strain tolerances are varied. The percent variation is relative to the plastic strain energy calculated when  $\sigma_{tol} = .01$  and  $\epsilon_{tol} = .01$ . It was noted that the stress/strain tolerances that kept the percent variation in plastic strain energy around one percent also kept the time-step size, during most of the computing, under Corneau's critical value,  $dt_m$ , in Equation 38. The amount of computer time increases rapidly as the tolerances are reduced to a value of .01. A good compromise between computer time required and apparent accuracy from Table 1 is a stress tolerance of .03. Note that for this stress tolerance, the strain tolerance can be relaxed all the way to .20 with little change in plastic strain energy. These results are in agreement with the recommendations for stress/strain tolerances in the MARC program (Reference 57).

b. Bodner Model

A similar stress/strain tolerance investigation was performed with the Bodner material model in plane stress. The V-notch model in Figure



TABLE 1  
PLASTIC STRAIN ENERGY VARIATIONS IN THE V-NOTCHED PLATE USING THE MALVERN MODEL

$\epsilon_{tol}$ / $\sigma_{tol}$	.01	.05	.10	.15	.20
.01	0.0%	---	---	---	---
.03	0.6%	1.4%	1.6%	1.6%	1.6%
.10	---	4.4%	6.6%	10.0%	10.0%
.20	---	4.6%	10.3%	26.0%	26.0%

11 was again employed. The material constants used for the Bodner equations were those matched to IN-100 and given previously. The ratio of applied remote stress to yield stress was again .593 which is based on 140 ksi for the initial yield stress. Maximum load was reached in 10 seconds and plastic strain energy results were then taken similar to the Malvern model investigation. Again several analyses of the V-notch were performed using different combinations of stress and strain tolerance values. The results for the Bodner model are given in Table 2. Comparing Tables 1 and 2 shows that the Bodner model develops less plastic strain energy variation for the given stress/strain tolerances than does the Malvern model. This comparison indicates that higher stress/strain tolerances could then be used for the Bodner model. However, if the analyses are continued into the creep phase, it was observed that the stress values tend to oscillate somewhat when they should be monotonically relaxing near the notch tip. This oscillation was fairly well damped out when a stress tolerance of 0.03 was used. Once this small value for the stress tolerance is chosen the strain tolerance has little effect as long as it is greater than or equal to the stress tolerance.

The average computation time for the Bodner model was about twice that required for the Malvern model. The average central processor time required on the CDC-6600 was 150 seconds for this 200 degree of freedom problem with the Bodner model.

#### 4. VALIDATION EXAMPLES

The following five examples were performed to demonstrate the validity of the VISCO computer program. The first four examples employ the Malvern model to compare with published time independent elastic-plastic solutions. The Bodner model is then tested in the fifth example by comparing its behavior with the results from coupling the Malvern and Norton flow laws together.

TABLE 2  
PLASTIC STRAIN ENERGY VARIATIONS IN THE V-NOTCHED PLATE USING THE BODNER MODEL

$\epsilon_{tol}$ $\sigma_{tol}$	.01	.05	.15	.20
.01	0.0%	0.0%	0.0%	0.0%
.05	0.0%	0.0%	0.0%	0.0%
.10	0.0%	1.2%	---	---
.20	0.0%	0.9%	5.5%	---
.30	0.0%	1.4%	---	5.9%

a. Infinite Sheet with Pressurized Hole

The first example employs the Malvern model to analyze the infinite sheet with a pressurized hole. Comparisons are made with the exact elastic-plastic strain history independent deformation solution by Hsu and Forman (Reference 70). The material properties for this plane stress solution were  $E = 10.5 \times 10^6$  psi,  $\nu = 0.5$ , and a Ramberg-Osgood stress-strain equation

$$\epsilon = \frac{\sigma}{E} \left( \frac{\sigma}{\bar{\sigma}_0} \right)^{n-1} \quad \text{for } |\sigma| \geq \bar{\sigma}_0 \quad (44)$$

where  $\epsilon$  is the total strain (i.e., elastic plus plastic),  $\bar{\sigma}_0$  is the initial yield stress ( $\bar{\sigma}_0 = 55000$  psi) and  $n$  determines the shape of the curve ( $n = 9$ ). Equation 44 must be inverted so that yield stress  $\bar{\sigma}$  is a function of plastic strain  $\epsilon^P$  in order to be used in the Malvern model. The first step in this inversion process was to split the total strain  $\epsilon$  into its elastic,  $\epsilon^E$ , and plastic,  $\epsilon^P$ , parts and then set the elastic strain,  $\epsilon^E$ , equal to  $\sigma/E$ . Equation 44 may then be rewritten as

$$\epsilon = \epsilon^E + \epsilon^P = \frac{\sigma}{E} + \epsilon^P = \frac{\sigma}{E} \left( \frac{\sigma}{\bar{\sigma}_0} \right)^{n-1} = \frac{\sigma^n}{E \bar{\sigma}_0^{n-1}} \quad (45)$$

Solving for  $\sigma^n$  results in

$$\sigma^n = \bar{\sigma}_0^{n-1} (\sigma + E \epsilon^P) \quad (46)$$

and taking the  $n^{th}$  root of Equation 46

$$\sigma = \bar{\sigma}_0 \frac{n-1}{n} (\sigma + E \epsilon^P)^{\frac{1}{n}} \quad (47)$$

The stress,  $\sigma$ , on the left-hand side of Equation 47 will now be redefined as the strain hardening yield stress  $\bar{\sigma}$  so that, approximately

$$\bar{\sigma} \approx \bar{\sigma}_0 \frac{n-1}{n} (\sigma + E \epsilon^P)^{\frac{1}{n}} \quad \text{for } |\sigma| \geq \bar{\sigma}_0 \quad (48)$$

Note when  $\sigma$  equals  $\bar{\sigma}_0$  and  $\epsilon^P$  is zero, Equation 48 is identically satisfied. Also when  $\sigma$  is greater than  $\bar{\sigma}_0$ , the plastic strain will be greater than zero and the product  $E \epsilon^P$  will have the major effect on  $\bar{\sigma}$ , which is desired.

AFWAL-TR-80-4140

The finite element mesh for modeling the infinite plate was similar to Figure 9b, however, 132 triangular elements were used. The outer radius to inner radius ratio of the element mesh was 15 which was assumed to approximate an infinite radius plate.

Figure 8 shows the radial and tangential stress profiles for three internal pressure ratios,  $P/\bar{\sigma}_0$ . Hsu and Forman indicated that, in consideration of Budiansky's criterion for the acceptability of deformation theory, their infinite plate solution should not disagree greatly with an incremental elastic-plastic solution. One may observe from Figure 8 a close approximation between the techniques thus lending validity to the incremental plane stress approach incorporated within VISCO.

#### b. Thick Cylinder with Internal Pressure

The second example employs the Malvern model to analyze a thick cylinder with internal pressure. In this case comparison is made with a non-finite element solution by Hodge and White (Reference 71) who again used deformation theory. This was an elastic-perfectly plastic plane strain analysis. The ratio of the elastic modulus to yield stress was  $E/\bar{\sigma} = 190.9$  with  $\nu = 0.33$ . The ratio of outer radius to inner radius for the cylinder is two. Figure 9 shows the finite element mesh used to model a symmetric section of the thick cylinder. The mesh incorporates 40 triangular elements. Figure 9 shows the tangential stress profile for a pressure ratio,  $P/\bar{\sigma}$ , of 0.76. Both the elastic and the elastic-plastic profiles are given. There is good agreement with Hodge and White and thus validity is again given to the incremental plane strain portion of the VISCO program.

#### c. V-Notched Plate in Tension

The third example employs the Malvern model to analyze a V-notched plate in tension. Comparison is made with another finite element solution by Yamada, et. al. (Reference 40). A time independent tangent

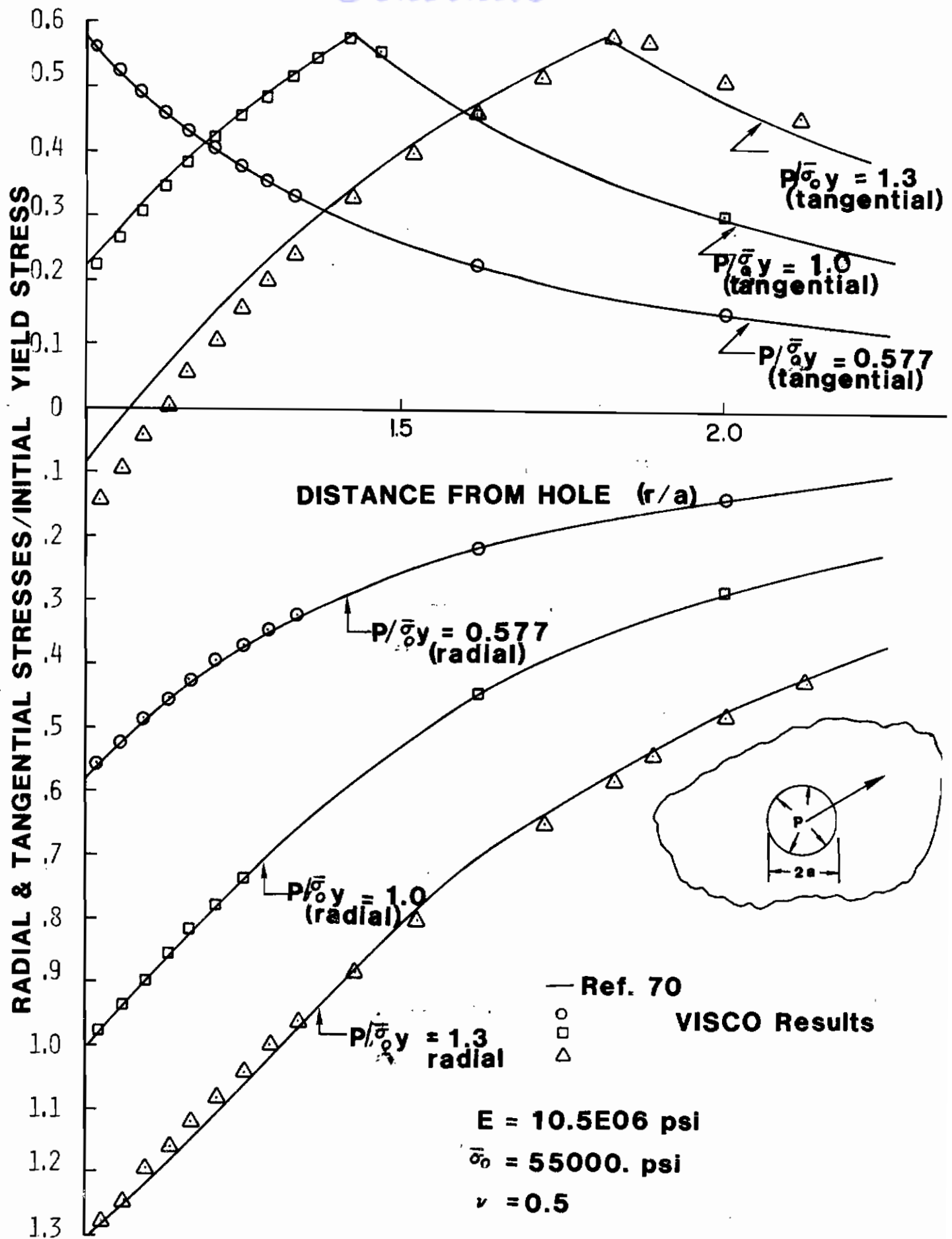


Figure 8. Radial and Tangential Stresses for the Infinite Plate with Pressurized Hole

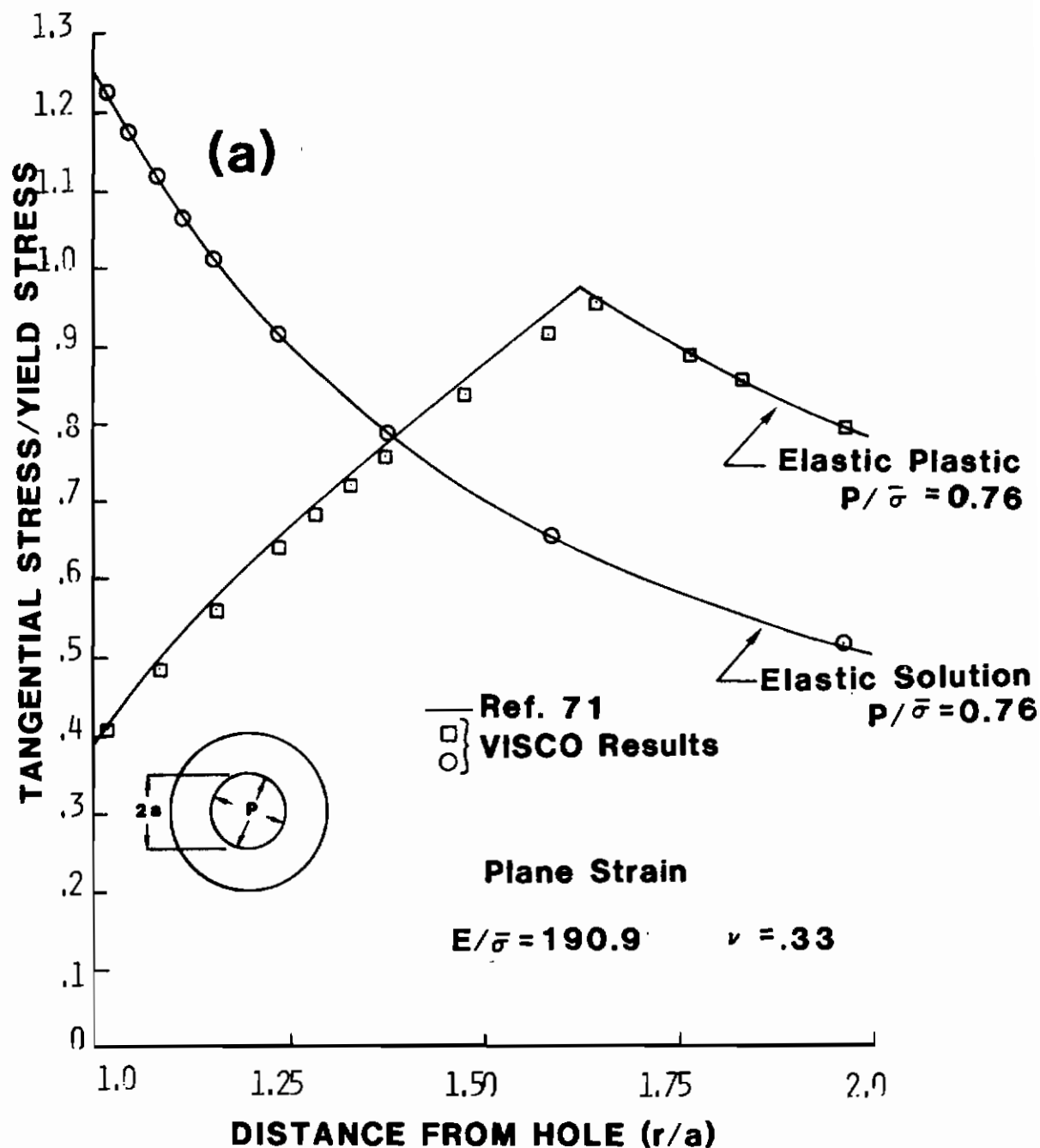


Figure 9a. Thick Cylinder with Internal Pressure, Tangential Stress Profile

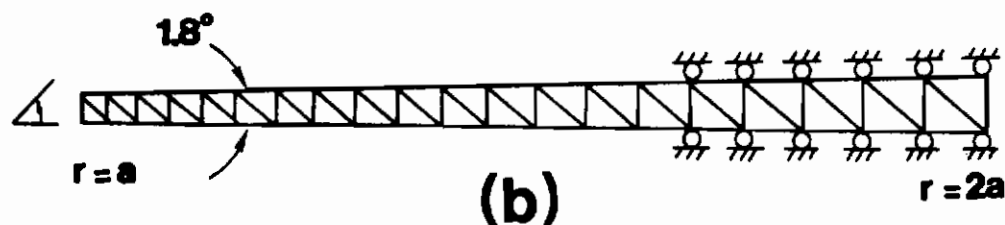


Figure 9b. Thick Cylinder with Internal Pressure, Finite Element Mesh

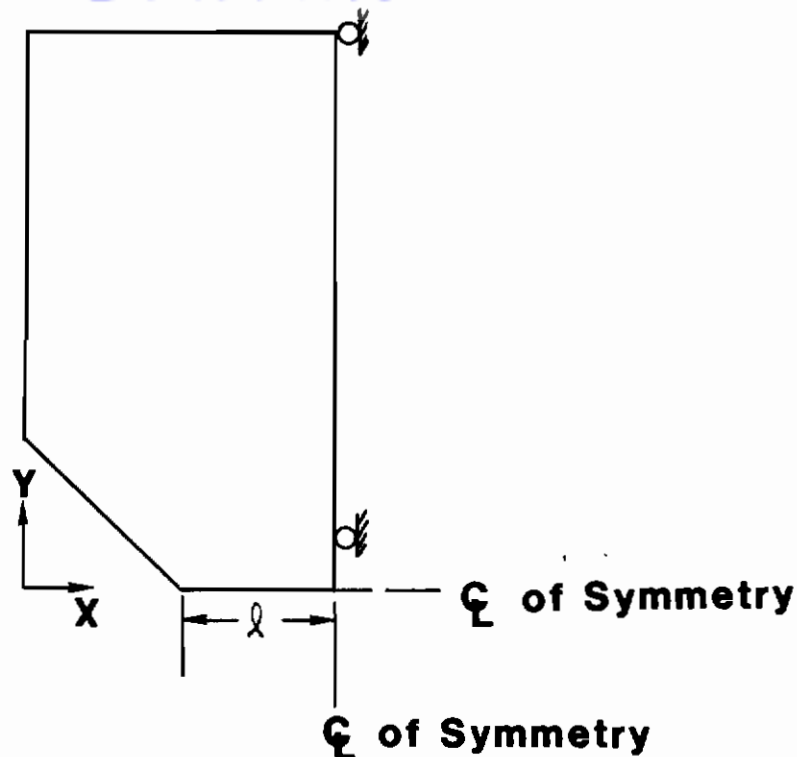


AFWAL-TR-80-4140

modulus approach was used by Yamada et. al. for their elastic-plastic analysis. This was an elastic-perfectly plastic plane stress solution where the ratio of the elastic modulus to yield stress  $E/\bar{\sigma} = 666.7$  and  $\nu = 0.3$ . The finite element mesh used herein was the same as given previously in Figure 7 where only one quarter of the plate is modeled due to symmetry. Element sizes were made smallest near the V-notch in order to capture the stress concentration there. A total of 182 constant strain triangular elements were employed which is somewhat less than used by Yamada et. al.

Figure 10 shows two y-component of stress profiles for the minimum section of the V-notched plate. Note for the applied stress of  $\sigma/\bar{\sigma} = 0.185$ , which was Yamada's initial yield load, the present results from VISCO agree very well except for the elements immediately at the notch. The high elastic stress concentration near the notch was not modeled as well by the present VISCO analysis due to larger element sizes being used in the notch vicinity. However, with yielding at the applied stress of  $\sigma/\bar{\sigma} = 0.584$ , comparison with Yamada's results at the notch are much better. Note that plastic action diminishes stress gradients and thus fewer elements are needed for an elastic solution can be used to produce good stress profiles after yielding occurs. However, it should be kept in mind that plastic action does not diminish the strain gradient like the stress gradient and therefore strain profiles, even after yielding, will be quite sensitive to element sizing.

Figure 11 displays the finite element mesh for the V-notched plate with those elements left out that have exceeded the yield stress for the applied stress of  $\sigma/\bar{\sigma} = 0.584$ . The absence of these elements thus describes the plastic zone size and compares well with that of Yamada. Numbers within the elements of Figure 11 reflect each elements effective stress as a percentage of yield stress.

*Contrails*

$E/\text{SIG BAR} = 666.7$   
 $\nu = 0.30$

— Yamada, Yoshimura, Sakurai  
 Ref. 38

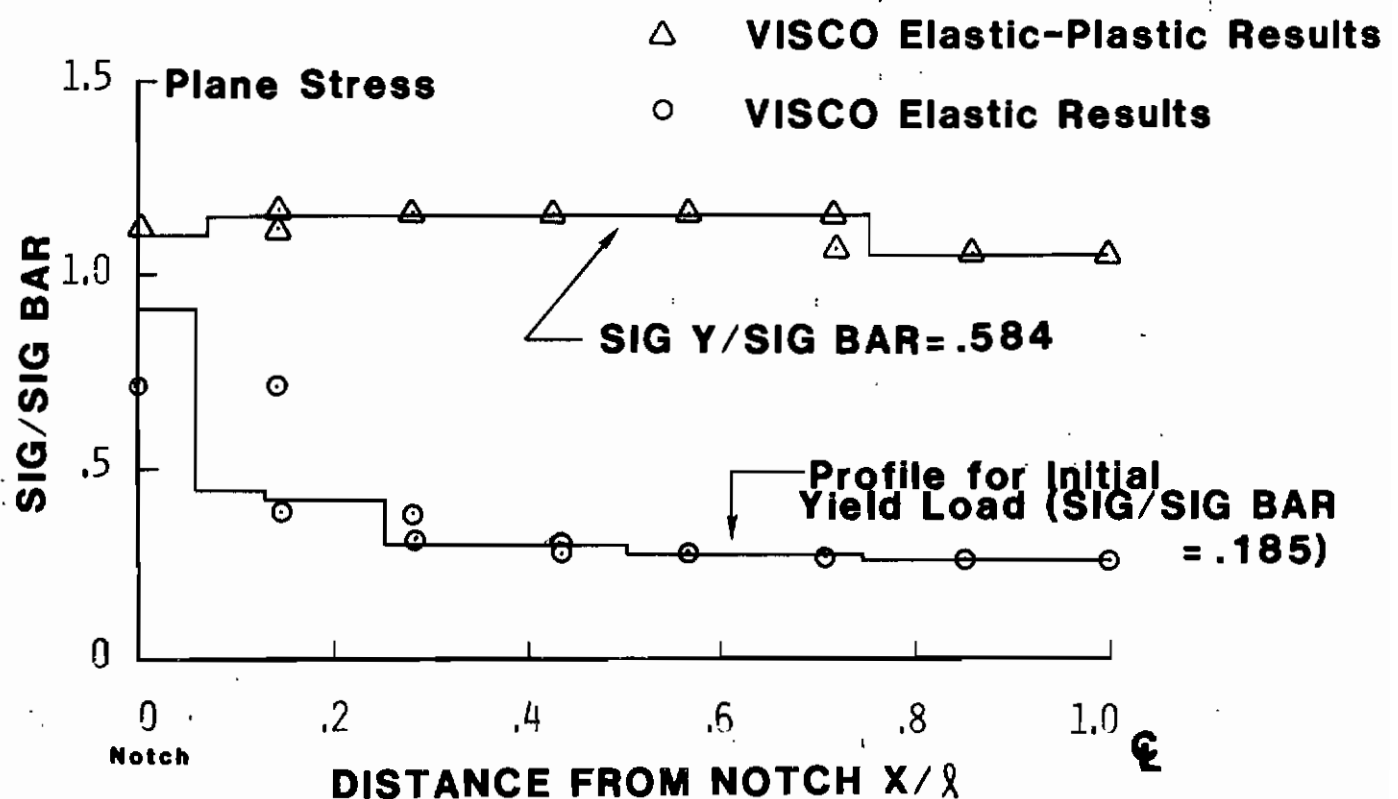


Figure 10. Stress Profile for V-Notched Plate in Tension

AFWAL-TR-80-4140

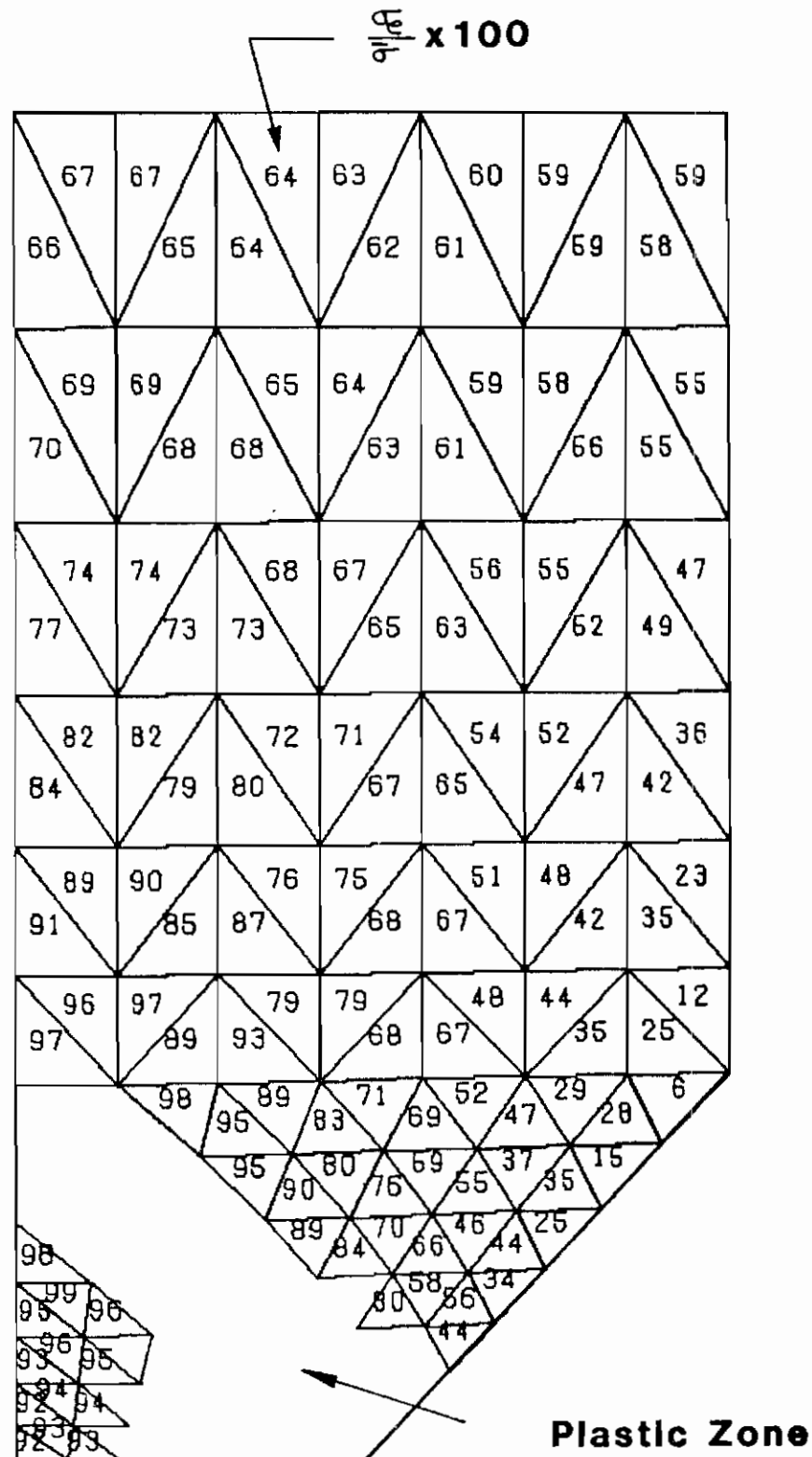


Figure 11. Plastic Zone in V-Notched Plate

d. Cracked Three Point Bend Specimen

The fourth example employs the Malvern model to analyze a cracked three-point bend specimen as shown in Figure 12. This will be the same problem as was solved with ten different computer codes for an ASTM analytical round robin and documented by Wilson and Osias (Reference 72). This was a plane strain crack problem where  $E=31.59 \times 10^6$  psi,  $\nu=0.30$ , and the following Ramberg-Osgood equation was used for the stress-strain curve

$$\epsilon = \frac{\sigma}{E} + \left( \frac{\sigma}{B_0} \right)^n \quad (49)$$

where  $\epsilon$  is the total strain (i.e., elastic and plastic),  $n$  is 10, and  $B_0$  is  $120 \times 10^3$  psi. To make Equation 49 compatible with the Malvern model, stress must be written as a function of plastic strain. Therefore, after subtracting the elastic strain (also equal to  $\sigma/E$ ) from both sides of Equation 49, solving for the stress  $\sigma$ , and redefining  $\sigma$  as  $\bar{\sigma}$

$$\bar{\sigma} = B_0 (\epsilon^P)^{\frac{1}{n}} \quad (50)$$

Due to symmetry only one half of the three-point bend specimen was modeled with the finite element mesh in Figure 13. This particular pattern for the element mesh was used by Ohtani and Nakamura (Reference 61) for a center cracked plate. Note how the element sizes are reduced as indicated in Figure 13 by arrows to the first and second reduction. This pattern provides for an unlimited number of element size reductions while also maintaining good element aspect ratios (e.g., from 1 to 0.5) and ensuring no two neighboring elements differ in size by more than a factor of 2. Accordingly, each reduction cuts the preceding element size in half. Eight element size reductions, incorporated in the Figure 13 mesh, stepwise reduced the 0.20 inch elements at the upper boundary to a  $7.8125 \times 10^{-4}$  inch element at the crack tip. This crack tip element size was slightly smaller than the smallest used in Reference 72. The total number of elements in Figure 13 was 584 with 388 nodes. Figures 14, 15, and 16 show the results of VISCO compared to ten times independent elastic-plastic solutions documented by Wilson and Osias. Eight of

AFWAL-TR-80-4140

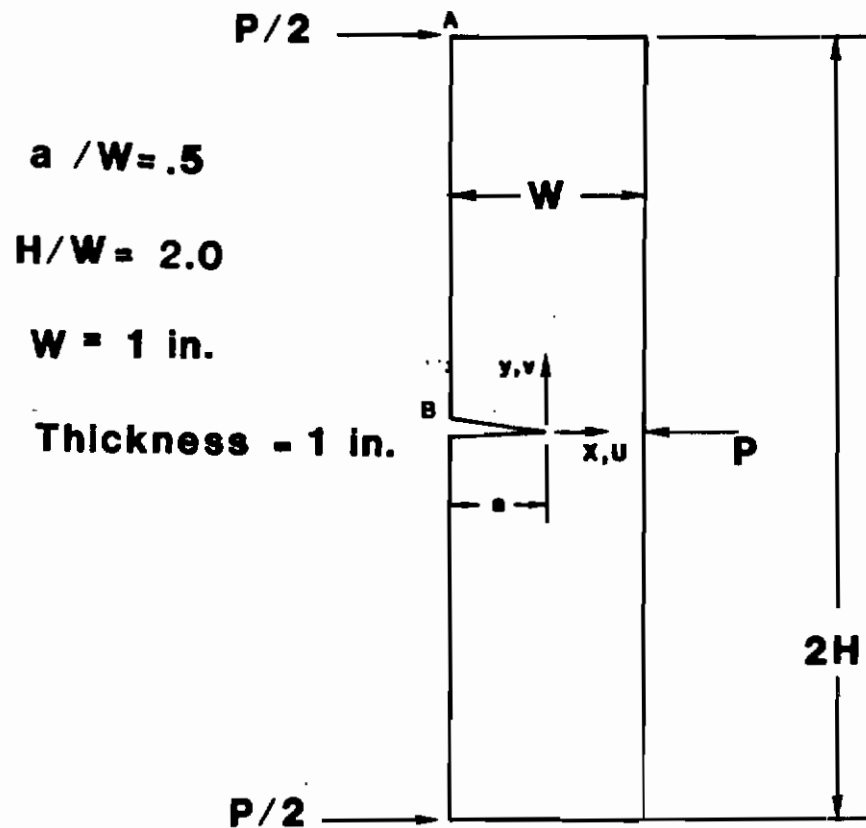


Figure 12. Three-Point Bend Specimen with Crack

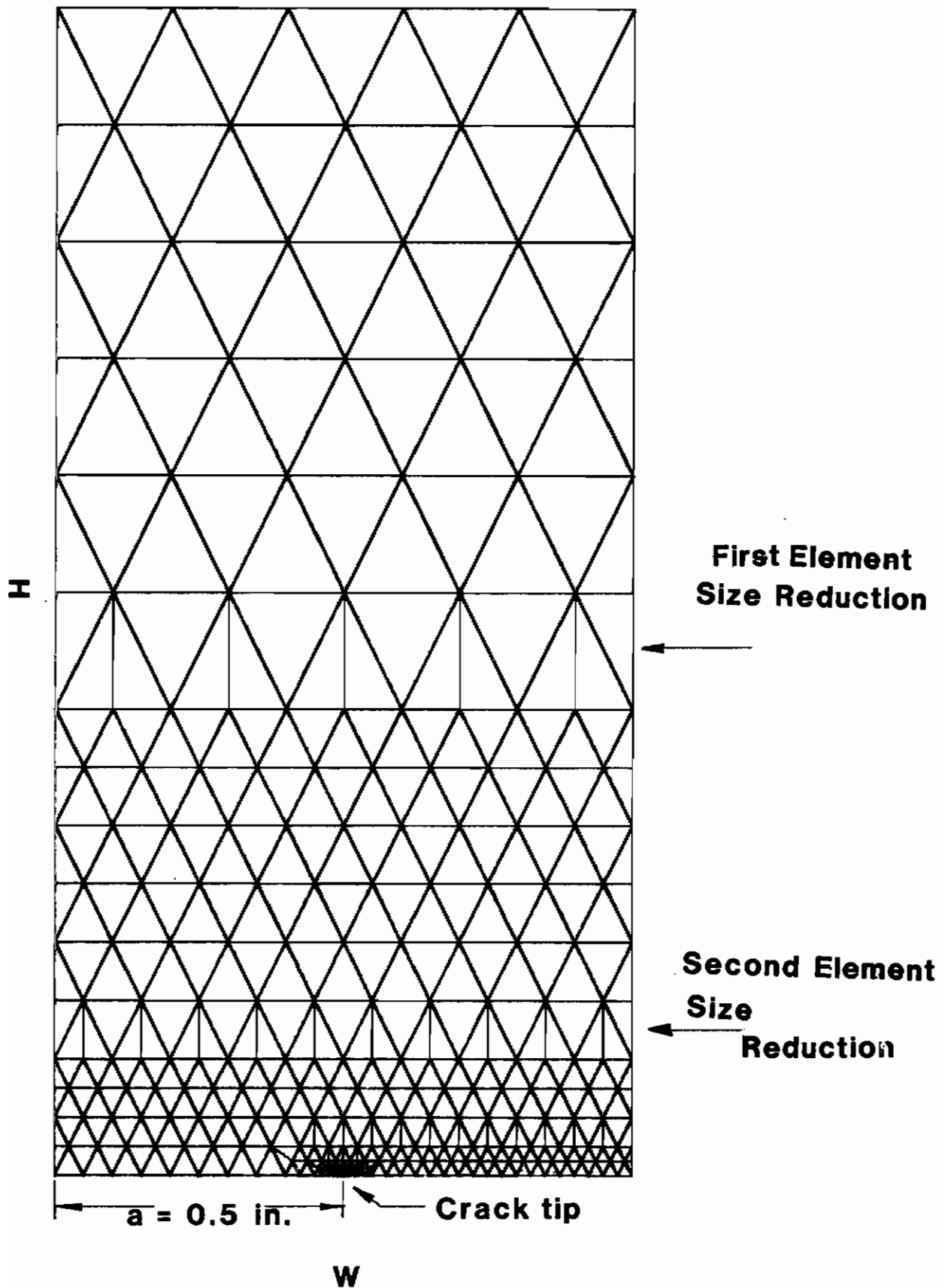


Figure 13. Three-Point Bend Finite Element Model

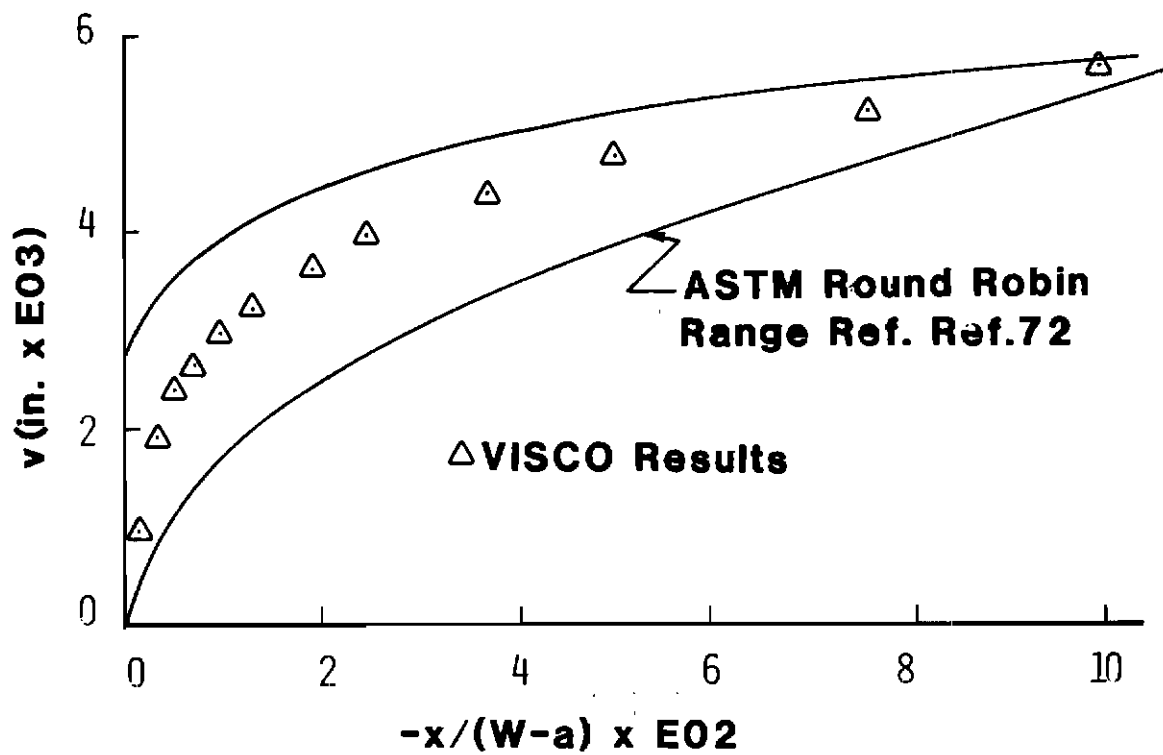


Figure 14. Crack Opening Displacement Profile @  $U_A = .050$  In. for Three-Point Bend Model



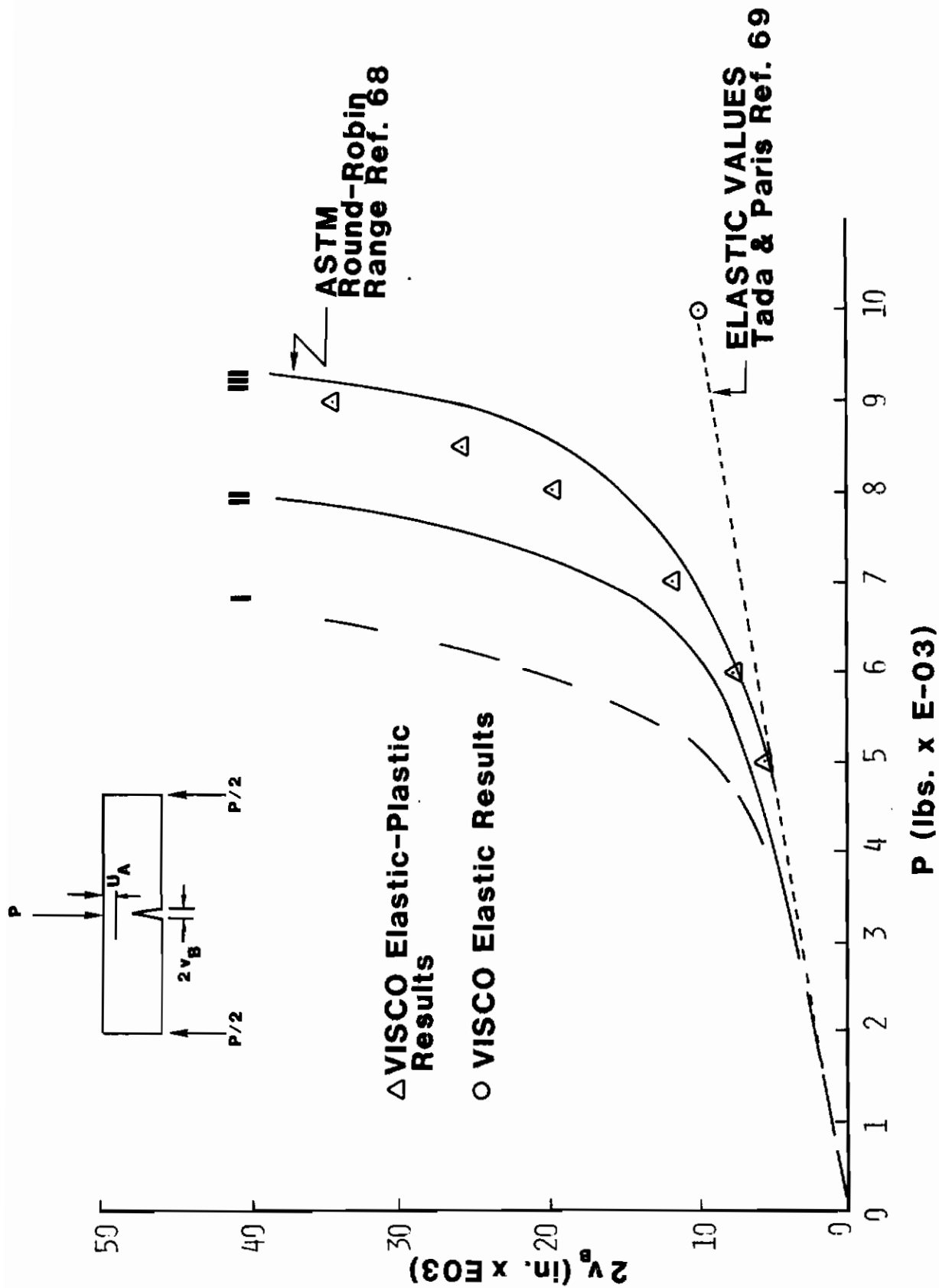


Figure 15. Crack Mouth Opening Displacement vs. Load for Three-Point Model

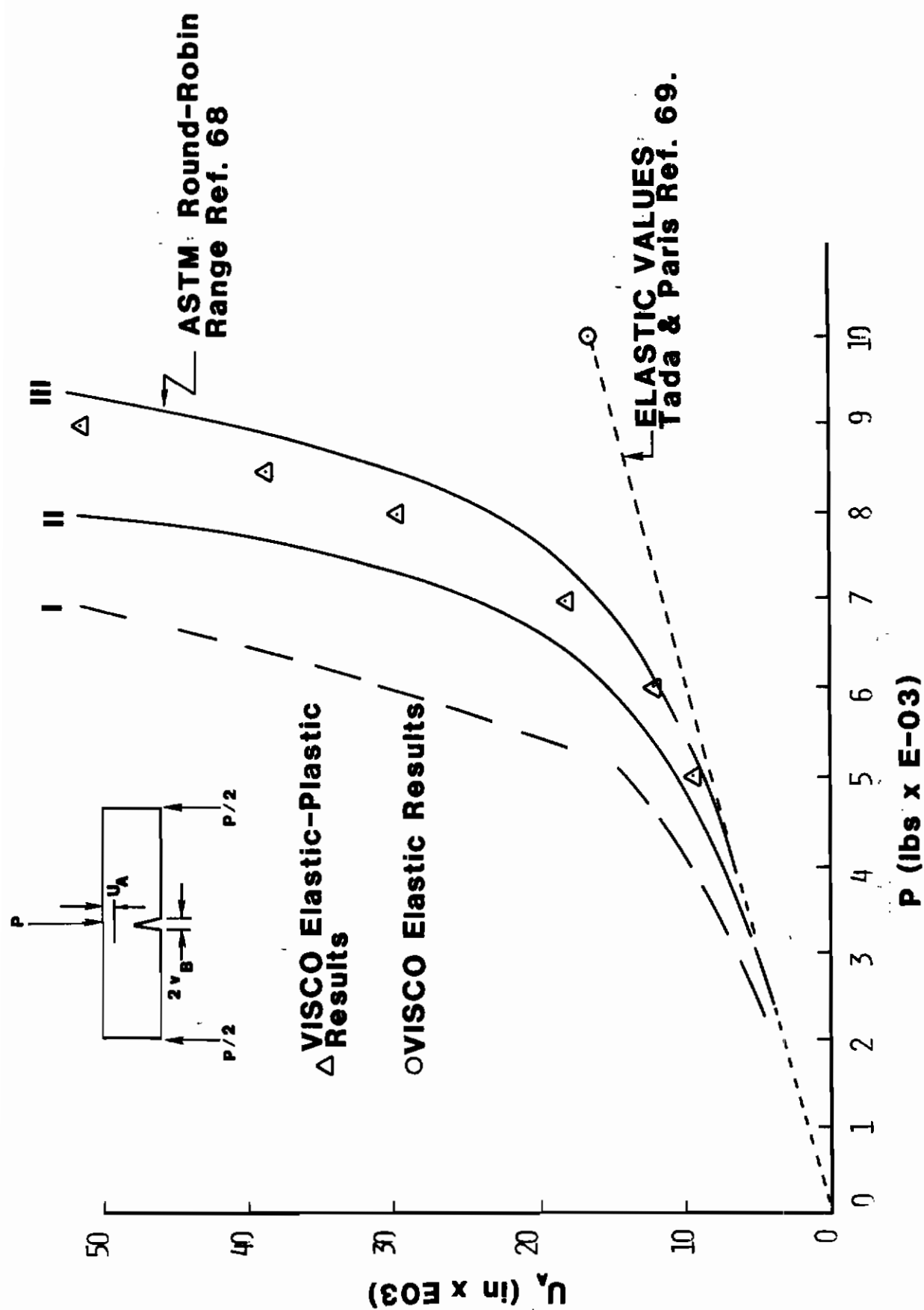


Figure 16. Load Point Displacement vs. Load for Three-Point Bend Model

these solutions fall within lines II and III in Figures 15 and 16. The other two solutions fall near line I in these two figures. In all cases the present results from VISCO fall within the ASTM round robin range as shown in these figures. Therefore the element sizing and arrangement in Figure 13 as used herein with VISCO, appears to give good results for a complex problem that includes a crack and load that induces bending.

#### e. Center Cracked Plate with Bodner Model

The fifth example employs the Bodner model to analyze a center cracked plate. Comparison will be made with results from a similar analysis using the Malvern model coupled with Norton's Law as follows

$$\dot{\epsilon}_{ij}^P = \begin{cases} [\gamma_p \left( \frac{\sigma_e}{\bar{\sigma}(\epsilon_e^P)} - 1 \right) + \gamma_c (\sigma_e)^\beta] \frac{3}{2} \frac{S_{ij}}{\sigma_e} & \text{if } \sigma_e > \bar{\sigma}(\epsilon_e^P) \\ [\gamma_c (\sigma_e)^\beta] \frac{3}{2} \frac{S_{ij}}{\sigma_e} & \text{if } \sigma_e \leq \bar{\sigma}(\epsilon_e^P) \end{cases} \quad (51)$$

This Malvern-Norton combination is a superposition approach suggested by Zienkiewicz (Reference 10) to model in a unified sense both initial load up viscoplasticity and creep under sustained load. Also, to assess the contribution of pure secondary creep in the Bodner model, comparison will be made to an analysis using only Norton's Law for the viscoplastic material model.

The material properties will be those matched to IN-100 at 1350°F. The constants for the Bodner model will be those previously given for IN-100. The yield stress as a function of plastic strain,  $\bar{\sigma}(\epsilon_e^P)$ , needed for the Malvern model will be a multilinear fit to the experimental stress-strain curve in Figure 4 and given as follows

$$\bar{\sigma}(\epsilon_e^P) = \begin{cases} 130. (1. + 76.2 \epsilon_e^P) \text{ ksi for } \epsilon_e^P < .00222 \\ 152. + 1591. (\epsilon_e^P - .00222) \text{ ksi for } .00222 \leq \epsilon_e^P < .01 \\ 164.4 \text{ ksi for } \epsilon_e^P \geq .01 \end{cases} \quad (52)$$

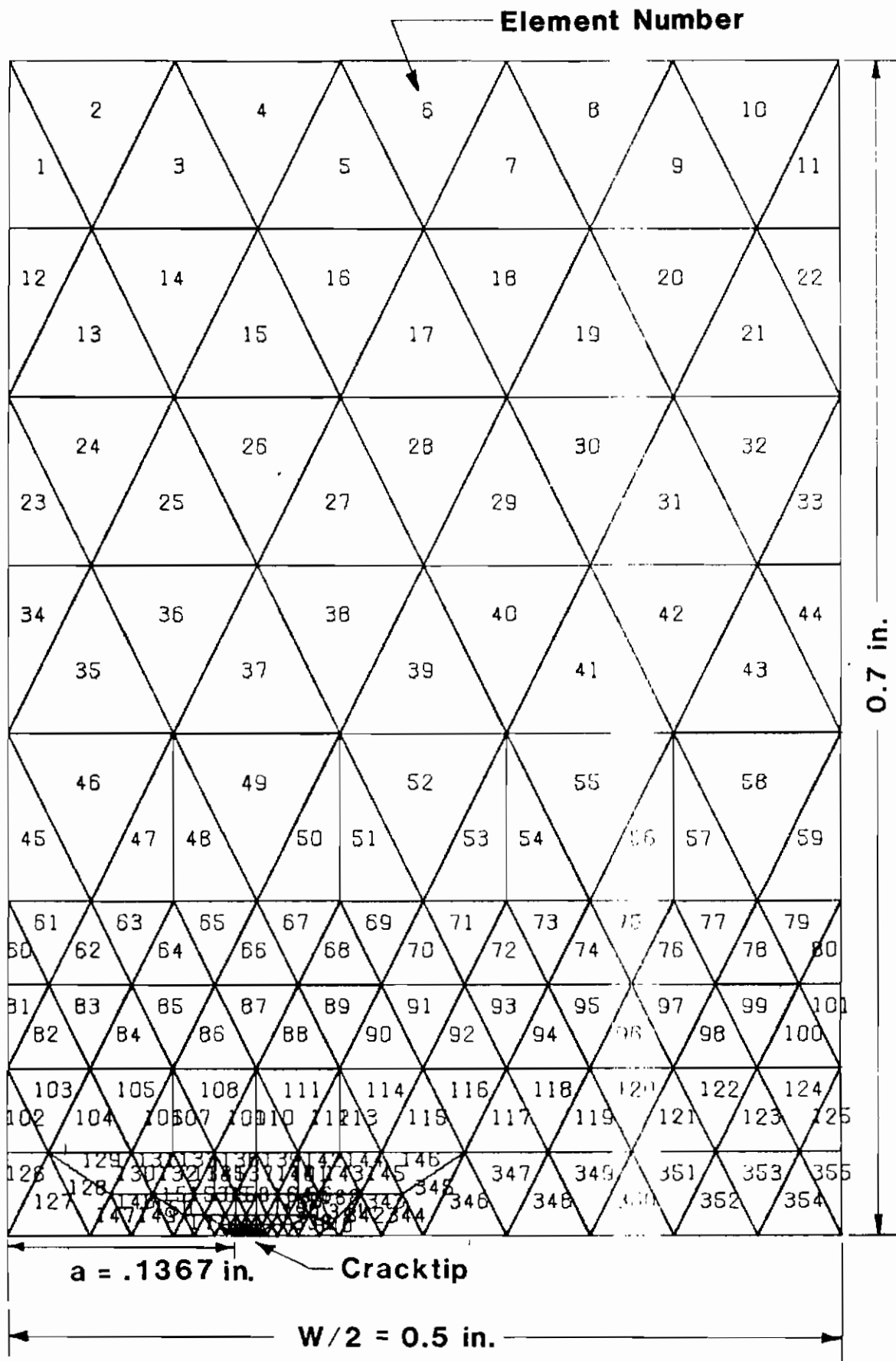
AFWAL-TR-80-4140

The fluidity constant  $\gamma_p$  for the Malvern model will be given a value of  $.58 \text{ sec}^{-1}$ . This value for  $\gamma_p$  is sufficiently high such that the given  $\bar{\sigma}$  function is followed very closely (e.g., recall Figure 3 for  $\gamma_p = \infty$ ). The constants for Norton's Law will be  $\gamma_c = 3.7394 \times 10^{-60} (\text{psi})^{-10.64}/\text{sec}$  and  $\beta = 10.64$ . These values were determined by matching the initial IN-100 creep behavior in Figures 5 and 6 as discussed in the Norton's Law for secondary creep section.

Due to symmetry only one fourth of the center cracked plate is modeled by the finite element mesh given in Figure 17. The plate's height is 2.8 inch, width is 1 inch, and thickness is 0.3 inch. The crack length,  $2a$ , is .2734 inch or  $a/W$  equal to .1367. The numbers inside the elements indicate a total of 355 elements were employed. The total number of nodes is 211. The triangular elements around the crack tip have a height and base dimension of  $7.8125 \times 10^{-4}$  inch. Further discussion of this element mesh will be presented in the Applications section since this particular mesh was also employed there to simulate the experimental program. A maximum stress of 36320 psi will be applied to the upper boundary of the center cracked plate in five seconds and then held constant for an elapsed time of 1000 seconds. This applied stress level corresponds to a load level also used in the experimental program to be simulated later.

A comparison of the behavior of these three material models is given in Figures 18, 19, and 20. The effective stress and plastic strain in Figures 18 and 19 are from the element at the crack tip which had the highest elastic stress concentration factor.

The stress-strain behavior in Figure 18 occurred over a time period of 1000 seconds. The values to the left of 6% strain occurred in approximately five seconds (the load up period) whereas to the right of 6% strain, stress relaxation and redistribution is taking place over approximately 1000 seconds of sustained load creep behavior. Note how

Figure 17. Center Cracked Plate Finite Element Model,  $a/W = 0.1367$

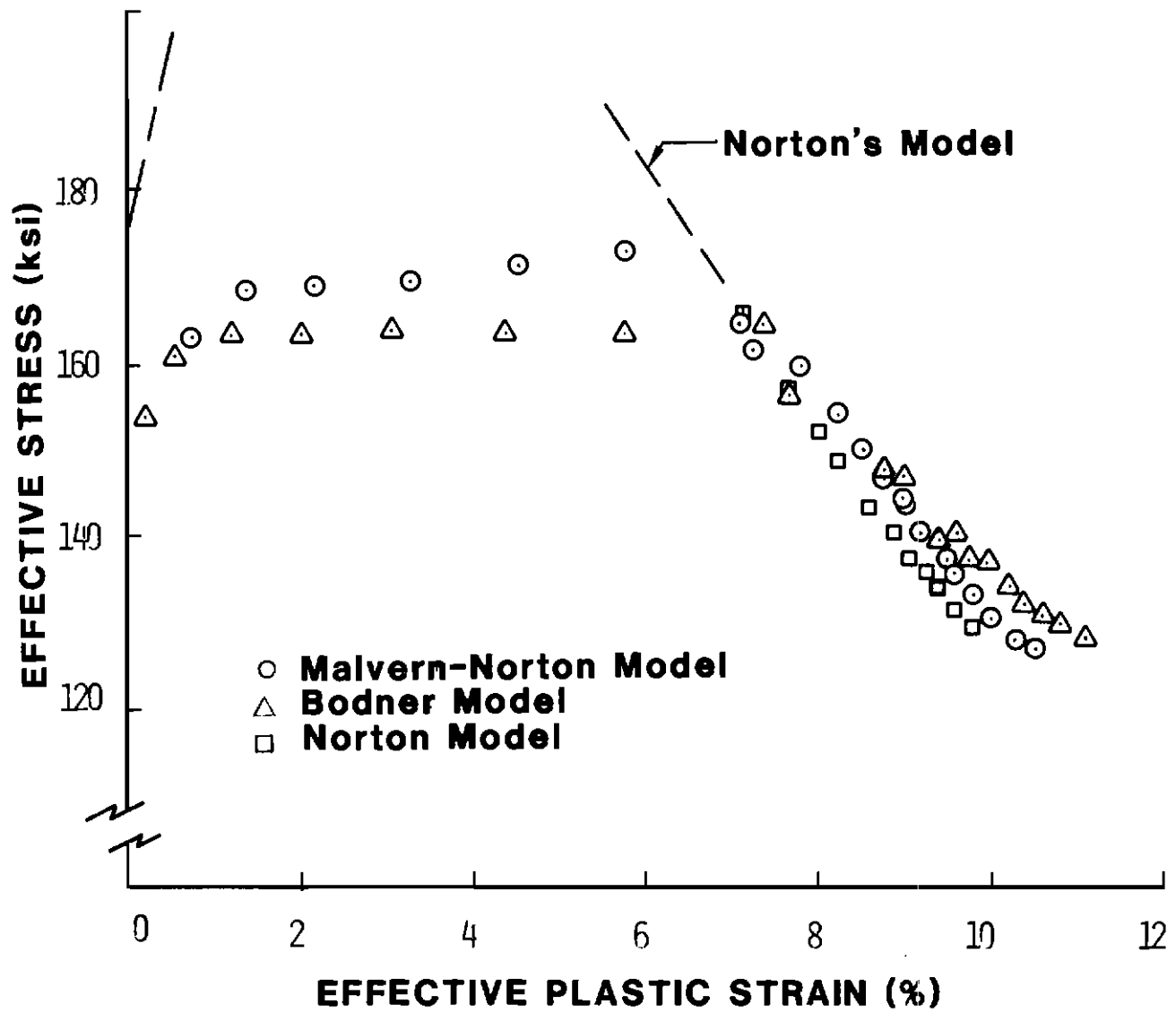


Figure 18. Stress vs. Strain at the Crack Tip for Bodner, Malvern-Norton, and Norton Material Models

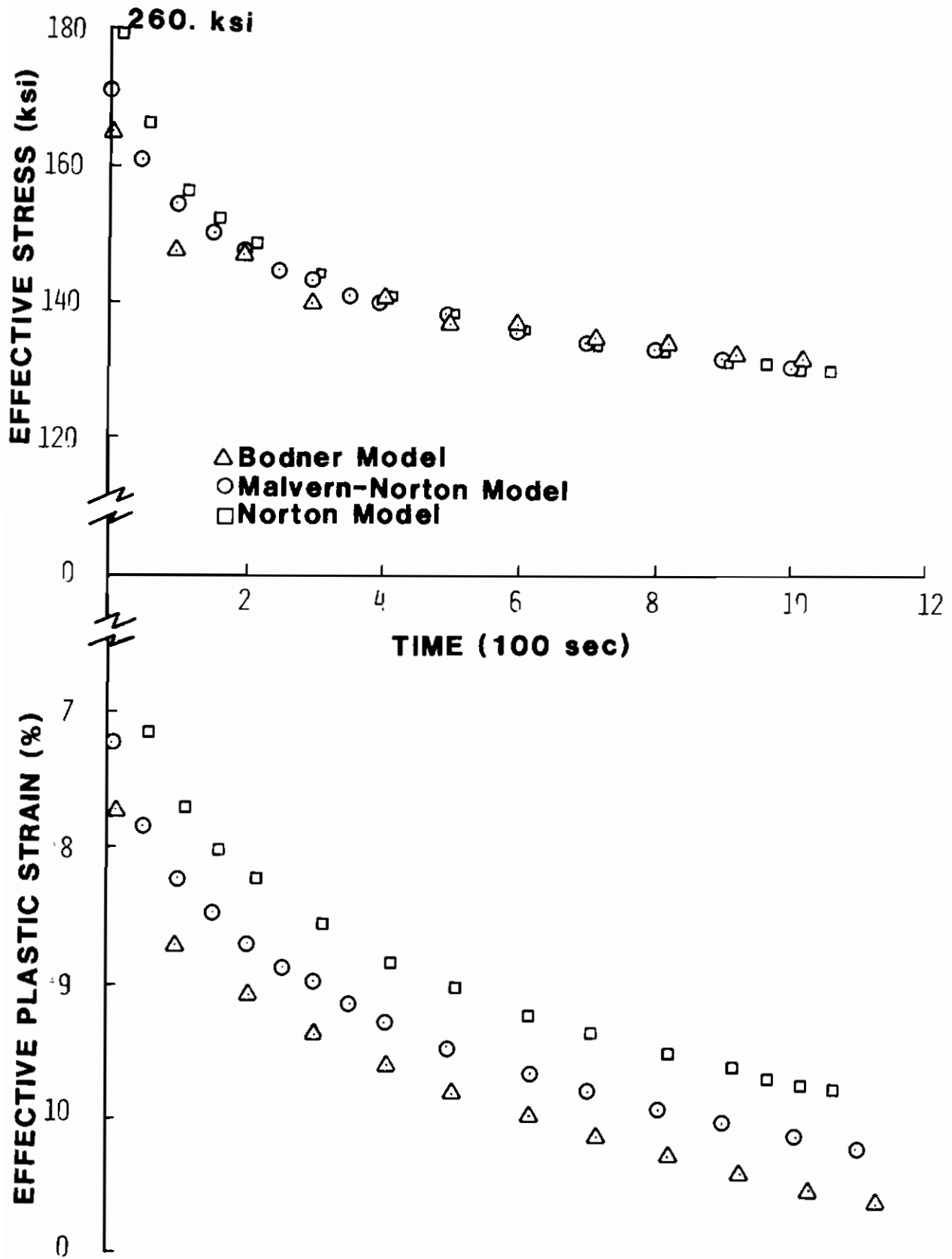


Figure 19. Effective Stress and Strain vs. Time at the Crack Tip for Bodner, Malvern-Norton, and Norton Material Models

AFWAL-TR-80-4140

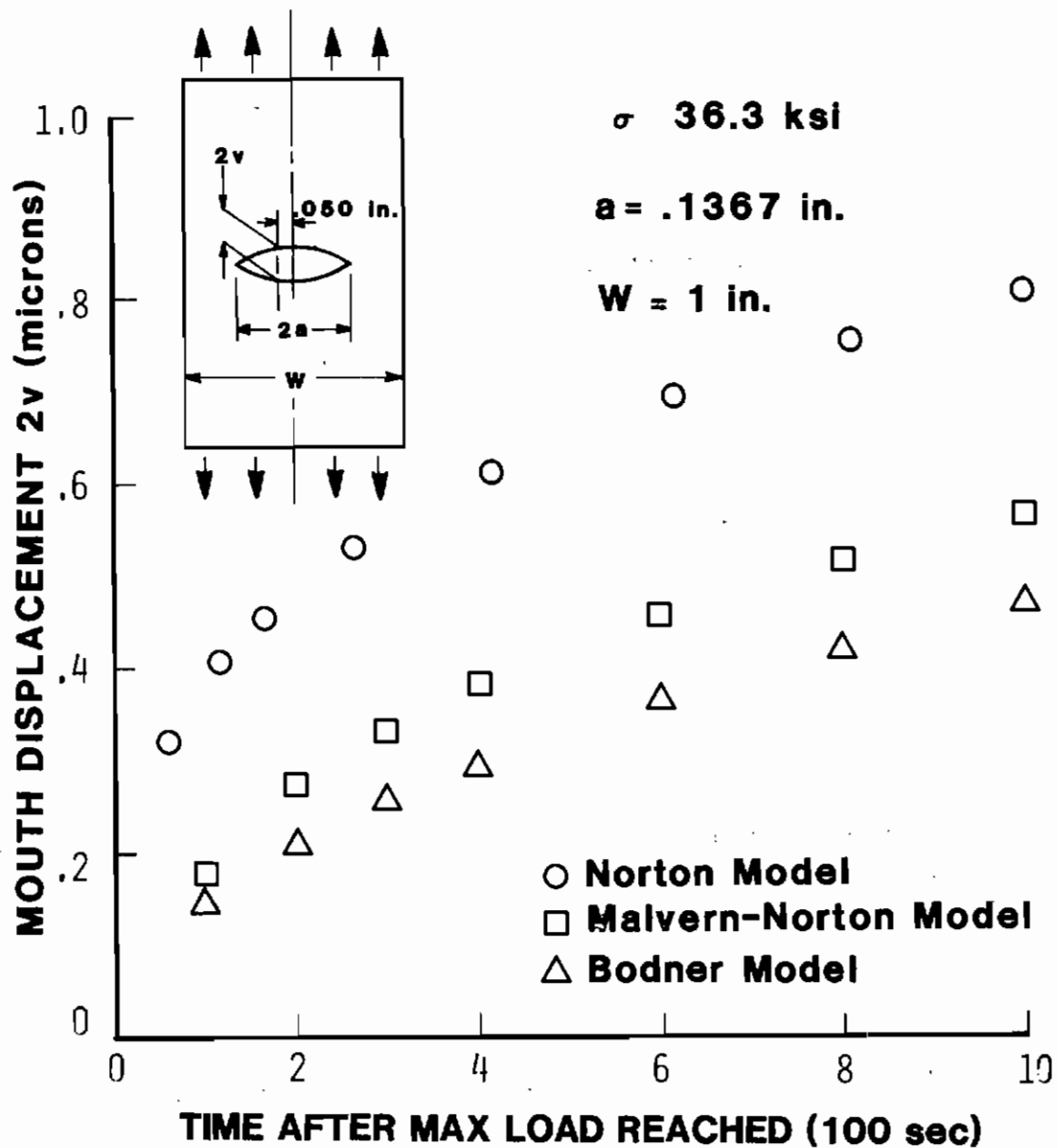


Figure 20. Crack Mouth Displacements in Center Cracked Plate for Bodner, Malvern-Norton, and Norton Material Models



AFWAL-TR-80-4140

the Norton model behaves during the load up period (i.e., strains less than 6%). Due to its slow creep response, the effective stress from the Norton model approaches the values that would occur during load up in an elastic analysis. However, the Norton model relaxes the stress down to values very similar to the other material model stress values. In general the Bodner model behaves very similar to the Malvern-Norton combination both during load up and the sustained load creep periods.

Figure 19 shows the time dependent behavior of the effective stress and plastic strain from the same crack tip element. After approximately 200 seconds, all three material models develop nearly identical effective stress values. Plastic strain behavior with time is also very similar for the three models except for under 100 seconds of time. The difference in percent plastic strain between the three curves developed primarily from different plastic strain rates during the load up phase and remains fairly constant for time greater than 200 seconds.

Figure 20 shows how the crack mouth displacement increases with time after the maximum load is achieved. The location of the crack mouth displacement is indicated in Figure 20 to be 0.050 inches from the vertical centerline. Again the three curves are very similar after 200 seconds and their separation is due primarily to dissimilar behavior for time under 200 seconds. The Norton model displays more displacement after maximum load than the other models since it is effectively making up for its slower plastic strain rates and associated displacements during the load up phase. This apparently is also true when comparing the Malvern-Norton to the Bodner model displacement curve, however, here the difference is much less.

Therefore, based on these comparisons with somewhat similar material models used to analyze the center cracked plate, the Bodner model within VISCO is considered to be working well. For further discussion and comparison of these material models see Reference 77.

AFWAL-TR-80-4140

## 5. SUMMARY OF FINDINGS

The following findings were determined from the preceding validation examples and the general development of the VISCO program.

1. The stress tolerance,  $\sigma_{tol}$ , which controls the variable time step size in VISCO's numerical time integration algorithm, provides good results for reasonable computer time requirements when set to the value of 0.03. The strain tolerance,  $\epsilon_{tol}$ , has little effect as long as its greater than or equal to the stress tolerance. This finding pertains to the Bodner, Malvern, and Norton material models.
2. The VISCO program, while employing the Malvern material model agrees well with so-called exact elastic-plastic deformation solutions both in plane stress and plane strain conditions. Agreement is also good with time independent elastic-plastic finite element solutions in a V-notched plate and a cracked three-point bend specimen whose results came from an ASTM analytical round robin.
3. The finite element mesh pattern in Figure 13 works well for modeling cracked plates. This pattern conveniently provides for an unlimited number of element size reductions to capture the crack tip singularity while also maintaining good element aspect ratios and minimizing the total number of elements required.
4. A crack tip element size to specimen width ratio of  $7.8125 \times 10^{-4}$  in a cracked three-point bend specimen provided good agreement with an ASTM analytical round robin.
5. The Bodner material model has been shown to behave similarly to the Malvern-Norton model for both load up and sustained load creep stages. Also, for time greater than 200 seconds after load is applied, the pure secondary creep Norton law behaves

AFWAL-TR-80-4140

similar to the Bodner model. In general, these similarities in material model behavior should be true for most any metal, however, the indicated 200 second time delay between the Norton and Bodner models pertains specifically to the IN-100 alloy at 1350°F.

Therefore, these findings support the validation of the VISCO computer program and provides some of the required details for applying the VISCO program with the Bodner model to creep crack growth simulation.

## SECTION IV

HYBRID EXPERIMENTAL-NUMERICAL PROCEDURE TO  
ANALYZE CREEP CRACK GROWTH

The simultaneous use of experimental data from crack growth tests and a theoretical model of the experimental cracked specimen has been termed the Hybrid Experimental-Numerical procedure by Kobayashi (Reference 16). One example of this procedure would be to grow a crack at experimentally determined rates through the theoretical model of the experimental specimen. Then, from the results, one could seek out potential crack growth criteria which hopefully, during crack growth, display themselves as fairly constant parameters independent of both crack length and load intensity (e.g., stress or strain at the crack tip, crack-opening displacement, etc.).

In the present investigation, the Hybrid Experimental-Numerical procedure required the theoretical model to track experimental displacement rates rather than crack growth rates. The theoretical model consisted of the VISCO program employing the Bodner constitutive equations and a finite element mesh of the experimental specimen. The experimental displacements were either measured near the crack tip or near the vertical centerline (crack mouth) of the center cracked plate test specimens as shown in Figure 21. The displacements were measured continuously with time by an optical interferometric displacement measurement technique developed by Sharpe (Reference 74). Figure 22 shows a typical experimental displacement versus time curve. The present numerical procedure required the crack to grow through the theoretical model such that the displacements due to elastic-plastic behavior and crack growth added up to the experimental displacements as time progressed. Therefore, crack length versus time became a product of the present analysis rather than an input.

## 1. CRACK LENGTH VERSUS TIME

Ideally for this investigation, the experimental data should be in the form of crack length versus time rather than displacement rates.

AFWAL-TR-80-4140

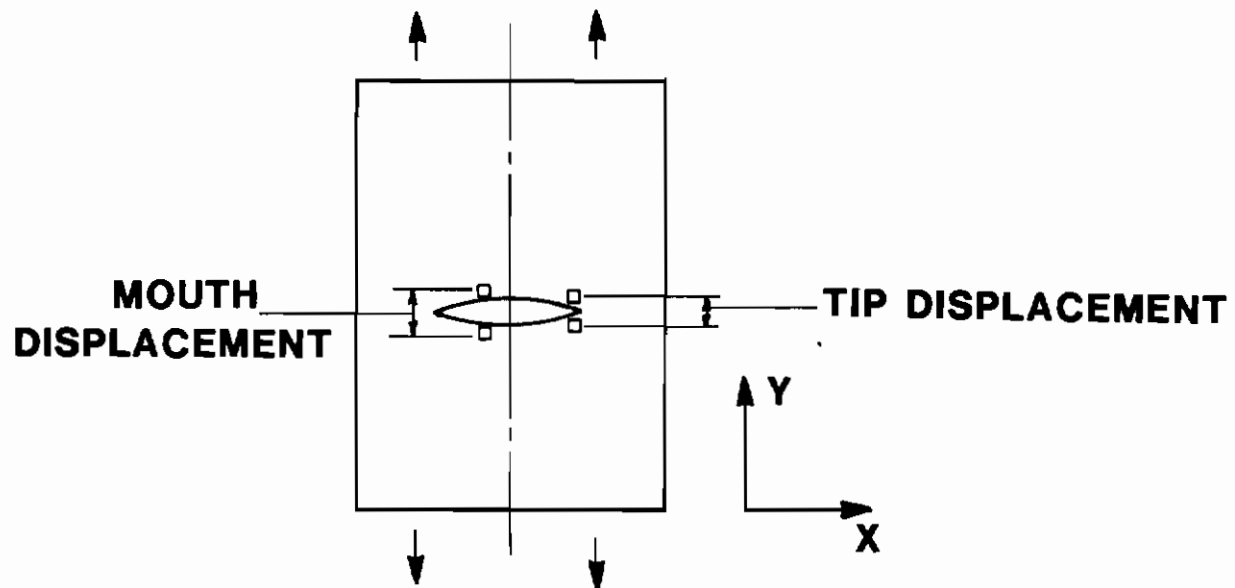


Figure 21. Center Cracked Plate Test Specimen

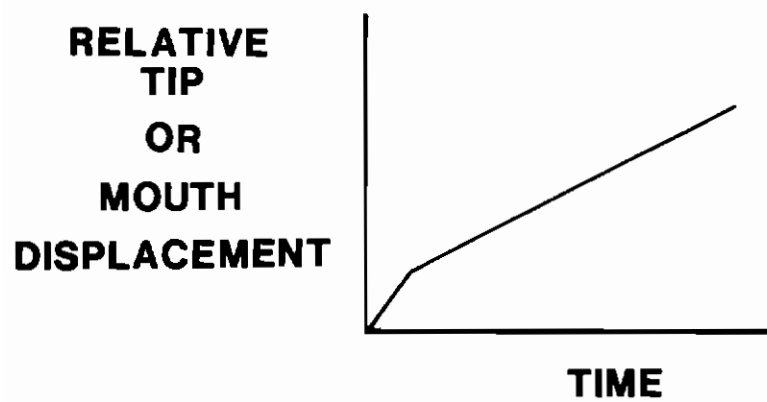


Figure 22. Displacement Under Constant Load

AFWAL-TR-80-4140

Unfortunately, it was nearly impossible, experimentally, to measure crack length as a function of time with any degree of precision or reliability on the surface since the total amount of crack growth in these tests was extremely small (e.g., 100 microns) and since the creep crack would grow internally or tunnel without associated surface crack growth.

Another attempt to measure crack growth rate indirectly employed the elastic compliance method first demonstrated by Clarke (Reference 75). This method utilizes the change in elastic compliance of the specimen with time and then with the aid of a compliance versus crack length relationship based on linear elastic fracture mechanics, crack growth with time may be determined. Figure 23 shows schematically an experimental creep crack growth load versus time history designed to provide discrete values of compliance at selected time intervals. The load is reduced approximately 20% and then restored as shown at times  $t_1$  through  $t_3$  to provide load displacement data at various times during the test. Figure 24 shows a typical set of load displacement data for increasing times  $t_1$  to  $t_4$  in a creep crack growth test. Compliance is defined as displacement divided by load and therefore the slope of each line in Figure 24 represents the compliance at each particular time. Note that compliance is shown to decrease in going from time  $t_1$  to  $t_2$  and then increase from time  $t_2$  to  $t_4$ . Comparing this behavior to a typical elastic compliance versus crack length curve given in Figure 25, the mathematical implication is that the crack shortens with time. Although this compliance decrease/increase behavior has also been observed by Donat (Reference 76), no known experimental data supports any physical shortening or healing of the crack. However, the important implication of this compliance behavior is that a one to one relation between crack length and compliance does not exist during creep crack growth. Therefore, the elastic compliance method cannot be used directly to measure crack length with time in creep crack growth tests.

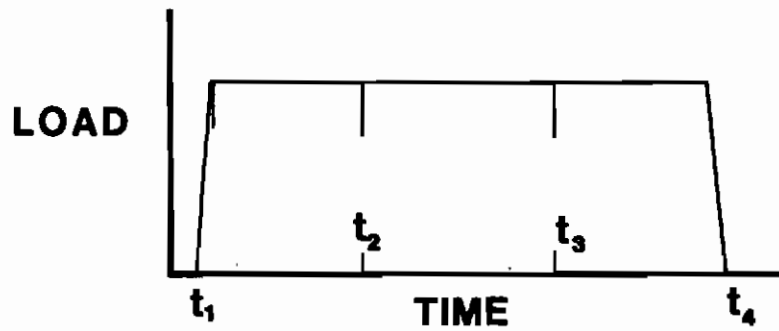


Figure 23. Experimental Load vs. Time

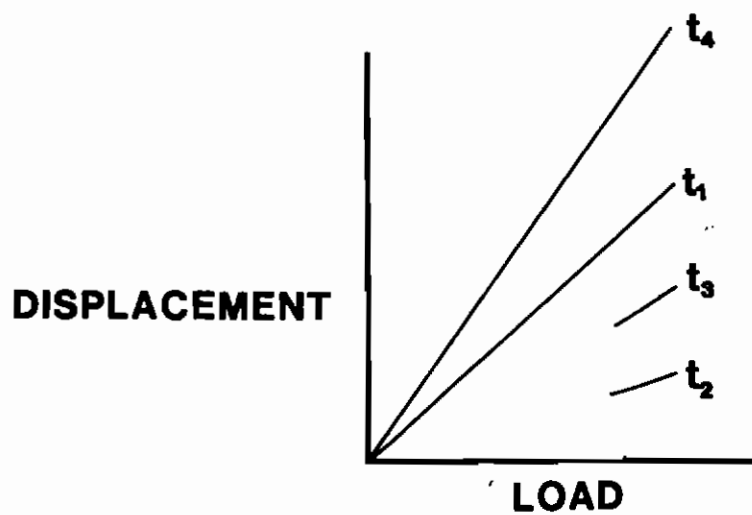


Figure 24. Experimental Compliance Changes with Time

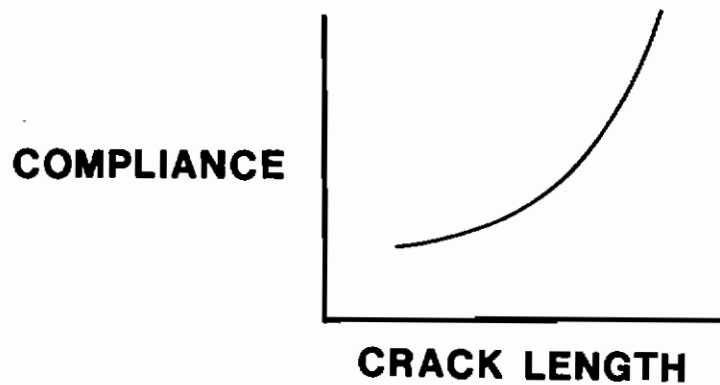


Figure 25. Elastic Compliance vs. Crack Length



## 2. MATCHING EXPERIMENTAL DISPLACEMENT DATA

In each Hybrid Experimental-Numerical application of the VISCO finite element model to simulate creep crack growth tests, the y-displacement of the node which was closest to the point where the experimental measurement was made was monitored with time. If the node's displacement became less than experimental displacement at a given time a crack tip node would begin to be released to simulate crack growth through the model.

## 3. CRACK TIP NODE RELEASE METHODS

Crack tip nodes were released in one of two different methods. The first method releases the node and totally unloads it in five seconds. The second method unloads the current crack tip node linearly with time over the total time span between the time when the current crack tip node is begun to be released and the time when the next crack tip node will be released. The five-second node release method for crack growth must be used when matching experimental displacements or when a crack growth criterion is used. In both of these cases when certain conditions are satisfied, the crack must grow so a node is released. However, when the current node is being unloaded it is not known when the next crack tip node will be released and therefore the continuous unload method cannot be used. The five-second unload time for the first method was based on the size of the crack tip elements and the maximum crack growth rates occurring in the creep crack growth test data (i.e., maximum crack growth rate equals element size divided by five seconds). If a crack growth rate criterion were used then it could be determined by extrapolation when the next crack tip will be released and thus the current crack tip node could be unloaded in a continuous fashion by the second method. The second node release method can also be employed when all node release times are specified at the beginning of the computer run (e.g., release times based on results from a prior computer run using release method one and matching experimental data).



In both node release methods, the node force required to hold the crack tip node at zero displacement would be calculated from the stresses in the adjacent elements as follows

$$\{f\} = \sum_{\substack{\text{Adjacent} \\ \text{Elements}}} \int_{\text{vol}} [B] \{\sigma_{ij}\} d \text{ vol} \quad (53)$$

which is consistent with the formulation of the stiffness matrix in Appendix A. The crack tip node restraint force,  $f_y$ , is then the component of  $\{f\}$  perpendicular to the crackline. The boundary condition on the node is converted from zero displacement to a force equal to  $f_y$ . This force  $f_y$  is then removed depending upon which node release method is chosen (Figure 26).

The change of the crack tip node's boundary condition from displacement to a force boundary condition is handled very conveniently with the Gauss-Seidel iterative linear equation solver as discussed in Appendix B. Whenever a node is fixed in a certain direction, its equilibrium equation in that direction is skipped over during the iterative solution procedure and when the node is released its equilibrium equation is included within the iterative procedure. No lengthy refactorization of the stiffness matrix is required for these boundary condition changes.

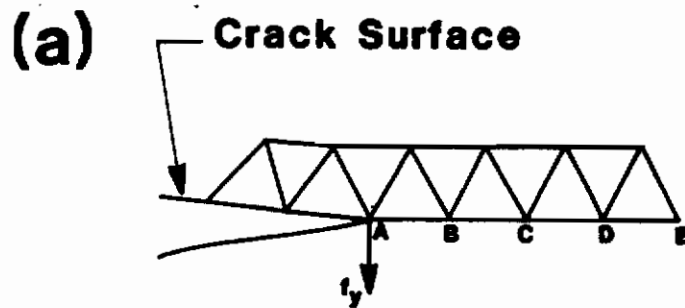


Figure 26a. Crack Tip Node Unload Methods, Finite Element Crack Tip.

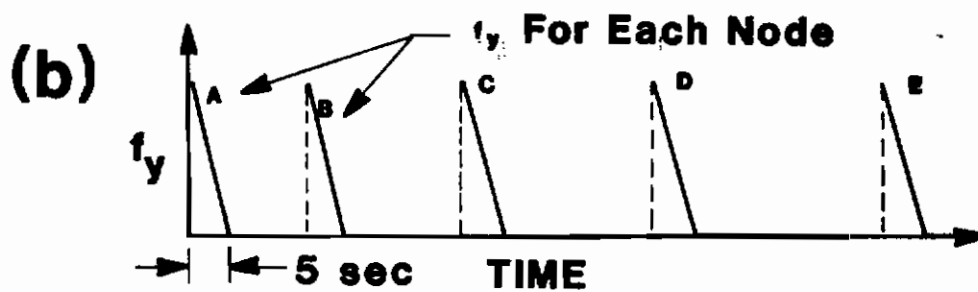


Figure 26b. Crack Tip Node Unload Methods, Five Seconds Node Unload Method

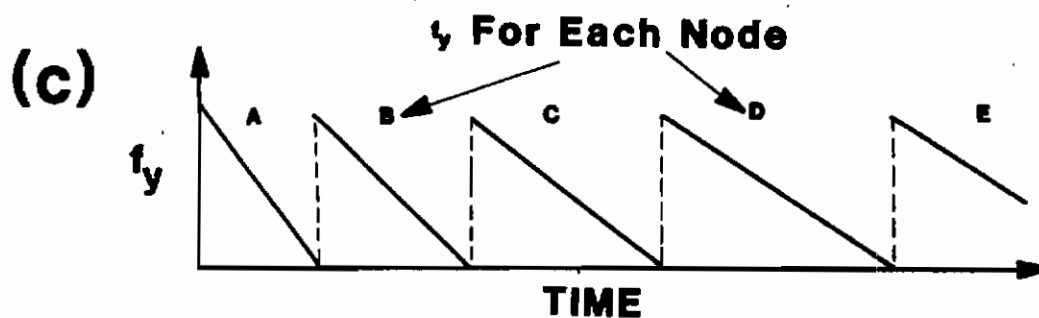


Figure 26c. Crack Tip Node Unload Methods, Continuous Node Unload Method

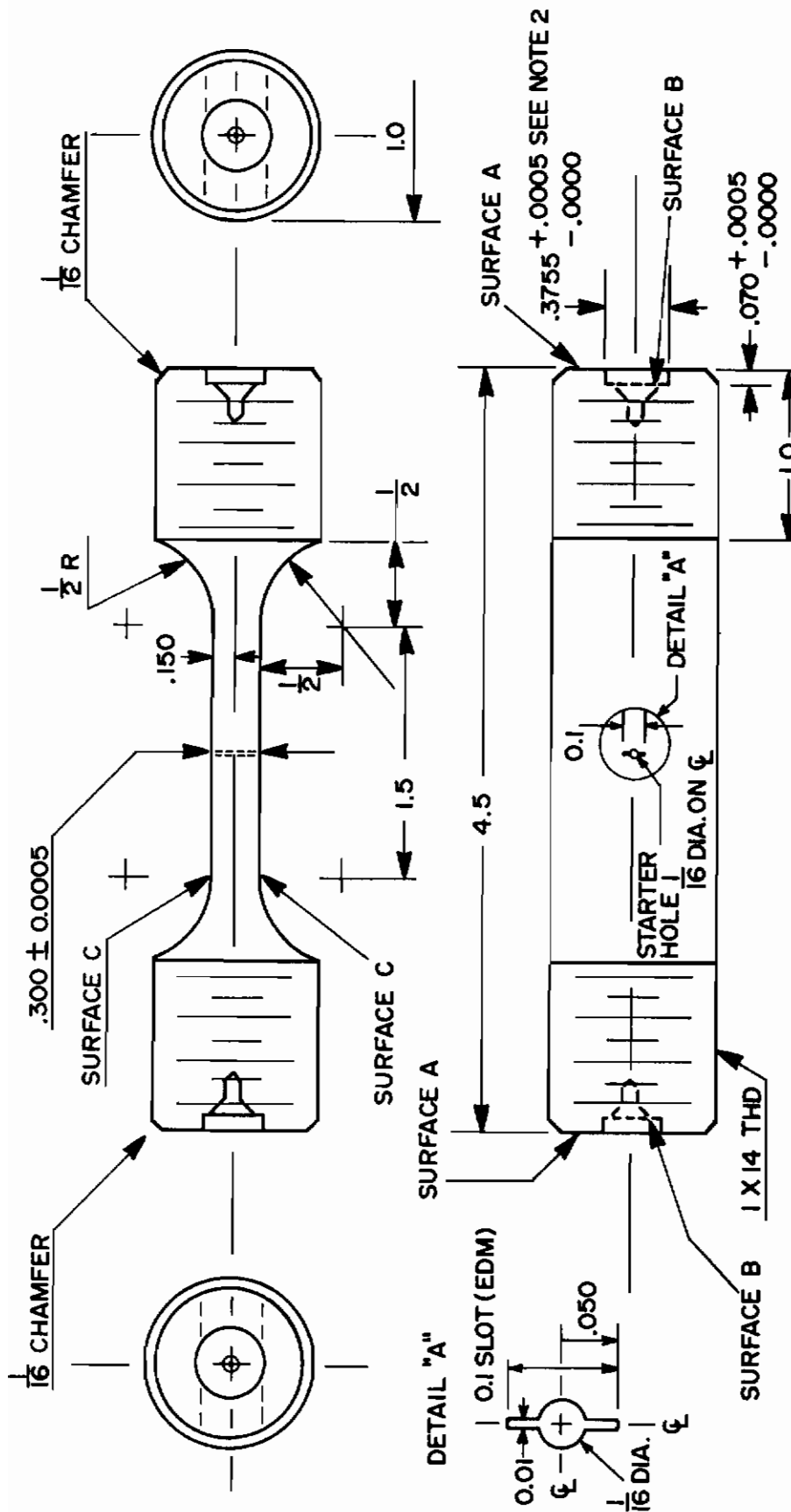
## SECTION V

APPLICATION OF THE HYBRID EXPERIMENTAL  
NUMERICAL PROCEDURE TO CREEP CRACK GROWTH

The first objective in the present research was to develop a method for getting crack growth behavior solely from displacement measurements made on a cracked specimen under constant load and at elevated temperature. This objective is extremely important since small but significant amounts of crack growth can not otherwise be resolved by conventional experimental crack measuring techniques. The second objective was to seek out crack growth criteria based on the crack growth behavior identified from the present work on the first objective and by examining various parameters around the crack tip in the theoretical model (e.g., stress, strain, crack opening displacement, etc.).

This section presents the results of applying the hybrid experimental numerical (HEN) procedure to creep crack growth in IN-100 at 1350°F. The experimental portion of the procedure consisted of displacement versus load (i.e., compliance) and displacement versus time test data reported by Sharpe (Reference 15). The numerical portion of the HEN procedure consisted of the VISCO finite element program employing the Bodner material model. The material constants for the Bodner model were those given in Section III.

The machining specifications for the specimens used in the experimental program are shown in Figure 27. Only the center uniform cross section part of the specimen was considered in the VISCO simulation and due to symmetry only one quadrant of this section was represented by the finite element meshes given in Figures 28, 29, and 30. Each of these meshes represent the center cracked plate test specimen with different crack lengths. The convergence of these meshes has been verified through the work in Section III and further discussion of their accuracy will be provided in subsequent paragraphs. Figures 28, 29, and 30 have half crack lengths,  $a$ , or 0.137 inches, 0.237 inches, 0.312 inches, respectively. Due to the variations of the initial crack



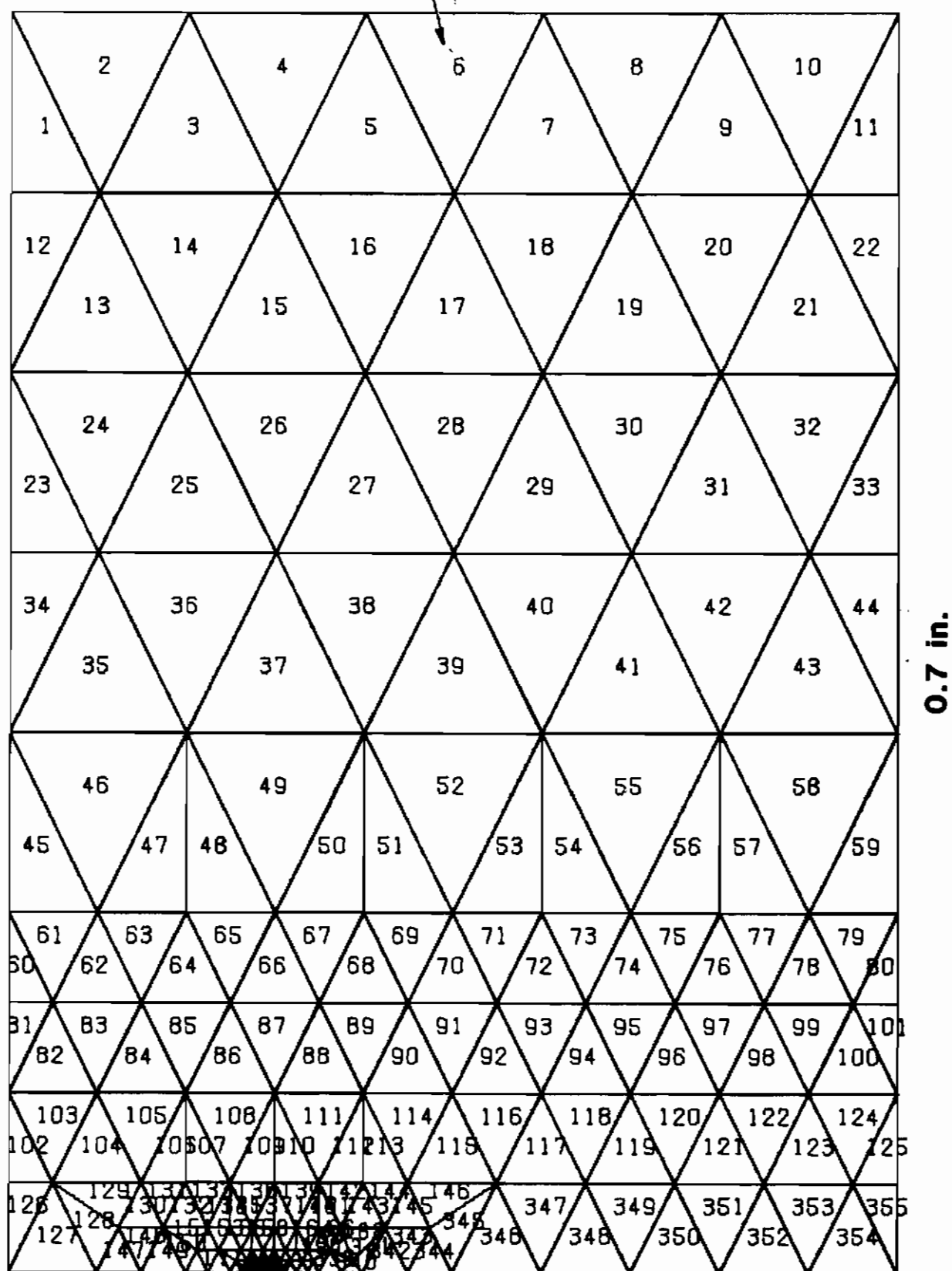
## NOTES:

1. All dimensions are in inches.
2. Surfaces A and surfaces B to be parallel to within 0.0005-in.
3. Threads and 0.3755-in. holes to be concentric to within 0.001-in.
4. Threads to be concentric with each other and 0.3755 holes to be concentric with each other to within 0.001-in.
5. Surfaces C to be square with surfaces A and surfaces B to within 0.001-in.
6. Rad. and gage section to blend smoothly without undercut.
7. All surfaces  $\sqrt{16}$ .

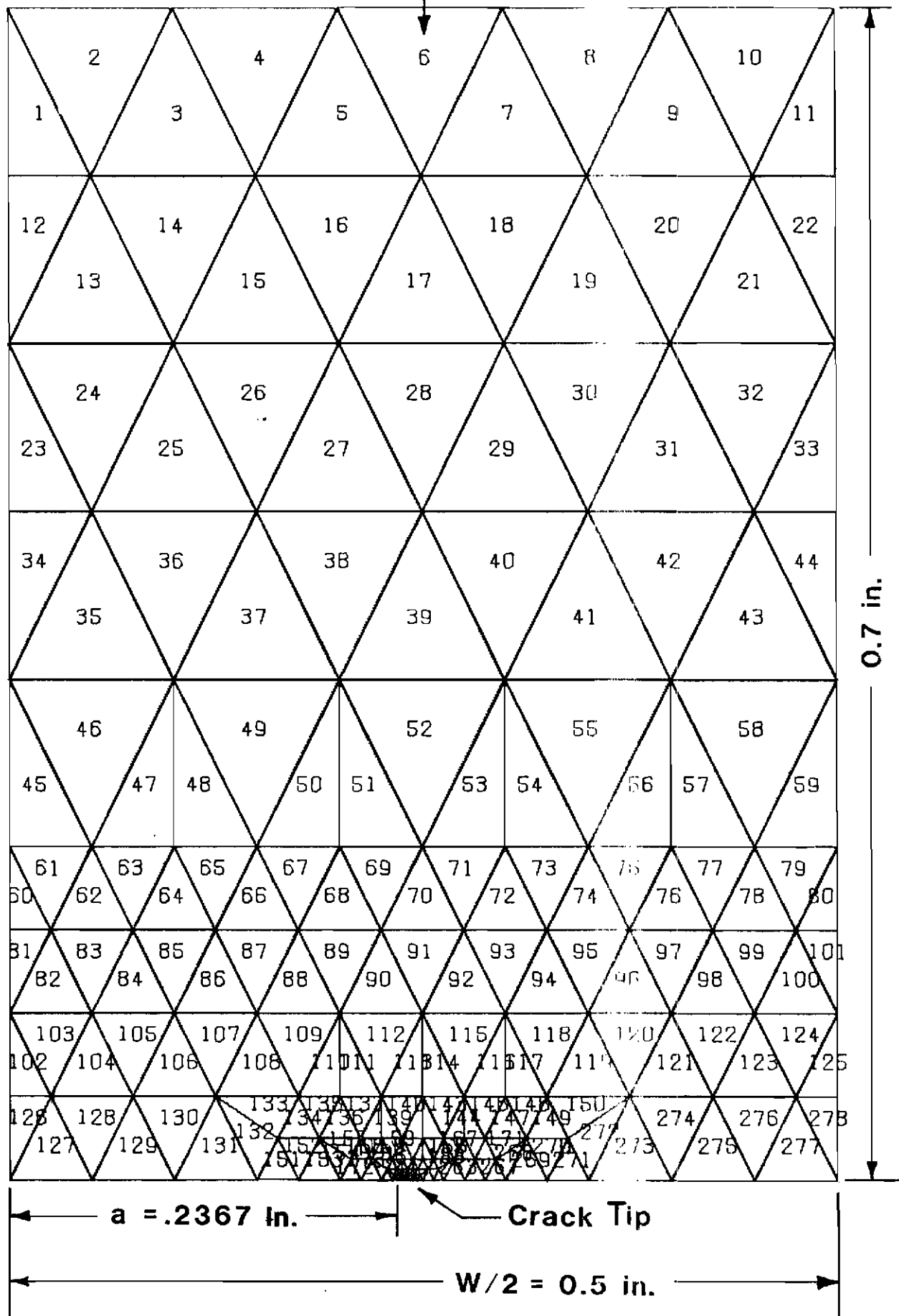
Figure 27. Experimental Creep Crack Growth Specimen

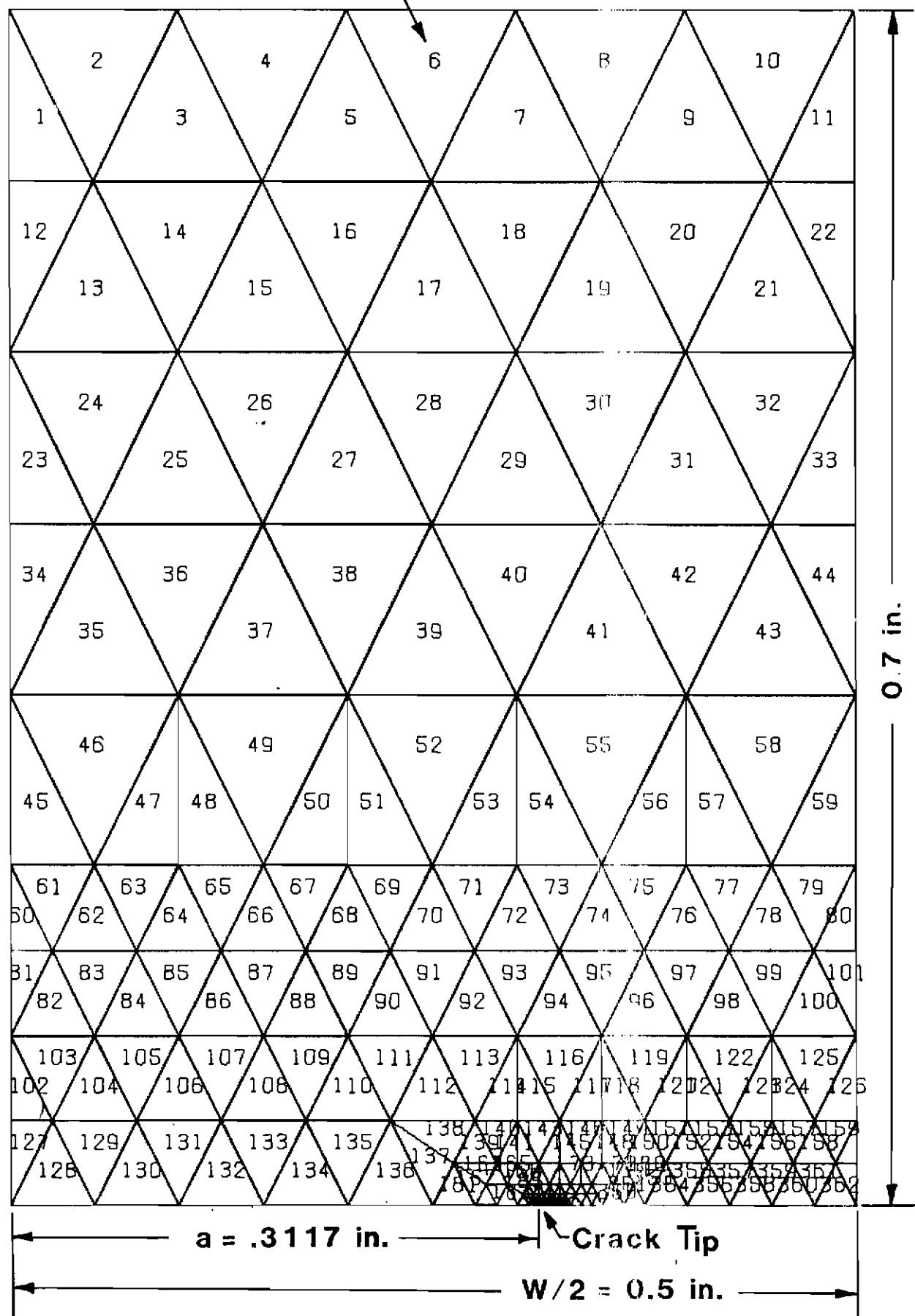
*Contrails*

Element Number

 $a = .1367 \text{ in.}$ **Cracktip** $W/2 = 0.5 \text{ in.}$ Figure 28. Center Cracked Plate Finite Element Model,  $a/W = 0.1367$ 

Approved for Public Release

*Contrails***Element Number**Figure 29. Center Cracked Plate Finite Element Model,  $a/W = 0.2367$

*Contrails***Element Number**Figure 30. Center Cracked Plate Finite Element Model,  $a/W = 0.3117$



AFWAL-TR-80-4140

length through the thickness, the surface measurement cannot be used directly and thus effective initial crack lengths must be determined. These effective initial crack lengths were determined by matching experimental load-displacement data along the crack such that the finite element model displayed elastically the same compliance as the experimental specimens did. For efficiency sake it has been found realistic to use the same element mesh for slightly different initial crack lengths.

The VISCO finite element program has both plane stress and plane strain analysis capability. The current investigation chose plane stress as reported in Reference 78 where theoretical plane stress  $J$  integral values agreed best with test data for an even thicker ( 1 inch thick) compact tension specimen. A theoretical model must display realistic compliance behavior in order to calculate  $J$  values that agree with test data. Likewise, in the present research realistic compliance behavior is a necessity.

Figures 28, 29, and 30 display the same general pattern of elements which worked well for the three-point bend specimen in Section III. The elements at the crack tip have a height and width of  $7.8125 \times 10^{-4}$  inch. This size crack tip element in combination with the given general element pattern, provided for 355, 278, and 362 elements respectively in the three figures. Figures 28 and 30 provided 20 uniform elements ahead of the crack tip for subsequent crack growth whereas Figure 29 had eight uniform elements. Figure 31 shows the expanded element layout around the crack tip from Figure 29. This region of uniform elements ahead of the initial crack tip avoids unrealistic changes in compliance, as the crack grows through the model, that can develop when nonuniform element sizes are used. The number of uniform elements incorporated ahead of the crack tip is a compromise between anticipated crack growth and computer time required.



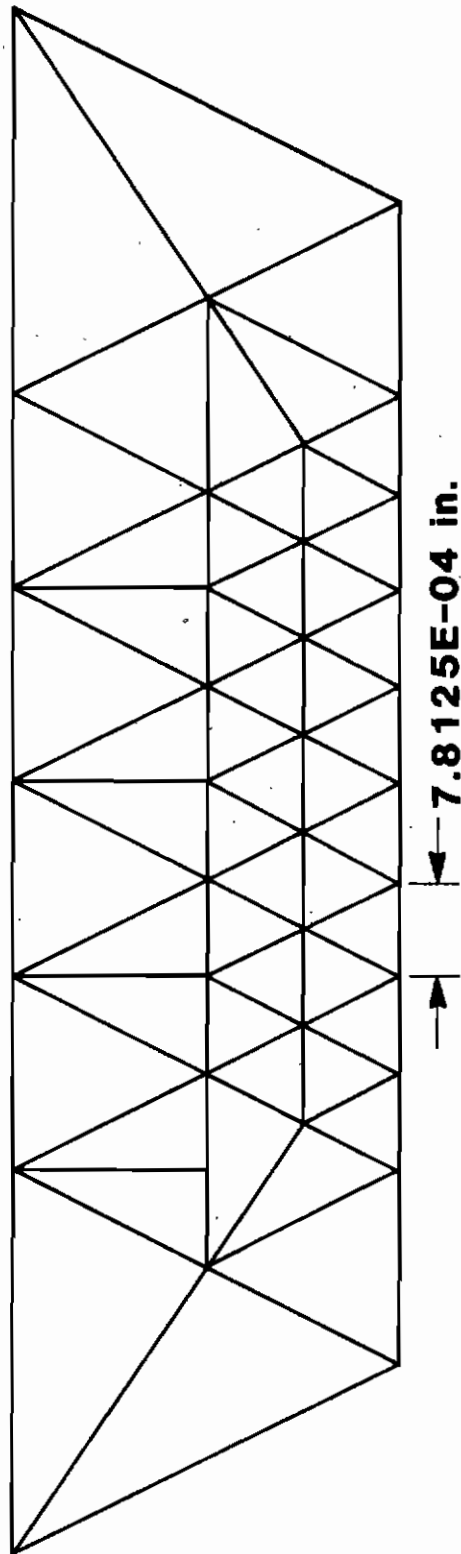


Figure 31. Uniform Mesh Ahead of Crack Tip

AFWAL-TR-80-4140

The elastic compliance of the specimens modeled by these three meshes in VISCO was compared to an empirical solution by Eftis and Liebowitz (Reference 79) in the form of

$$\frac{2EV}{\sigma W} = \frac{4}{\pi} \sqrt{\frac{\pi a}{W} \csc\left(\frac{\pi a}{W}\right)} \cosh^{-1}\left[\sec\left(\frac{\pi a}{W}\right)\right] \quad (54)$$

This comparison is shown in Figure 32, with the symbols  $a$ ,  $v$ , and  $W$  as defined in the figure. Also shown is nondimensionalized compliance versus crack length for locations off the vertical centerline and relatively near the crack tip. These locations correspond to the displacement measurement locations used in the experimental program. It can be seen that the centerline compliance agrees very well with published results. Also note that if the off centerline results are linearly extrapolated (i.e., dashed line) back to the Eftis and Liebowitz curve they intersect at  $a/W$  values which correspond to their distance behind the crack tip. These results all support the validity of the finite element meshes used in the present investigation.

Figure 33 shows elastic crack opening displacement profiles using VISCO and the mesh in Figure 28 compared to the Westergaard equation for elastic displacements around the crack tip. The following form of the Westergaard equation is restricted to plane stress displacements behind the crack tip and on the crack surface (i.e., crack opening displacement)

$$v = \frac{4K_I}{E} \sqrt{\frac{r}{2\pi}} \quad (55)$$

where  $r$  is the distance behind the crack tip and  $K_I$  is the mode I elastic stress intensity factor which for the center crack plate can be written as (Reference 73)

$$K_I = \sigma \sqrt{(\pi a) \sec\left(\frac{\pi a}{W}\right)} \quad (56)$$

where again  $a$  and  $W$  are the half crack length and specimen width respectively. Note that agreement with the Westergaard equation is

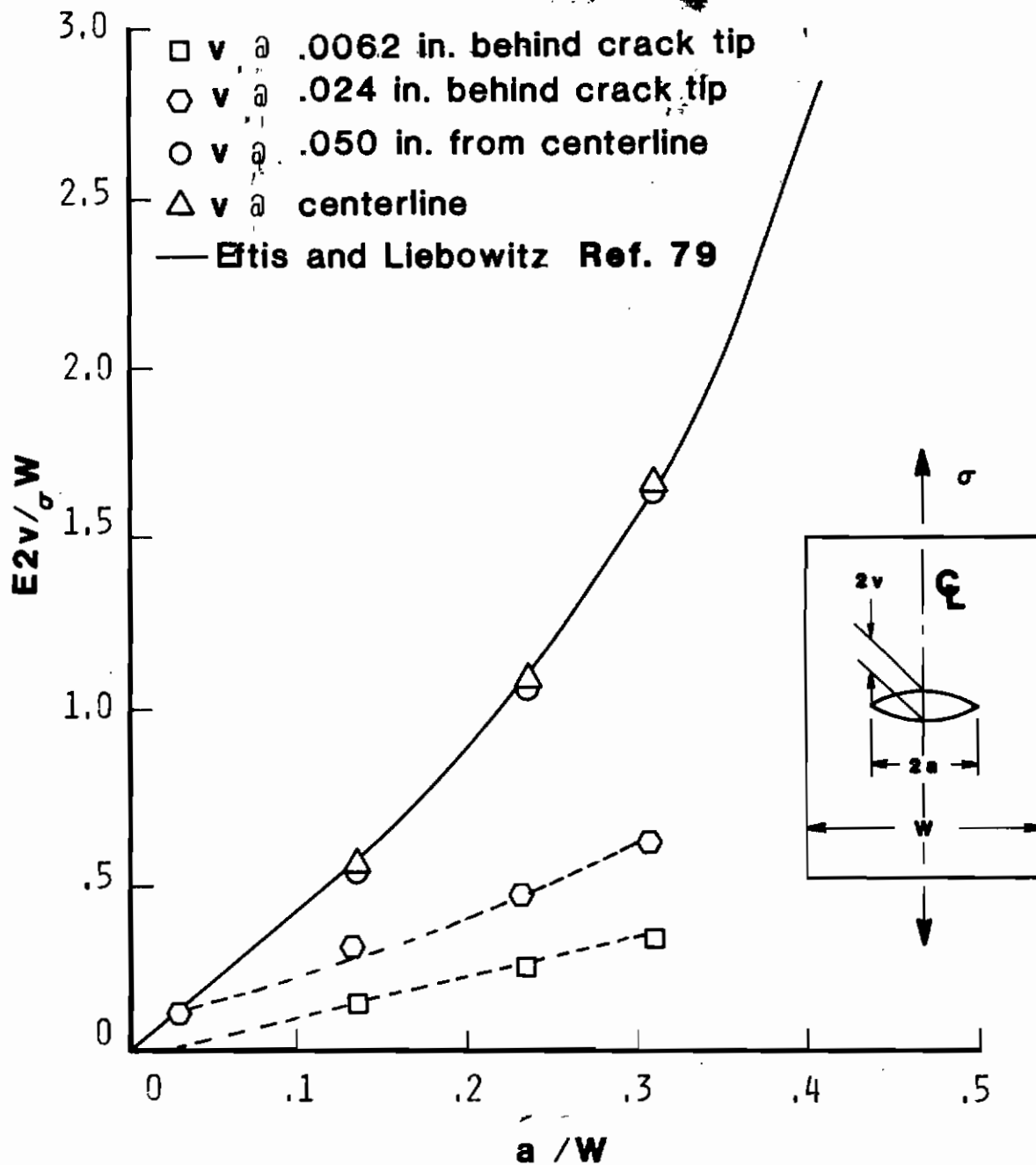


Figure 32. Comparison of Compliance from VISCO with Eftis & Liebowitz for the Center Cracked Plate

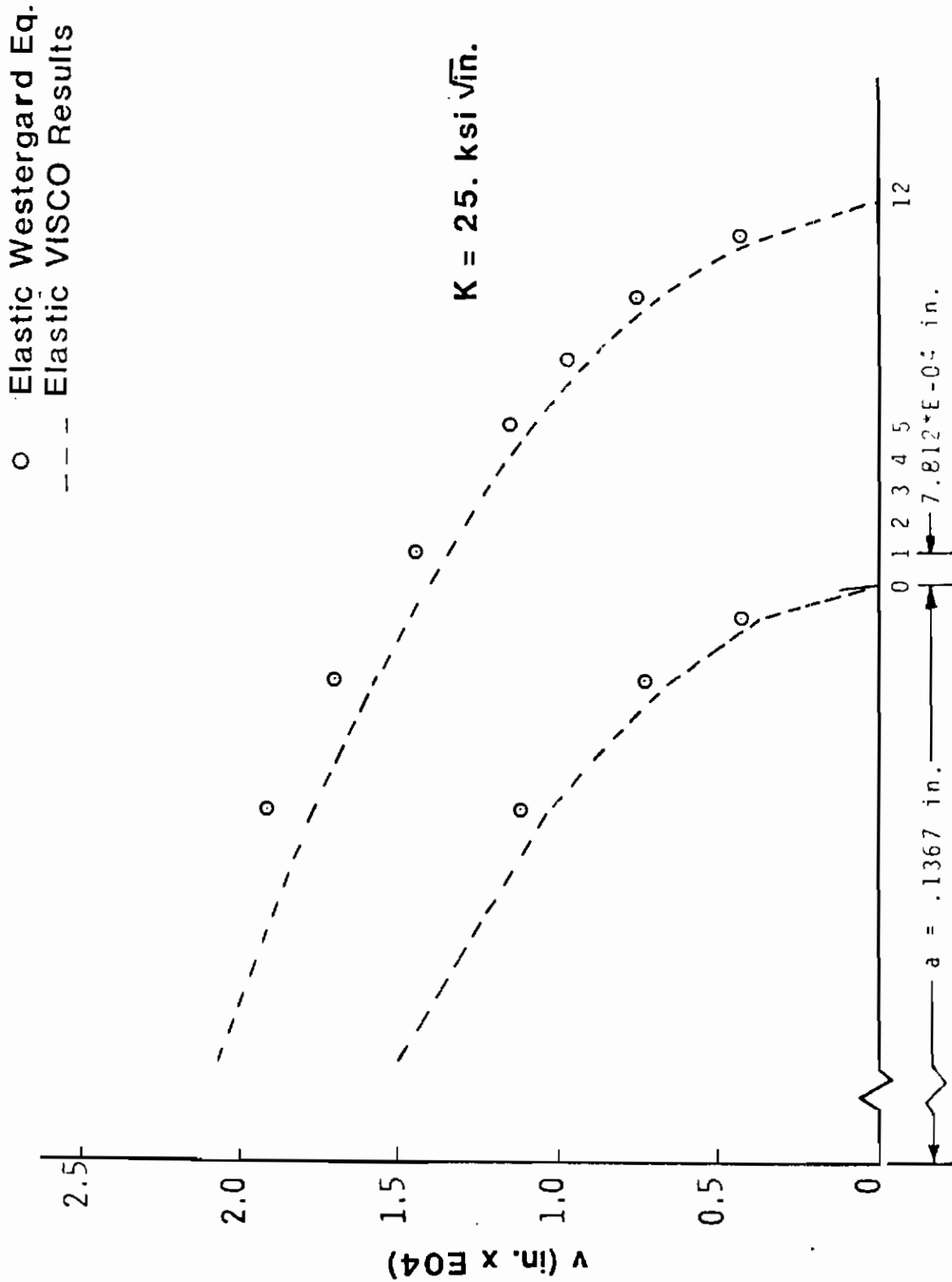


Figure 33. Elastic Crack Opening Displacement Profiles from VISCO

quite good here for the results from VISCO using the mesh with the shortest crack length (Figure 28). The same crack tip element size was used in all three crack length models. Therefore, agreement with Equation 55 would even be better for the longer crack length models since the ratio of element size to crack length will be smaller. It has been shown through elastic finite element convergence studies that as this ratio of crack tip element size to crack length decreases, accuracy increases (Reference 81).

Another consideration supporting this size crack tip element (i.e.,  $7.8 \times 10^{-4}$  in.) is that IN-100 grains are approximately the same dimension (Reference 13). It may be argued that the finite element method is a continuum analysis tool and that accuracy should only improve as elements are refined. However, realistically a continuum does not exist at and below the grain size, especially around the crack tip. Thus incorporation of elements smaller than the grain size might be unrealistic. Furthermore, it is postulated that the physical blunting of the crack tip that can be associated with noncontinuous grain structured material might be more effectively considered by the finite element model used herein since the crack tip elements have a dimension on the order of a grain size.

## 1. CRACK GROWTH PREDICTIONS

A summary of the creep crack growth test data reported by Sharpe (Reference 15) is given in Tables 3 and 4. In general the experimental program objectives were to generate creep crack growth data in the center cracked plate specimen at 1350°F for several different loads and cracked lengths. The loads were specified in terms of a range of stress intensity factor values from approximately 15.0 to 35.0 ksi  $\sqrt{\text{in}}$  for each respective initial crack length. With these objectives in mind and the limited number of test specimens, only one test was done at each of the test conditions. In the process of developing the experimental procedure, several tests did not result in good data and consequently were not used in the present investigation as implied by the discontinuous test numbers in Table 3.

*Contrails*

TABLE 3  
SUMMARY OF SHARPE TEST DATA (Reference 15)

Test #	Specimen #	Initial Surface Crack length $a_s$ (in.)	Load, P (lbs.)	Indent Location (in.) from $\bar{C}$	Test Duration (sec.)
5	2	.1350	10089	.1336 (tip)	3600
6	2	.226	8160	.2216 (tip)	3600
8a	5	.118	7110	.1115 (tip)	3600
8b	5	*	8528	.1115 (tip)	1800
8c	5	*	9713	.1115 (tip)	1800
8d	5	*	10897	.1115 (tip)	1800
9	4	.124	16060	.053 (mouth)	3600
12a	3	.201	5190	.059 (mouth)	1800
12b	3	*	7670	.059 (mouth)	1800

\*Crack length not measured.

TABLE 4  
SUMMARY OF MEASURED VERSUS CALCULATED INITIAL CRACK LENGTHS AND APPLIED  
FINITE ELEMENT MODEL,  $K_{FE}$  VERSUS EFFECTIVE EXPERIMENTAL,  $K_{EFF}$

TEST #	Initial Surface Crack length $a_s$ (in.)	Measured Interpal Crack length $a_m$ (in.)	Crack length from Compliance $a_c$ (in.)	Crack length used in Fin. Elem. $a_o$ (in.)	$K_{eff}$ (ksi $\sqrt{in.}$ )	$K_{FE}$ (ksi $\sqrt{in.}$ )
5	.135	.148	No-Data	.1367	24.2	25.0
6	.226	.219	.238	.2367	25.7	27.9
8a	.118	.152	.137	.1367	17.4	16.3
9	.124	.162	.145	.1267	40.9	36.8
12a	.201	.230	.231	.2367	17.0	17.5
12b	No-Data	.265	.282	.3117	28.4	29.5

The initial surface crack lengths,  $a_s$ , were measured on the surface of the test specimens after fatigue precracking and prior to the load application for the creep crack growth tests. Displacements across the crack were measured at the indent locations, qualitatively referred to as mouth or tip locations described in Section IV. In each of these creep crack growth tests, the load was applied in five seconds and held constant for the given test duration time (excluding small unload/reload cycles for compliance referred to in Section IV).

Figure 34 is a photograph of the fracture surface of specimen number 2. This photograph was taken after breaking open the center cracked plate specimen following creep crack growth tests 5 and 6. The two dark bands indicated with arrows are the creep crack extensions from tests 5 and 6 whereas the remaining fracture surface is either pre-test or post-test fatigue crack growth.

Post-test crack length measurements were made on the fracture surface as described in Figure 35. The average of the four crack length measurements was defined as the experimental crack length  $a_m$ . This averaging was done to smooth out crack length differences due to asymmetric crack growth and variations through the thickness. Table 4 gives a tabulation of the initial crack length,  $a_s$  and  $a_m$ . In addition, a crack length determined by compliance,  $a_c$ , and the initial crack length used in the finite element model,  $a_o$ , is given. The  $a_c$  crack length was determined as discussed earlier by varying the crack length in the finite element model until the model's compliance matched experimental compliance data.

For convenience a modified form of the above compliance technique for crack length determination was also employed which reduced the number of element meshes for different crack lengths required. This modification to the compliance method made use of the experimental compliance,  $C_E$ , and the finite element model compliance,  $C_{FE}$ , for a crack length near the test value. To determine the test specimen's



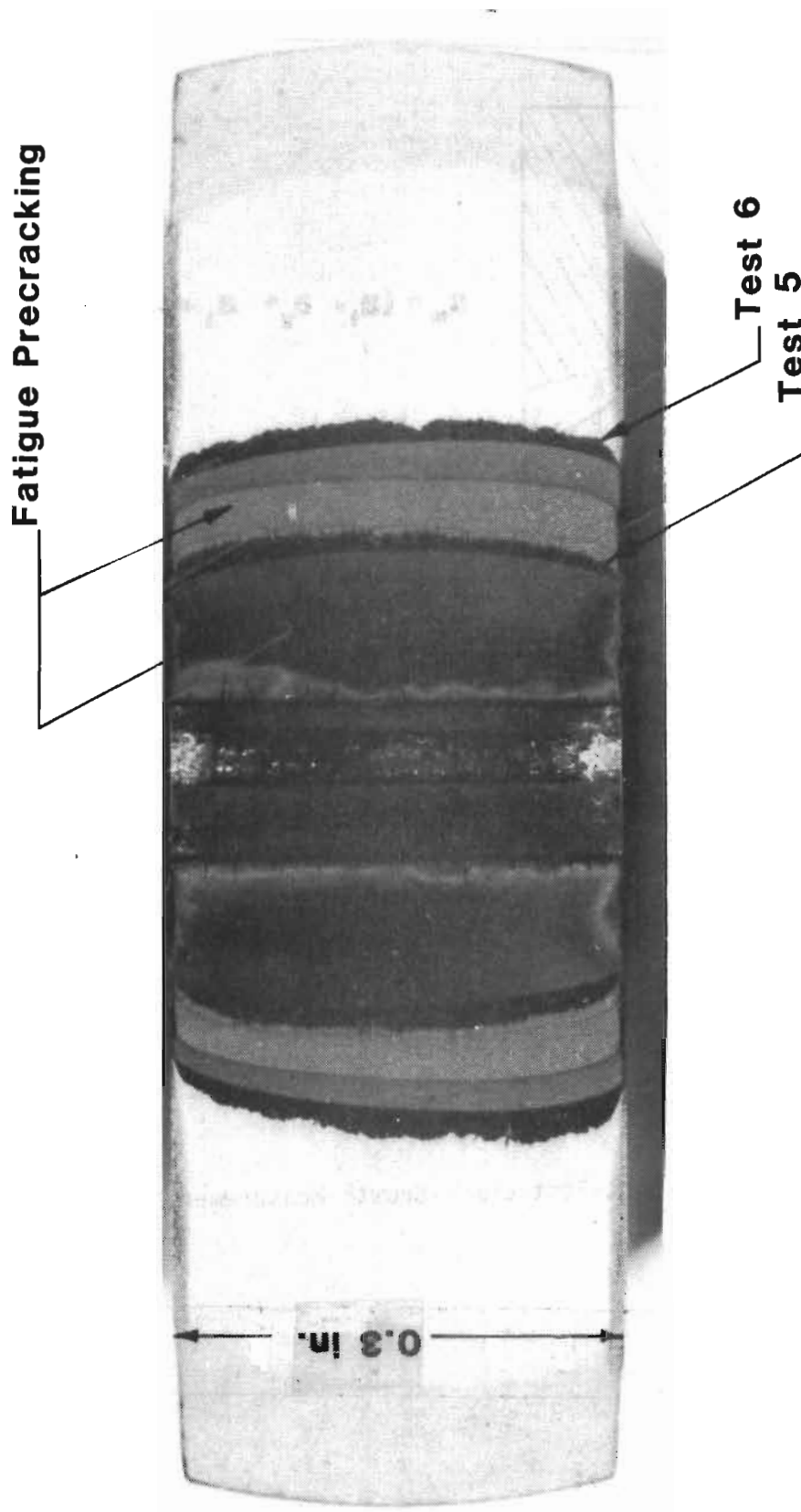


Figure 34. Fracture Surface of Specimen No. 2

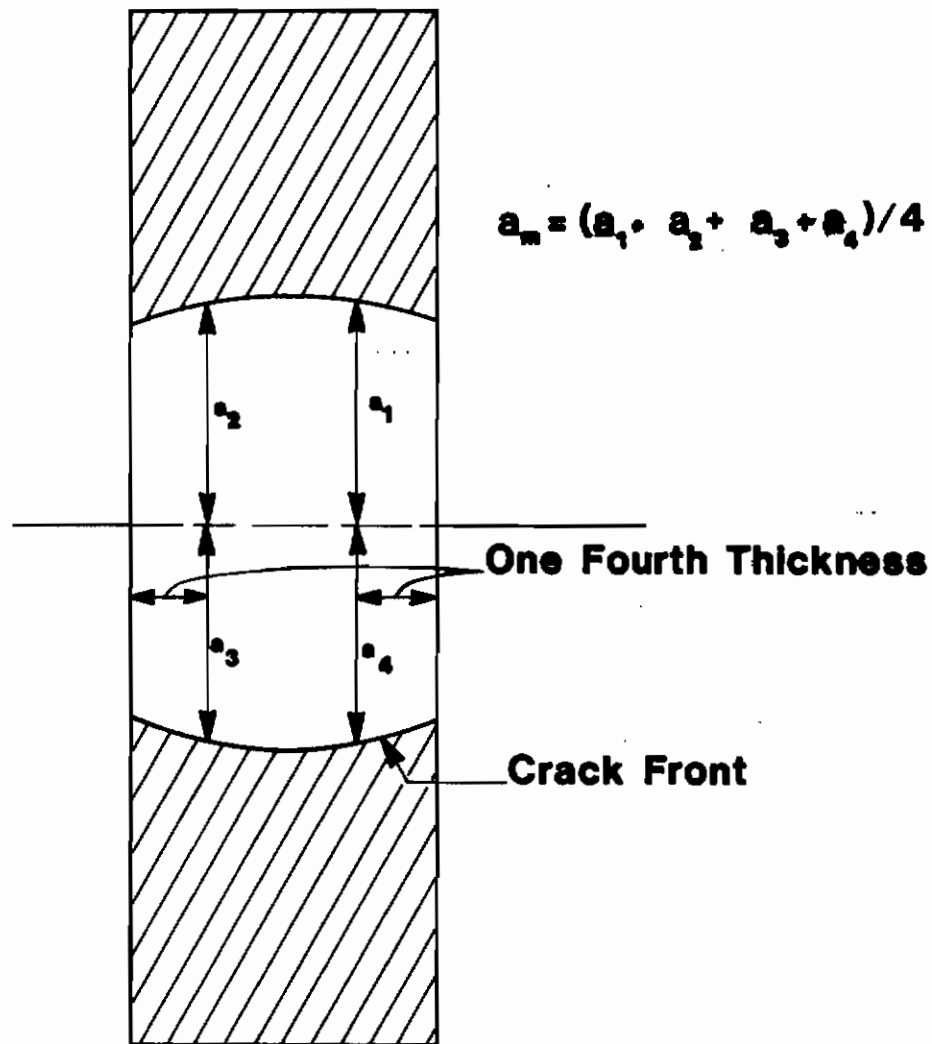


Figure 35. Post-Test Crack Growth Measurements

crack length, the difference between  $C_E$  and  $C_{FE}$  was divided by the rate of change of compliance with crack length  $\Delta C/\Delta a$  (i.e., slope of curve in Figure 32 as follows and added to the model's crack length

$$a_c = a_o + \frac{C_E - C_{FE}}{\Delta C/\Delta a} \quad (57)$$

where  $c/a$  is determined from the model for nearby crack lengths. The compliance  $C_{FE}$  pertains to a model crack length of  $a_o$ .

The effective stress intensity factor,  $K_{eff}$ , in Table 4 was calculated from Equation 56 using the crack length,  $a_m$ , and the load given in Table 3. The stress intensity factor,  $K_{FE}$ , is also calculated for convenience from Equation 56 but using the crack length  $a_o$ . For another check on the element mesh, the elastic stress intensity factor,  $K_{FE}$ , was also calculated based on J integral values determined from VISCO for several paths. For linear elastic plane stress behavior (Reference 73)

$$K_I = \sqrt{EJ} \quad (58)$$

(Appendix C describes the VISCO routine for calculating the J integral).

Figure 36a shows a scaled drawing giving four different J integral paths used in VISCO for the center cracked plate specimen. Figure 36b shows normalized stress intensity factors calculated from Equation 57 and the J values along paths one through four in Figure 36a. These J values were from a linear elastic VISCO analysis. For linear elastic material, the J integral is theoretically path independent and this path independence is demonstrated in Figure 36. It should be noted that the good agreement between VISCO results and Equation 56 in Figure 36b also indicates that the finite element mesh (i.e., Figure 28) accurately represents the center cracked plate.

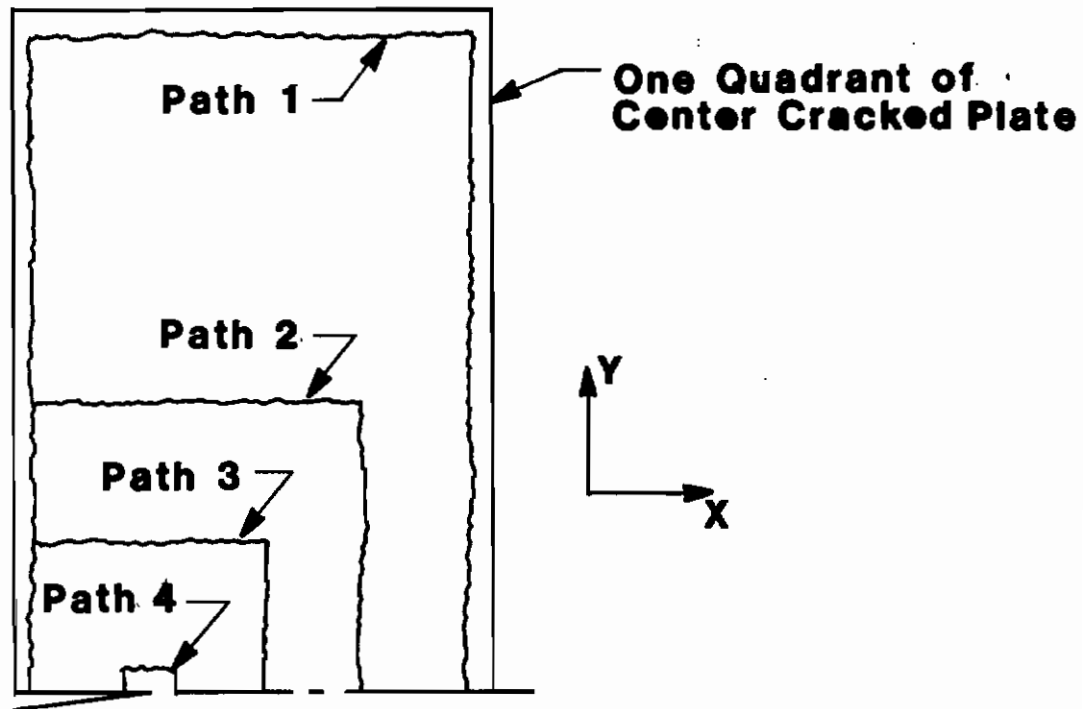


Figure 36a. J Integral Paths Used by VISCO

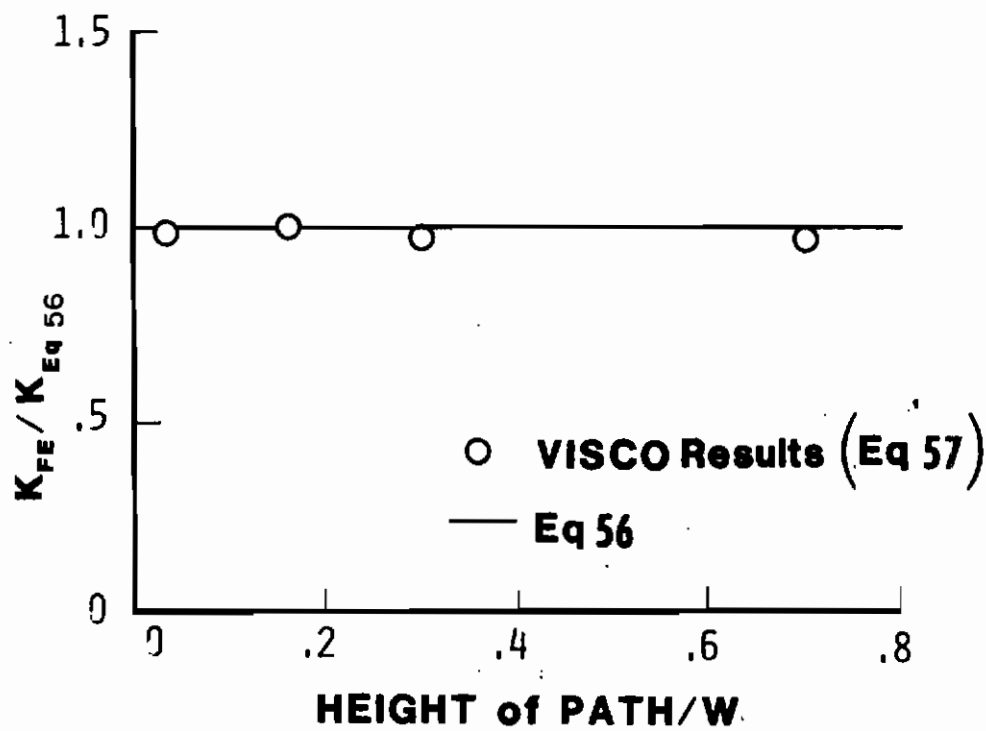


Figure 36b. Stress Intensity Factors from VISCO J Integrals & Equation 57

Table 5 summarizes the basic details of the VISCO computer runs which employed the HEN procedure. The computer run numbers designated by S1 through S7 will frequently be referred to in the following discussions. As described in Section IV, each of these runs incorporated the Bodner material model and the crack was grown in the model at a sufficient rate such that model displacements matched test data with time. Each node released was unloaded in five seconds except runs S1 and S7 as indicated in Table 5. Table 6 summarizes the basic details for VISCO runs similar to Table 5 but with no crack growth allowed. It can be seen from these tables that the computer time required for the high load runs (e.g., S2 and A3) is much higher than for the lower K levels. In the case of run A3, computer time required is high due to a large load causing a great amount of plastic flow to occur. Recall from Section III that high plastic strain rates result in small time step size which then requires more time steps to simulate a given amount of time relative to the case of low plastic strain rates. Furthermore, in the case of run S2, extensive crack growth occurred requiring 19 nodes to be released. Each node release also requires relatively small time steps due to the redistribution of stress and the associated plastic straining around the crack tip.

Figures 37 through 42 show the match of VISCO displacements with each particular test's displacement data. Also, the amount of displacement in VISCO for no crack growth under load is given. These displacements are relative to the displacements existing at the time maximum load is achieved which means all displacements prior to reaching maximum load were not included in this test data. Maximum load was normally achieved in five seconds. The experimental optical technique for measuring displacements is highly sensitive and can resolve displacements in the neighborhood of 0.1 micron. However, this technique loses sensitivity when displacement measurements are much larger than a micron. Since the main interest was to record displacements after reaching maximum load (i.e., the creep crack growth data), and due to the desire to maintain high measurement resolution, the load application displacements were

TABLE 5  
SUMMARY OF HYBRID EXPERIMENTAL-NUMERICAL VISCO RUNS

Run #	Test #	Crack Length $a_o$ (in.)	Load P (lbs.)	$K_{FE}$ (ksi $\sqrt{in.}$ )	Analysis Time $t_{max}$ Max Load (sec)	Nodes Released	Central Processor Time (sec)
S1 <sup>a</sup>	8a	0.1367	7140	16.3	3600	3	2248
S2	9	0.1367	16060	36.8	400	19	3988
S3	5	0.1367	10896	25.0	3600	19	2326
S4	12b	0.3117	6676	29.5	1800	15	1926
S5	6	0.2367	8160	27.9	1800	7*	937
S6	12a	0.2367	5190	17.5	1800	5	489
S7 <sup>a</sup>	5	0.1367	10896	25.0	3485	19	2114

\* No Crack Growth Allowed During First 300 Seconds

<sup>a</sup> Continuous Node Release

TABLE 6  
SUMMARY OF VISCO RUNS WITH NO CRACK GROWTH

Run #	Test #	Crack Length $a_s$ (in.)	Load P (lbs.)	$K_{FE}$ ( $\text{ksi}\sqrt{\text{in.}}$ )	Time @ Max Load (sec)	Central Processor Time (sec)
A1	8a	.1367	7140	16.3	3600	500
A2	5	.1367	10896	25.0	1800	1309
A3	9	.1367	16060	36.8	1800	2286
A4	12a	.2367	5190	17.5	1800	264
A5	6	.2367	8160	27.9	1800	591
A6	12b	.3117	6676	29.5	1800	867

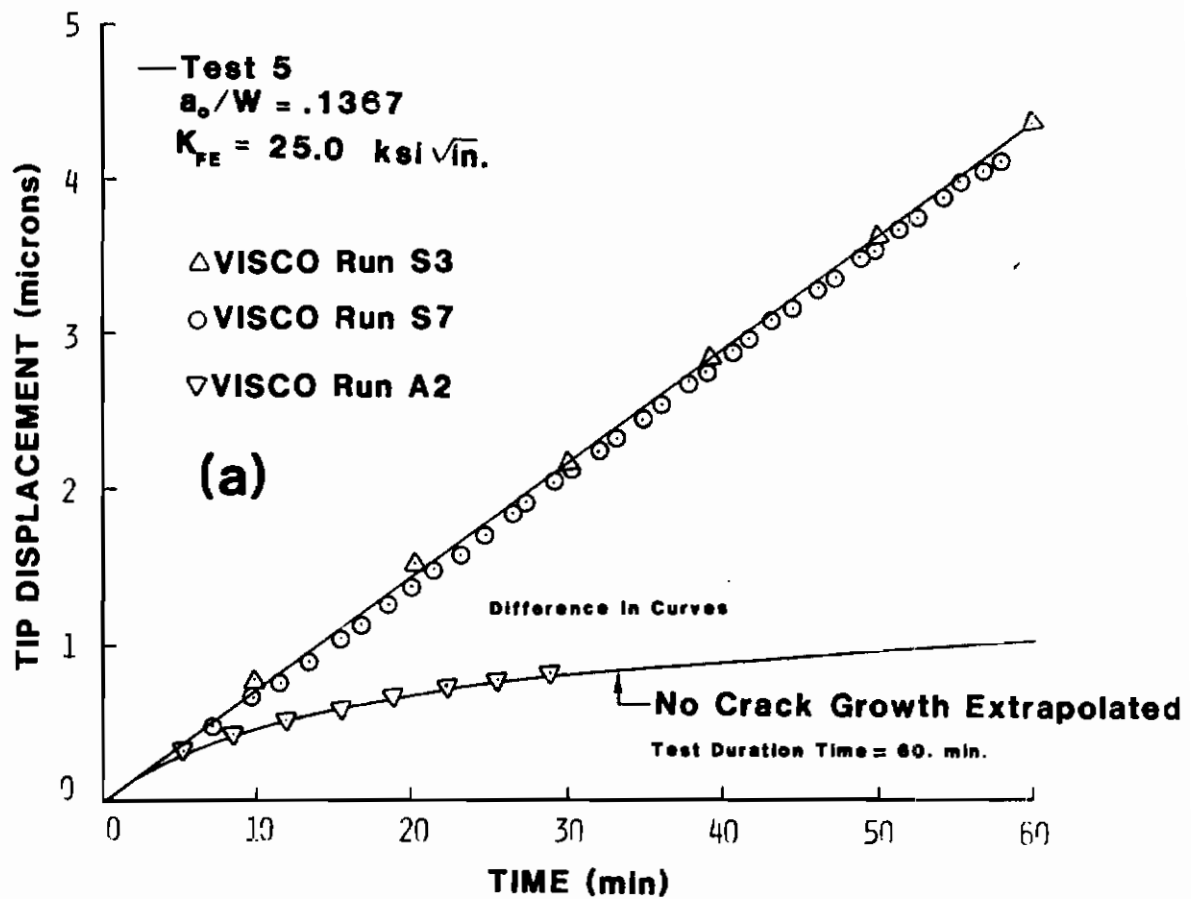


Figure 37a. Test 5 HEN VISCO Results, Displacements Matched to Test Data

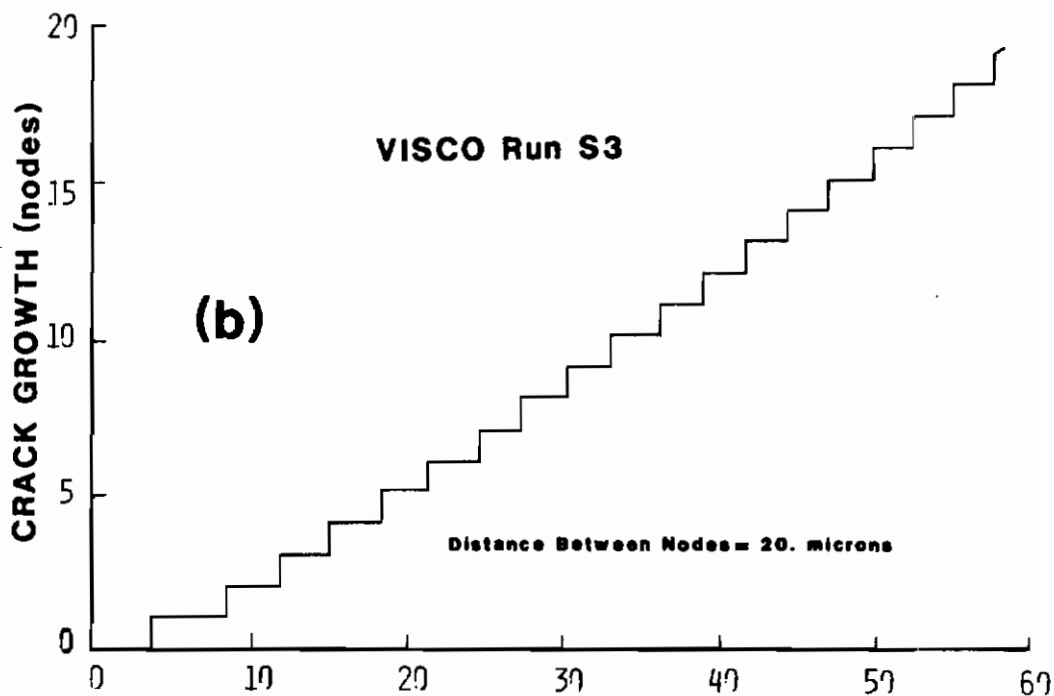


Figure 37b. Test 5 HEN VISCO Results, Crack Growth



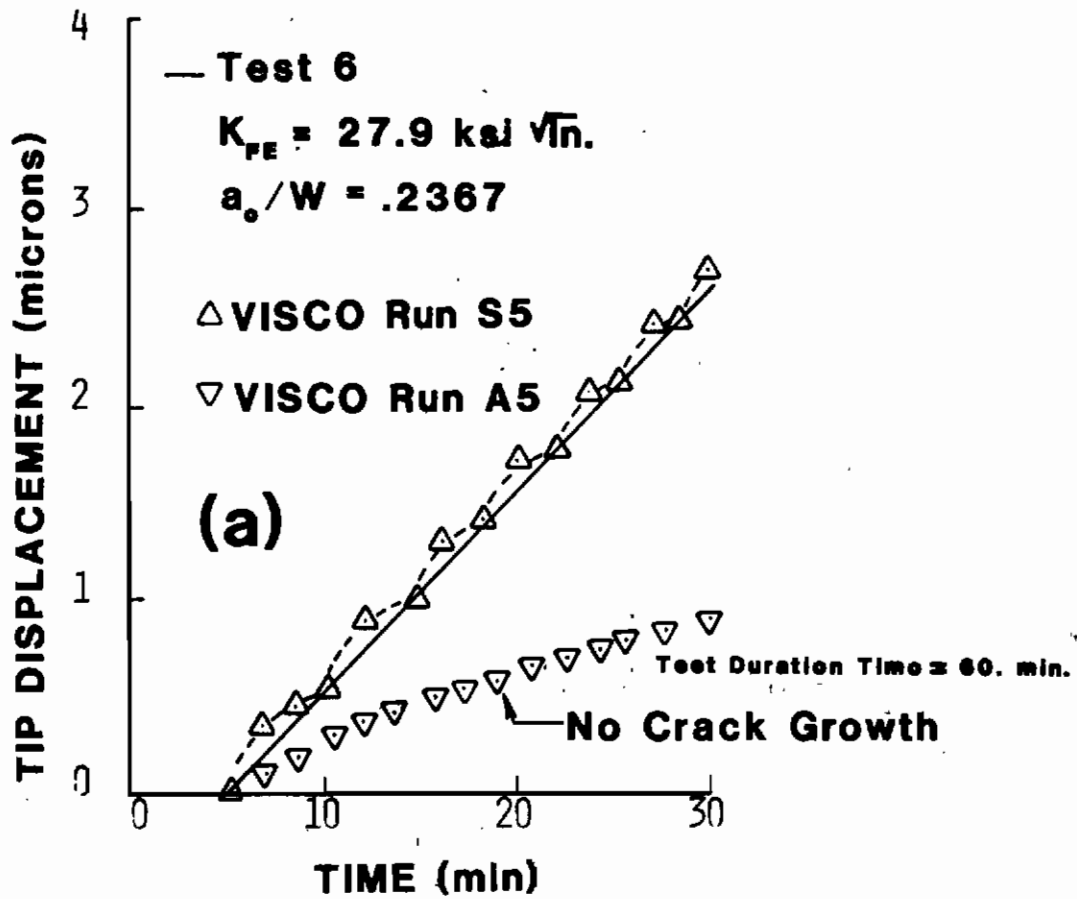


Figure 38a. Test 6 HEN VISCO Results, Displacements Matched to Test Data

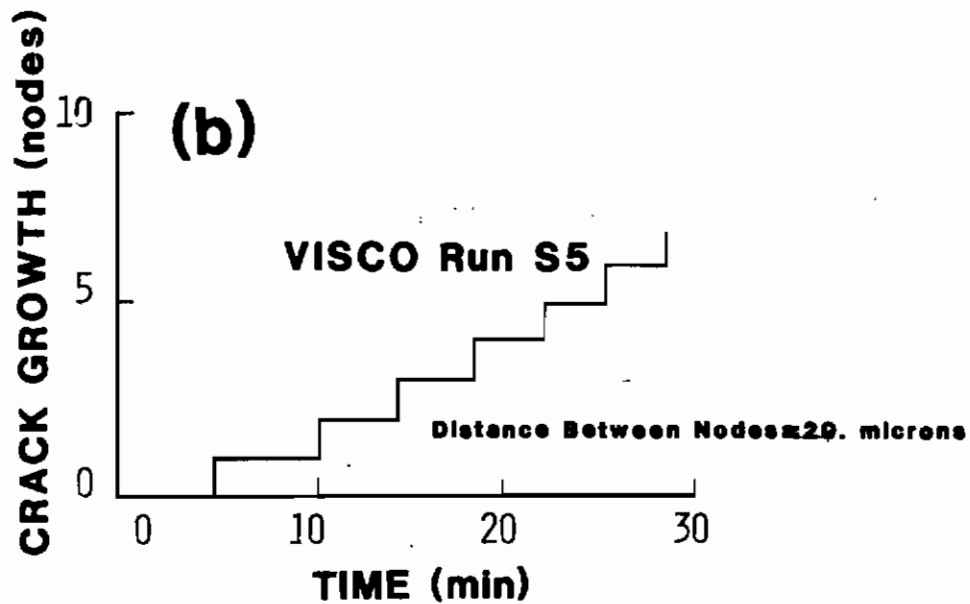


Figure 38b. Test 6 HEN VISCO Results, Crack Growth

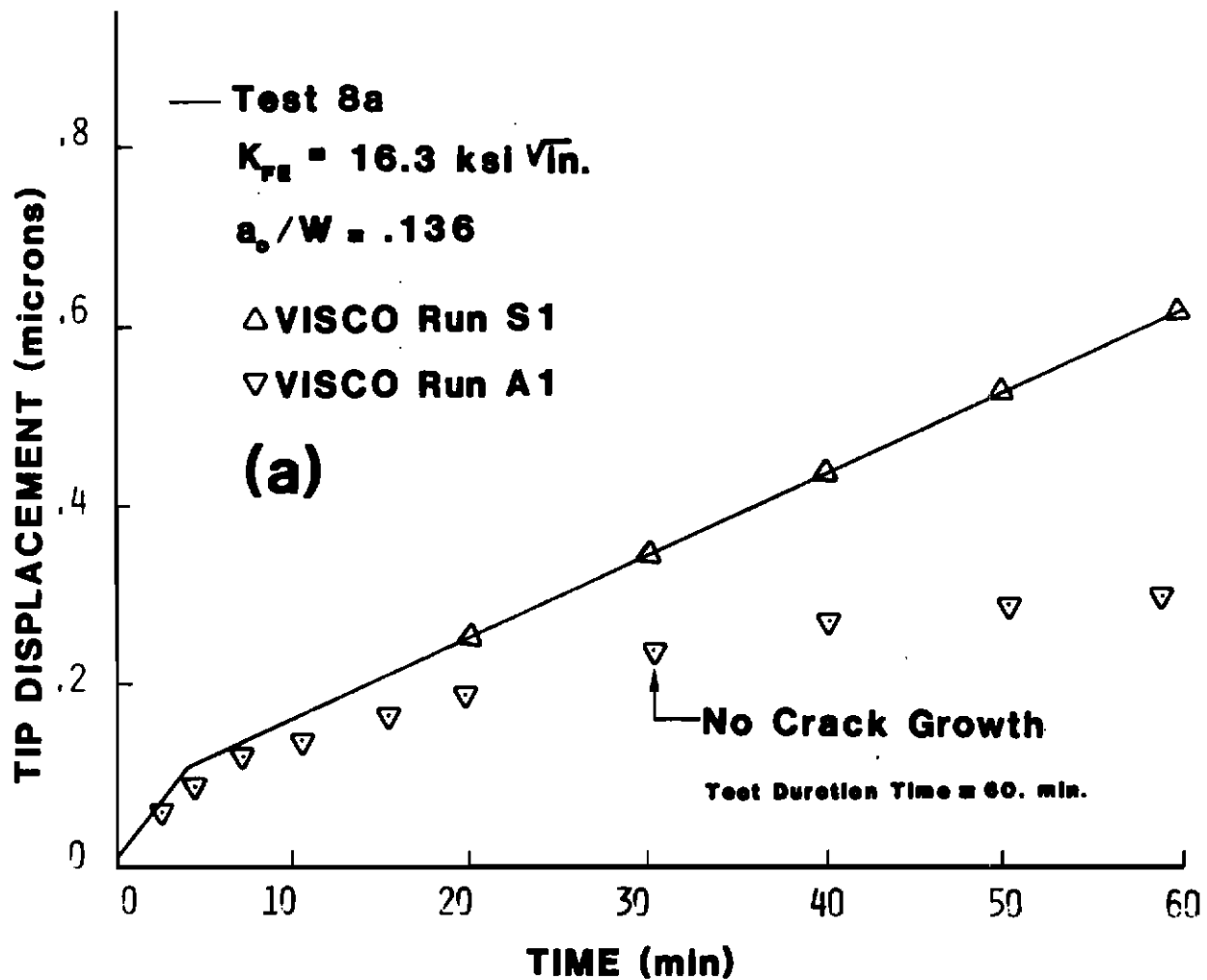


Figure 39a. Test 8a HEN VISCO Results, Displacements Matched to Test Data

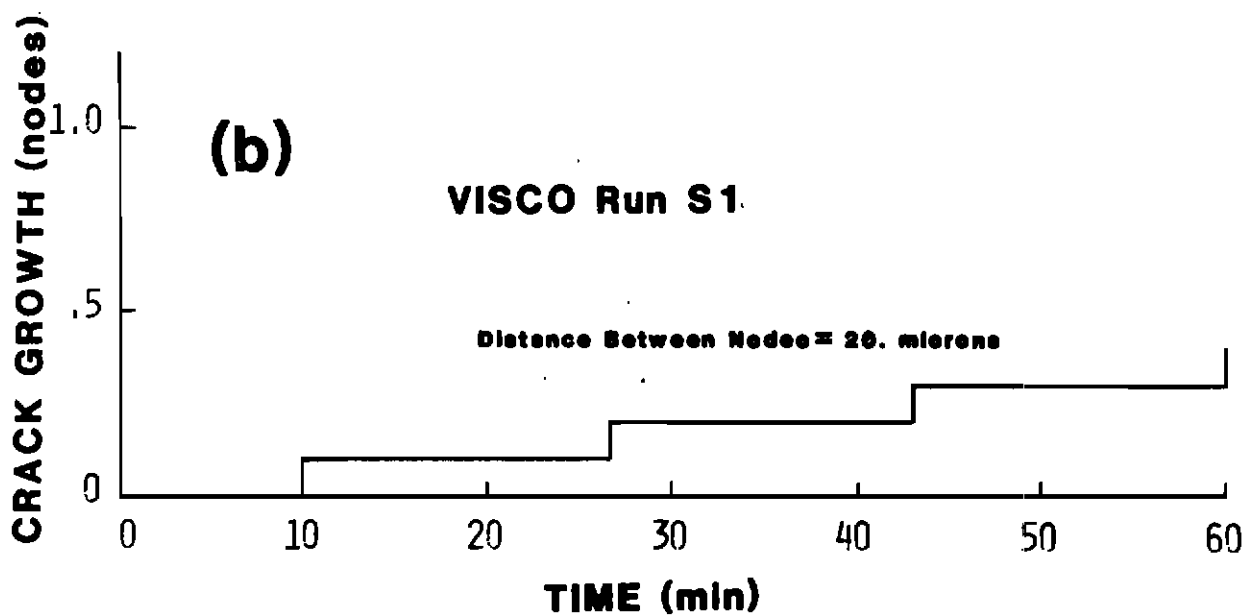


Figure 39b. Test 8a HEN VISCO Results, Crack Growth

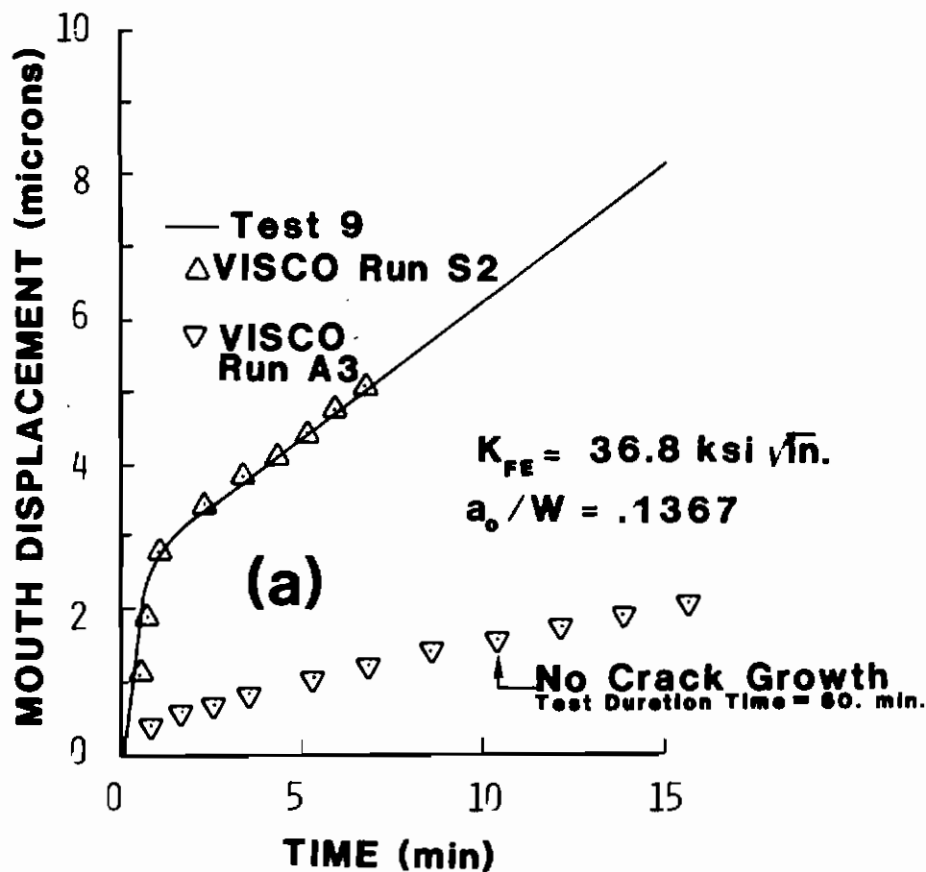


Figure 40a. Test 9 HEN VISCO Results, Displacements Matched to Test Data

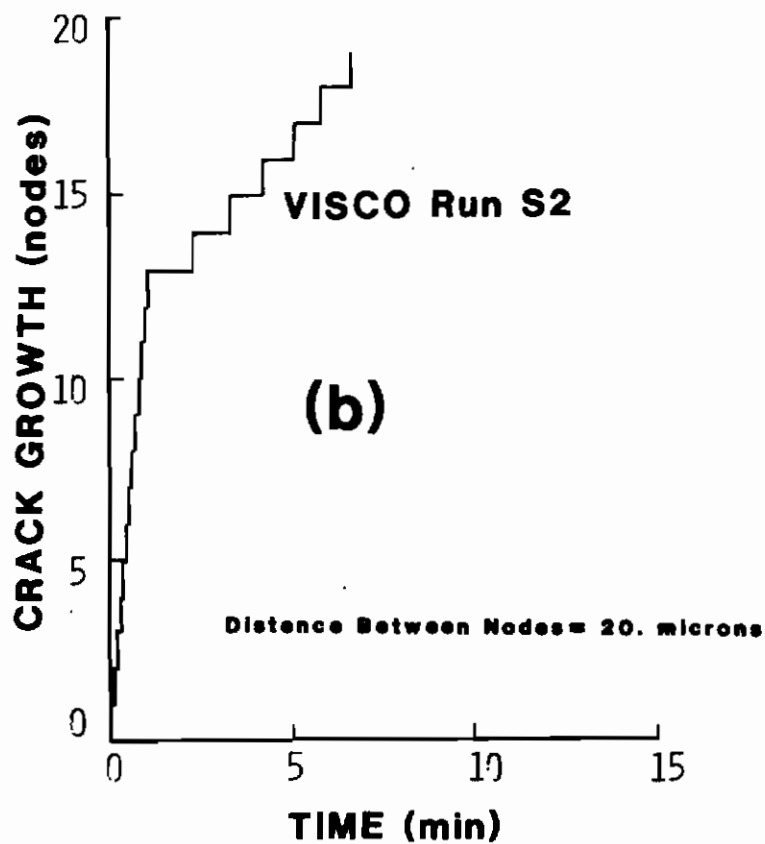


Figure 40b. Test 9 HEN VISCO Results, Crack Growth

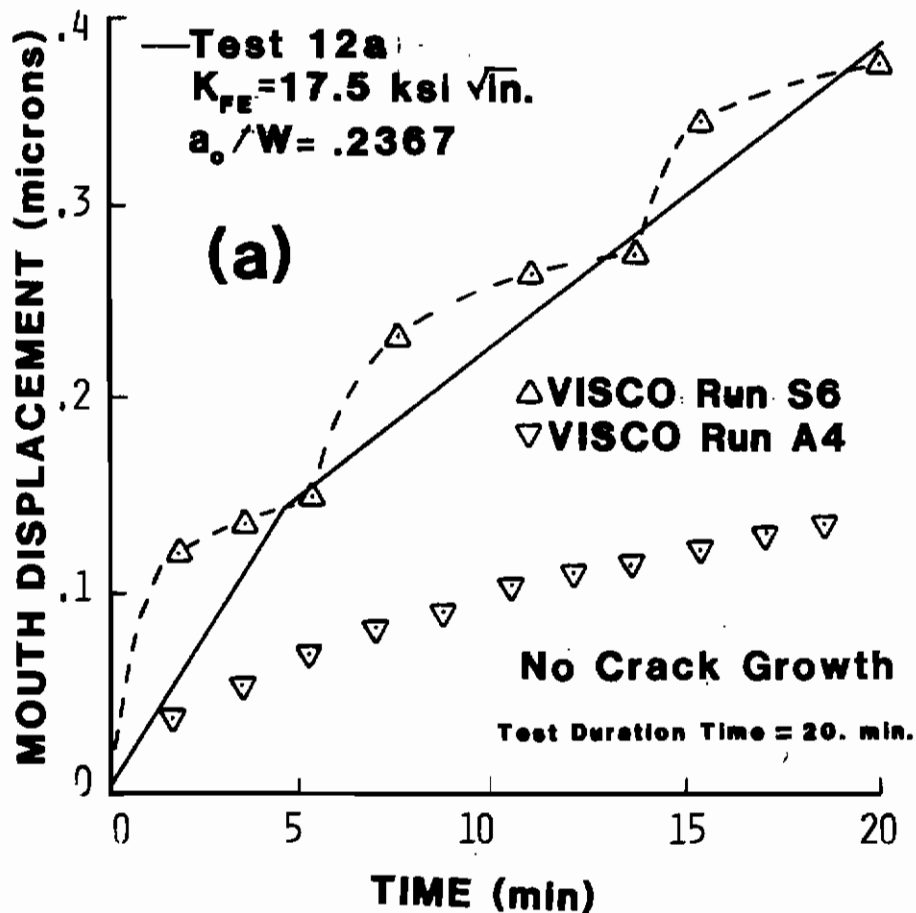


Figure 41a. Test 12a HEN VISCO Results, Displacements Matched to Test Data

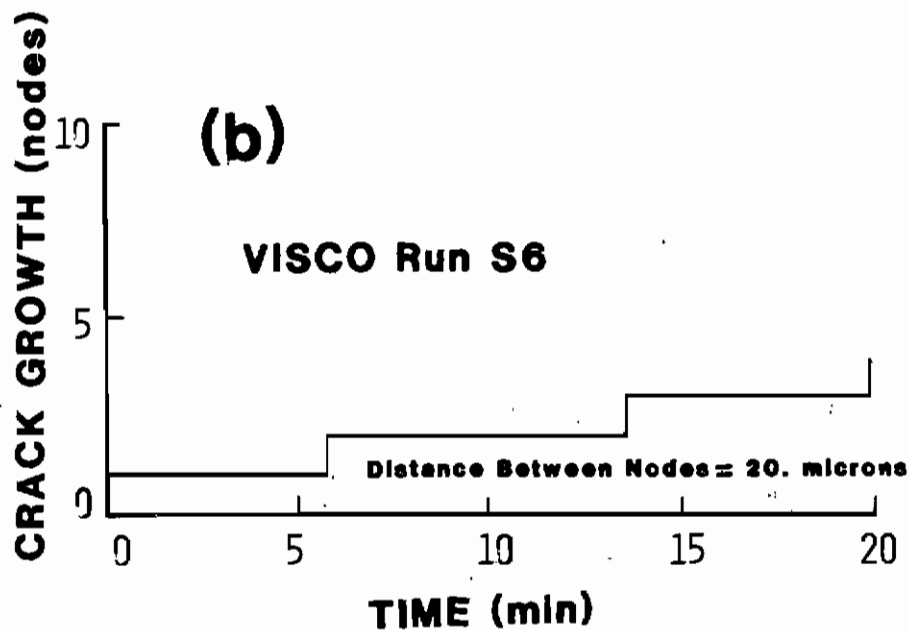


Figure 41b. Test 12b HEN VISCO Results, Crack Growth

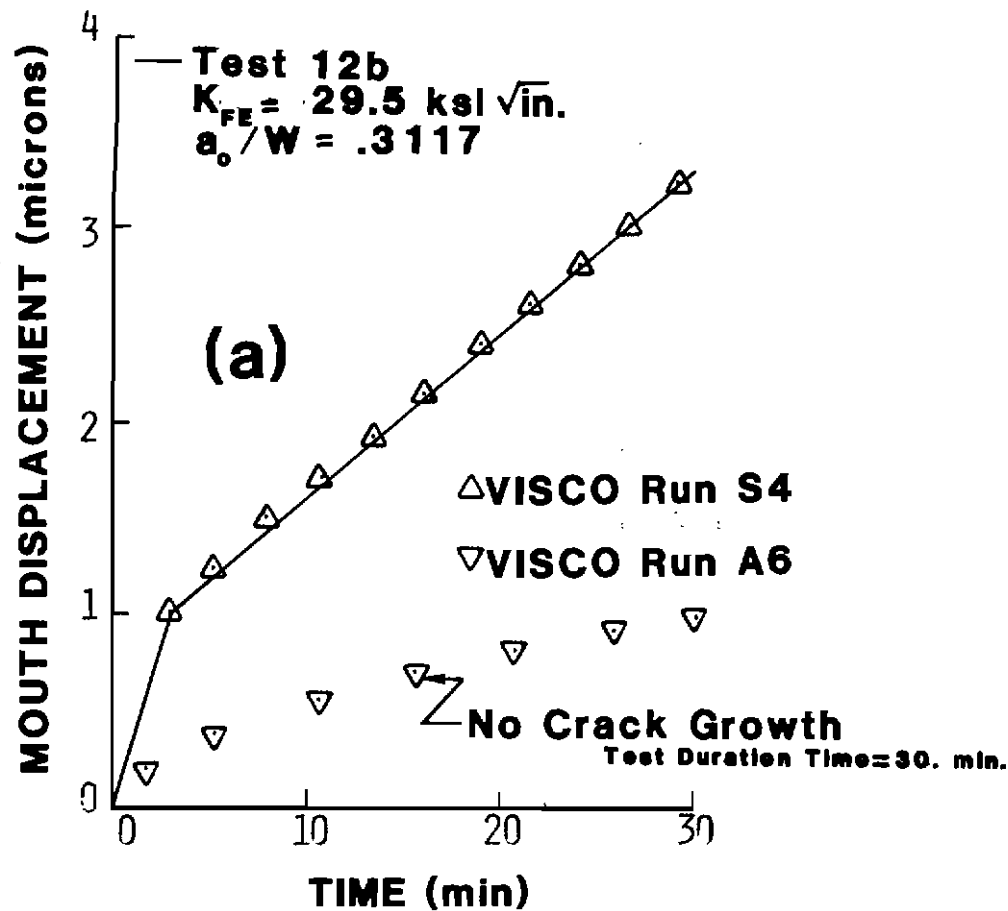


Figure 42a. Test 12b HEN VISCO Results, Displacements Matched to Test Data

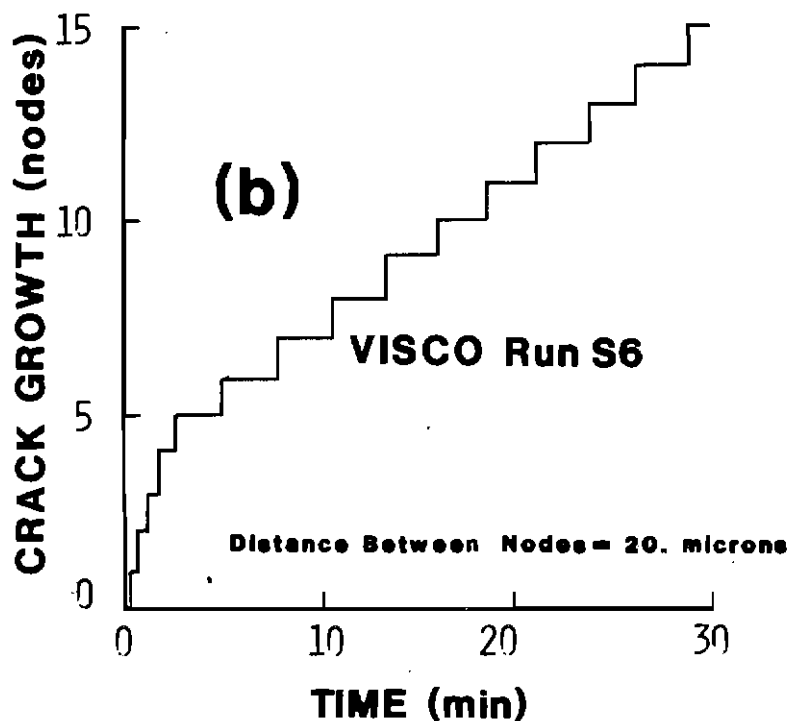


Figure 42b. Test 12b HEN VISCO Results, Crack Growth

AFWAL-TR-80-4140

left out of the creep crack growth displacement data. Test 6 was an exception where displacement measurements began after five minutes of test time had expired.

The main details of the HEN procedure can be graphically seen in Figures 37a and b. Observe in Figure 37a the two specific curves of crack tip displacement. One from VISCO with no crack growth and the other being test data. These curves start to deviate from each other at a time of approximately four minutes and for a time of 20 minutes the difference is fairly great as is shown by a bracket in Figure 37a. This bracketed difference is attributed to physical crack growth and requires release of crack tip nodes in this simulation.

Figures 37b through 42b depict the resulting crack growth from the HEN VISCO runs for each test. Note that due to this discrete finite element analysis technique, the crack growth is a step function (i.e., release of individual crack tip nodes) whereas realistically the crack might in general be growing in a smoother manner with time.

a. Comparison of Results from Using Different Node Unloading Methods

In cases where the total creep crack growth is only a few node distances ( $7.81 \times 10^{-4}$  in.  $\approx$  20 microns) the displacements developed by VISCO deviate significantly from the test displacement versus time curve (e.g., see Figure 41a) which implies that the model is too compliant or the unloading of the crack tip nodes is too rapid. These deviations become less significant for larger amounts of crack growth as seen in Figure 37a. One approach to minimize these deviations for small crack growth cases is to make a second VISCO run for the same test. In this second run, node release times from the first VISCO run are input. Therefore, the continuous node unload method can then be used as described in Section IV.

Figure 37a shows VISCO displacements from employing the five second node unload method (VISCO Run S3) and the continuous node unload method

AFWAL-TR-80-4140

(VISCO Run S7). Note that the displacements from Run S7 are only slightly below and run parallel to the test data with no excursions. Also, Run S1 in Figure 39a matches test data with no excursions and this is a case similar to Figure 41a where overall crack growth was small and deviations were large.

Later on crack growth criteria will be postulated based on stress and/or strain at the crack tip and therefore reliable data from the HEN procedure is required for these two quantities. Figures 43 and 44 show the differences in stress and plastic strain at the crack tip which develop between VISCO runs using the two different node unload methods. For large amounts of crack growth in this case, the relative difference in effective stress at the crack tip is seen to reach a steady state value of approximately 7%. The relative differences of the y-component of plastic strain at the crack tip, as seen in Figure 44 is much less. These differences in stress and strain are relatively small and it is concluded that essentially the same results (i.e., stress and strain at the crack tip) can be achieved for either node unload method for cases with large amounts of crack growth. For crack growth under small loads or for small crack growth rates more time is allowed for stress relaxation ahead of the crack tip. Thus on the average crack tip stress and strain also differ little between the two unload methods for slow crack growth. With this as background, it was decided that all subsequent solutions would be carried out using the five second node unloading scheme.

#### b. Dependence on Deformation History

Tests 8b through 8d were not included in the HEN VISCO runs since no fatigue precracking was done prior to these tests. Without fatigue precracking these tests were considered to be atypical due to their different prior deformation history. To check out dependence on prior deformation history the following VISCO analysis was performed.

Three VISCO runs with no crack growth were made to simulate Test 8b and its dependence on prior deformation. Each run had one of three

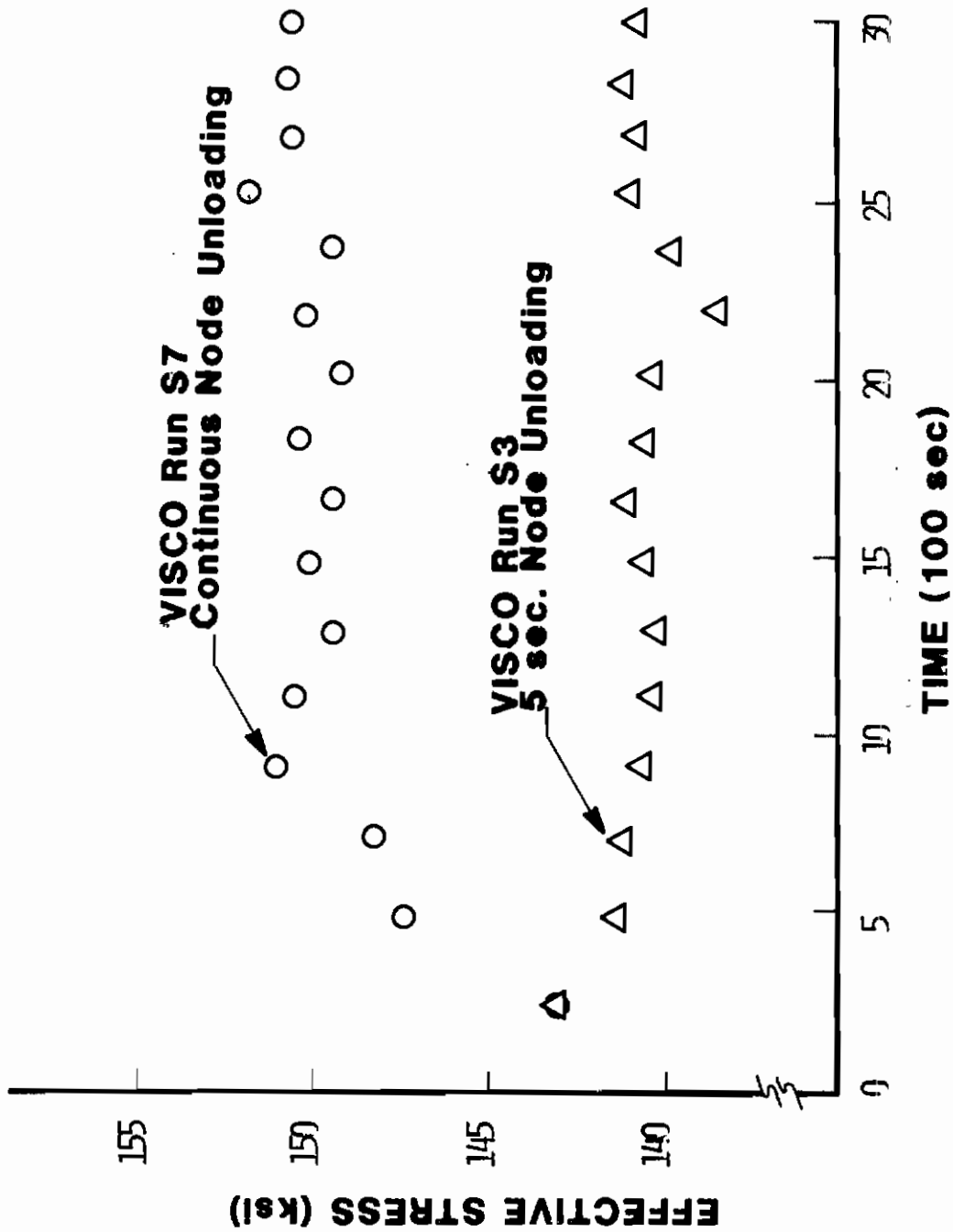


Figure 43. Crack Tip Effective Stress at the Time the Crack Tip Node Is Begun to be Released



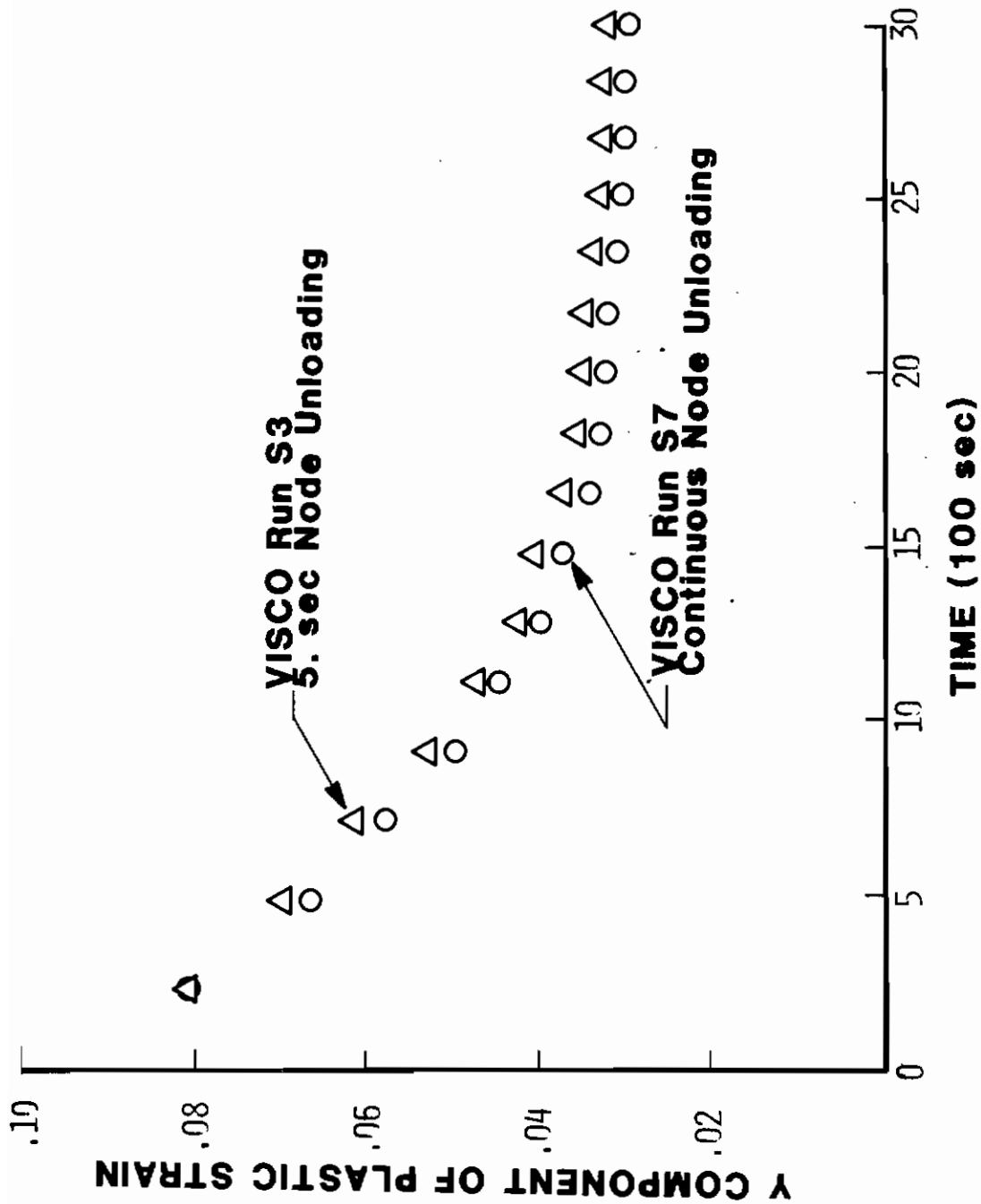


Figure 44. Crack Tip Plastic Strain at the Time the Crack Tip Node Is Begun to be Released

AFWAL-TR-80-4140

load-time profiles in Figure 45 input to it. The VISCO run A7 had no prior load history, run A8 had Test 8a load history with a total unload and re-load cycle, which is the most realistic load-time model of Tests 8a and b, and finally run A9 had Test 8a load history with no unload, but a load increase to the Test 8b load level. The top of Figure 45 shows the displacement versus time profile for each of these VISCO runs compared to Test 8b data. Again these displacements are relative to the displacements existing when the maximum Test 8b load is achieved.

In the case of run A8 where complete unloading occurs prior to Test 8b load, the VISCO results showed that plastic flow reoriented itself during the unloading due to the reversing of the principal stress at the crack tip to compression. This stress develops during unloading since the material has prior tensile plastic strains from the Test 8a load and cannot return to its original strain free state. This compressive behavior, if associated with crack growth, leads to the crack closure phenomenon described by Newman (Reference 83).

Comparing displacements of runs A8 and A9, where no unloading was done, indicates quite similar behavior. When no prior deformation history exists as for run A7 the displacements differ significantly, as shown in Figure 45, from those with prior load-deformation history. Note that run A7 fits the test data curve best. However, test compliance data indicates that some crack growth occurred in Test 8b. If displacements associated with this crack growth were included in these VISCO runs, experience with Test 8a would indicate that runs A8 and A9 would be brought up to the test data and run A7 would be much in excess of test results. It should also be noted that the form of the Bodner model employed in VISCO does not include the Bauschinger effect prevalent in metals when compressive yielding follows tensile yielding. Therefore, for the current investigation Tests 8b through 8d will not be further studied in order to minimize dependence on pretest deformation history in this investigation.

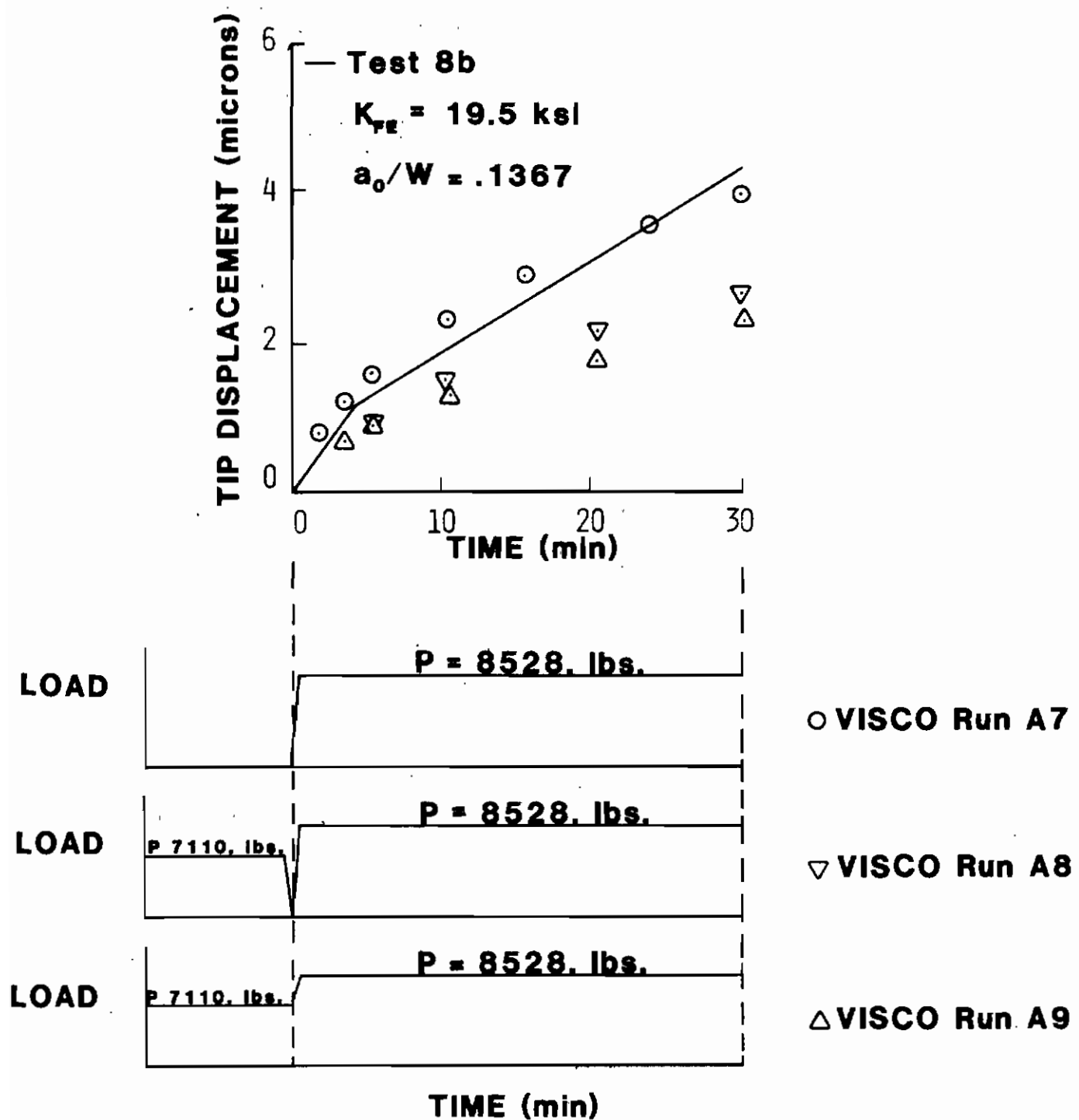


Figure 45. Load History Dependence of Displacements

### c. Crack Growth Results

Table 7 displays the total creep crack growth increments measured and calculated for the indicated test. The column entitled  $\Delta a_m$  presents the measured crack growth based on the average of four measurements across the thickness as shown in Figure 45. The column entitled  $\Delta a_1$  is the total crack growth calculated in the HEN VISCO runs and shown previously in Figures 37b through 42b. Two other convenient methods for calculating crack growth without the need of HEN VISCO runs were also used and their results are presented as  $\Delta a_2$  and  $\Delta a_3$ . The method for calculating  $\Delta a_2$  is an original technique developed in the present investigation and will be discussed subsequently.

The column entitled  $\Delta a_3$  is the crack growth calculated by Clarke's elastic compliance method (Reference 75). This method predicts negative crack growth in some instances where compliance was observed to decrease as discussed in Section IV. Figure 46 compares crack growth calculated by Clarke's method to the results from a HEN VISCO run for Test 9. Note that experimental elastic compliance changes from Test 9 indicate some unrealistic negative crack growth while incorporating Clarke's method whereas the VISCO results show a realistic monotonically increasing amount of crack growth with time. However, for times greater than twenty minutes, both curves are approximately parallel which lends support to Clarke's method for large amounts of creep crack growth also demonstrated by Donat (Reference 76).

The column in Table 7 entitled  $\Delta a_2$  is the crack growth calculated by a variation of Clarke's elastic compliance method as described below. In this variation no unload/reload cycle data are necessary during a creep crack growth test as discussed in Section IV. The VISCO simulation of the test is also simplified since a VISCO run is made using test conditions, but no crack growth is allowed in the VISCO model. Thus any increase in displacements after reaching maximum load in the no-crack-growth VISCO run can only occur due to time dependent plastic deformation allowed by the Bodner material model. Examples of these no-crack-growth

TABLE 7  
SUMMARY OF MEASURED AND CALCULATED CRACK GROWTH

Test #	$a_m$ (in.)	$K_{FE}$ (ksi $\sqrt{in.}$ )	$\Delta a_m$ (in.)	$\Delta a_1$ (in.)	$\Delta a_2$ (in.)	$\Delta a_3$ (in.)
5	.148	25.0	.0148	.0148 □ ∇	.0143	no data
6	.219	27.9	.0171	.0131	.00954 □	.0113
8a-8d	.152	16.3-24.0	.01028	* ∇	* ∇	.00997
9	.162	36.8	no data	.0662	.0856	.0298
12a	.230	17.5	.00320	.00312Δ	.00339	.021
12b	.265	29.5	.0132	.0119	.0110	.00691

\*Did not model due to prior deformation history of specimen.

∇Only modeled part of test due to excessive crack growth, value given is extrapolated.

□Test Displacement measurements begun five minutes after load application.

ΔOnly modeled part of test due to insufficient data.

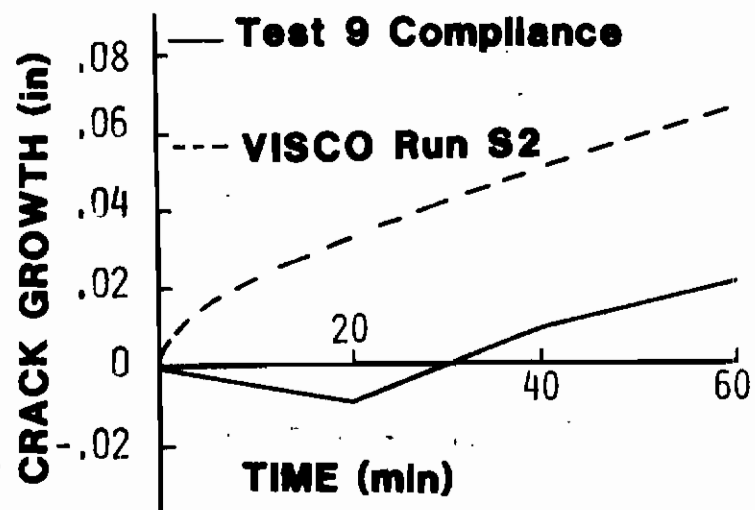


Figure 46. Comparison of Crack Growth from Experimental Compliance with HEN VISCO Results

VISCO displacements were given in Figures 37a through 42a. Through simultaneous use of test displacement data and the no-crack-growth VISCO results, the crack growth  $\Delta a_2$  is calculated as follows

$$\Delta a_2 = \frac{(\delta_{\text{Test}} - \delta_v)/P}{\Delta c/\Delta a} \quad (59)$$

where  $\delta_{\text{Test}}$  is the experimental displacement. The displacement  $\delta_v$  is the value calculated in VISCO for the same test conditions but no crack growth is allowed. The denominator term,  $\Delta c/\Delta a$  is the rate of change of elastic compliance with crack length generated from elastic VISCO runs of the test specimens. By releasing crack tip nodes and dividing the resulting VISCO displacements by the load to get the respective compliances, the curve of compliance versus crack length was determined for each test's indent or displacement measurement location (Figure 32). The slope of this compliance versus crack length curve then provided  $\Delta c/\Delta a$  ratio. The applied load  $P$  is divided into the difference of  $\delta_{\text{Test}}$  and  $\delta_v$  to generate a change in compliance. This change in compliance is assumed to be primarily dependent on crack growth which means that the plastic zone developing around this fixed crack tip is approximately the same size for an extending crack and simply translates along with the crack tip.

Figure 47 graphically defines  $\delta_{\text{Test}}$  and  $\delta_v$  at an arbitrary measurement time  $t_m$ . Note that this  $\Delta a_2$  method is effectively the same as the HEN VISCO procedure for small amounts of crack growth where, as mentioned previously, the plastic zone size is assumed constant. Therefore a curve of crack growth versus time could also be generated by this  $\Delta a_2$  method by applying Equation 59 continuously along the test data curve.

Consider the measured crack growth column  $\Delta a_m$  and the HEN VISCO results  $\Delta a_1$ . The differences between these two columns is only  $\pm 10\%$  for those tests totally modeled. Only part of Test 6 was modeled since the number of uniform crack growth elements ahead of the initial crack

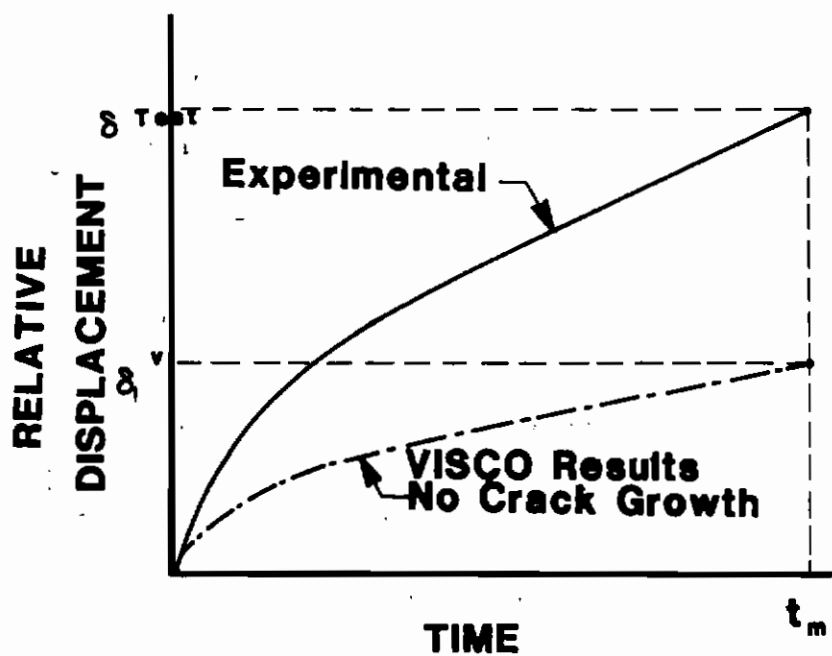


Figure 47. Schematic of Displacements Used to Calculate Crack Growth by Equation 59



tip were already exhausted after half of the test duration. This also occurred in modeling Test 9. Hence, in both Tests 6 and 9 the value of  $\Delta a_1$  was determined by extrapolating the final or relatively steady state slope of the crack growth versus time curves in Figures 38b and 40b. Another special characteristic of Test 6 is that displacement data versus time was not measured during the first five minutes of the test. Thus, based on other test behavior, a significant amount of the early relatively rapid displacement rates were ignored. Some of this early displacement would apparently have required more crack growth in VISCO than the existing data did while using the HEN procedure.

The crack growth values,  $\Delta a_2$ , in Table 7 also correlate quite well with the measured values  $\Delta a_m$ . The good correlation of  $\Delta a_2$  with test data provides support to this convenient method developed herein for calculating creep crack growth. The significant convenience feature in calculating  $\Delta a_2$  is that once a no-crack-growth VISCO run is made for a given set of test conditions, Equation 59 can simply be applied for analyzing all further experiments with approximately the same test conditions (e.g., load, crack length and geometry).

A somewhat similar HEN analysis was done by HSU et. al (Reference 32) to predict crack growth in zirconium at elevated temperatures. HSU's crack growth predictions were 2.5 times greater than actual test data. In the present HEN analysis, crack growth predictions were within approximately 10% of test data for the tests that were totally simulated. The extremely good correlation using the present method is attributed to both higher resolution experimental displacement data than HSU's and a more realistic material model that includes creep behavior. Additional displacements due to creep in HSU's analysis would have reduced the amount of crack growth predicted. Since HSU's predictions were high, this reduction would be in the direction of better correlation with test data.

Another comparison of current results can qualitatively be made with Newman's finite element analysis of fatigue crack propagation (Reference

83). Figure 48 shows crack opening displacement profiles during creep crack growth from the VISCO model as represented by the solid lines. Note that with the crack tip at point zero, the elastic crack opening displacement profile (i.e., the dashed line in Figure 48) is lower than the solid line which incorporates the Bodner material model. However, as the crack grows a wake of residual plastic deformation is left behind the crack tip. After 12 increments of crack growth, Figure 48 shows how this plastic wake diminishes the elastic-plastic crack profile below a purely elastic profile for the same crack length "a". The residual plastic deformation indicated by the cross-hatched area in Figure 48 was also displayed in a similar figure by Newman.

## 2. CRACK GROWTH CRITERION

Based on the good correlation between actual and predicted crack growth, the VISCO results from the HEN applications were examined for potential crack growth parameters. The local crack tip parameters such as strain and crack opening displacement (C.O.D.) were examined initially since these parameters have shown promise elsewhere (References 84,85) for correlating finite element results with crack growth test data.

The main goals here were to check out the validity of existing crack growth criteria (i.e., critical C.O.D. and strain), possibly modify one of these existing criteria to better fit test data, and postulate a new criterion that might better account for creep damage accumulation and crack growth displayed by the HEN VISCO analysis.

### a. Critical Strain Criterion

Examination of the strains in the elements adjacent to the crack tip prior to each node release for crack growth in the HEN VISCO runs revealed that no single value for the critical strain would satisfy all test conditions. However, a few VISCO runs were made using a fixed critical strain criterion to further evaluate its applicability.

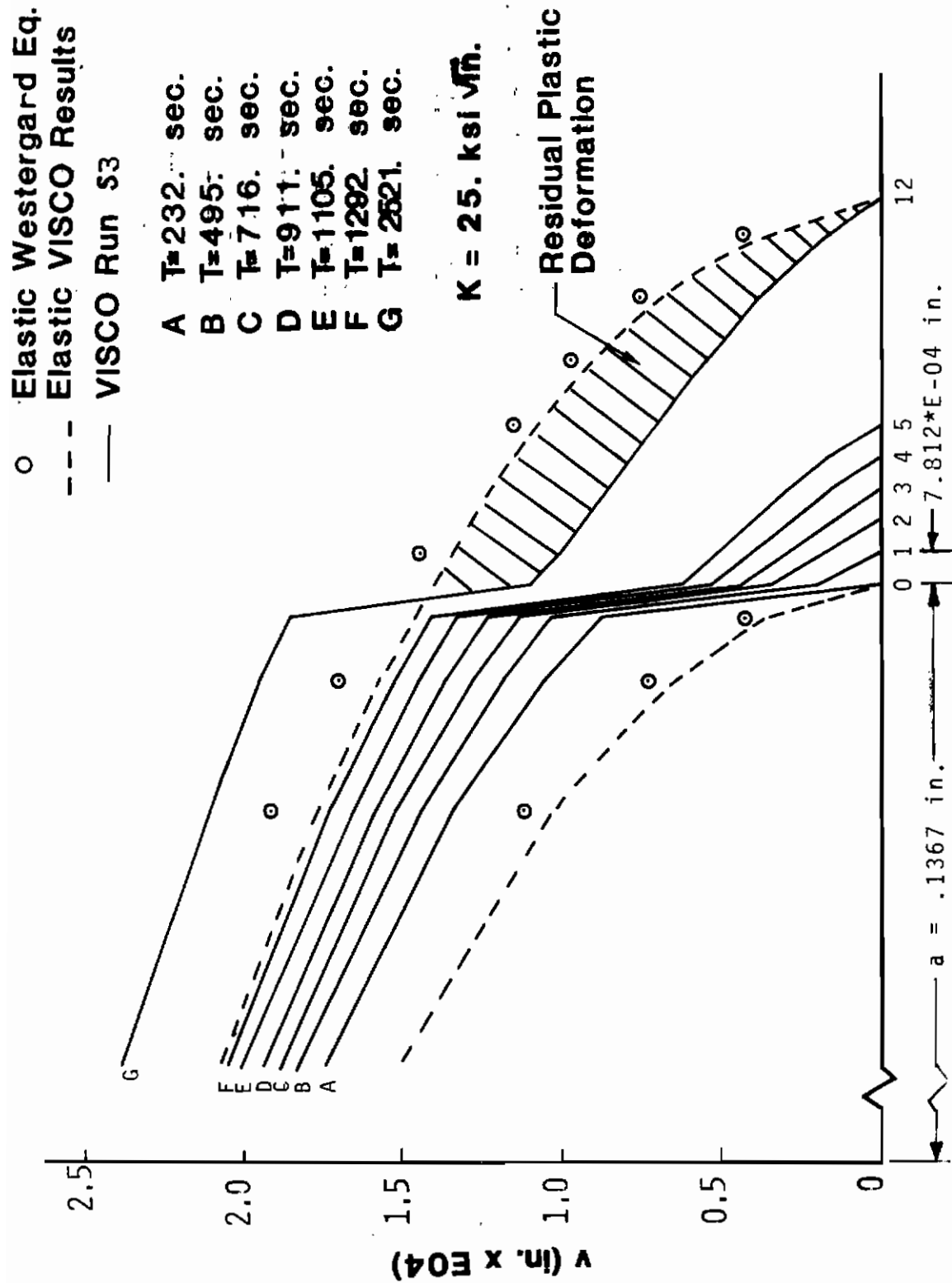


Figure 48. Crack Opening Displacement Profiles During Creep Crack Growth

The critical strain criterion was implemented in VISCO by comparing the average of the plastic strain components normal to the crack and within elements adjacent to the crack tip with a critical strain value,  $\epsilon_{crit}$ , as time progressed. When the average crack tip plastic strain exceeded the critical value,  $\epsilon_{crit}$ , the crack tip node was released and unloaded in five seconds. Table 8 gives a summary of the basic details for VISCO runs employing the critical strain criterion. A  $\epsilon_{crit}$  value of 0.030 was found to work well from the HEN VISCO runs of Test 8a where  $K_{FE}$  was 16.3 ksi $\sqrt{in}$ . However for Test 9 where  $K_{FE}$  was 36.8 ksi $\sqrt{in}$  the  $\epsilon_{crit}$  value needed to be 0.090 to work well as shown in Figure 49a. The corresponding  $\epsilon_{crit}$  dependent crack growth versus time is given in Figure 49b. The  $\epsilon_{crit}$  value of 0.075 allowed too much displacement compared to test data as seen in Figure 49. The displacement results for a  $\epsilon_{crit}$  value of 0.090 appear to fit the data quite well over the first five minutes of the test. Likewise the resulting crack growth in Figure 49b agrees quite well with the HEN data in Figure 39b. However based on examination of the prior HEN VISCO runs, if the simulation time were continued, the  $\epsilon_{crit}$  value of 0.090 would have been too large. Therefore, insufficient crack growth would have resulted and the displacements would have fallen away from the test data as shown by the extrapolated dashed curve.

Figure 50 displays the HEN VISCO crack tip strain values taken at the time a crack tip node was to be released in the HEN VISCO runs. This plot was motivated in an attempt to find a general trend of the critical strain values or to determine a mathematical relationship with time to envelope the HEN results. Note that in general the strains are high for short times and then diminish with time to a common value of approximately 0.03. In order to develop a critical strain functional expression one can see a need for a decaying parameter which would fit the upper bound strain values in Figure 50 related to rapid crack growth. In addition the expression must have the capability of allowing

*Contrails*

TABLE 8  
SUMMARY OF VISCO RUNS WITH CRITICAL STRAIN CRITERIA

Run #	Test #	Crack Length $a_o$ (in)	Load P (lbs)	$K_{FE}$ (ksi $\sqrt{\text{in}}$ )	Time @ Max Load (sec)	Nodes Released	$\epsilon_{crit}$	Central Processor Time (sec)
E1	8a	.1367	7150	16.3	3600	3	.030	1000
E2	9	.1367	16060	36.8	150	19	.075	4484
E3	9	.1367	16060	36.8	260	14	.090	4000

TABLE 9  
SUMMARY OF VISCO RUNS WITH CRITICAL C.O.D. CRITERIA

Run #	Test #	Crack Length $a_o$ (in)	Load P (lbs)	$K_{FE}$ (ksi $\sqrt{\text{in}}$ )	Time @ Max Load (sec)	Nodes Released	Critical C.O.D. (in)	Central Processor Time (sec)
C1	9	.1367	16060	36.8	1200	13	.520x10 <sup>-4</sup>	3530
C2	9	.1367	16060	36.8	353	19	.452x10 <sup>-4</sup>	4000

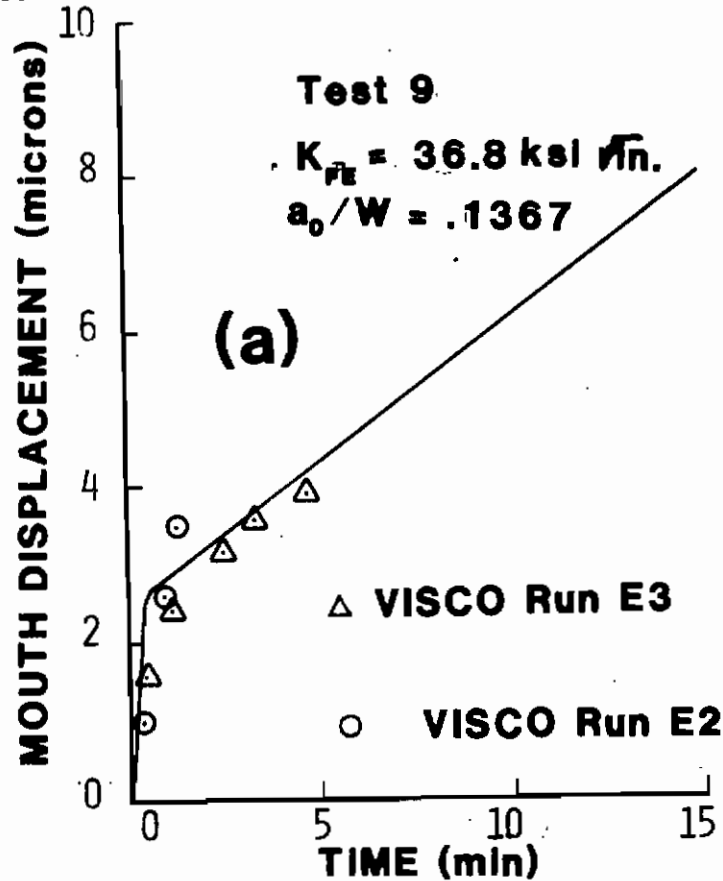


Figure 49a. VISCO Critical Strain Crack Growth Criterion, Resulting Displacements Due to Crack Growth

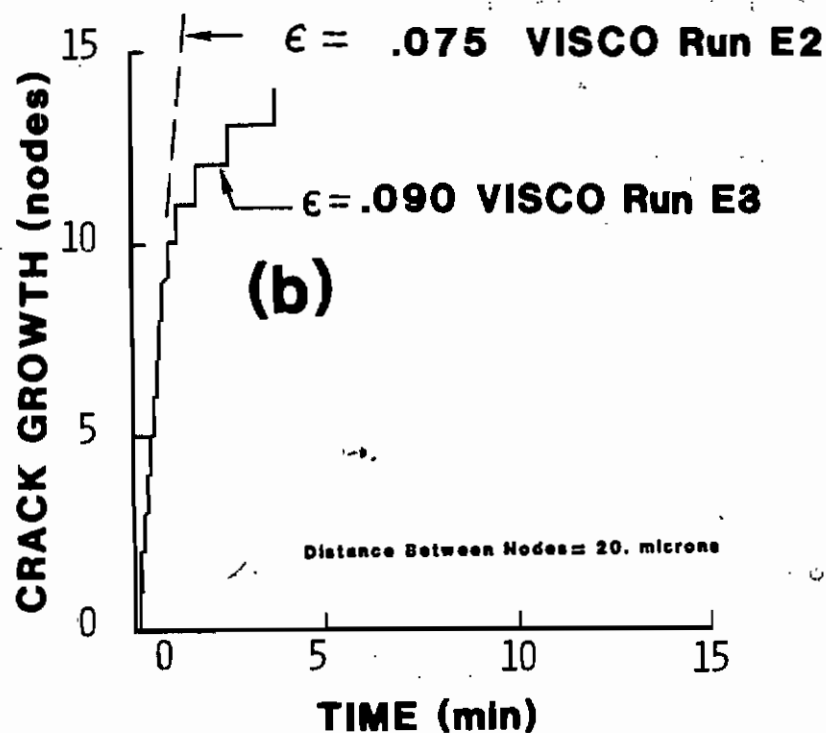


Figure 49b. VISCO Critical Strain Crack Growth Criterion, Resulting Crack Growth

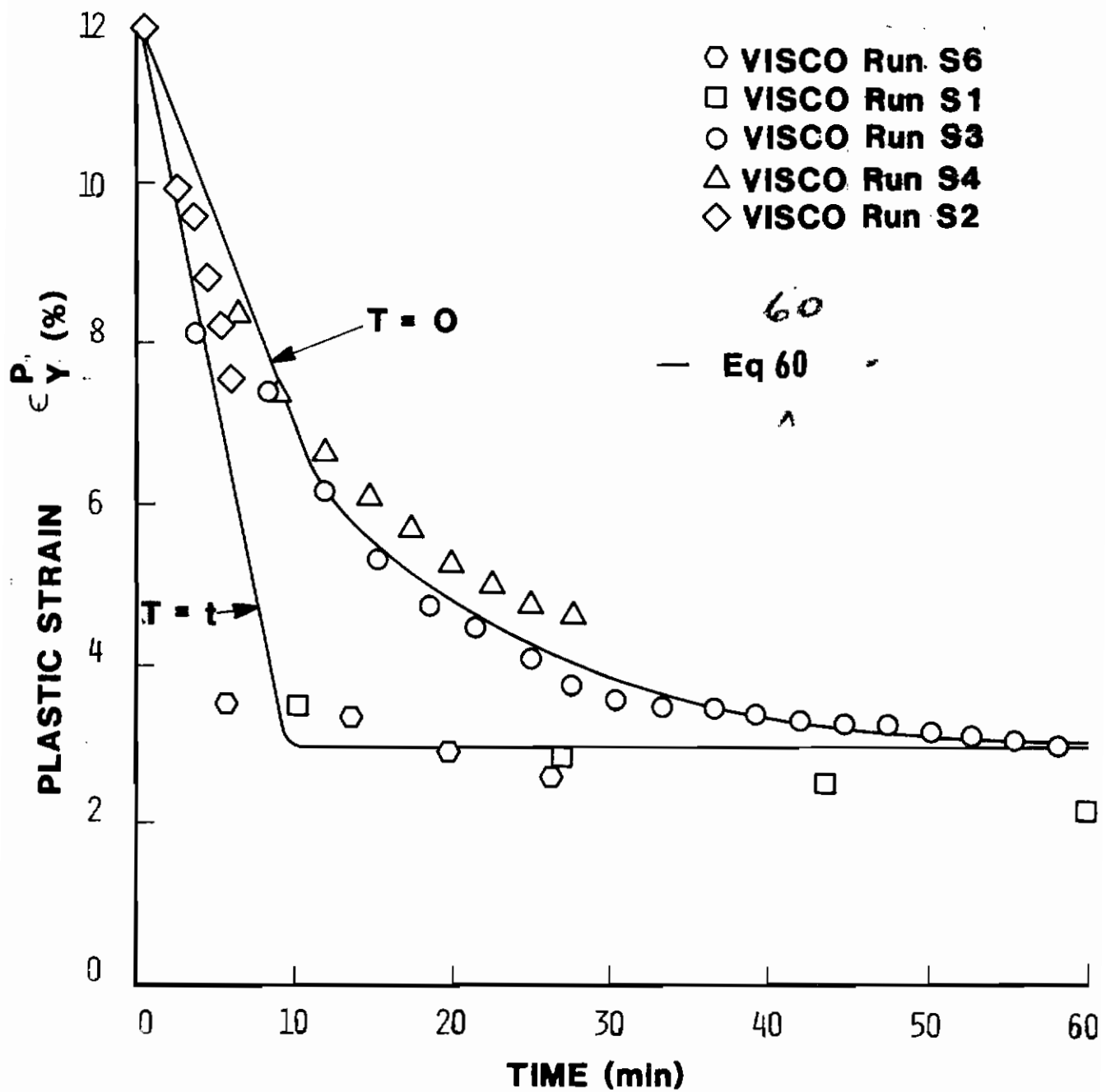


Figure 50. Time Dependent Critical Strain Crack Growth Criterion



the region around the crack tip node to deteriorate with exposure to the crack tip environment (i.e., not only the environment external to the specimen but also the singular strain state internal to the specimen). Crack tip deterioration is considered to be displayed by the lower bound of strain values in Figure 50. Therefore, the general properties of the critical strain function have been stated. The curve must be decaying with test time, thus a negative exponential function is in order. And since critical strain values appear to diminish with crack tip exposure time, but not as rapidly as an exponential function would dictate, the cosine function was examined.

An empirical expression for the critical strain that fits the HEN VISC0 results fairly well is given by

$$\epsilon_{\text{crit}} = \begin{cases} \epsilon_0 \left[ A \exp(-bt) \cos\left(\frac{\pi T}{2T_0}\right) + 1 \right] & \text{if } T \leq T_0 \\ \epsilon_0 & \text{if } T > T_0 \end{cases} \quad (60)$$

where  $\epsilon_0 = 0.03$ ,  $A=3.0$ ,  $b=1.34 \times 10^{-3} \text{ sec}^{-1}$ ,  $T_0=600.\text{sec.}$

The value of  $\epsilon_0$  represents the critical strain for large time. The coefficient  $A$  is determined at  $t$  equal to zero. Once  $A$  and  $\epsilon_0$  are chosen  $b$  is determined by best fitting the upper bound where crack tip exposure time is small and set to zero (i.e.,  $T = 0$ ). The parameter  $T_0$  determines how rapidly the critical strain diminishes to  $\epsilon_0$  with crack tip exposure time  $T$ .

Motivation for the development of Equation 60 comes from environmental effects such as oxidation at these high temperatures from exposure to laboratory air. This oxidation is then associated with changing material properties at the crack tip such as the critical strain value. Crack growth in alloys similar to IN-100 has been found to be quite sensitive to the environment and the resulting oxidation that can occur when an elevated temperature crack growth test is done in air (Reference 86). Therefore, Equation 60 is an attempt to represent the rate at which the critical strain for crack growth is diminished with time due to environmental effects.



The critical strain criterion just formulated would be employed in VISCO in the following steps.

1. Register both total test simulation time,  $t$ , and crack tip exposure time,  $T$ .
2. Evaluate the critical strain level during each time step from Equation 60.
3. Compare with crack tip element's plastic strain accumulating in the VISCO analysis.
4. Release crack tip node when VISCO plastic strain at the crack tip exceeds  $\epsilon_{crit}$  from Equation 60.
5. Crack tip exposure time  $T$  is set to zero and the above steps 1-4 are repeated for the next crack tip node.

b. Critical Crack Opening Displacement Criterion

The crack opening displacement is defined here as the C.O.D. at the first node behind the crack tip in the finite element model. Examination of C.O.D.'s taken from HEN VISCO runs in Table 5 just prior to releasing a crack tip node revealed no single C.O.D. value that could be used for all test conditions as a critical C.O.D. A value of  $0.280 \times 10^{-4}$  inches was found from HEN VISCO results for Test 8a with  $K_{FE} = 16.3 \text{ ksi}\sqrt{\text{in}}$  to work best, yet when a few VISCO runs, as summarized in Table 9, were done with a critical C.O.D. criterion and an increase to  $K_{FE} = 36.8 \text{ ksi}\sqrt{\text{in}}$  for Test 9, the best critical C.O.D. became approximately  $0.500 \times 10^{-4}$  inches as shown in Figure 51. Further observance of Table 9 and Figure 51 shows that this criterion was very sensitive to small changes in critical C.O.D. Therefore further evaluation of this criterion was deemed unnecessary as compared with the less sensitive critical strain criterion.

c. Critical Damage Accumulation Criterion

In several theoretical works and as stated recently by Goodall and Chubb (Reference 62), creep rupture of uncracked components under a

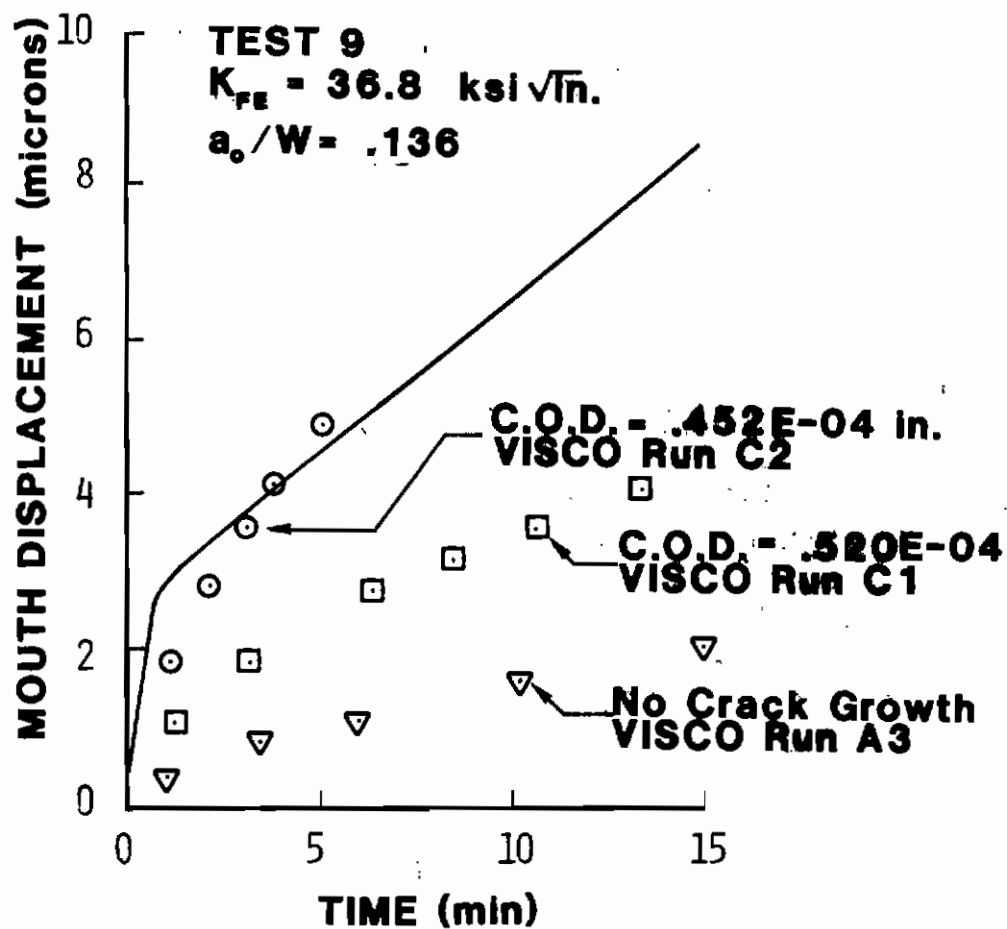


Figure 51. VISCO Critical C.O.D. Criterion, Resulting Displacements

varying stress history is governed by the life fraction rule. Consequently, this reference indicated that for a uniaxial stress history,  $\sigma(t)$ , rupture occurs at a time  $t_r$  given by

$$\int_0^{t_r} \frac{dt}{t_r(\sigma)} = 1 \quad (61)$$

where  $t_r(\sigma)$  is the rupture time corresponding to a constant stress level,  $\sigma$ . When experimental stress values are plotted against their rupture times on logarithmic scales the relationship is often linear in the region of practical interest. Thus if  $M$  and  $C$  are material constants it is assumed that

$$\sigma^M t_r(\sigma) = C \quad (62)$$

Substituting Equation 62 into 61 yields

$$\int_0^{t_r} \sigma^M dt = C \quad (63)$$

The description of creep rupture given by Equations 61 through 63 was discussed by Goodall and Chubb. The reference mentions that this rupture model is only one of several possible formulations. However, neither experimental nor theoretical work has provided an alternative to Equation 61 that gives a significantly better description of material response.

It is recognized that Equation 62 applies most directly to creep rupture of uncracked uniaxial components. However, the present author considers that similar behavior might be possible in creep crack propagation. A schematic of the postulated behavior involved with creep crack propagation is given in Figure 52. This figure shows a creep damage front preceding the crack. Within this front, the material is accumulating creep damage in the form of microcracks. This type of creep damage is also associated with creep rupture of uncracked components.

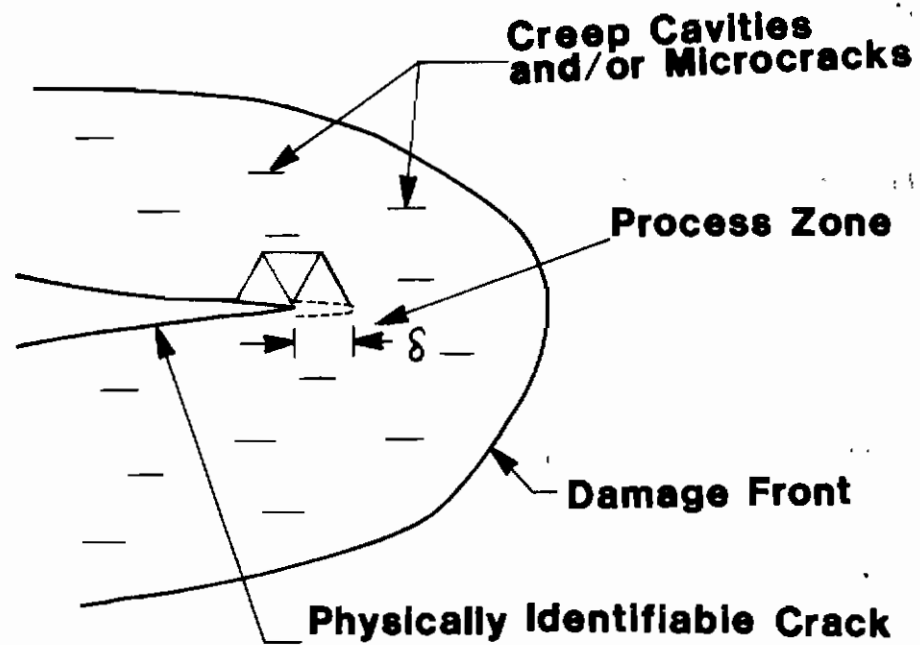


Figure 52. Schematic Representation of Creep Crack Propagation

In order to apply Equation 63 as a crack growth criterion, a process zone  $\delta$  is required and defined in Figure 52. In addition, the rupture time  $t_r$  is redefined from Equation 61 to the elapsed time the crack requires to grow from one node, in the HEN VISCO results, to the next node. In other words, it is the time period during which the process zone  $\delta$  is exposed to the crack tip stress field prior to rupture. In the VISCO finite element analysis, this process zone was taken as one element preceding the crack tip. The average component of stress normal to the crackline from three elements adjacent to the crack tip was used as the stress,  $\delta$ , in Equation 63 as shown in Figure 52.

Since the greatest stress exists at the crack tip and environmental degradation is considered to be most prevalent there, most damage accumulation was assumed to occur in the process zone after the arrival of the crack tip to the process zone's border. Therefore time in Equation 63 was measured from crack tip arrival time to the current crack tip node,  $t_A$ , or

$$\int_{t_A}^{t_A+t_r} \sigma^M dt = C \quad (64)$$

The constants M and C were determined based on results from the HEN VISCO runs. To accomplish this, Equation 64 was approximated as

$$\sigma_{avg}^M t_r = C \quad (65)$$

The rupture time or crack growth times  $t_r$  were taken from HEN VISCO results. The stress,  $\sigma_{avg}$ , also based on HEN results, was an average over time  $t_r$  of the crack tip stress defined previously. Since the interest here is to develop values for M and C which apply to the entire set of tests, it became obvious that there were more combinations of  $t_r$  and  $\sigma_{avg}$ , than necessary to uniquely define M and C. Consequently, to include the data from each HEN VISCO run, a least square fit of the data on a log-log plot was used to best fit the time-stress data. The values chosen were

$$M=15$$

$$C=8.63 \times 10^{79} (\text{psi})^{15} \text{ sec}$$

Equation 64 along with the previous constants were then incorporated into VISCO as a critical damage accumulation criterion for crack growth. Table 10 summarizes the basic details of the VISCO runs using this crack growth criterion.

Figures 53 through 58 give the results of applying VISCO with the critical damage accumulation criterion to the indicated test number in each figure. The resulting VISCO displacements are compared to test data in Figures 53a through 58a whereas the resulting crack growth from VISCO is given in Figures 53b through 58b. For the higher loadings such as Test 9 in Figure 56a the difference between test data and VISCO results is greatest. Part of this difference may be due to the fact that at this high load ( $K_{FE}=36.8 \text{ ksi}\sqrt{\text{in}}$ ) the damage zone as indicated in Figure 52 is larger than the process zone used herein (i.e., one element size or a characteristic dimension of  $7.81 \times 10^{-4}$  inches). Hence significant damage accumulation may occur in the material before arrival of the crack tip or time  $t_A$  for a given element in the crack path. This damage occurring in an element prior to  $t_A$  for that respective element was neglected in the present damage accumulation criterion. However, for the lower loads agreement with the test data is quite good considering that creep rates for the same test conditions can easily vary by a factor of two or three which is why log-log plots are used to plot creep data (Reference 29).

It should also be noted that the M and C values used were determined from the approximate Equation 65 expression. Crack growth results from this criterion might be improved by iterating or making small changes to M and C and making further VISCO runs in an effort to better fit test data.

### 3. CRACK GROWTH RATE CRITERIA

In this section crack growth rate criteria will be discussed based on the steady state crack growth rates developed by the HEN VISCO runs.

*Contrails*

TABLE 10  
SUMMARY OF VISCO RUNS WITH DAMAGE ACCUMULATION CRITERION

Run #	Test #	Crack Length $a_o$ (in)	Load P (lbs)	$K_{FE}$ (Ksi/in.)	Time @ Max Load (sec)	Nodes Released	Central Processor Time (sec)
D1	5	.1367	10896	25.0	3600	11	1820
D2	6	.2367	8160	27.9	1280	7	973
D3	8a	.1367	7140	16.3	3600	4	606
D4	9	.1367	16060	36.8	1800	15	3110
D5	12a	.2367	5190	17.5	1800	4	400
D6	12b	.3117	6676	29.5	1800	10	1611

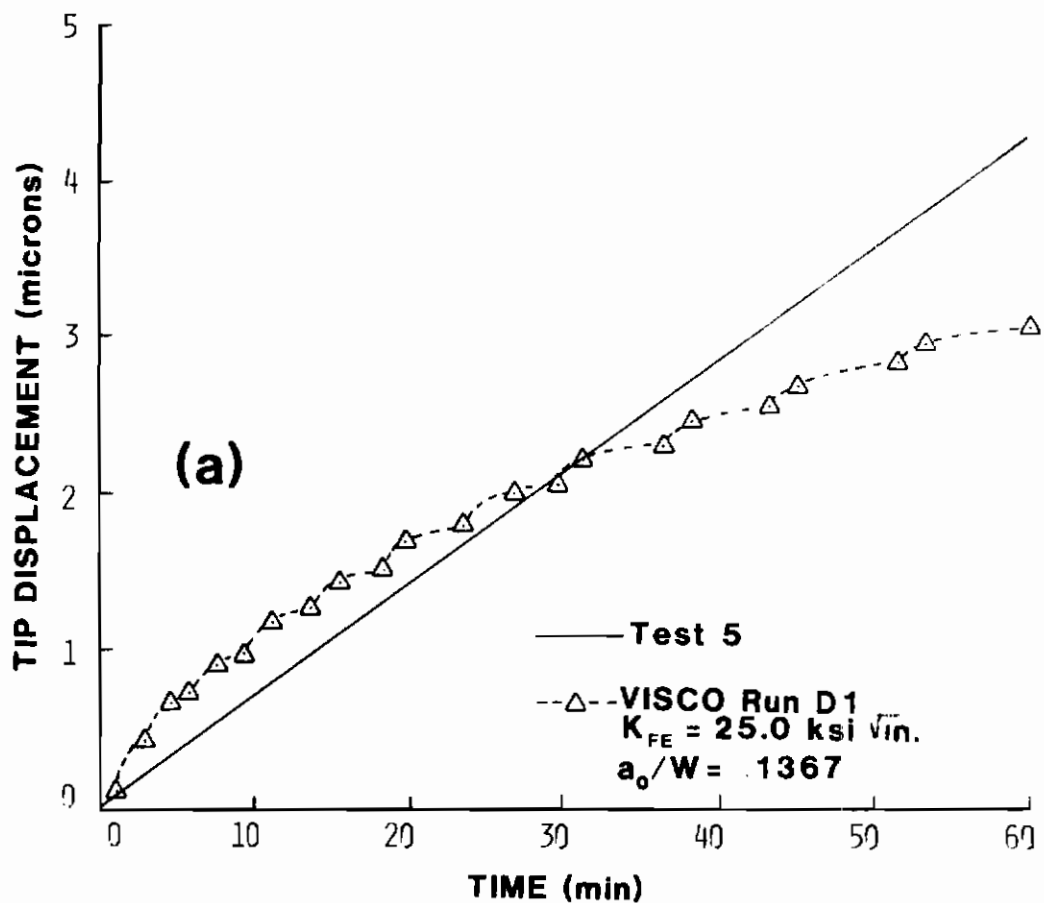


Figure 53a. Test 5 - VISCO Critical Damage Accumulation Criterion Displacement Results

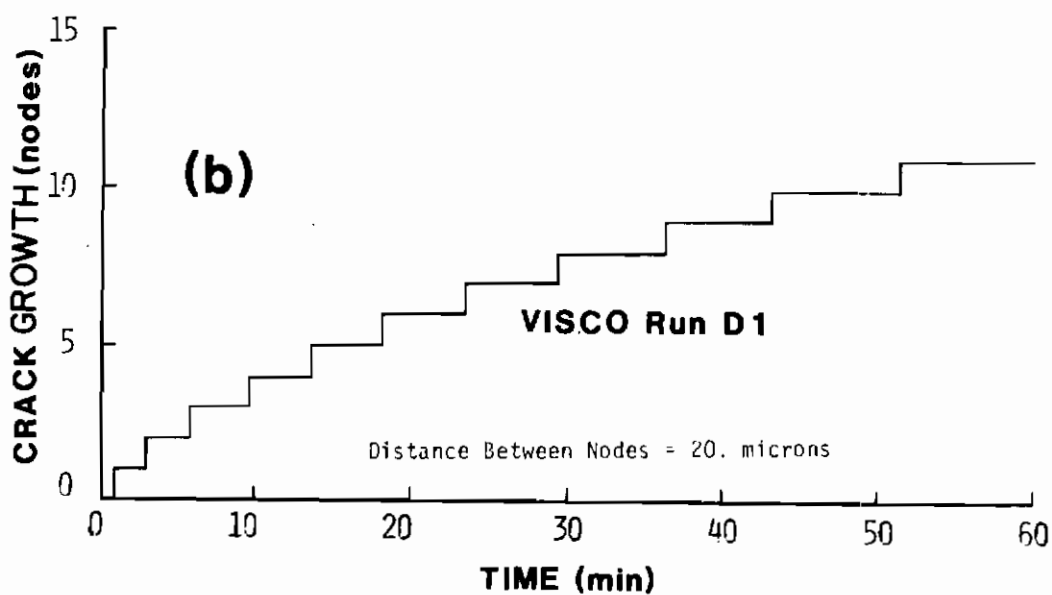


Figure 53b. Test 5 - VISCO Critical Damage Accumulation Criterion Crack Growth Results



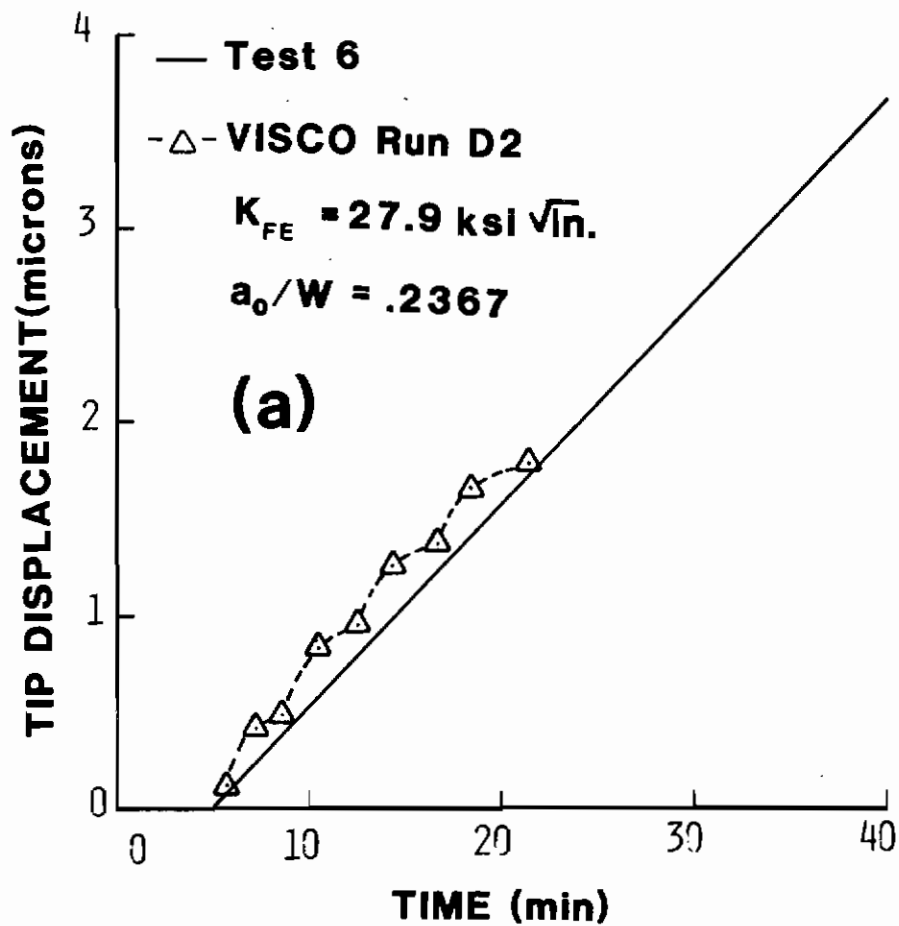


Figure 54a. Test 6 - VISCO Critical Damage Accumulation Criterion Displacement Results

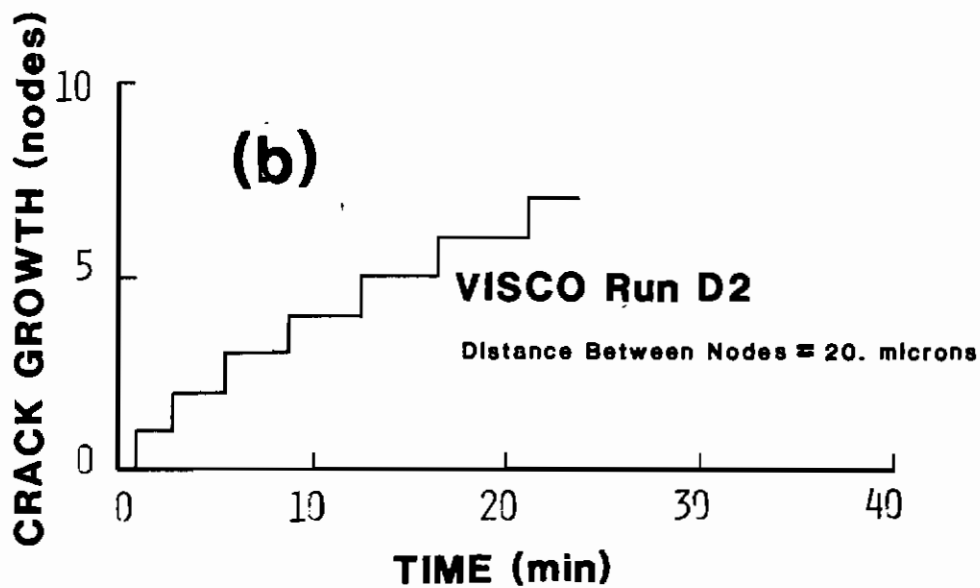


Figure 54b. Test 6 - VISCO Critical Damage Accumulation Criterion Crack Growth Results

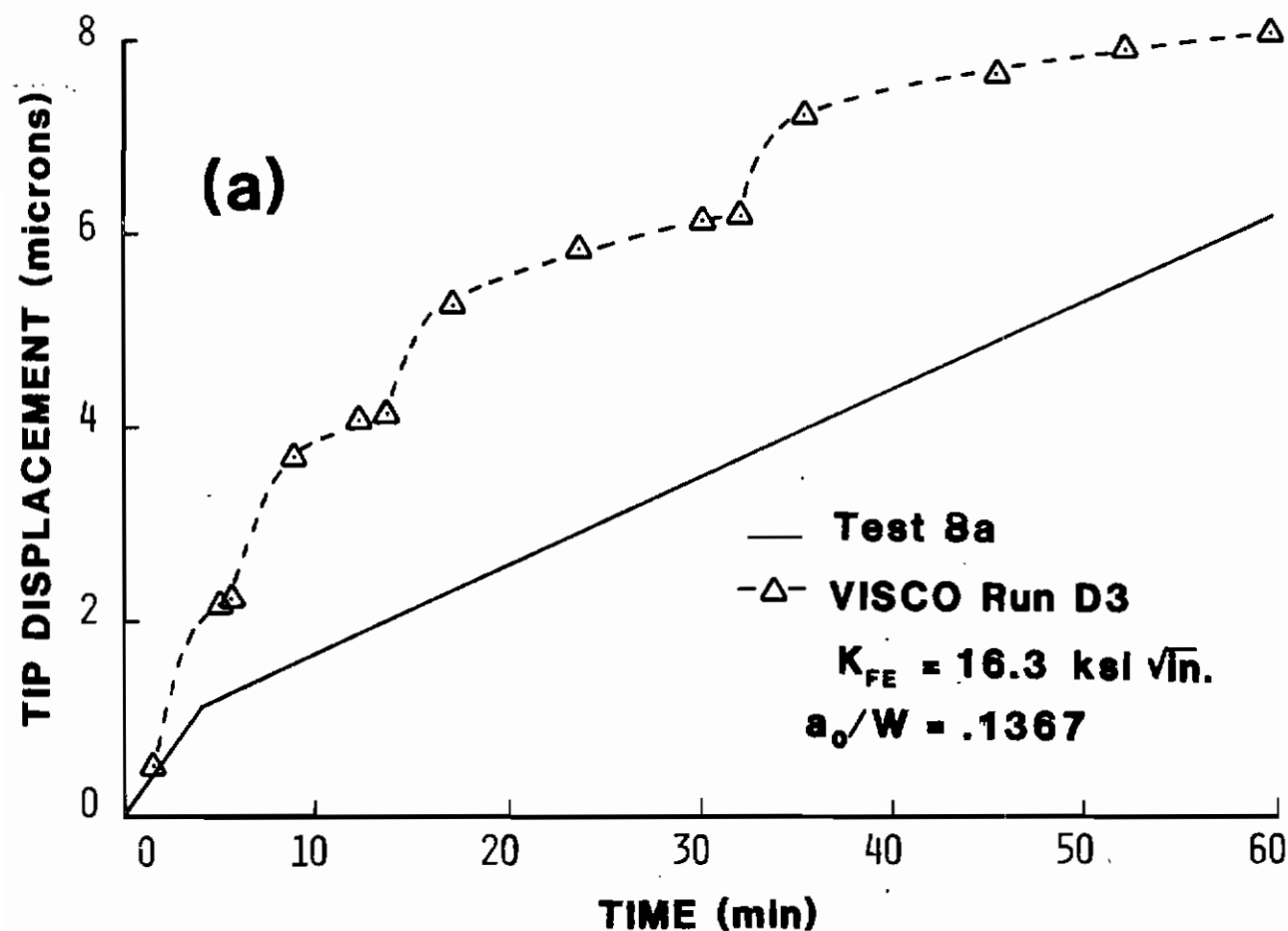


Figure 55a. Test 8a - VISCO Critical Damage Accumulation Criterion Displacement Results

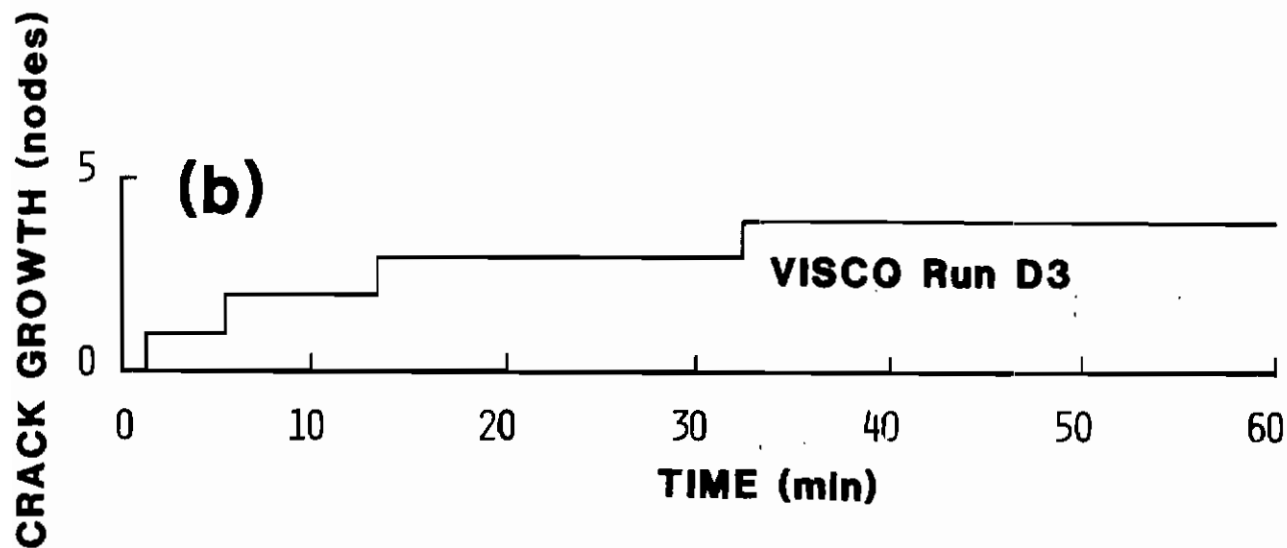


Figure 55b. Test 8a - VISCO Critical Damage Accumulation Criterion Crack Growth Results

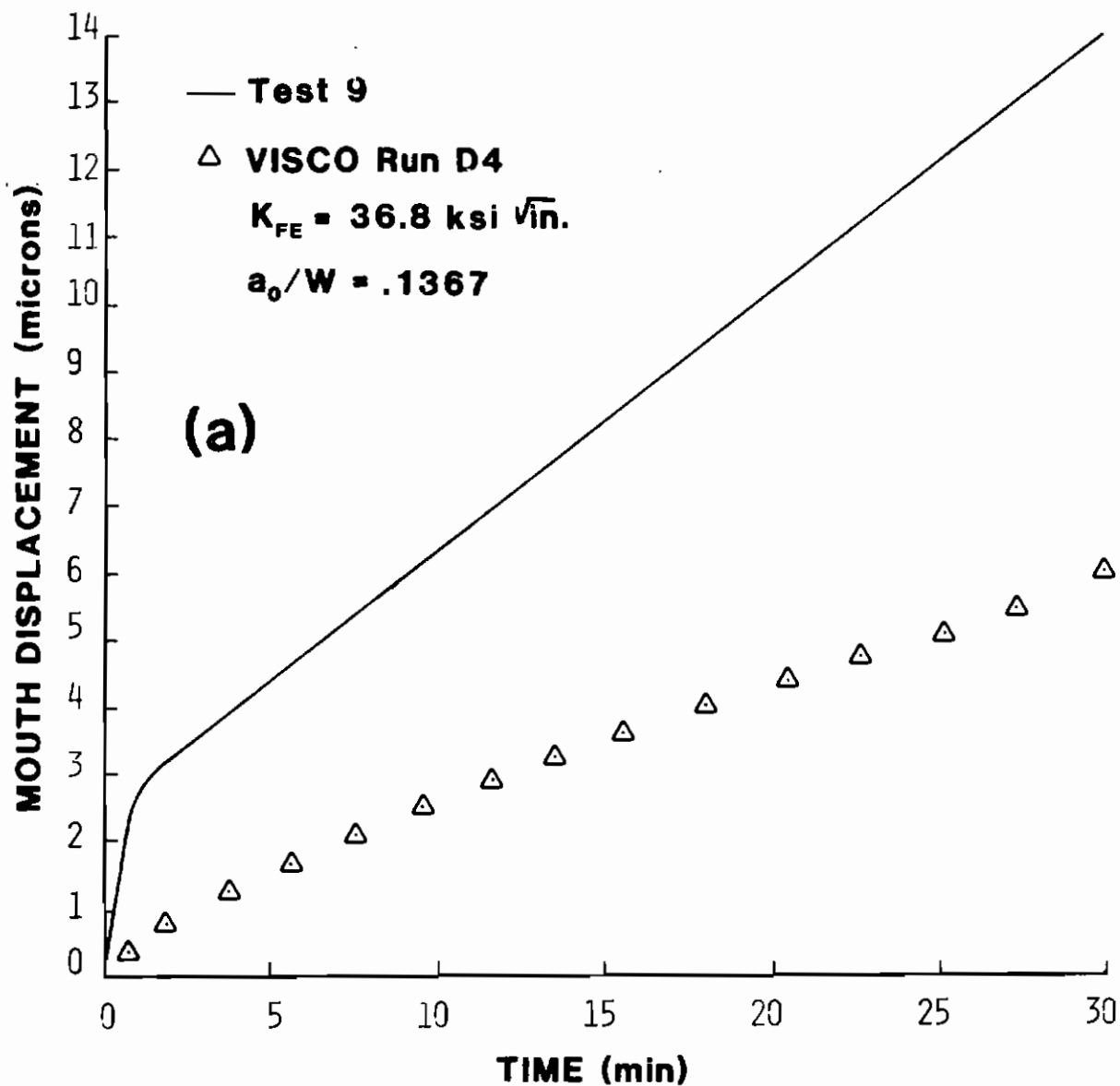


Figure 56a. Test 9 - VISCO Critical Damage Accumulation Criterion Displacement Results

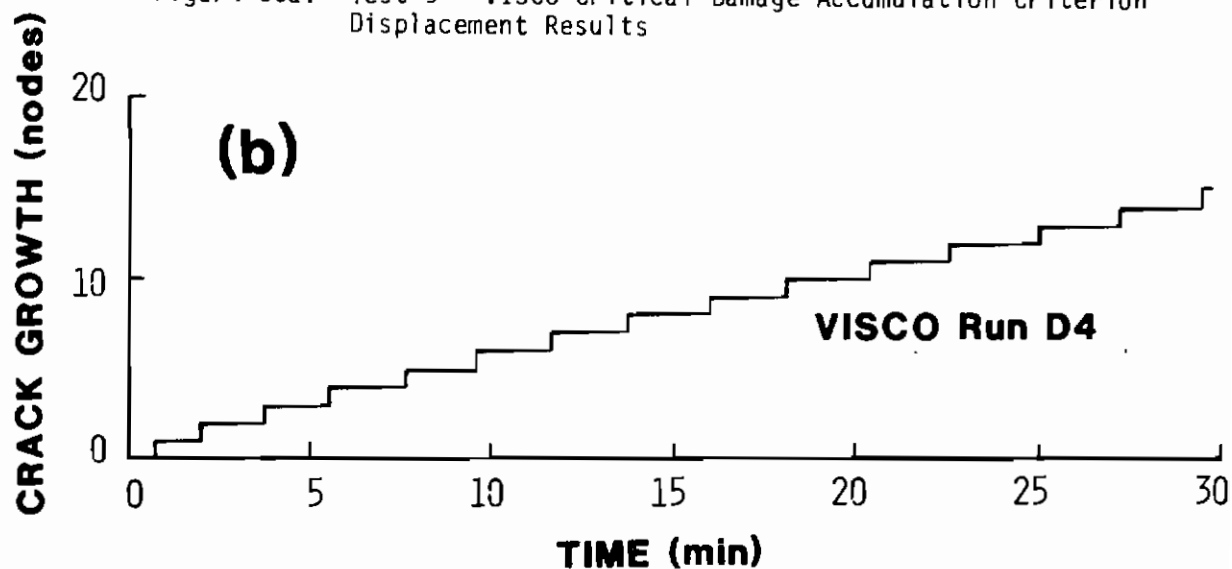


Figure 56b. Test 9 - VISCO Critical Damage Accumulation Criterion Crack Growth Results

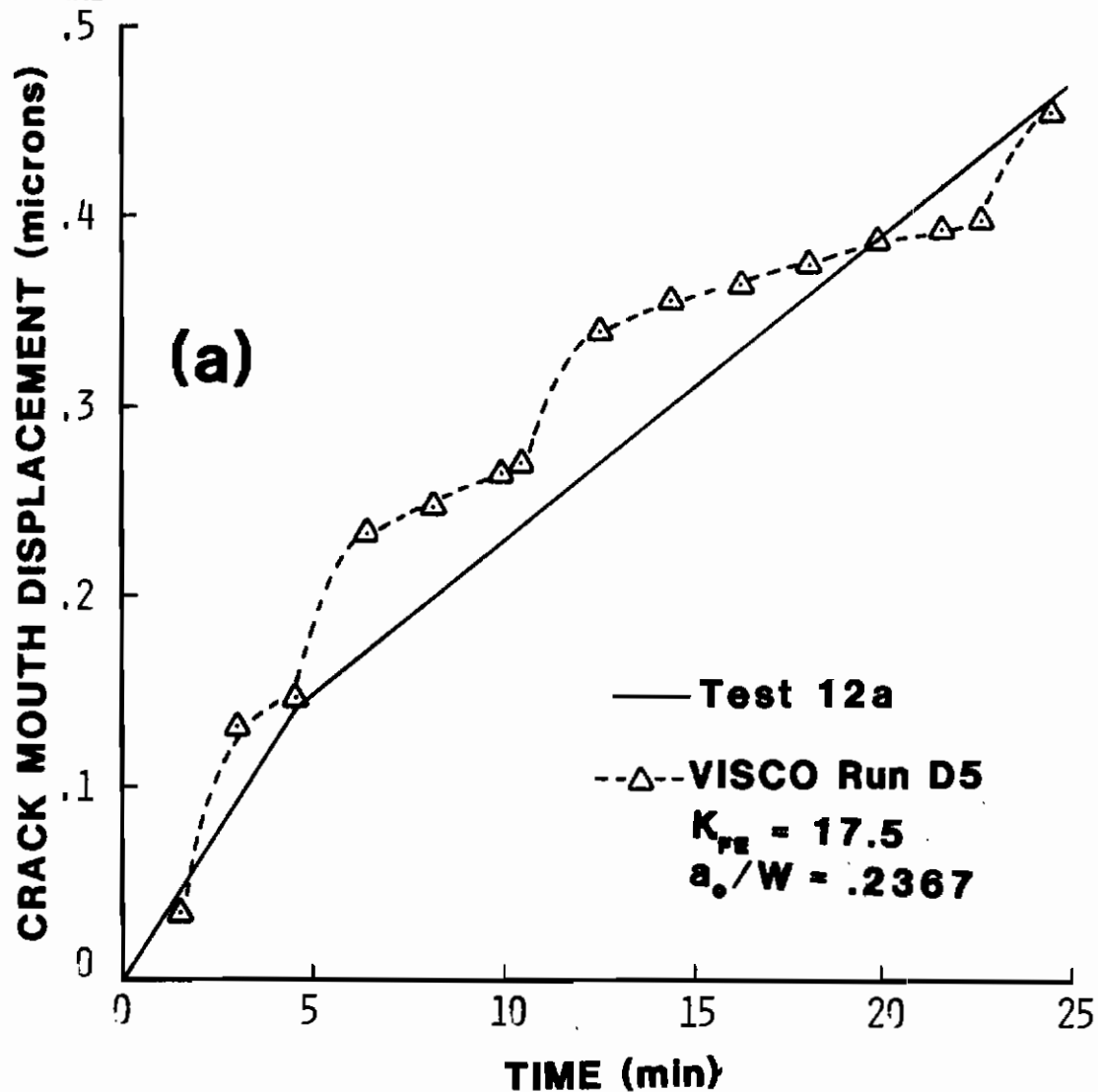


Figure 57a. Test 12a - VISCO Critical Damage Accumulation Criterion Displacement Results

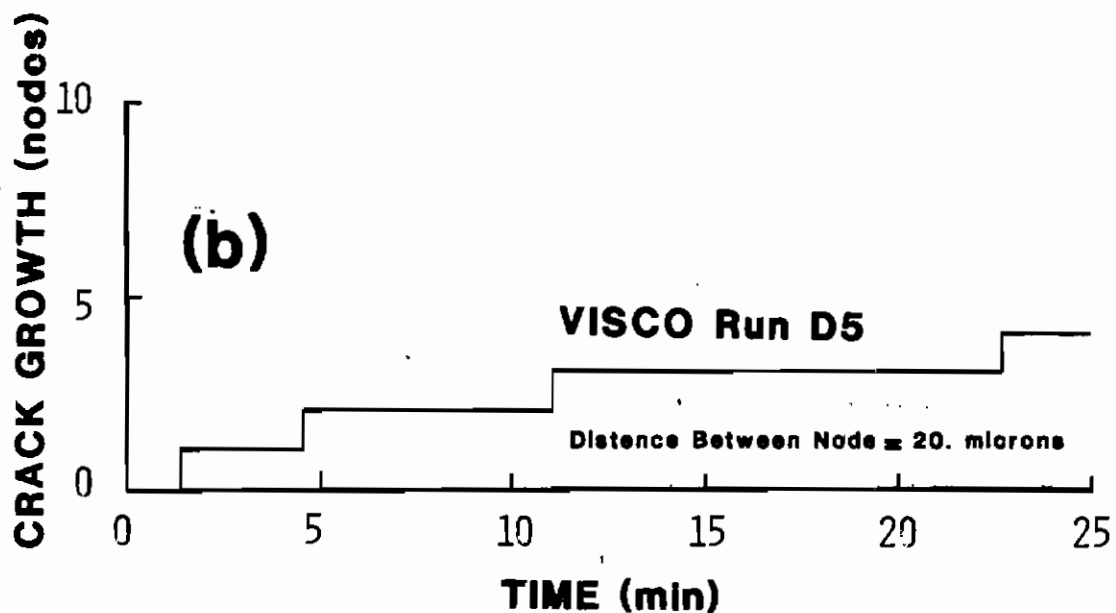


Figure 57b. Test 12a - VISCO Critical Damage Accumulation Criterion Crack Growth Results

AFWAL-TR-80-4140

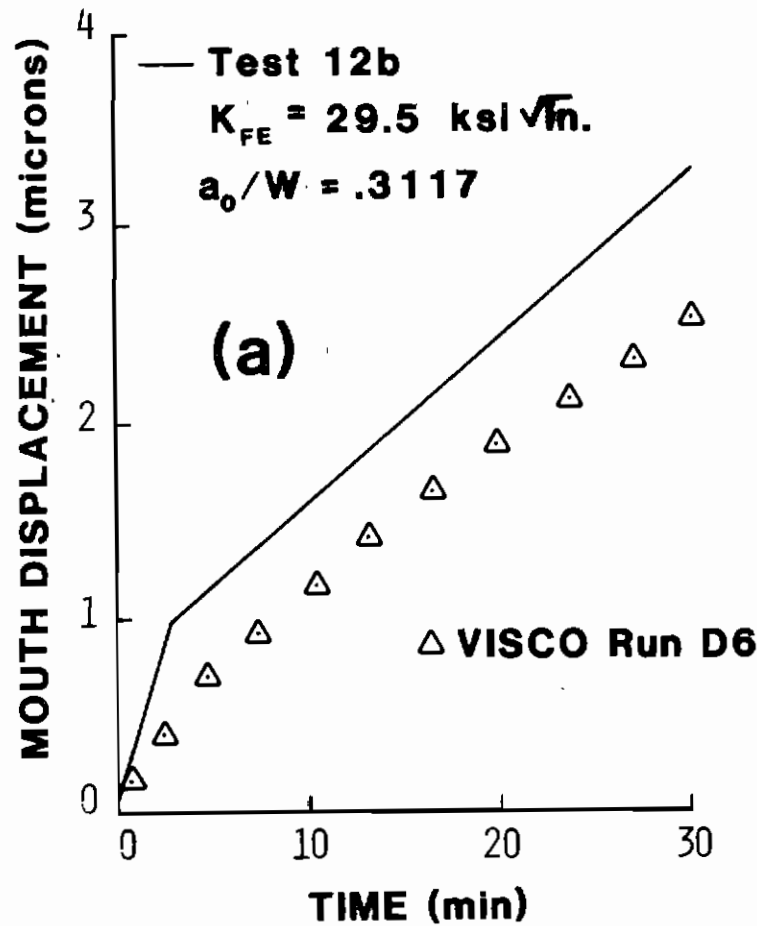


Figure 58a. Test 12b - VISCO Critical Damage Accumulation Criterion Displacement Results

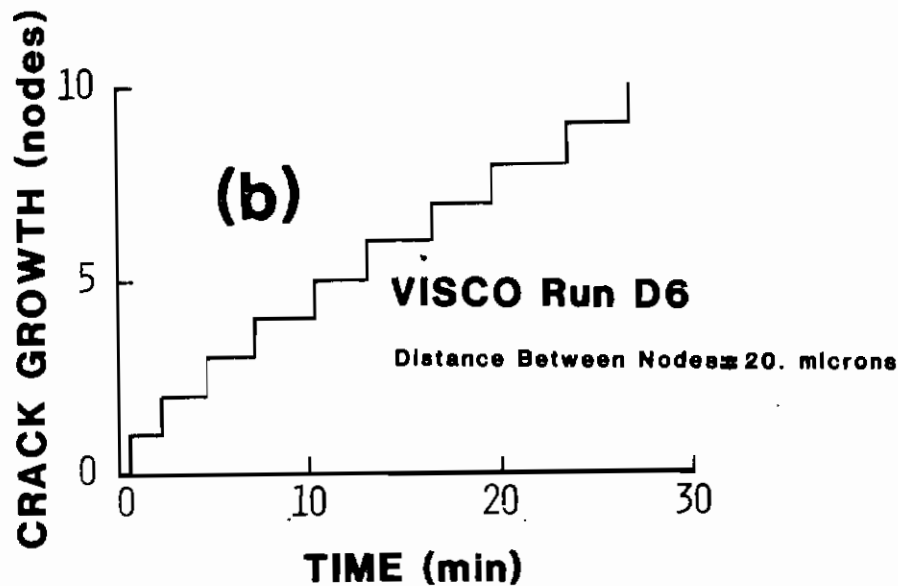


Figure 58b. Test 12b - VISCO Critical Damage Accumulation Criterion Crack Growth Results

AFWAL-TR-80-4140

The steady state crack growth rates were determined by best fitting a straight line to the crack growth curves in Figures 37b through 42b. The initial transient portion of these crack growth curves was ignored for these steady state values. Also a discussion of the merits of the  $\dot{C}$  integral as a crack growth rate criterion will be given.

a. Stress Intensity Factor Criterion

Crack growth rate,  $\dot{a}$ , has previously been found to correlate with the elastic stress intensity factor as given in Equation 2 and recalled here

$$\dot{a} = A (K)^\alpha \quad (66)$$

This relationship plots as a straight line on log-log paper, as shown in Figure 59. The experimental data referred to in Figure 59 was for IN-100 behavior at 1350°F which is the same alloy and temperature used in the present investigation. Note that Donat's experimental data (Reference 76) covered a range in K values from 30 to approximately 80 ksi inches. In order to compare with the lower K levels in the current investigation, the line representing the best fit to Donat's data was extrapolated as shown by the dashed line in Figure 59. Agreement with the present HEN VISCO results, in which  $K_{FE}$  is taken from Table 5 and  $\dot{a}$  from Figures 37b through 42b is good especially considering the fact that the test data line was extrapolated.

This criterion has the distinct advantage relative to criteria presented earlier that once the constants A and  $\alpha$  are determined, it can be used independent of finite element analyses. This advantage is due to the fact that K can be calculated for most test geometries by relatively simple equations like Equation 56. Thus the so-called steady state creep crack growth rate can be simply calculated from Equation 66, but it should be kept in mind that incubation time for crack initiation nor the initial rapid crack growth observed in the HEN VISCO results is captured with this criterion.

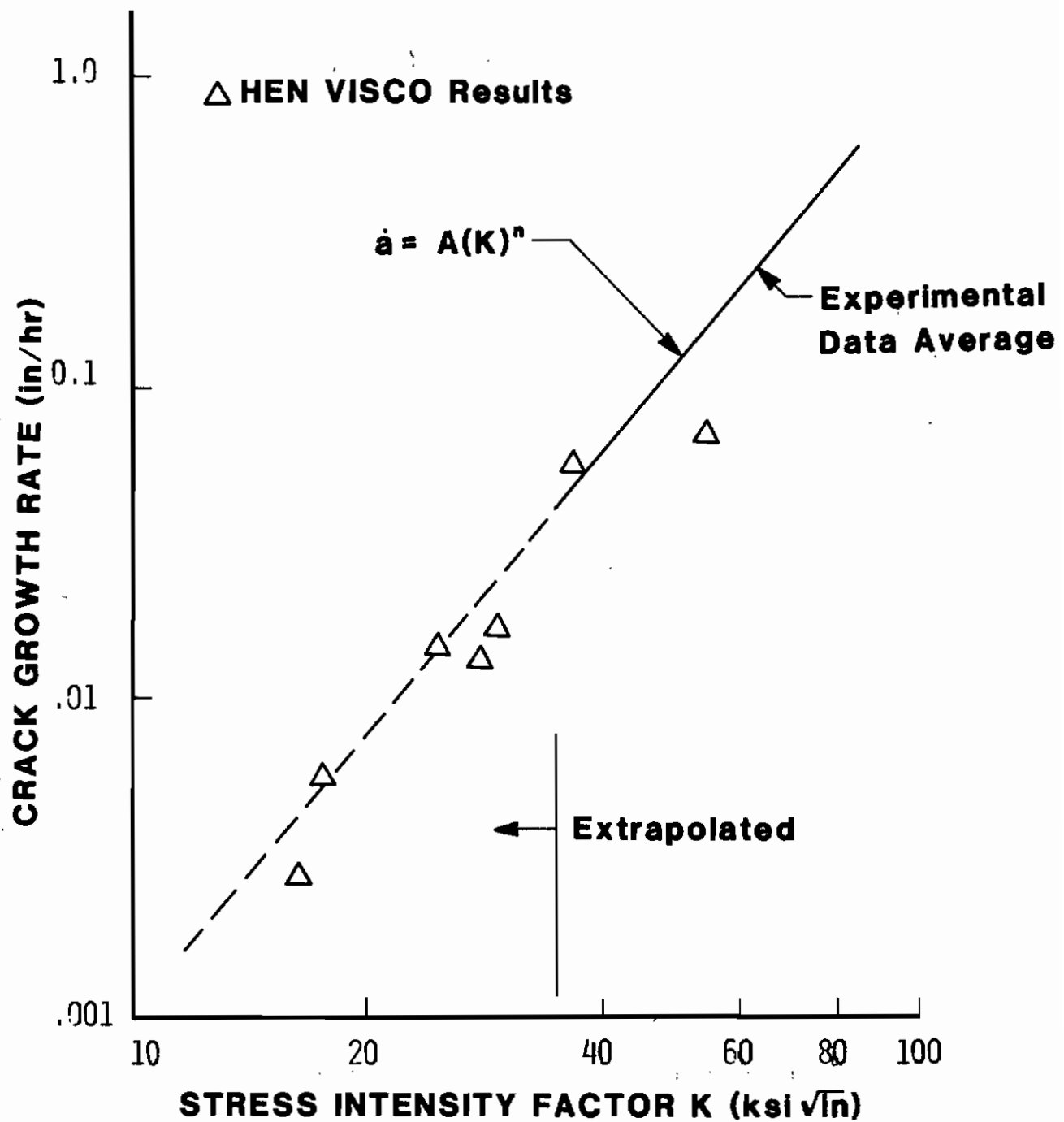


Figure 59. Crack Growth Rate vs. Stress Intensity Factor

AFWAL-TR-80-4140

b. Net Section Stress Criterion

Crack growth rates have also been shown to be related to net section stress as given in Equation 3 and recalled here

$$\dot{a} = B(\sigma_n)^\beta \quad (67)$$

Figure 60 shows how Equation 66 also plots as a straight line (the dashed line) on log-log paper. The present results seem to correlate to Equation 67 as well as they did to Equation 65 on log-log paper. This is not surprising since for the center cracked plate it can be shown that  $K$  is approximately directly proportional to  $\sigma_n$  for crack lengths of  $a/W$  from .2 to .7 which spans the crack lengths in the current study. The net section stress criterion, like the  $K$  criterion, also neglects crack growth characteristics.

c.  $C^*$  Integral Criterion

The  $C^*$  integral is an extension of the  $J$  integral concept for application to creep crack growth (a detailed discussion of  $C^*$  is given in Appendix C). Theoretically the  $C^*$  integral is path independent for a creeping solid where stress is only a function of the plastic strain rate and elastic strain rates do not enter into the formulation. In the present research,  $C^*$  was calculated as shown in Appendix C. In this calculation total strain rates were attributed to creeping plastic strain rates which implies no elastic strain rates exist. For a realistic material that includes elastic behavior, if the elastic strain rates are zero then the stress state is constant with time, and therefore, the creeping plastic strains, since they are a function of stress must also be constant. Accordingly, with constant stress and strain rate the  $W^*$  integral was integrated directly in Appendix C.

The previous description for calculating  $C^*$  in VISCO was implemented and applied to a realistic elastic-viscoplastic material (i.e., IN-100) being studied herein. It was observed that during load application the  $C^*$  values were extremely high due to the elastic strain rate contribution.



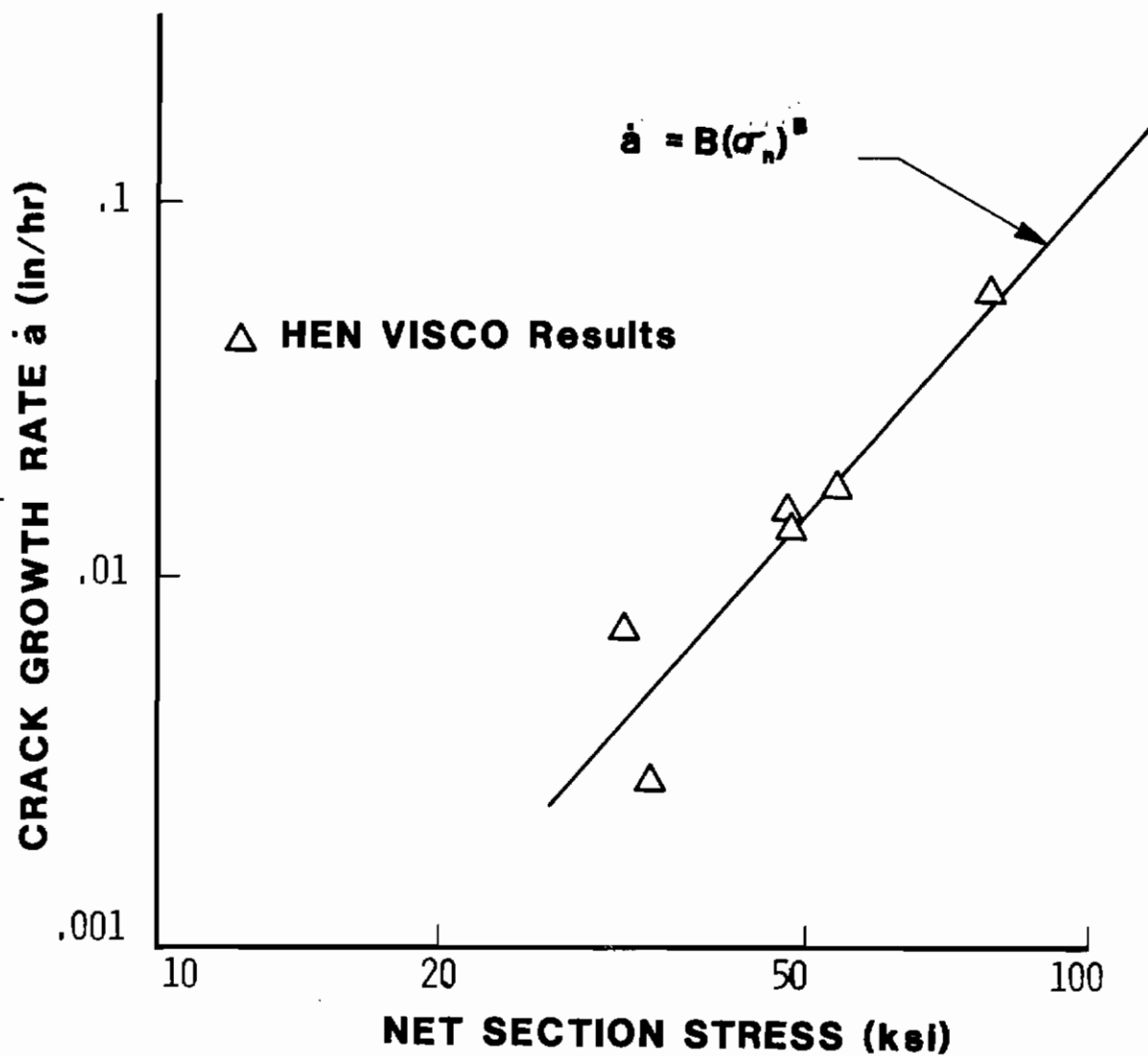


Figure 60. Crack Growth Rate vs. Net Section Stress

After maximum load was achieved  $C^*$  values reduced down to much lower steady state values until crack growth began in the HEN VISCO runs. Again as crack growth began, the  $C^*$  values increased significantly due to the elastic strain rate contribution as stress was redistributing around the moving crack tip. It should be noted that any attempt to remove elastic contributions to strain and displacements will result in an ill-posed problem since the displacement rate components needed in Equation 7 cannot be resolved into an elastic and plastic portion.

Thus far evaluation of the  $C^*$  integral given in Equation 7, the elastic part of the strain rate is neglected, otherwise the integral has no meaning. But when the elastic strain rates are ignored,  $C^*$  should only be calculated after the stresses are fairly constant and prior to crack initiation,  $C^*$  will then be a constant until the crack begins to grow. Therefore, it is impossible to relate  $C^*$  to any incubation time for crack growth. Moreover, during crack growth the contribution from elastic strain rates is again substantial and cannot be ignored. Thus, it appears that the  $C^*$  integral is ineffective as a fracture criterion in a finite element model for creep crack growth in the current investigation.

#### d. Load Point Displacement Rate Criterion

An expression relating crack growth rates to load point displacement rate was given in Equation 4. Unfortunately this criterion suffers from problems similar to the  $C^*$  integral. The load point displacement rate after reaching maximum load is the sum of the displacement rate due to crack growth as well as the displacement rate due to plastic deformation. Hence the load point displacement rate may have several values for the same crack growth rate depending on the rate of plastic deformation such as demonstrated in Equation 59. One can get an appreciation of how much plastic deformation contributes to the overall displacements by looking at the no-crack-growth displacements versus time in Figures 37a through 42a which are totally a result of plastic deformation. Therefore the load displacement rate does not provide a unique solution to the crack growth rate unless variations in the plastic deformation rate can be neglected.

## SECTION VI

## SUMMARY AND CONCLUSIONS

A two-dimensional (plane stress/plane strain) finite element program has been developed which accounts for both nonlinear viscoplastic material behavior and changing boundary conditions due to crack growth. Three viscoplastic material models: (1) Malvern Flow Law, (2) Norton's Creep Law, and (3) Bodner-Partom Flow Law were incorporated into the program. These time dependent material models were numerically integrated through time by a linear Euler extrapolation technique. A variable time step algorithm was included that maximized time step size during the analysis while maintaining good accuracy. This program was used as the plane stress theoretical model for the hybrid experimental-numerical procedure employed to analyze sustained load creep crack growth test data. The test specimens were center cracked plates made of IN-100 and tested at 1350°F.

The following statements and conclusions are based on the creep crack growth analysis herein.

1. A method for getting crack growth behavior solely from displacement measurements in conjunction with a cracked specimen model which utilizes realistic constitutive relationships has been developed. The constitutive law was especially tailored to the nickel-base alloy studied which displays time dependent nonlinear inelastic behavior at elevated temperatures. It has been demonstrated that the technique can be applied where crack extension is very small and could not otherwise be resolved by conventional experimental crack measuring techniques (e.g., compliance techniques or using a travelling microscope). This method provides realistic monotonically increasing crack growth values with resolution better than 0.001 inch. Crack growth predictions agreed to within 10% of post-test measurements.

2. Numerical procedures were developed to efficiently integrate the nonlinear time dependent material models and simulate crack growth by two crack tip node unloading methods. The numerical time integration procedure utilized an Euler linear extrapolation technique with a variable time step algorithm that maximized time step size during the simulation while maintaining good accuracy. One crack tip node unload method diminished the restraining force on the finite element crack tip node in a specified five-second time period independent of crack growth rate whereas the second method continuously unloaded crack tip nodes in proportion to a predetermined crack growth rate. Unloading the nodes continuously provided a closer fit to displacement versus time test data however the average displacement versus time was approximately the same for both node unloading methods.
3. A procedure was developed for determining crack extension using calculations of viscoplastic deformation with no crack growth. In this procedure, the difference between total test deformation and viscoplastic deformation is attributed to crack extension. Extremely good crack growth predictions were made.
4. The elastic compliance method for resolving creep crack extension has been shown to imply negative unrealistic crack growth and is unreliable especially during the first part of a creep crack growth test.
5. Several parameters were studied for their potential as creep crack growth controlling parameters.
  - a. No single fixed value of strain for a critical strain crack growth criterion was found to match all test conditions in this investigation. Environmental effects apparently tend to lower the critical strain magnitude with time, under load. An empirical relationship was developed, based on the HEN results, which gives the critical strain a diminishing value with time.

This investigation did not include any plane strain analyses. Due to higher constraint at the crack tip for plane strain, less stress redistribution would occur. Therefore, it seems possible that the critical strain for all test conditions may vary less in a plane strain simulation.

- b. No single fixed value for C.O.D. was found to match all test conditions using a critical C.O.D. crack growth criterion. The C.O.D. behaved similar to the crack tip strain with time, however, its percent variation was less.
  - c. A critical damage accumulation criterion for crack growth was developed based on a modification of the life fraction rule for creep rupture to account for environmental effects at the crack tip. Application of this criterion provided good agreement with the low to medium load test conditions. For the highest load test cases, this criterion predicted crack growth rates somewhat lower than the HEN results. It appears that accumulation of damage over all time and not just crack tip exposure time might improve the results.
6. Data obtained in this investigation through numerical calculations provided crack growth versus time and thus crack growth rate time,  $\dot{a}$ . The  $\dot{a}$  data compared well with published data for the same material and temperature when plotted against stress intensity factor. The present data was obtained for  $\dot{a}$  and K values lower than the referenced data. Net section stress also provided good correlation with the predicted crack growth rates.
7. The  $C^*$  integral and load line displacement rate were investigated as possible parameters controlling crack growth rate,  $\dot{a}$ . The  $C^*$  integral is an unreliable parameter for predicting creep crack growth due to its formulation which is based on a creeping solid behavior that neglects elastic strain rates. The load line displacement rate which can be shown to be proportional to  $C^*$  also

AFWAL-TR-80-4140

does not provide a unique solution for the crack growth rate unless variations in plastic deformation rate can be ignored. In general these parameters appear to have no applicability to crack growth rate prediction using numerical modeling of materials. However these parameters seem to correlate with data fairly well once the solution is known as seen in the literature.

8. Constant strain triangular finite elements of the size of grains at the crack tip work well for resolving small increments of creep crack growth through the method developed herein.
9. VISCO results using the Bodner-Partom material model were very similar to the VISCO results incorporating the Malvern-Norton superposition model for the center cracked plate, especially for times greater than 200 seconds after load application. Also for times greater than 200 seconds, Norton's law alone in VISCO was very similar to VISCO results using the Bodner-Parton material model.
10. Displacements and the associated crack growth were found to be significantly dependent on prior deformation history. Prior deformation history became very important in the case of Test 8 where no fatigue precracking was done between creep crack growth tests.

The above advancements in the understanding of creep crack growth behavior at elevated temperature are especially suited for aiding future slow crack growth tests for determining the threshold load levels for creep crack growth. In addition the crack growth criteria investigations provide significant progress towards life prediction of actual turbine disks.



AFWAL-TR-80-4140

The following additional research work is recommended to further the life prediction capability developed in the present work.

1. Use present approach to analyze other test specimen geometries (e.g., compact tension specimen) to determine dependence/independence of results on specimen geometry and also assess repeatability and material data scatter.

2. As computers become faster and more efficient finite element techniques are developed, a three-dimensional analysis of creep crack growth should be accomplished to correctly model through the thickness variations in test specimen behavior. As a first step in this direction, plane strain analyses similar to the present work might provide additional insight into creep crack growth behavior.

3. Future work needs to include cyclic or engine spectrum loading conditions.

4. Additional material characterization test data is needed in general for IN-100. Tests providing this data should be done at several temperatures such that the constitutive model could be further developed and include temperature dependence.

5. Environmental effects should be further researched by performing creep crack growth testing in several different environments such as vacuum, inert, salt spray, high sulfur content, variable oxygen partial pressures, etc.

In summary the technique developed herein is worth exploring further in that it has potential for providing information on crack growth rate behavior in engine materials under typical operating conditions which might not be readily obtained using conventional techniques. This information in turn, is necessary in order to implement a retirement for cause philosophy for U.S. Air Force jet engine components.

## REFERENCES

1. "Aircraft Structural Integrity Programs, Airplane Requirements," Military Standard MIL STD-1530-A, (11), (USAF), 11 December 1975.
2. "Airplane Damage Tolerance Requirements," Military Specification MIL-A-83444, (USAF), 2 July 1974.
3. T. Nicholas and J.M. Larsen, "Life Prediction for Turbine Engine Components," presented at 27th Sagamore Army Materials Research Conference, Bolton Landing, N.Y., July 1980; to be published in Conference Proceedings: Fatigue-Environment and Temperature Effects.
4. R.J. Hill, "Report with Recommendations on Turbine Engine Component Fatigue Life Prediction," Air Force Materials Laboratory, Wright-Patterson Air Force Base, December, 1974.
5. M.O. Speidel, "Fatigue Crack Growth at High Temperatures," High Temperature Materials in Gas Turbines, edited by P.R. Sahm and M.O. Speidel, ELSVIER Scientific Publishing Company, New York, 1974.
6. M. Newman, F. Zaphir, and S.R. Bodner, "Finite Element Analysis for Time Dependent Inelastic Material Behavior," Computers and Structures, Vol. 6, 157-162, 1975.
7. A. Merzer and S.R. Bodner, "Analytical Formulation of a Rate and Temperature Dependent Stress Strain Relation," Journal of Engineering Materials and Technology, ASME, July 1979.
8. S.R. Bodner, Representation of Time Dependent Mechanical Behavior of RENE'95 by Constitutive Equations, AFML-TR-79-4116, Wright-Patterson Air Force Base, August 1979.
9. S.R. Bodner and Y. Partom, "Constitutive Equations for Elastic-Viscoplastic Strain Hardening Materials," Journal of Applied Mechanics, Trans. ASME, 42, 385-389, 1975.
10. O.C. Zienkiewicz and I.C. Cormeau, "Visco-Plasticity-Plasticity and Creep in Elastic Solids-A Unified Numerical Solution Approach," International Journal for Numerical Methods in Engineering, Vol. 8, 821-845, 1974.
11. H. Armen, "Assumptions, Models, and Computational Methods for Plasticity," Computers and Structures, Vol. 10, 161-174, 1978.
12. D.C. Stouffer, A Relationship Between Theory and Experiment for a State Variable Constitutive Equation, AFWAL-TR-80-4194, Wright-Patterson Air Force Base, January 1981.
13. D.L. Sims, C.G. Annis Jr., and R. Wallace, Application of Fracture Mechanics at Elevated Temperatures, AFML-TR-76-176 Part 11, Wright-Patterson Air Force Base, 1977.



## REFERENCES (Continued)

14. Alan Jennings, Matrix Computation for Engineers, Chapter 6, pp. 182-188, John Wiley and Sons, New York, 1977.
15. W.N. Sharpe Jr., Unpublished Data on USAF Contract F33615-77-C-5003, Wright-Patterson Air Force Base, Ohio, 1979.
16. A.S. Kobayashi, "Current and Future Experimental Methods," Fracture Mechanics, Edited by N. Perrone, H. Liebowitz, D. Mulville, W. Pilkey, Symposium on Naval Structural Mechanics, 10th, Washington, 1978.
17. W.G. Knauss, "On the Steady Propagation of a Crack in a Visco-elastic Sheet: Experiments and Analysis," Deformation and Fracture of High Polymers, Edited by H. Henning Kaasch, John A. Hassell, and Robert I. Jaffee, Plenum Press, 501-541, 1974.
18. R.A. Schapery, "A Theory of Crack Initiation and Growth in Visco-elastic Media, I. Theoretical Development," International Journal of Fracture, Vol. 11, No. 1, February, 1975.
19. R.A. Schapery, "A Theory of Crack Initiation and Growth in Visco-elastic Media, II. Approximate Methods of Analysis," International Journal of Fracture, Vol. 11, No. 3, June 1975.
20. R.A. Schapery, "A Theory of Crack Initiation and Growth in Visco-elastic Media, III. Analysis of Continuous Growth," International Journal of Fracture, Vol. 11, No. 4, August 1975.
21. M.P. Wnuk, "Quasi-Static Extension of a Tensile Crack Contained in a Viscoelastic-Plastic Solid," Journal of Applied Mechanics, 234-242, March 1974.
22. L.S. Fu, Quasi-Static Crack Growth in Metals at Elevated Temperature-A Review, Air Force Materials Laboratory Technical Report, AFML-TR-78-136, Wright-Patterson Air Force Base, 1978.
23. J.D. Landes and J.A. Begley, "A Fracture Mechanic's Approach to Creep Crack Growth," ASTM STP 590, 128-148, 1976.
24. H.P. Van Leeuwen, "The Application of Fracture Mechanics to Creep Crack Growth," Engineering Fracture Mechanics, Vol. 9, 951-974, 1977.
25. K. Sadananda and P. Shahinian, "Application of Fracture Mechanics Techniques to High-Temperature Crack Growth," Fracture Mechanics, Edited by N. Perrone, H. Liebowitz, D. Mulville, W. Pilkey, Symposium on Naval Structural Mechanics, 10th, Washington, 1978.
26. S. Floreen, "The Creep Fracture of Wrought Nickel-Base Alloys by a Fracture Mechanic's Approach," Metall. Trans. A 6A 1741-1749, 1975.

## REFERENCES (Continued)

27. R.D. Nicholson and C.L. Formby, "The Validity of Various Fracture Mechanics Methods at Creep Temperatures," Int. Journ. Fract., 11, 595-604, 1975.
28. D.J.F. Ewing, "Strip Yield Models of Creep Crack Incubation and Growth," Int. Journ. Fract., Vol. 14, No. 1, 101-117, February 1978.
29. R. Koterazawa and T. Mori, "Applicability of Fracture Mechanics Parameters to Crack Propagation Under Creep Conditions," Journal of Engineering Materials and Technology, Vol. 99, Series H, No. 4, October 1977.
30. A. Hrenikoff, "Solution of Problems in Elasticity by the Framework Method," Journal of Applied Mechanics, AB, 169-175, 1941.
31. O.C. Zienkiewicz, The Finite Element Method, 3rd Edition, McGraw-Hill, 1977.
32. J.C. Newman Jr., "Finite-Element Analysis of Crack Growth Under Monotonic and Cyclic Loading," Cyclic Stress-Strain and Plastic Deformation Aspects of Fatigue Crack Growth, ASTM STP 637, 56-80, 1977.
33. K.J. Miller and A.P. Kfoury, "An Elastic-Plastic Finite Element Analysis of Crack Tip Fields Under Biaxial Loading Conditions," Intl. Journ. of Fract., Vol. 10, No. 3, September 1974.
34. G.C. Nayak and O.C. Zienkiewicz, "Elasto-Plastic Stress Analysis. A Generalization for Various Constitutive Relations Including Strain Softening," Int. Journ. for Numerical Methods in Engineering, Vol. 5, 113-135, 1972.
35. J.D. Lee and H. Liebowitz, "Considerations of Crack Growth and Plasticity in Finite Element Analysis," Computers and Structures, Vol. 8, 403-410, 1978.
36. H. Anderson, "Finite Element Methods Applied to Problems of Moving Cracks," Computational Fracture Mechanics, ASME, E.F. Rybicki and S.E. Benzley, editors, 1975.
37. J.L. Swedlow, "Crack Tip Finite Element Analyses," Fracture Mechanics, edited by N. Perrone, H. Liebowitz, D. Mulville, W. Pilkey, Symposium On Naval Structural Mechanics, 10th, Washington, 1978.
38. A.R. Luxmore, M.F. Light, and W.T. Evans, "A Comparison of Finite-Element and Experimental Studies on Plane Stress Crack Geometries," Journ. of Strain Analysis, Vol. 12, No. 3, 1977.

## REFERENCES (Continued)

39. S.G. Larsson and G. Harkegard, "On the Finite Element Analysis of Crack and Inclusion Problems in Elastic-Plastic Materials," Computers and Structures, Vol. 4, 293-305, 1974.
40. Y. Yamada, N. Yoshimura, and T. Sakurai, "Plastic Stress-Strain Matrix and Its Application for the Solution of Elastic-Plastic Problems by the Finite Element Method," Int'l Journ. of Mechanical Sciences, Vol. 10, 343-354, 1968.
41. W.S. Blackburn, A.D. Jackson, and T.K. Helen, "An Integral Associated with the State of a Crack Tip in a Non-Elastic Material," Int'l Journ. of Fract., Vol. 13, No. 2, April 1977.
42. C.F. Shih, H.G. DeLorenzi, and W.R. Andrews, "Studies on Crack Initiation and Stable Crack Growth," Report No. 78CRD129, General Electric Co., Corp. Research and Development, Schenectady, N.Y., June 1978.
43. A.S. Kobayashi, S.T. Chiu, and R. Beeuwkes, "A Numerical and Experimental Investigation on the Use of the J Integral," Engineering Fracture Mechanics, Vol. 5, No. 2, 1973.
44. O.C. Zienkiewicz, S. Vallipian, and I.P. King, "Elasto-Plastic Solutions of Engineering Problems, "Initial Stress" Finite Element Approach," Int'l Journ for Numerical Methods in Engineering, Vol. 1, 75-100, 1969
45. P.V. Marcal, "A Comparative Study of Numerical Methods of Elastic-Plastic Analysis," A.I.A.A. Tech Note, 157-158, January 1968.
46. J.C. Nagtegaal, D.M. Parks, and J.R. Rice, Comp. Meth. Appl. Mech. Engr., Vol. 4, 153-177, 1974.
47. R.D. Henshell and R.D. Shaw, "Crack Tip Finite Elements Are Unnecessary," Int'l Journ. for Numerical Methods in Engineering, Vol. 9, 495-507, 1975.
48. J.W. Hutchinson, "Plastic Stress and Strain Fields at a Crack Tip," J. Mech. Phys. Solids, Vol. 16, 1968.
49. P.P. Hilton and J.W. Hutchinson, "Plastic Intensity Factors for Cracked Plates," Engr. Fract. Mech., Vol. 3, No. 4, Dec 1971.
50. W.E. Haisler and D.R. Sanders, "Elastic-Plastic Creep Large Strain Analysis at Elevated Temperature by the Finite Element Method," Computers and Structures, Vol. 10, 375-380.
51. O.C. Zienkiewicz, M. Watson, and I.P. King, "A Numerical Method of Viscoelastic Stress Analysis," Int'l Journ of Mechanical Sciences, 1968.

## REFERENCES (Continued)

52. O.C. Zienkiewicz and I.C. Corneau, "Visco-Plasticity Solution by Finite Element Process," Archives of Mechanics, 24, 5-6, 873-888, 1972.
53. M. Kawahara, "Large Strain, Viscoelastic, and Elasto-Viscoplastic Numerical Analysis by Means of the Finite Element Method," Archives of Mechanics, 27, 3, 417-443, 1975.
54. P. Sharifi and D.N. Yates, "Nonlinear Thermo-Elastic-Plastic and Creep Analysis by the Finite Element Method," AIAA Journal, Vol. 12, No. 9, 1210-1215, 1974.
55. Z. Zudans, M.M. Reddi, H.M. Fishman, and H.C. Tsai, "Elastic-Plastic Creep Analysis of High Temperature Nuclear Reactor Components," Nuclear Engineering and Design, 28, 414-445, 1974.
56. S. Narajan and E.P. Popov, "Nonlinear Elastic-Viscoplastic Analysis Using the Finite Element Method," The Texas Inst. for Computational Mechanics, 979-988, 1974.
57. MARC-CDC Demonstration Problems Manual, Publication No. 17311700, Revision H, Vol. III, Control Data Corp., Minneapolis, Minn., September 1976.
58. B.V. Winkel, K.H. Gerstle and H.Y. Ko, "Analysis of Time-Dependent Deformations of Openings in Salt Media," Int'l Journ. of Rock Mech. Min. Science, Vol. 9, 249-260, 1972.
59. J.H. Arggris and K.J. William, "Finite Element Modelling of Inelastic Behavior," Mechanics in Engineering, ASCE-EMD, May 26-28, 1976, Univ. of Waterloo Press, 1977.
60. L.M.S. Dinis and R.R.S. Owen, "Elastic-Viscoplastic Analysis of Plates by the Finite Element Method," Computers and Structures, Vol. 8, 207-215, 1977.
61. R. Ohtani and S. Nakamura, "Crack Propagation in Creep (Finite Element Analysis)," Journal of the Society of Materials Science, Japan, Vol. 25, No. 275, August 1976.
62. I.W. Goodall and E.J. Chubb, "The Creep Ductile Response of Cracked Structures," Int'l Journ. of Fracture, Vol. 12, No. 2, April 1976.
63. Z. Zaphir and S.R. Bodner, "Implementation of Elastic-Viscoplastic Constitutive Equations into "NONSAP" with Applications to Fracture Mechanics", Nonlinear Finite Element Analysis and ADINA, Proceedings of the ADINA Conference, K. Bathe editor, Mass. Inst. Tech., August, 1979.
64. A. Mendelson, "Plasticity: Theory and Application," Collier-Macmillan Limited, London, England, 1968.

## REFERENCES (Continued)

65. I. Cormeau, "Numerical Stability in Quasi-Static Elasto Visco-Plasticity," Int'l Journ. for Numerical Methods in Engineering, Vol. 9, 109-127, 1975.
66. L.E. Malvern, "The Propagation of Longitudinal Waves of Plastic Deformation in a Bar of Material Exhibiting a Strain-Rate Effect," J. Appl. Mech. 18, 203-208, 1951.
67. Piotr Perzyna, "Fundamental Problems in Viscoplasticity," Advances in Applied Mechanics, Vol. 9, Academic Press, New York, 1966.
68. J.A.H. Hult, Creep in Engineering Structures, Blaisdell Publishing Co., Waltham, Mass., 1965.
69. J.D. Lubahn and R.P. Felgar, Plasticity and Creep of Metals, John Wiley & Sons, Inc., New York, 417-437, 1961.
70. Y.C. Hsu and R.G. Forman, "Elastic-Plastic Analysis of an Infinite Sheet Having a Circular Hole Under Pressure," Journ. of Applied Mechanics, ASME, June 1975.
71. P.G. Hodge Jr., and G.N. White Jr., "A Quantitative Comparison of Flow and Deformation Theories of Plasticity," J. Appl. Mech., 17, 180-184, 1950.
72. W.K. Wilson and J.R. Osias, "A Comparison of Finite Element Solutions for an Elastic-Plastic Crack Problem," Int'l Journ. of Fracture, 14, R95-R108, 1978.
73. H. Tada, The Stress Analysis of Cracks Handbook, Del Research Corporation, Hellertown, Pennsylvania, 1973.
74. W.N. Sharpe Jr. and D.R. Martin, "Optical Measurement of In-Plane Strain/Displacement Near Crack Tips at High Temperature," Sixth Int'l Congress on Experimental Stress Analysis, Munich, 1978.
75. G. Clarke, W.R. Andrews, P.C. Paris, and D.W. Schmidt, in Mechanics of Crack Growth, ASTM STP 590, American Society for Testing and Materials, 27-42, 1976.
76. R.C. Donat, Crack Growth Behavior of Alloy IN-100 Under Sustained Load at 732°C (1350°F), AFWAL-TR-80-4131, Wright-Patterson Air Force Base, February 1981.
77. T. Hinnerichs and A. Palazotto, "Overstress Versus Continuous Functional Stress-Strain Formulation for Viscoplasticity as Applied to a Cracked Geometry," accepted for presentation ASCE Hollywood-by-the-Sea, Florida, October 27-31, 1980.
78. S.N. Atluri and M. Nakagaki, A.I.A.A. Journal, Vol. 15, No. 7, 923-931, 1977.



## REFERENCES (Concluded)

79. J. Eftis and H. Liebowitz, Int'l Journ. of Fract. Mech., Vol. 8, No. 4, December 1972.
80. Y.C. Fung, Foundations of Solid Mechanics, Prentice-Hall, Inc., Englewood Cliffs, N.J., 1965.
81. D. Brock, Elementary Engineering Fracture Mechanics, Sijhoff & Noordhoff.
82. T.R. Hsu, R. Lewak, and B.J.S. Wilkins, "Measurements of Crack Growth in a Solid at Elevated Temperature by Holographic Interferometry," Experimental Mechanics, 297-302, August 1978.
83. J.C. Newman Jr., "Finite Element Analysis of Fatigue Crack Propagation-Including the Effects of Crack Closure," PhD. Dissertation, Dept. of Engineering Mechanics, Virginia Polytechnic Inst. 1974.
84. R.G. Belie and J.N. Reddy, "Direct Prediction of Fracture for Two Dimensional Plane Stress Structures," Computers & Structures, Vol. 11, 49-53, 1980.
85. R. Ohtani and A. Nitta, "Crack Propagation in Creep (Experimental Results on Crack Propagation Rates)," Journal of the Society of Materials Science, Japan, Vol. 25, No. 275.
86. P. Shahinian and K. Sadananda, "Creep-Fatigue - Environment Interactions on Crack Propagation in Alloy 718", in Engineering Aspects of Creep, Vol. 2, Institution of Mechanical Engineers, 1980.
87. E.L. Wilson, R.W. Clough, and "WILSON", A Finite Element Analysis Program of Two-Dimensional Structures, Univ. of California, Berkeley, June, 1963.

## APPENDIX A

### FINITE ELEMENT FORMULATION

In the following sections the basic concepts and equations used in the finite-element analysis of elastic and elastic-plastic materials are briefly reviewed. These equations provide background for the elastic-viscoplastic nonlinear finite-element computer program development.

The basic philosophy of the finite-element method (Reference 31) is that an approximate solution to a complicated problem can be obtained by subdividing the region of interest into a finite number of discrete elements and then choosing appropriate relatively simple functions to represent the solution within each element. These functions are simple compared to the so-called "exact" solutions which account for the entire region of interest. In this section the equations associated with representing a two-dimensional body as a finite number of elements are presented. The displacements in each element were expressed as a simple polynomial and the equations relating displacements to applied loading for both plane-stress and plane-strain conditions are given.

#### 1. DISPLACEMENT MODEL

The displacement function used in the displacement formulation is generally selected as a polynomial. The polynomial expression allows for simple differentiation and integration. Also, as the element size becomes small, the polynomial expression permits a simple approximation to the exact solution. A polynomial of infinite order corresponds to an exact solution. However, for practical purposes the polynomial must be truncated to a finite number of terms. Thus, the number of elements in a structure must be large enough so that the displacement function for each element closely approximates the exact displacements in that particular region.

In any numerical method, the solution should converge to the exact solution as the size of the elements become small. For the displacement

formulation, it has been shown that under certain conditions the solution provides a lower bound to the exact displacements (Reference 31). To assure this convergence certain conditions must be satisfied. First, the displacement function must be chosen so that rigid body displacements do not cause straining of the element. Second, the function must also be chosen so that a constant state of strain is obtained as the element size approaches zero. The simplest polynomial function which satisfies these two requirements and also maintains displacement continuity between adjacent elements is the linear-displacement function.

#### a. Displacement Function

Figure A-1 shows a typical triangular element,  $m$ , with nodes  $i$ ,  $j$ ,  $k$  numbered in a counter-clockwise direction. The linear-displacement function which defines the displacements within the element is given by

$$\begin{aligned} U &= \alpha_1 + \alpha_2 X + \alpha_3 Y \\ V &= \alpha_4 + \alpha_5 X + \alpha_6 Y \end{aligned} \quad (A-1)$$

where the constants  $\alpha_i$  are determined from the six nodal displacements and nodal coordinates as

$$\begin{Bmatrix} \alpha_1 \\ \alpha_2 \\ \alpha_3 \end{Bmatrix} = \frac{1}{2A_m} \begin{bmatrix} a_i & a_j & a_k \\ b_i & b_j & b_k \\ c_i & c_j & c_k \end{bmatrix} \begin{Bmatrix} u_i \\ u_j \\ u_k \end{Bmatrix} \quad (A-2)$$

and

$$\begin{Bmatrix} \alpha_4 \\ \alpha_5 \\ \alpha_6 \end{Bmatrix} = \frac{1}{2A_m} \begin{bmatrix} a_i & a_j & a_k \\ b_i & b_j & b_k \\ c_i & c_j & c_k \end{bmatrix} \begin{Bmatrix} v_i \\ v_j \\ v_k \end{Bmatrix} \quad (A-3)$$

where  $A_m$  is the in-plane area of the element. The coefficients  $a_i$ ,  $b_i$ , and  $c_i$  are given by

$$a_i = x_j y_k - x_k y_j \quad (A-4)$$



AFWAL-TR-80-4140

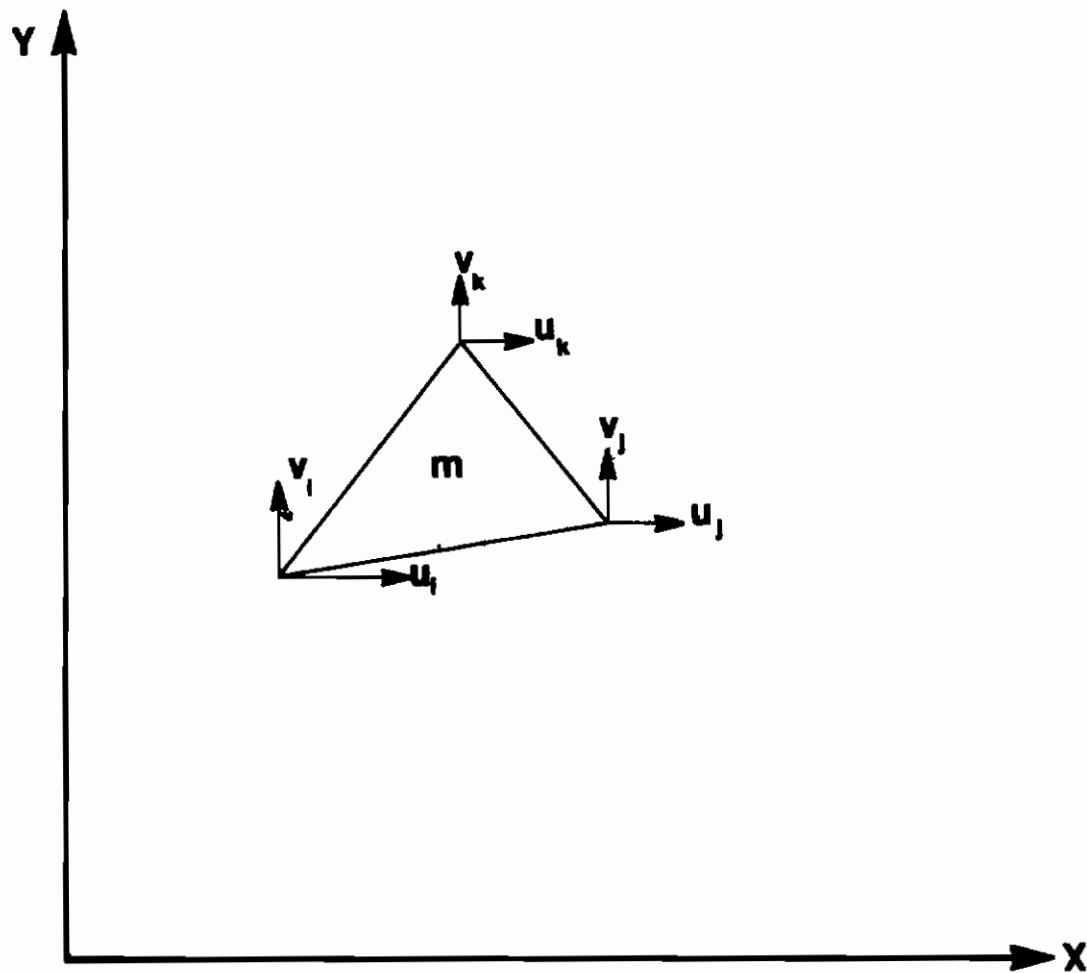


Figure A-1. Constant Strain Triangular Element

$$b_i = y_j - y_k \quad (A-4)$$

$$c_i = x_k - x_j$$

where  $x$  and  $y$  are coordinates of the nodal points. The other coefficients for subscripts "j" and "k" are obtained by cyclic permutation of the subscripts i, j, and k.

#### b. Element Strain

The total strains at any point within an element are defined in terms of the displacement derivatives as

$$\{\epsilon\} = \begin{Bmatrix} \epsilon_x \\ \epsilon_y \\ \gamma_{xy} \end{Bmatrix} = \begin{Bmatrix} \frac{\partial u}{\partial x} \\ \frac{\partial v}{\partial y} \\ \frac{\partial u}{\partial y} + \frac{\partial v}{\partial x} \end{Bmatrix} \quad (A-5)$$

From Equations A-1 to A-5, the total strains are written in terms of nodal displacements and coordinates as

$$\{\epsilon\} = [B] \{U\} \quad (A-6)$$

where  $\{U\}$  is the generalized nodal displacement  $\{U\}^T = \{u_i, v_i, u_j, v_j, u_k, v_k\}$  and

$$[B] = \frac{1}{2A_m} \begin{bmatrix} b_i & 0 & b_j & 0 & b_k & 0 \\ 0 & c_i & 0 & c_j & 0 & c_k \\ c_i & b_i & c_j & b_j & c_k & b_k \end{bmatrix} \quad (A-7)$$

The superscript T denotes the matrix transpose.

## 2. ELASTIC ANALYSIS

For linear elastic and isotropic materials, the relationship between stresses  $\{\sigma\}$ , strains  $\{\epsilon\}$ , initial stresses  $\{\sigma_0\}$  and any initial strains  $\{\epsilon_0\}$  is given by

$$\{\sigma\} = \begin{Bmatrix} \sigma_x \\ \sigma_y \\ \sigma_{xy} \end{Bmatrix} = [D] \{\{\epsilon\} - \{\epsilon_0\}\} + \{\sigma_0\} \quad (A-8)$$

AFWAL-TR-80-4140

where  $[D]$  is the elastic material property matrix. The matrix  $[D]$  for plane-stress conditions where  $\sigma_z = \sigma_{xz} = \sigma_{yz} = 0$  is given by

$$[D] = \frac{E}{1-\nu^2} \begin{bmatrix} 1 & \nu & 0 \\ \nu & 1 & 0 \\ 0 & 0 & \frac{1-\nu}{2} \end{bmatrix} \quad (A-9)$$

where  $E$  and  $\nu$  are the modulus of elasticity and Poisson's ratio, respectively. For plane-strain conditions where  $\epsilon_z = 0$ , the elastic material property matrix is given by

$$[D] = \frac{E(1-\nu)}{(1+\nu)(1-2\nu)} \begin{bmatrix} 1 & \nu/1-\nu & 0 \\ \nu/1-\nu & 1 & 0 \\ 0 & 0 & \frac{1-2\nu}{2(1-\nu)} \end{bmatrix} \quad (A-10)$$

Under plane-strain conditions a normal stress also exists and is given by

$$\sigma_z = \nu (\sigma_x + \sigma_y) \quad (A-11)$$

#### a. Method of Solution

The equation which governs the elastic response of a discretized structure can be derived from the principle of virtual work (Reference 31) and is given by

$$[K] \{U\} = \{P\} + \{Q\} \quad (A-12)$$

where  $[K]$  is the elastic stiffness matrix of the structure,  $\{U\}$  is the generalized displacement vector,  $\{P\}$  is the external applied load vector, and  $\{Q\}$  is the force vector due to the presence of initial stress and/or initial strain.

The coefficients of the elastic stiffness matrix are obtained from

$$[K] = \sum_{m=1}^M \int [B]^T [D] [B] dvol \quad (A-13)$$

where the integration is taken over the volume of each element and the summation is over all elements in the structure. The nodal forces due to initial stresses are given by

$$\{Q\}_{\sigma_0} = \sum_{m=1}^M \int [B]^T \{\sigma_0\} d vol \quad (A-14)$$

and the nodal forces due to initial strains are given by

$$\{Q\}_{\epsilon_0} = \sum_{m=1}^M \int [B]^T [D] \{\epsilon_0\} d vol \quad (A-15)$$

### 3. ELASTIC-PLASTIC ANALYSIS

The application of the finite element method to problems involving materials that obey linear constitutive laws is straightforward because the material properties are constant. Therefore only one solution is required to obtain displacements for the elastic structure. However, for elastic-plastic problems the coefficients in the stiffness matrix vary as a function of loading. Thus, the elastic-plastic displacements are usually obtained by applying small load increments to the structure and updating the coefficients of the stiffness matrix. Another technique called the "residual force" method (Reference 11) avoids modifications of the stiffness matrix by adding on a so-called plastic load vector to the force side of the equilibrium equation (i.e., Equation A-12). Only the residual force method will be discussed herein.

#### a. Yield Criterion

In any elastic-plastic material the elastic formulation can be used prior to plastic yielding. Thereafter it is necessary to have a yield criterion to determine the state of stress at which yielding occurs. The

von Mises yield criterion is one of the most widely used. This criterion assumes yielding is caused by the maximum distortion energy (Reference 64). The yield criterion for plane stress conditions is given by

$$F = F\{\sigma\} = [\sigma_x^2 + \sigma_y^2 - \sigma_x\sigma_y + 3\sigma_{xy}^2]^{\frac{1}{2}} - \bar{\sigma} \quad (A-16)$$

and for plane strain

$$F = F\{\sigma\} = [\sigma_x^2 + \sigma_y^2 + \sigma_z^2 - \sigma_x\sigma_y - \sigma_x\sigma_z - \sigma_y\sigma_z + 3\sigma_{xy}^2]^{\frac{1}{2}} - \bar{\sigma} \quad (A-17)$$

where  $\bar{\sigma}$  is the uniaxial yield stress. If the state of stress is such that  $F < 0$ , the material is still in the elastic range. When  $F = 0$ , a plastic state is obtained and one of the flow theories of plasticity must be employed to determine subsequent plastic behavior under increasing stress or strain.

#### b. Flow Theory

One of the basic assumptions in the theory of plasticity is that the total strain  $\{\epsilon\}$  or total strain increment  $\{d\epsilon\}$  can be decomposed into elastic and plastic strain components as follows:

$$\{\epsilon\} = \{\epsilon^E\} + \{\epsilon^P\} \quad (A-18)$$

or, incrementally,

$$\{d\epsilon\} = \{d\epsilon^E\} + \{d\epsilon^P\} \quad (A-19)$$

In the incremental theory of plasticity the plastic strain increment vector  $\{d\epsilon^P\}$  is a function of the current state of stress and is related to the yield criterion through the Theory of Plastic Potential (Reference 80)

$$\{d\epsilon^P\} = \lambda \left\{ \frac{\partial F}{\partial \{\sigma\}} \right\} \quad (A-20)$$

where  $\lambda$  is a positive scalar quantity. This flow law is also written in terms of strain rate

$$\{\dot{d\epsilon}^P\} = \dot{\lambda} \left\{ \frac{\partial F}{\partial \{\sigma\}} \right\} \quad (A-21)$$

In this case  $\lambda'$  has the significance of the coefficient of viscosity. Equations A-20 and A-21 are also known as Drucker's Normality Principle (Reference 64) which by its name specifies that the plastic-strain increment vector is to be aligned normal to the yield surface in nine-dimensional stress space. When the von Mises yield criterion is used with Equation A-20 the resulting expression for  $\{d\epsilon^P\}$  is identical to that proposed by Prandtl and Reuss (Reference 64). The total strain increment vector can now be written as

$$\{d\epsilon\} = [D]\{d\sigma\} + \lambda \left\{ \frac{\partial F}{\partial \{\sigma\}} \right\} \quad (A-22)$$

where the elastic strain increment vector has been related to the stress increments  $\{d\sigma\}$  through the elasticity matrix. Therefore, if  $\lambda$  was known, then the desired stress-strain relation for an elastic-plastic material would be obtained. When yielding is occurring, the total differential of Equation A-16 or Equation A-17 gives

$$dF = \left\{ \frac{\partial F}{\partial \{\sigma\}} \right\}^T \{d\sigma\} - d\bar{\sigma} = 0 \quad (A-23)$$

The increment in yield stress  $d\bar{\sigma}$  is obtained from a uniaxial tensile test as

$$d\bar{\sigma} = d\sigma^U = \left( \frac{d\sigma^U}{d\epsilon^P} \right) d\epsilon^P = H' d\epsilon^P \quad (A-24)$$

where  $H'$  is the slope of the stress-plastic strain curve,  $d\sigma^U$  is the uniaxial stress increment,  $d\epsilon^P$  is the uniaxial plastic strain increment. Using Equation A-20 for the uniaxial case gives  $d\epsilon^P = \lambda$ . Thus Equation A-23 becomes

$$\left\{ \frac{\partial F}{\partial \{\sigma\}} \right\}^T \{d\sigma\} - H' \lambda = 0 \quad (A-25)$$

AFWAL-TR-80-4140

Eliminating  $\lambda$  from Equations A-22 and A-25 results in an explicit expression relating increments in stress to increments in total strain (Reference 44). This expression is

$$\{d\sigma\} = [D_{EP}] \{d\epsilon\} \quad (A-26)$$

where

$$[D_{EP}] = [D] - [D] \left\{ \frac{\partial F}{\partial \{\sigma\}} \right\} \left\{ \frac{\partial F}{\partial \{\sigma\}} \right\}^T [D] \left[ H' + \left\{ \frac{\partial F}{\partial \{\sigma\}} \right\} [D] \left\{ \frac{\partial F}{\partial \{\sigma\}} \right\} \right]^{-1} \quad (A-27)$$

The matrix  $[D_{EP}]$  is the elastic-plastic matrix which replaces the elasticity matrix  $[D]$  in an incremental analysis. For an elastic-perfectly plastic material,  $H'$  is set equal to zero. In general the slope of the uniaxial stress-plastic strain curve,  $H'$ , varies with plastic strain. Therefore, to relate a multiaxial plastic strain state to a uniaxial experimental stress-plastic strain curve, an effective plastic strain is defined in incremental form as

$$d\epsilon_e^p = \sqrt{\frac{2}{3}} d\epsilon_{ij}^p d\epsilon_{ij}^p \quad (A-28)$$

#### 4. ELASTIC-PLASTIC SOLUTION TECHNIQUES

The procedures used to solve small displacement elastic-plastic problems incrementally within a finite element computer program may be divided into two categories. In one the effects of plasticity are accounted for directly in the stiffness matrix. The second category treats plastic behavior as an additional plastic load that is combined with applied or external loads in the equilibrium equation (i.e. Equation A-12). These two procedures are referred to as the "tangent modulus" and "residual force" methods respectively. Only the residual force method in the form of "initial stress" and "initial strain" will be summarized herein.

## a. Initial Stress Method (Reference 44)

The equation which governs the response of a discretized structure under loads which cause plastic deformation (Reference 31) is

$$[K] \{U\}_I^i = \{P\}^i + \{Q\}_{I-1}^{i-1} \quad (A-29)$$

where  $[K_E]$  is the elastic stiffness matrix,  $\{U\}$  is the generalized displacement vector,  $\{P\}$  is the applied load vector, and  $\{Q\}$  is the "effective" plastic-load vector which accounts for elements in a plastic state. The initial stress method approaches the solution to an elastic plastic problem by applying a series of small load increments to the structure until the desired load is reached ( $\{P\}^i = \{P\}^{i-1} + \{dP\}$ ). The superscript  $i$  denotes the current increment and  $i-1$  denotes the preceding increment. After each load increment an iterative process is required to stabilize the plastic-load vector. The subscript  $I$  denotes the current iteration and  $I-1$  denotes the preceding iteration. During the  $i$ th increment a purely elastic problem is solved and the increments in total strain  $\{d\epsilon\}$  and corresponding elastic stress  $\{d\sigma_E\}$  are computed from the displacement increments  $\{dU\}$  for every element. Because of the material nonlinearity the stress increments are not, in general correct or if the correct stress increment for the corresponding strain increment is  $\{d\sigma\}$ , then a set of body forces or plastic-load vectors  $\{dQ\}$  caused by the "initial" stress  $\{d\sigma_0\} = \{d\sigma_E\} - \{d\sigma\}$  is required to maintain the stress components on the yield surface or compatible with the uniaxial stress-strain curve. The correct stress increment is computed with Equation A-26. The plastic load increments are computed from Equation A-14

$$\{dQ\} = \sum_{m=1}^M \int [B]^T \{d\sigma_0\} d vol \quad (A-30)$$

Elements are in the elastic state when  $\{d\sigma_0\} = 0$ . The total plastic-load



vector is then computed as

$$\{Q\}_I^i = \{Q\}_{I-1}^{i-1} + \{dQ\}_I \quad (A-31)$$

At the second stage of computation the new force system  $\{Q\}_I^i$  is added to the applied load vector and a new set of displacements is obtained. Again, some of the stresses are likely to exceed the yield criterion and a new set of plastic-load increments are computed. This iteration process is repeated until the change in the plastic-load vector is sufficiently small. See Figure A-2 for a uniaxial schematic of this iterative procedure and Figure A-3 for the mathematical algorithm. Consider points A, B, and C in Figure A-2. Point A is the state prior to the load increment. Point B is the state after the load increment has been applied and one "initial" stress iteration has been accomplished. Point C is the state of stress and strain sought after which satisfies equilibrium with external loads and compatibility with the material's stress-strain curve. Notice point B satisfies compatibility but not equilibrium since  $\{d\sigma\}_I \leq \{d\sigma_E\}_I$ .

## 5. INITIAL STRAIN METHOD

The initial strain method parallels the initial stress method somewhat and accordingly this development will begin just after Step 4 in the "Initial Stress" algorithm in Figure A-3.

The elastic-plastic material matrix  $[D_{EP}]$  is used as follows

$$\{d\epsilon^P\}_I = \{d\epsilon\}_I - [D]^{-1} [D_{EP}] \{d\epsilon\}_I \quad (A-32)$$

This plastic strain increment  $\{d\epsilon^P\}_I$  is then used to calculate a plastic force vector increment

$$\{dQ\}_I = \sum_{m=1}^M \int [B]^T [D] \{d\epsilon^P\}_I d vol \quad (A-33)$$

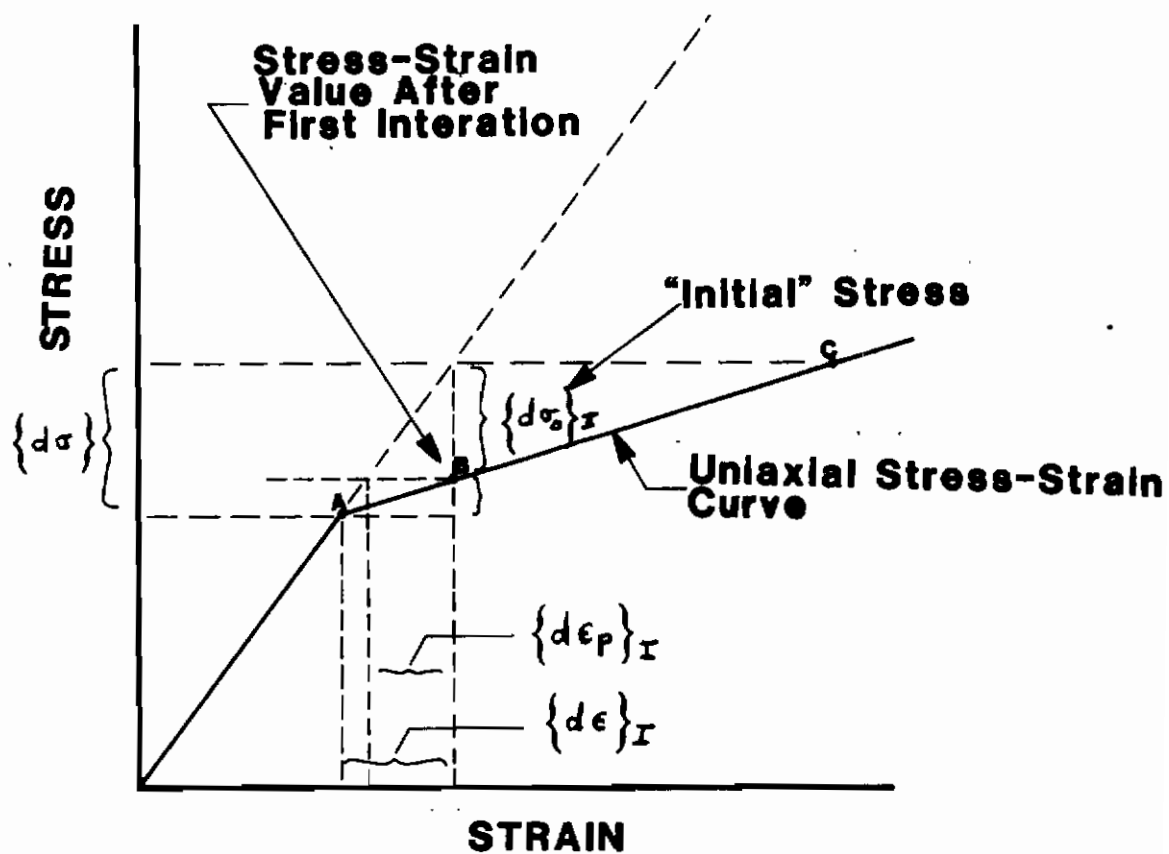


Figure A-2. Uniaxial "Initial" Stress Iteration Schematic

For Each Load Increment dP in Plastic Range 44

1.  $\{dU\}_I = [K]^{-1} (\{dP\} + \{dQ\}_{I-1})$
2.  $\{d\epsilon\}_I = [B] \{dU\}_I$
3.  $\{d\sigma_E\}_I = [D] \{d\epsilon\}_I$
4.  $\{\sigma'\}_I = \{\sigma\}_{I-1} + \{d\sigma_E\}_I$
5.  $\{d\sigma\}_I = [D_{EP}]_I \{d\epsilon\}_I$
6.  $\{d\sigma_o\} = \{d\sigma_E\}_I - \{d\sigma\}_I$
7.  $\{\sigma\}_I = \{\sigma'\}_I - \{d\sigma_o\}_I$   
 $\{\epsilon\}_I = \{\epsilon\}_{I-1} + \{d\epsilon\}_I$
8.  $\{dQ\}_I = \int [B]^T \{d\sigma_o\}_I dvol$
9. Continue steps 1→8 until  $\{dQ\}_I \approx \{dQ\}_{I-1}$

Figure A-3. Initial Stress Algorithm

This plastic force vector increment is added to the external force vector increment  $\{dP\}$  for the augmented global force vector used in the next iteration as follows:

$$\{dU\}_{I+1} = [K]^{-1} \{ \{dP\} + \{dQ\}_I \} \quad (A-34)$$

$$\{d\epsilon\}_{I+1} = [B] \{dU\}_{I+1} \quad (A-35)$$

The stress increment  $\{d\sigma\}$  is calculated as follows

$$\{d\sigma\}_{I+1} = [D] \{ \{d\epsilon\} - \{d\epsilon^p\}_I \} \quad (A-36)$$

Steps (1) - (4) of the Initial Stress algorithm and Equations A-32 through A-36 above are repeated until compatibility with the materials stress-strain curve is established. Compatibility is shown to be achieved after "n" iterations in Figure A-4. Also, compatibility would display itself by little or no change in the plastic strain increment between iterations. Note that equilibrium is continually satisfied in this initial strain method. This version of the initial strain method differs from Marcal (Reference 45) by the fact that iterations within a load increment are done globally rather than within each element as the "constant strain" method of iteration implies in Marcal's paper.

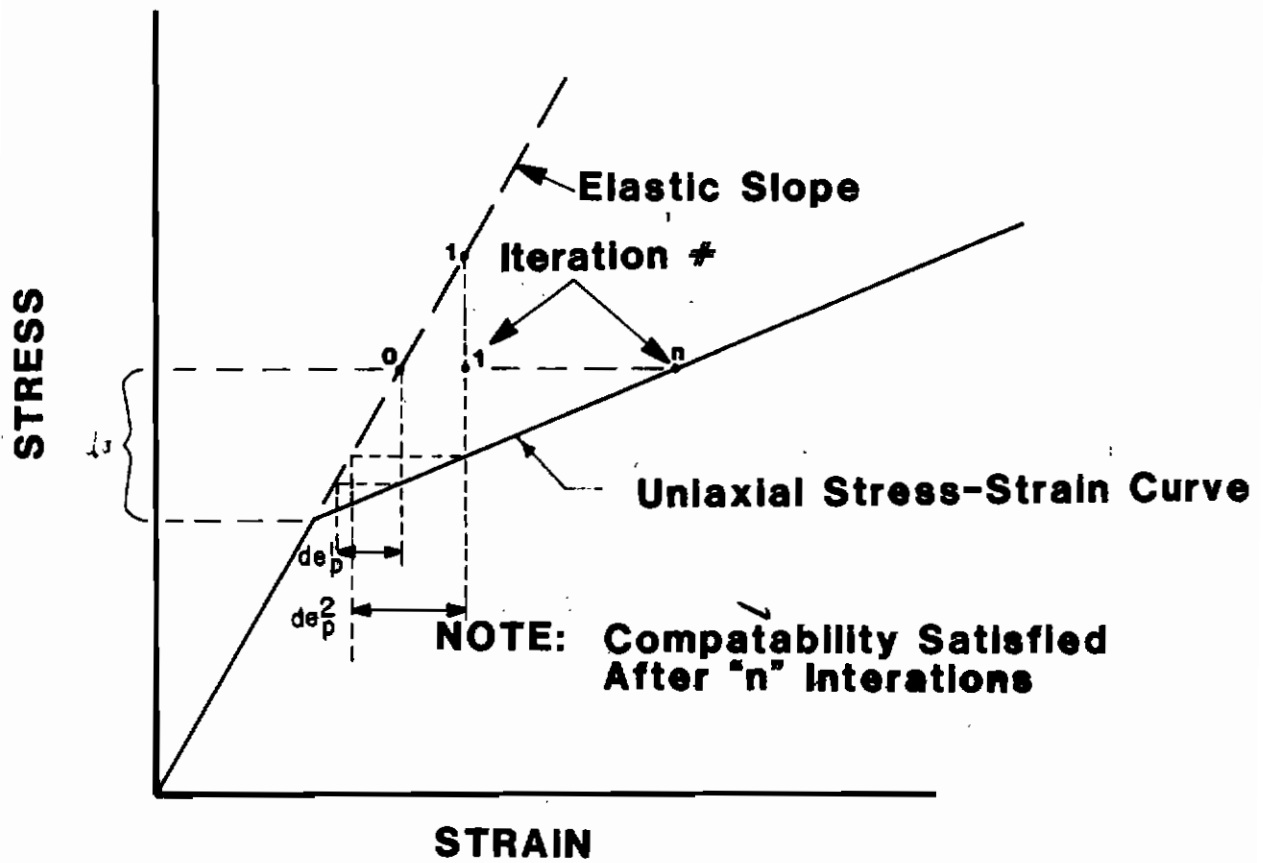


Figure A-4. Uniaxial Initial Strain Iteration Schematic

## APPENDIX B

ITERATIVE SOLUTION TECHNIQUE  
FOR NODE POINT DISPLACEMENTS

The matrix equation which governs the response of a discretized structure is

$$[K] \{U\} = \{P\} \quad (B-1)$$

where  $[K]$  is a symmetric positive-definite  $n \times n$  matrix,  $\{U\}$  is the unknown node point displacement vector, and  $\{P\}$  is a known load vector. In the finite element method for structural analysis, the matrix  $[K]$  is usually highly banded and if stored in compacted form (i.e., only nonzero terms retained) requires much less space in the computer than the product  $n \times n$  reflects. Also, if there are changing boundary conditions, such as freeing nodes to simulate crack growth, then the  $[K]$  matrix must be recomputed. A solution technique that works well with compacted  $[K]$  matrices and conveniently admits boundary condition changes, is the Gauss-Seidel iterative technique with over-relaxation (Reference 14). This technique may be implemented in the following manner (Reference 87). Consider Equation B-1 rewritten as

$$[K] \{U\} = \begin{bmatrix} S_{XX} & S_{XY} \\ S_{YX} & S_{YY} \end{bmatrix} \begin{Bmatrix} U_x \\ U_y \end{Bmatrix} = \begin{Bmatrix} P_x \\ P_y \end{Bmatrix} \quad (B-2)$$

where  $U_x$  and  $U_y$  represent node point displacement vectors in the  $x$  and  $y$  direction respectively,  $P_x$  and  $P_y$  represent the node force vectors in the  $x$  and  $y$  direction respectively. The submatrices  $S_{XX}$ ,  $S_{XY}$ ,  $S_{YX}$ , and  $S_{YY}$  in the matrix  $[K]$  have dimensions  $\frac{n}{2} \times \frac{n}{2}$ , but due to their bandedness can be compacted to a matrix which is  $\frac{n}{2} \times 9$ . The dimension 9 minus 1 reflects how many adjacent nodes can be connected to any given node.

AFWAL-TR-80-4140

This is not very restrictive since triangular finite elements develop undesirable aspect ratios if there are more than eight nodes connected to any one node.

Appropriate terms of the matrix [K] are retrieved from the compacted submatrices with the help of a matrix NP and a vector NAP. The vector NAP has the dimension  $\frac{n}{2}$  and the matrix NP has the dimension  $\frac{n}{2} \times 9$ . The Ith component of NAP or NAP(I) stores the number of adjacent node points connected to node point I. The (I, J) component of NP or NP(I,J) stores the address of the terms in the submatrices associated with the Jth adjacent node point connected to node point I. Note that for node I, J may go from 1 to NAP(I).

Consider the governing equation for node point I displacements written as

$$\begin{bmatrix} S_{XX}(I, 1) & S_{XY}(I, 1) \\ S_{YX}(I, 1) & S_{YY}(I, 1) \end{bmatrix} \begin{Bmatrix} U_x(I) \\ U_y(I) \end{Bmatrix} = \begin{Bmatrix} P_x(I) \\ P_y(I) \end{Bmatrix} - \sum_{J=2}^{NAP(I)} \begin{bmatrix} S_{XX}(I, J) & S_{XY}(I, J) \\ S_{YX}(I, J) & S_{YY}(I, J) \end{bmatrix} \begin{Bmatrix} U_x(J) \\ U_y(J) \end{Bmatrix} \quad (B-3)$$

If the right-hand side of Equation B-3 is defined as the vector  $\begin{Bmatrix} FRX \\ FRY \end{Bmatrix}$  then solving for the displacements at node I yields

$$\begin{Bmatrix} U_x(I) \\ U_y(I) \end{Bmatrix} = \begin{bmatrix} S_{XX}(I, 1) & S_{XY}(I, 1) \\ S_{YX}(I, 1) & S_{YY}(I, 1) \end{bmatrix}^{-1} \begin{Bmatrix} FRX \\ FRY \end{Bmatrix} \quad (B-4)$$

Note that the matrix to be inverted in Equation B-4 is only a  $2 \times 2$ . Also since this is the only place these terms of the submatrices are used this  $2 \times 2$  may be inverted and its components stored in their original submatrix locations.

To incorporate an over-relaxation factor, Equation B-4 is modified as follows

$$\begin{Bmatrix} \Delta U_x(I) \\ \Delta U_y(I) \end{Bmatrix}^m = \begin{bmatrix} S_{XX}(I, 1) & S_{XY}(I, 1) \\ S_{YX}(I, 1) & S_{YY}(I, 1) \end{bmatrix}^{-1} \begin{Bmatrix} FRX \\ FRY \end{Bmatrix}^m - \begin{Bmatrix} U_x(I) \\ U_y(I) \end{Bmatrix}^{m-1} \quad (B-5)$$

where the superscripts  $m$  and  $m-1$  refer to iteration number. The left-hand side of Equation B-5 is the change in displacements between iterations without applying an over-relaxation factor. But the new total displacements for iteration  $m$  using an over-relaxation factor are

$$\begin{Bmatrix} U_x(I) \\ U_y(I) \end{Bmatrix}^m = \begin{Bmatrix} U_x(I) \\ U_y(I) \end{Bmatrix}^{m-1} + X \text{ FAC} \begin{Bmatrix} \Delta U_x(I) \\ \Delta U_y(I) \end{Bmatrix}^m \quad (B-6)$$

where XFAC is the over-relaxation factor which normally ranges from 1.8 to 1.9 for structural analysis.

Convergence of these iterations is checked by computing an effective force unbalance term, SUM, defined as

$$SUM = \sum_{I=1}^{n/2} [|\Delta U_x(I) * S_{XX}(I,1)| + |\Delta U_y(I) * S_{YY}(I,1)|] \quad (B-7)$$

If SUM becomes less than a specified small value,  $\theta$ , iterations are stopped and the node point displacement solution is obtained. The value of  $\theta$  is chosen based on examining solutions for various sizes of  $\theta$ . A good starting value for  $\theta$  is one tenth of the applied load. The final  $\theta$  is then chosen based on the amount of accuracy desired.

Displacement boundary conditions are easily input to this solution routine by simply specifying the desired node point displacements and then



AFWAL-TR-80-4140

require the iteration algorithm to skip over the node displacement equations which have fixed displacements. Likewise, if a fixed node is released during the analysis such as for modeling crack growth, this node's displacement equation may be reactivated in the iteration algorithm.

Convergence of this solution technique (i.e., when  $SUM \leq \theta$ ) is dependent on the initial guess for the node displacements. Usually for convenience all unknown displacements are initialized at zero. However, for each succeeding solution, such as in a nonlinear incremental analysis, much better initial displacement values are available from the prior solution. These initial displacements from prior solutions significantly reduce the number of iterations to convergence.

## APPENDIX C

### THE J AND C\* INTEGRALS

#### 1. J INTEGRAL

Rice's J integral is defined as

$$J = \oint_{\Gamma} \left[ W(\epsilon_{ij}) dy - T_i \frac{\partial u_i}{\partial x} ds \right] \quad (C-1)$$

where

$$W(\epsilon_{ij}) = \int_0^{\epsilon_{mn}} \sigma_{ij} d\epsilon_{ij} \quad (C-2)$$

and  $\Gamma$  is a closed loop around the crack tip as shown in Figure 2.

Expanding J and integrating along a rectilinear path in the x and y directions results in

$$J = \oint_{\Gamma} \left[ \left( W - \sigma_x \frac{\partial u}{\partial x} - \sigma_{xy} \frac{\partial v}{\partial x} \right) dy + \left( \sigma_{xy} \frac{\partial u}{\partial x} + \sigma_y \frac{\partial v}{\partial x} \right) dx \right] \quad (C-3)$$

The following describes a numerical procedure for calculating the J integral with a finite element program that incorporates constant strain triangles. Consider Figure C-1 which is a region of elements taken from a finite element model of a cracked geometry. Paths 1 and 2 are two possible paths. The contribution to Path 1 from Element 2 is

$$\Delta J_{\text{Elem 2}}^{\text{Path 1}} = \left[ W(2) - \sigma_x(2) \frac{\partial u}{\partial x}(2) - \sigma_{xy}(2) \frac{\partial v}{\partial x}(2) \right] \Delta y \quad (C-4)$$

where the number inside parenthesis refers to the element number these values came from. A similar contribution would come from Element 5 for Path 1. Path 2 which also runs through Element 2 would also have the above contribution from Element 2 but as Path 2 turns and runs along

AFWAL-TR-80-4140

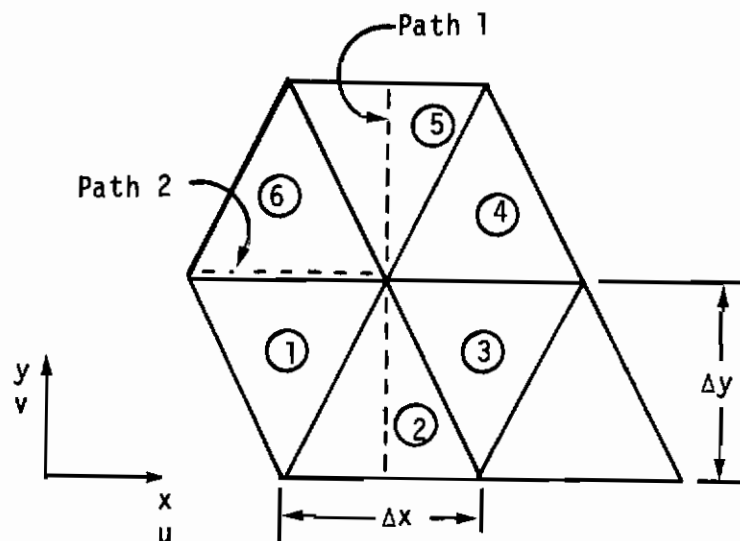


Figure C-1. J Integral Paths within a Constant Strain Triangular Finite Element Model

the border of Elements 6 and 1 the following is the contribution

$$\begin{aligned} \Delta J_{\text{Path 2}} \\ \text{Elements} \\ 1 \text{ \& 6}} &= [\sigma_{xy} (6) \frac{\partial u}{\partial x} (6) + \sigma_y (6) \frac{\partial v}{\partial x} (6)] \left( \frac{-\Delta x}{2} \right) \\ &+ [\sigma_{xy} (1) \frac{\partial u}{\partial x} (1) + \sigma_y (1) \frac{\partial v}{\partial x} (1)] \left( \frac{-\Delta x}{2} \right) \end{aligned} \quad (C-5)$$

Notice in this case an average of the stresses and strains in the two elements is taken by effectively running half the element length in Element 6 and half in Element 1.

The strain energy term  $W_{(2)}$  in Equation C-4 is calculated as follows

$$W(2) = \frac{1}{2} \sigma_{ij} (2) \epsilon_{ij}^E (2) + \int_0^P \epsilon_{mn}^P \sigma_{ij} \quad (C-6)$$

Although these equations are shown for specific element numbers their form is used for all elements along the J integral path.

## 2. C\* INTEGRAL

The C\* Integral (Reference 23) defined as

$$C^* = \oint_{\Gamma} [W^* dy - T_i \frac{\partial \dot{u}_i}{\partial x} ds] \quad (C-7)$$

where

$$W^* = \int_0^{\cdot P} \epsilon_{mn}^{\cdot P} \sigma_{ij} d \epsilon_{ij}^{\cdot P} \quad (C-8)$$

and  $\Gamma$  is the same type of path as for the J integral.  $C^*$  may be obtained by replacing strain and displacement in the J integral with strain rate and displacement rate respectively. The rational behind this is based

AFWAL-TR-80-4140

on the assumption that the material being analyzed behaves as a creeping solid such that

$$\dot{\epsilon}^p = \gamma (\sigma)^\beta \quad (C-9)$$

or in a multiaxial sense

$$\sigma_{ij} = \frac{\partial W^* (\dot{\epsilon}_{ij}^p)}{\partial \dot{\epsilon}_{ij}^p} \quad (C-10)$$

where  $W^*$  was defined in Equation C-8. Notice Equation C-9, which is considered a plastic strain rate, makes no provision for admitting elastic strain rates. Hence the claim of path independence for the  $C^*$  integral can only be approached in a realistic elastic-plastic material once the stresses have reached a steady state value (i.e.,  $\dot{\sigma}_{ij} = 0$ ). With this restriction on stresses,  $C^*$  may also be defined as  $\dot{J}$  or the time rate of change of the  $J$  integral. In general  $\dot{J}$  would include the time derivatives of stress and traction but if they are restricted to zero then  $\dot{J}$  is equal to  $C^*$  for a creeping solid. Also with  $\dot{\sigma}_{ij}$  equal to zero, Equation C-8 may be directly integrated to

$$W^* = \sigma_{ij} \dot{\epsilon}_{ij}^p \quad (C-11)$$

Using this form of  $W^*$ ,  $C^*$  may be numerically calculated in the same fashion as the  $J$  integral with the exception of using strain rates and displacement.

## APPENDIX D

### DETERMINATION OF BODNER MATERIAL MODEL CONSTANTS

This appendix describes how each of the material constants for the Bodner-Partom material model can be determined. Normally high costs and material shortages prevent obtaining more than one or two stress-strain curves and the same number of creep tests. Ideally, to best characterize the material, several stress-strain curves should be generated over a wide range of strain rates, similar to Figure 5. Likewise, several creep tests should be performed over a wide spectrum of stress levels.

In general the Bodner material constants are dependent on temperature. However, the temperature dependence is suppressed by performing the material characterization tests (i.e., stress-strain and creep) at the same temperature that the Bodner model will be applied.

To determine the Bodner constants from uniaxial test data, the Bodner equations are written in uniaxial form as follows: (the total strain rate is the sum of plastic and elastic strain rates)

$$\dot{\epsilon} = \frac{\dot{\sigma}}{E} + \dot{\epsilon}^p \quad (D-1)$$

and the plastic strain rate for uniaxial tension is

$$\dot{\epsilon}^p = \frac{2}{\sqrt{3}} D_0 \exp\left[-\frac{1}{2}\left(\frac{Z}{\sigma}\right)^{2n} \frac{n+1}{n}\right] \quad (D-2)$$

where

$$Z = Z_1 - (Z_1 - Z_0) \exp[-mW_p] \quad (D-3)$$

$$\dot{W}_p = \sigma \dot{\epsilon}^p + \frac{\dot{Z}_{rec}}{m(Z_1 - Z)} \quad (D-4)$$

$$\dot{Z}_{\text{rec}} = -A \left( \frac{Z - Z_i}{Z_1} \right)^r Z_1 \quad (\text{D-5})$$

over small time intervals, such as a typical stress-strain test at  $10^{-3} \text{ sec}^{-1}$  strain rate, the recovery term,  $\dot{Z}_{\text{rec}}$ , may be ignored and then

$$\dot{W}_p = \sigma \dot{\epsilon}_p \quad (\text{D-6})$$

Since test data can be resolved into the forms,  $\dot{\epsilon}_p$  and  $\sigma$ , Equation D-2 is solved for  $Z$  which then is a function of  $\dot{\epsilon}_p$  and  $\sigma$  as follows

$$Z = \sigma \left[ \frac{2n}{n+1} \ln \left( \frac{2}{\sqrt{3}} \frac{D_0}{\dot{\epsilon}_p} \right) \right]^{\frac{1}{2n}} \quad (\text{D-7})$$

The viscoplastic material constants in these equations are broken into "short time response" and "creep" groupings for determination.

## 1. SHORT TIME RESPONSE CONSTANTS

The short time response constants for the Bodner model are  $D_0$ ,  $n$ ,  $m$ ,  $Z_0$ ,  $Z_1$ . These constants are primarily determined by using stress-strain test data.

The constant  $D_0$  is normally assigned the value of  $10^4 \text{ sec}^{-1}$ . For high strain rate applications,  $D_0$  may be set higher (e.g.,  $10^6 \text{ sec}^{-1}$ ) which would result in small changes to the other constants.

The constant  $n$  is directly related to the model's strain rate sensitivity. High  $n$  values reflect low strain rate sensitivity and vice versa. Changes in  $n$  affect the stress values for a given strain rate by shifting up or down the family of stress-strain curves, but the shape of the curve is preserved. The value of  $n$  is determined in an

iterative fashion. The first estimate of  $n$  should be between 1 and 10 based on past material modeling efforts (Reference 8). Plots of  $Z$  versus  $W_p$  are then made by simultaneous use of each stress-strain curve, Equations D-1, D-6, and D-7. The value of  $n$  is then adjusted with the objective of making all  $Z$  versus  $W_p$  curves from each stress-strain test fall on top one another. This value of  $n$  will then satisfy the requirement that  $Z$  is a single value function of  $W_p$  as given in Equation D-3.

The first approximation of  $Z_0$  can also be determined from Equation D-7. A small value of  $\dot{\epsilon}_p$  (e.g.,  $10^{-6} \text{ sec}^{-1}$ ) and the lowest apparent initial yield stress from the stress-strain test data are substituted into Equation D-7. The resulting value of  $Z$  is defined as  $Z_0$ . Note that  $Z_0$  is the primary constant that determines the stress level at which significant plastic straining (i.e.,  $\dot{\epsilon}^p \geq 10^{-6} \text{ sec}^{-1}$ ) begins.

The constants  $Z_1$  and  $m$  are determined by rewriting Equation D-3 as

$$\ln (Z_1 - Z) = \ln (Z_1 - Z_0) - m W_p \quad (\text{D-8})$$

An iterative process is now begun to determine  $Z_1$ . The first estimate of  $Z_1$  should be larger than  $Z_0$  (e.g.,  $1.5 Z_0$ ) since  $Z_1$  is the maximum value for  $Z$ . By incorporating this estimate of  $Z_1$ , a plot of  $\ln (Z_1 - Z)$  versus  $W_p$  is made based again on stress-strain test data, Equations D-1, D-6, and D-7. This should approximate a straight line whose slope is the constant  $m$  and extrapolation of the line to  $W_p = 0$  provides a value of  $Z_0$ . If this  $Z_0$  obtained graphically does not agree with the previous value for  $Z_0$ , adjust  $Z_1$  accordingly and reiterate.

These values for  $n$ ,  $m$ ,  $Z_0$ , and  $Z_1$  which primarily govern the short-term stress-strain behavior should be input to a computer program



that numerically integrates Equations D-1 through D-4. Stress-strain predictions from the model should be made for each experimental strain rate to see how good the fit is. Only minor adjustments to the short-time-response constants should be necessary to best fit test data.

## 2. CREEP CONSTANTS

The creep constants for the Bodner model are  $Z_i$ ,  $A$ , and  $r$ . These constants are determined based on data from at least two creep tests at different stress levels.

During secondary creep, when plastic strain rate is approximately constant, it follows from Equation D-7 that  $Z$  must also be a constant. In addition, if  $Z$  is a constant it follows from Equation D-3 that  $\dot{W}_p$  is a constant which makes  $\dot{W}_p = 0$ . Hence, with  $\dot{W}_p = 0$  in Equation D-4 and combining with Equation D-5

$$\sigma \dot{\epsilon}^p = A \left( \frac{Z - Z_i}{Z_1} \right)^r Z_1 / m(Z_1 - Z) \quad (D-9)$$

The constant  $Z_i$  represents the minimum value for  $Z$  corresponding to secondary creep. If creep occurs below the apparent yield stress implied by  $Z_0$ , the value of  $Z_1$  must be less than  $Z_0$ . Moreover,  $Z_i$  must be less than or equal to the smallest value of  $Z$  from Equation D-7 when using creep test data (i.e.,  $\dot{\epsilon}^p$  and  $\sigma$ ). After selecting a value for  $Z_i$ , the constants  $A$  and  $r$  can be determined after rewriting Equation D-9 in terms of natural logarithms

$$\ln(\sigma \dot{\epsilon}^p) + \ln[m(Z_1 - Z)] = \ln(A Z_1^r) + r \ln \left( \frac{Z - Z_i}{Z_1} \right) \quad (D-10)$$

Stress and plastic strain rate are substituted into Equation D-10 along with the appropriate  $Z$  from Equation D-7 and creep test data. With data from creep tests at two different stress levels two linear equations in

AFWAL-TR-80-4140

terms of the two unknowns A and r are developed. The constants A and r are then determined by simultaneous solution of these two equations based on Equation D-10 and creep test data.

The complete Bodner model should then be tried out in a computerized numerical integration scheme in an effort to make final adjustments to the constants for a best fit to the test data.

It became apparent to the author that in working with this material model a sensitivity study is required in order to see the effect of changes in the respective constants on creep crack growth. Yet it is felt that the results and conclusions presented in the main body of this report provide realistic directions and trends of creep crack growth.